

Title	Development of thermoelectric materials and micro-devices for cooling and power generation
Authors	Lal, Swatchith
Publication date	2020-12
Original Citation	Lal, S. 2020. Development of thermoelectric materials and micro-devices for cooling and power generation. PhD Thesis, University College Cork.
Type of publication	Doctoral thesis
Rights	© 2020, Swatchith Lal. - https://creativecommons.org/licenses/by-nc-nd/4.0/
Download date	2025-10-06 19:02:34
Item downloaded from	https://hdl.handle.net/10468/11453

Ollscoil na hÉireann, Corcaigh
National University of Ireland, Cork



**Development of Thermoelectric Materials and Micro-
Devices for Cooling and Power Generation**

Thesis presented by

Swatchith Lal

for the degree of

Doctor of Philosophy

University College Cork

[Tyndall National Institute]

Supervisor: Dr. Kafil M. Razeeb

DECEMBER 2020

Declaration

This dissertation is the result of the work carried out in Advanced Energy Materials Group at Tyndall National Institute from January 2016 to August 2020.

This is to certify that the work I am submitting is my own and has not been submitted for another degree, either at University College Cork or elsewhere. All external references and sources are clearly acknowledged and identified within the contents. Except where otherwise stated this dissertation is the result of my own work and is not substantially the same as any I have already submitted, or that I am in the process of submitting, for any degree either at University College Cork or elsewhere.

Swatchith Lal
Tyndall National Institute,
University College Cork,
December 2020

Abstract

Thermoelectric materials have been widely used for solid-state cooling (as thermoelectric cooler) and power generation (as thermoelectric generator) applications. Integration of thermoelectric thin-film materials into micro-device fabrication offers various advantages compared to bulk thermoelectric devices such as miniaturized size, high-density integration and substantial reduction of the material usage that helps in reducing the weight of the system.

Thermoelectric coolers play a vital role in optoelectronic devices. Active photonic device (e.g. lasers) generate incredibly high heat flux levels ($\sim 10 \text{ kW/cm}^2$) that must be efficiently removed to maintain their performance and reliability; furthermore, active photonic devices must be controlled with a precision of $\pm 0.1 \text{ }^\circ\text{C}$. Today's photonic integrated circuits (PICs) employ macro thermoelectric coolers (TECs) that are inefficient in the thermal management of the device and cannot scale with the growing trends of miniaturisation and high-density integration. On the other hand, micro-thermoelectric coolers (μ -TECs) integrated directly on the laser or other photonic component can more efficiently perform the thermal management of the device. Similarly, these micro-thermoelectric devices can be applied to convert heat into usable electricity as a thermoelectric generator, which has a wide range of applications including wearable electronics and biomedical devices. These micro-thermoelectric generators (μ -TEGs) can convert the body heat to usable electrical energy which can, in turn, be used for powering various wearable vital health monitoring systems, particularly using the low-temperature gradients.

This thesis deals with the development of high-performance room temperature thermoelectric materials using electrodeposition technique that offers cost-effectiveness, ease of process control and industrial batch production compatibility. Further, this work aims to integrate the developed materials in the micro-thermoelectric devices, both for cooling and power generation, particularly using available low-temperature gradients near room temperature regimes. As part of this work, p-type BiSbTe material has been developed using a pulse amperometry technique employing a suitable nitric acid bath, and the thermoelectric properties of the developed material are enhanced using additives, particularly sodium dodecyl sulfate surfactant. From the following investigations, it was observed that the overall power factor of the developed materials with the surfactant was 149% higher than the material with no surfactant added into the system due to the

densification of the films. Later, this material is optimised using an annealing time-temperature profile to achieve better thermoelectric properties. The inclusion of the Te material layer in between the BiSbTe layers prevented the loss of Te during annealing and helped in maintaining the proper stoichiometry of the material. Using this annealing study, the charge carrier concentration and mobility of the materials are optimised for the higher performance, which led to an increase in the power factor of the material from $11 \mu\text{W}/\text{mK}^2$ to $225 \mu\text{W}/\text{mK}^2$, when annealed for the duration of 1 hr at 350°C in the N_2 atmosphere.

As a part of the n-type material development, Cu doped BiTe and Cu doped Te have been developed, both exhibiting significantly improved thermoelectric properties for the electrodeposited materials. Both the materials showcased a crystal symmetry breakdown beyond a certain percentage of copper inclusion in the system, which has led to a significant enhancement of the thermoelectric properties of the material. Cu doped BiTe and Cu doped Te showed a power factor of $3.02 \text{ mW}/\text{mK}^2$ and $5.60 \text{ mW}/\text{mK}^2$ respectively, which are one of the best values reported so far.

The developed p- and n-type materials are integrated in a silicon-based micro-thermoelectric device for both cooling and power generation applications. Two different approaches to device fabrication have been used. The first approach deals with the reduction of overall cost of the device fabrication, for which flip-chip bonding approach has been undertaken where p- and n-type materials are fabricated on different wafers, which reduced the overall lithographic processing. In the second approach, both p- and n-type materials are fabricated on a single wafer using multiple lithographic steps. This single wafer approach has various advantages such as minimized electrical contact resistances and improved thermal contact over the first method. The micro-devices developed using this method has been employed for both cooling and power generation applications and has been thoroughly investigated. The devices fabricated using flip-chip bonding generated an output voltage of 90 mV for a 10 K temperature gradient with an average electrical resistance of 0.87Ω for individual thermoelectric leg pair. The average electrical resistance was dropped to 0.28Ω for device fabricated using a single wafer approach. An average cooling of 2 K was observed for the devices in cooling mode. The improved thermoelectric materials and optimized fabrication of micro-thermoelectric devices makes them a promising system for both cooling and power generation applications.

List of Publications

List of Journal Publications:

- [1] **Swatchith Lal**, D. Gautam, K. M. Razeeb, The Impact of Surfactant Sodium Dodecyl Sulfate on the Microstructure and Thermoelectric Properties of p-type $(\text{Sb}_{1-x}\text{Bi}_x)_2\text{Te}_3$ Electrodeposited Films, **ECS Journal of Solid State Science and Technology**, 2017, 6, N3017.
- [2] **Swatchith Lal**, D. Gautam, K. M. Razeeb, Optimization of annealing conditions to enhance thermoelectric performance of electrodeposited p-type BiSbTe thin films, **APL Materials**, 2019, 7, 031102.
- [3] **Swatchith Lal**, D. Gautam, K. M. Razeeb, Fabrication of micro-thermoelectric devices for power generation and the thermal management of photonic devices, **Journal of Micromechanics and Microengineering**, 2019, 29, 065015.
- [4] **Swatchith Lal**, D. Gautam, K. M. Razeeb, Enhanced thermoelectric properties of electrodeposited Cu-doped Te films, **ACS Applied Energy Materials**, 2020, 3(4): 3262–3268.
- [5] Abhishek Singh Dahiya, Jerome Thireau, Jamila Boudaden, **Swatchith Lal**, Umair Gulzar, Yan Zhang, Thierry Gil, Nadine Azemard, Peter Ramm, Tim Kiessling, Cian O’Murchu, Fredrik Sebelius, Jonas Tilly, Colm Glynn, Shane Geary, Colm O’Dwyer, Kafil M. Razeeb, Alain Lacampagne, Benoit Charlot and Aida Todri-Sanial. Energy autonomous wearable sensors for smart healthcare: a review, **Journal of the Electrochemical Society**, 2020, 167(3): 037516.
- [6] N. Padmanathan, **Swatchith Lal**, D. Gautam, K. M. Razeeb, Amorphous framework in electrodeposited CuBiTe thermoelectric Thin-films with High Room Temperature performance, **ACS Applied Electronic Materials** (In press).
DOI: <https://doi.org/10.1021/acsaelm.1c00063>.
- [7] Simon Corbett, D. Gautam, **Swatchith Lal**, Kenny Yu, Naveen Balla, Graeme Cunningham, Kafil M. Razeeb, Ryan Enright, David McCloskey, Electrodeposited thin-film micro-thermoelectric coolers with extreme heat flux handling and microsecond time response, **ACS Applied Materials & Interfaces**, 2021, 13(1): 1773–1782.

[8] Amit Tanwar, **Swatchith Lal** and Kafil M. Razeeb, Structural Design Optimization of Micro-Thermoelectric Generator for Wearable Biomedical Devices, **Energies** 2021, 14(8):2339.

[9] **Swatchith Lal**, Amit Tanwar and Kafil M. Razeeb, Design and fabrication of cross-plane micro thermoelectric devices for human body wearable applications, (under preparation).

[10] Amit Tanwar, **Swatchith Lal** and Kafil M. Razeeb, Design and development of micro-thermoelectric characterization setup (under preparation).

List of Conference Publications:

[1] **Swatchith Lal**, D. Gautam, K. M. Razeeb, Effect of annealing on the thermoelectric properties of electrodeposited BiSbTe films, Meeting abstracts, MA2017-02(27);1167.

[2] **Swatchith Lal**, D. Gautam, K. M. Razeeb, Efficient thermal management of photonic device using micro thermoelectric coolers, **International Conference and Exhibition on Integration Issues of Miniaturized Systems** 2017, SSI 2017, Pages 403-406.

[3] **Swatchith Lal**, D. Gautam, K. M. Razeeb, Fabrication of micro-thermoelectric cooler for the thermal management of photonic devices, 2018 **IEEE 18th International Conference on Nanotechnology (IEEE-NANO)**, Cork, Ireland, 2018.

[4] Naveen K. Balla, Kenny Yu, **Swatchith Lal**, Devendraprakash Gautam, Kafil M. Razeeb, Ronan Frizzel, Ryan Enright, David McCloskey, Quantifying thermal conductance of thin-film thermoelectrics using frequency-domain thermoreflectance, **HEFAT 2019**, 22-24 July 2019, Wicklow, Ireland.

[5] Amit Tanwar, Rajvinder Kaur, **Swatchith Lal** and Kafil M. Razeeb, Finite element analysis of miniature thermoelectric cooler for the thermal management of Si-based photonic integrated circuits, **240th ECS Meeting**, 2021 (Submitted).

Acknowledgements

I take this opportunity to sincerely thank my supervisor Dr. Kafil M. Razeed who not only guided me in pushing my research in the correct direction but also enriched me as a person by continually enlightening with his broad knowledge. The personal support extended by him during my lowest points and encouragement to perform better was the biggest support, for which I will always be grateful. Apart from research, he also mentored me in project management and developing my networking skills.

I would like to acknowledge funding support of my work from the European Union's Horizon 2020-funded projects "Thermally Integrated Smart Photonics Systems (TIPS)", under the Grant Agreement No. 644453 and "SmartVista" under grant agreement no. 825114.

I am greatly thankful to Dr. Devenraprakash Gautam for sharing his valuable time and expertise to guide me in thermoelectric materials analysis and being a great source of inspiration for me.

I would also like to extend my special thanks to Prof. Saibal Roy for always being a supportive mentor and for the fruitful discussions regarding the PhD progresses over these years. His valuable feedback and support through half-yearly and annual reports, along with his technical expertise, immensely helped my overall work.

I would like to thank my group members Dr. Padmanathan Narayanasamy, Han Shao, Vasu Prasadam and Amit Tanwar for their constant support, friendship and sharing their knowledge in my PhD journey.

I thank the Specialty Products & Services (SP&S) for their expertise and support in the mask design, fabrication, packaging and characterization. A special mention to Richard Murphy, Dan O'Connell, Krimo Khalfi, Ann Foley, Finbarr Waldron, Paul Tassie, Joe O'Brien and many others.

I would like to especially thank Kankana Paul for being a well-wisher and supporting throughout my journey. I thank Dr. Dhiman Mallick and Dinesh R. Gawade for their unconditional friendship and being great flatmates.

Special thanks to Yashdeep, Sanjeev Kumar, Pranay Poddar, Tuhin Maity, Ricky Antony, Sarita and Saroj for the lovely times we had over this journey.

I will always be grateful for the encouragement, support, belief, and love from my family. I would like to thank my father Shri. Sunder Lal, who always believed in me and pushed me for my dreams and my mother Sharada Sunder for her unconditional love. My sister Swarnitha, the strong pillar of my family for always encouraging me and I would like to thank Hari Prasad, my brother-in-law for being silent support and taking care of my family in my absence. During this journey, I was blessed with my nephew Nidhish Sunder who has been a constant source of joy since his birth. This accomplishment is the sole result of their sacrifice and belief in me.

Finally, I would like to thank all my friends in Cork who have supported me over the years.

To My Father

Table of contents

Declaration	i
Abstract	ii
List of Publications	iv
Acknowledgements	vi
Table of contents	ix
List of figures	xiv
List of tables	xix
Chapter 1: Introduction	1
1.1 Introduction	1
1.2 Thermoelectric cooling.....	1
1.3 Thermoelectric power generation.....	4
1.4 Research Objectives	7
1.5 Thesis structure.....	8
1.6 References	10
Chapter 2: Electrodeposition of thermoelectric material and micro-device fabrication: State-of-the-art	13
2.1 Introduction	13
2.2 Thermoelectric material theory	13
2.3 Bismuth telluride thermoelectric material.....	19
2.4 Electrochemical Deposition.....	21
2.4.1 Basic setup of three-electrode cell	22
2.4.2 Cyclic voltammetry	23
2.4.3 Pulsed Electrodeposition.....	24
2.4.4 Constant potential and constant current deposition	25
2.5 Electrodeposition of Bismuth Telluride	25

Development of Thermoelectric Materials and Micro-Devices for Cooling and Power Generation

2.6	State-of-the-art material.....	26
2.7	State-of-the-art device	34
2.7.1	Literature review on thermoelectric generator devices:.....	34
2.7.2	State-of-the-Art Vertical structure μ TED	36
2.8	References	42
Chapter 3: The impact of the surfactant sodium dodecyl sulfate on the microstructure and thermoelectric properties of p-type $(\text{Sb}_{1-x}\text{Bi}_x)_2\text{Te}_3$ electrodeposited films.....		
3.1	Abstract.....	49
3.2	Introduction	49
3.3	Experimental.....	51
3.4	Results and Discussion	52
3.5	Conclusions	58
3.6	References	58
3.7	Supplementary material.....	61
Chapter 4: Optimization of annealing conditions to enhance thermoelectric performance of electrodeposited p-type BiSbTe thin films.....		
4.1	Abstract.....	63
4.2	Introduction	63
4.3	Experimental.....	65
4.4	Results and Discussion	67
4.4.1	Effect of annealing temperature on TE properties	68
4.4.2	Effect of annealing time of TE properties.....	73
4.5	Conclusion.....	78
4.6	References	78
Chapter 5: Amorphous framework in electrodeposited CuBiTe thermoelectric Thin-films with High Room Temperature performance.....		
5.1	Abstract.....	82

Development of Thermoelectric Materials and Micro-Devices for Cooling and Power Generation

5.2	Introduction	82
5.3	Experimental.....	85
5.3.1	Electrodeposition of CuBiTe.....	85
5.3.2	Material Characterization.....	86
5.4	Results and Discussion	86
5.4.1	Cyclic voltammetry	86
5.4.2	Morphology and Phase Analysis.....	88
5.4.3	Raman Analysis	90
5.4.4	XPS Analysis	92
5.4.5	Thermoelectric Studies.....	94
5.4.6	Structure Property Relation.....	97
5.5	Conclusion.....	99
5.6	References	99
5.7	Supplementary material.....	107
Chapter 6: Enhanced thermoelectric properties of electrodeposited Cu-doped Te films		112
6.1	Abstract.....	112
6.2	Introduction	112
6.3	Experimental.....	114
6.4	Results and Discussion	115
6.4.1	Electrochemical Deposition	115
6.4.2	Structural Properties.....	117
6.4.3	Thermoelectric Properties	121
6.5	Conclusion.....	123
6.6	References	124
6.7	Supplementary material.....	128
Chapter 7: Fabrication of micro-thermoelectric devices for power generation and the thermal management of photonic devices		135

Development of Thermoelectric Materials and Micro-Devices for Cooling and Power Generation

7.1	Abstract.....	135
7.2	Introduction	135
7.3	Experimental Procedure	137
7.3.1	Thermoelectric pillars deposition.....	137
7.3.2	The separation layer and bonding material deposition	138
7.4	Fabrication.....	139
7.5	Results and Discussion.....	143
7.5.1	Challenges and feasible solutions	143
7.5.2	Structural and electrical characterization.....	146
7.6	Conclusion.....	150
7.7	References	151
Chapter 8: Cross plane Micro-Thermoelectric device: Fabrication, Simulation and Evaluation		154
8.1	Introduction	154
8.2	Material fabrication	156
8.3	Device Fabrication.....	157
8.4	Simulations	160
8.5	Device characterisation	166
8.5.1	Cooling Performance	167
8.5.2	Power Generation performance.....	169
8.6	Conclusion.....	171
8.7	References	172
Chapter 9: Conclusions and Future Works.....		177
9.1	Thesis summary and main results.....	177
9.2	Material development for high performance thermoelectric thin films	178
9.2.1	Material property enhancement through additives.....	178
9.2.2	Material property enhancement through post-deposition annealing.....	178
9.2.3	Material property enhancement through doping/co-deposition strategy	180

Development of Thermoelectric Materials and Micro-Devices for Cooling and Power Generation

9.3	Micro thermoelectric device (μ -TED) fabrication	181
9.3.1	Micro-Thermoelectric device fabrication using flip-chip and single wafer approach	181
9.4	Recommendation for Future Work.....	183
9.4.1	Development of materials	183
9.4.2	Development of micro-thermoelectric devices	184

List of figures

Figure 1.1: Increasing data usage over the past two decades.....	2
Figure 1.2: Illustrates the projected increase in the data trafficking and the the measures to meet the increase	3
Figure 1.3: Cut away schematic of the current state-of-the-art thermal solution within a photonics integrated circuit package	3
Figure 1.4: High-level schematic of the thermally integrated photonics system architecture	4
Figure 1.5: Schematic illustrating the self-powered system for powering wearable electronics	5
Figure 1.6: The SmartVista smart patch for monitoring vital information.....	6
Figure 1.7: Various development stages	7
Figure 2.1: Schematic illustration of thermoelectric modules(a) power generation (Seebeck effect) and (b) refrigeration (Peltier effect)	14
Figure 2.2: Schematic illustrating power generation model	17
Figure 2.3: Schematic illustrating Power refrigeration model.....	19
Figure 2.4: The crystal structure of bismuth telluride	21
Figure 2.5: Schematic of basic three electrode cell setup	22
Figure 2.6: Cyclic voltammetry of Bi-Sb-Te solution vs Ag/AgCl reference electrode.....	24
Figure 2.7: Pourbaix diagram of Bi ₂ Te ₃ electrodeposition with 7.5 mM Bi and 10 mM Te in 1M HNO ₃ in the electrolyte	26
Figure 2.8: Schematic of different device structure (a) lateral (b) hybrid and (c) vertical device	36
Figure 2.9: The picture of the thermoelectric watch marketed by Seiko (left), schematic of the thermoelectric powered wristwatch (right)	37
Figure 2.10: A depiction of the 'two wafers' process implemented by MicroPelt to develop micro thermoelectric devices (left), the schematic of one of the applications of the bonded thermoelectric pairs as a cooler (right).....	37
Figure 2.11: Process flow of the 'single wafer' process imeplemented by the Jet Propulsion Laboratory	38
Figure 2.12: Process flow of the micro thermoelectric generator implemented by Glatz et al.....	39
Figure 2.13: Schematic of the high density arrangement of Si-nanowires in chip-scale thermoelectric generator	39

List of figures

Figure 2.14: Process flow of the fabrication of cross-plane μ TEG as proposed and implemented by Kim et al.40

Figure 2.15: Process flow of the bottom-up approach undertaken to fabricate the high power density micro thermoelectric generator41

Figure 2.16: Schematic of the fabrication process of the micro thermoelectric coolers with rapid response time.42

Figure 3.1: (a) Cyclic voltammograms of gold working electrode without and with 0.8 mM SDS. All the voltammograms were recorded at room temperature at a scan rate of 10 mVs⁻¹ (b) Schematic of triple pulse deposition potentials.53

Figure 3.2:(a) XRD of as-deposited films with different concentrations of SDS, (b) Annealed 0.8 mM SDS.57

Figure 3.3:(a) Seebeck measurement of as-deposited films with different concentrations of SDS and their comparison with values obtained post-annealing; (b) Electrical and thermoelectric properties of annealed films deposited with different concentration..... 57

Figure 3.4: Cyclic voltammograms of gold working electrode without and with different concentrations of SDS. All the voltammograms were recorded at room temperature at a scan rate of 10 mVs⁻¹.....61

Figure 3.5: SEM images of with different concentrations of SDS, as-deposited and annealed at 350 °C.61

Figure 4.1: Cyclic voltammogram recorded on a gold working electrode in the electrolyte containing 0.005M Bi³⁺, 0.010M SbO⁺, 0.015M HTeO₂⁺, and 1M HNO₃. The CV's are recorded at room temperature at a scan rate of 10 mV/s.....68

Figure 4.2: SEM images of (a) as-deposited samples and samples annealed at (b) 250 °C, (c) 300 °C, (d) 350 °C, and (e) 400 °C.....69

Figure 4.3: XRD patterns of the as-deposited and the annealed BiSbTe films. The annealing temperatures are mentioned in the pattern.....70

Figure 4.4: (a) Seebeck coefficient of BiSbTe films annealed at different temperatures for 1 h with the error bars. (b) Seebeck coefficient, electrical conductivity, and calculated power-factor of asdeposited and annealed films.....72

Figure 4.5: Carrier mobility and carrier concentration of BiSbTe thin films as a function of the annealing temperature.73

Figure 4.6: SEM images of (a) as-deposited samples and samples annealed at 350 °C for a duration of (b) 15 min, (c) 30 min, (d) 45 min, and (e) 60 min.75

Figure 4.7: XRD patterns of BiSbTe films annealed at 350 °C for different annealing time.76

List of figures

Figure 4.8: Thermoelectric properties of BiSbTe films annealed at 350 °C for different annealing times.....	76
Figure 4.9: Mobility and carrier concentration as a function of the annealing time of BiSbTe films annealed at 350 °C.....	77
Figure 5.1: (a) Cyclic voltammograms of BiTe and Cu added BiTe bath measured at 10 mV s ⁻¹ and (b) Elemental composition of electrodeposited thin films with respect to Cu concentration in the bath solution.	87
Figure 5.2: (a-f) SEM images of Bi ₂ Te ₃ and Cu-added Bi ₂ Te ₃ thin films (a) Bi ₂ Te ₃ , (b) Cu _{0.5} BiTe, (c) Cu _{1.0} BiTe, (d) Cu _{1.5} BiTe, (e) Cu _{2.0} BiTe, and (f) Cu _{4.0} BiTe.	89
Figure 5.3: (a-c) HRTEM images of Cu _{1.0} BiTe thin films and the corresponding SAED pattern.....	89
Figure 5.4: XRD patterns of as deposited Bi ₂ Te ₃ thin films with and without addition of copper.....	90
Figure 5.5: Raman spectra of pristine Bi ₂ Te ₃ and CuBiTe thin films.....	92
Figure 5.6: The core level XPS signals of Bi _{4f} (a), Cu _{2p} (b) and Te _{3d} (c) for the as-deposited pure and Cu added BiTe thin films at film surfaces.	93
Figure 5.7: (a) Electrical conductivity of as deposited pure Bi ₂ Te ₃ and CuBiTe at different Cu concentration measured at two conventional techniques, (b) The correlation between Hall mobility and carrier concentration of the films with respect Cu concentration and measured Seebeck and calculated power factor variation of the film with Cu content. .	97
Figure 6.1: Cyclic voltammogram recorded on a standard gold working electrode in the Cu, Te, CuTe electrolyte and magnified image of reduction peaks (right).....	116
Figure 6.2: (a) Elemental composition of films at different deposition potentials and (b) The thickness of electrodeposited films with different Cu%.	117
Figure 6.3: SEM and TEM micrographs of Cu doped Te films (a) -50 mV, (b) -100 mV, (c) -150 mV, (d) -200 mV, (e) -250 mV, (f) TEM image of the film deposited at -50 mV with SAED inset and (g) TEM image of the film deposited at -50 mV showing nano features along with SAED inset.	118
Figure 6.4: X-ray diffraction patterns of the deposited films with increasing Cu at. % in the films.....	118
Figure 6.5: (a) Room temperature Raman scattering spectra of films without and with increasing Cu % in the films and (b) Raman spectra peak shift of A1, E1 and E2 peaks.	121

List of figures

Figure 6.6: (a) Thermoelectric properties of electrodeposited Cu doped Te films with different Cu content in the films and (b) Mobility and carrier concentration as a function of Cu percentage in the films. 122

Figure 6.7: The calculated power factor of the films with different Cu% in the films. 122

Figure 7.1: SEM image of electrodeposited pillars along with respective elemental compositions of (a) BiTe, (b) CuTe (c) In bump electrodeposited on top of electrodeposited Au interconnect material. 139

Figure 7.2: Schematic illustration of device fabrication process 142

Figure 7.3: Images show non-adherence of pillars to the seed and delamination of pillars. 143

Figure 7.4: Schematic of sequential electrodeposited materials on the Au seed. 144

Figure 7.5: Schematic sketch of the non-uniformity in the electrodeposited pillar height. 145

Figure 7.6: The SEM image of (a) an edge pillar after applying a bonding force, (b) electrodeposited In bumps after bond forces are applied. 146

Figure 7.7: Images of the device using Nordson Dage Diamond XD7600NT X-ray Imaging system. 148

Figure 7.8: SEM images of the flip-chip bonded device using FineTech flip-chip bonder. 148

Figure 7.9: Measured electrical resistance of the flip-chip bonded device. 149

Figure 7.10: a) The schematic of internal resistances of thermoelectric pillar pair, b) Flip-chip bonded μ -TED device. 150

Figure 8.1: Schematic of the fabrication process flow of the micro-thermoelectric device. 159

Figure 8.2: SEM images of the electrodeposited thermoelectric pillars before and after CMP. 159

Figure 8.3: SEM image of the fabricated micro-thermoelectric device. 160

Figure 8.4: Schematic of a thermoelectric leg-pair. 161

Figure 8.5: Schematic of the unicouple along with the respective materials used. 163

Figure 8.6: Simulation results of unicouple for $\Delta T=5K$ (a) Temperature distribution (b) Output voltage distribution. 164

Figure 8.7: Simulation results of unicouple for $\Delta T = 1-5 K$. (a) current vs load resistance, (b) voltage vs load resistance, (c) output power vs load resistance and (d) maximum power vs. ΔT 165

List of figures

Figure 8.8: (a) Schematic diagram of the TEG module and (b) Voltage distribution of TEG module for $\Delta T=5$ K. 166

Figure 8.9: Simulation results of TEG module for $\Delta T=5$ K, (a) output power vs load resistance (b) Voltage and output power as a function of current..... 166

Figure 8.10: Resistance dependence on the number of thermoelectric leg pairs. 167

Figure 8.11: (a) CCD based thermoreflectance microscopy set-up, (b) Thermal image of the single daisy chain line activated and (c) Thermal image of the double lines activated with the temperature scale bar..... 168

Figure 8.12: (a) IR surface thermal image of the device with no current applies, (b) IR surface thermal image of the device applied with 80 mA current and (c) Temperature differential plot recorded on the top interconnect with the time..... 169

Figure 8.13: (a) Micro thermoelectric device characterisation set-up and (b) Micro device mounted on the test board. 171

Figure 8.14: Schematic of the measurement set-up for obtaining the open-circuit voltage of the fabricated micro-TEGs at different ΔT 171

List of tables

Table 2-1: List of state-of-the-art high performing thin film materials along with their fabrication technologies.	32
Table 3-1: Atomic composition of Bi-Sb-Te films with different concentrations of SDS in electrolyte and change in the composition after annealing.	55
Table 3-2: Composition of Bi-Sb-Te films with different concentrations of SDS before and after annealing.	55
Table 3-3: Average crystallite size of films prepared with different concentrations of SDS.	56
Table 4-1: Atomic composition of Bi-Sb-Te as-deposited films and films annealed at different annealing temperatures.	69
Table 4-2: Crystallite size of films annealed at different annealing temperatures.	70
Table 4-3: Atomic composition of Bi-Sb-Te as-deposited films and films annealed at 350 °C for different annealing time.	74
Table 4-4: Crystallite size of films annealed at 350 °C for different annealing time.	75
Table 6-1: Average crystallite size of the films with increasing Cu% in the films.	119
Table 6-2: Tellurium vibrational modes measured in comparison with the data published in the literature.	120
Table 7-1: Individual material thickness of electrochemically deposited materials.	144
Table 7-2: Bonding parameters used in the flip-chip bonding process.	146
Table 8-1: Materials properties along with the geometrical dimensions used for the simulations.	163

Chapter 1: Introduction

1.1 Introduction

The inherent capability of thermoelectric devices in converting ambient thermal energy into usable electrical energy and vice-versa makes them a potential candidate for power generation (Seebeck effect) and heating/cooling (Peltier effect) applications. Microscale thermoelectric devices outpace macroscopic counterparts owing to their small size, which offers ease in integration into microsystems. Such miniaturized structures enhance the integration density by significantly increasing the number of thermocouples in the device, which results in high power outputs, especially when subjected to small temperature differences [1-4]. The present state of the art micro thermoelectric devices (μ TEDs) are mainly fabricated using complementary metal-oxide-semiconductor (CMOS) and micro-electromechanical systems (MEMS) compatible techniques. CMOS/MEMS are the basis of many rapidly growing technologies because they combine miniature sensors and actuators with communications and electronics at a low-cost level. Among the wide range of applications of μ TED, we have been working on both power generation and cooling applications.

Thermoelectric devices are solid-state transducers that take thermal energy and converts it to useful electrical forms and vice versa. The advantages of using thermoelectric energy harvesters are that they can be used to convert waste heat into useful electrical energy without any moving parts, vibration, noise or refuelling. Moreover, they have high reliability, low maintenance, and very reliable longevity over a wide range of temperatures [1, 5-7]. The other advantage of thermoelectric devices is for their cooling applications with no moving parts and refrigerant free heat extraction [4].

1.2 Thermoelectric cooling

Technology is changing at a swift pace, and due to this increase, telecommunication is struggling to maintain its pace in the fast-growing world. Data traffic is projected to increase rapidly, driving an increase in network complexity and the requirement for scalable optoelectronic integration as shown in figure 1.1[8]. Thermal management has typically been relegated to the last step in the design process and traditionally considered only to ensure long-term operation of the optoelectronic devices. Today, thermal management represents one of the major bottlenecks to releasing next-generation equipment across the entire network. The efficient nature of transmitting the data a large distance with minimal losses at a high speed makes photonic devices and components key

enablers to support the massive growth in data traffic. However, due to the high level of integration, it poses significant challenges due to the very different thermal profiles associated with photonics as compared to electronics.

Active photonic devices generate high heat flux levels ($\sim 10 \text{ kW/cm}^2$) that must be efficiently removed to maintain performance and reliability; furthermore, active photonic devices must be controlled at a temperature precision of better than $\pm 0.1 \text{ K}$ as illustrated in figure 1.2. Today's thermal technology is at the limit and cannot scale with growth in the network. As a comparison, electronics produce lower heat flux levels ($\sim 100 \text{ W/cm}^2$) and have a less restrictive temperature requirement of $\leq 85 \pm 2 \text{ }^\circ\text{C}$ [9].

The present photonic devices are cooled by a macro-thermoelectric coolers (macro-TECs), as shown in figure 1.3. The schematic representation of present thermal management of photonic systems by the use of macro coolers close to the vicinity of the lasers so as to cool them and also the use of resistive heaters to re-tune to the desired temperature of lasers, which doubles the local thermal load. The heat load is coupled to the photonics package via many intermediate layers, and the entire package is air-cooled. Due to a large number of the component in the package and lack of proper thermal design, the present cooling systems by the use of macro thermoelectric coolers do not allow integration of more lasers in the same footprint and thereby are not capable of meeting the increasing traffic.

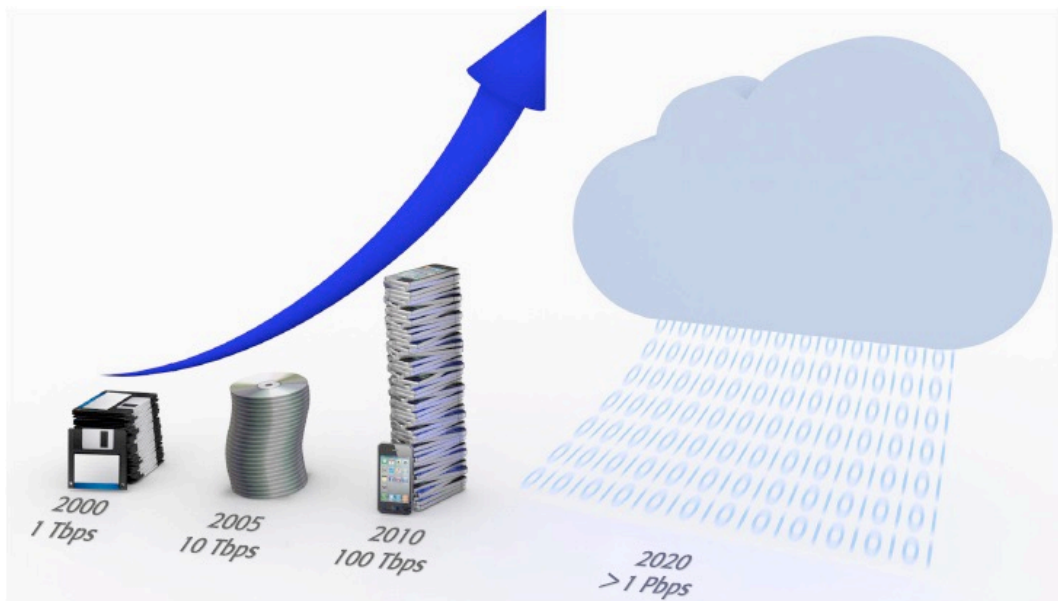


Figure 1.1: Increasing data usage over the past two decades [9]

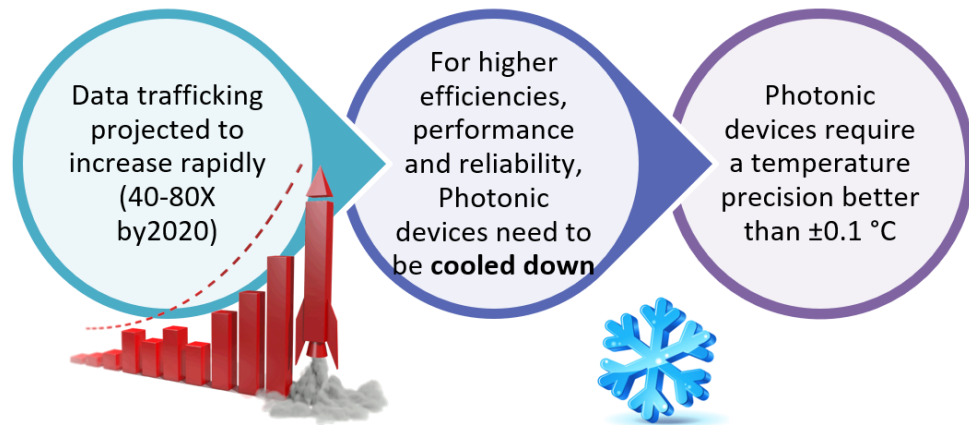


Figure 1.2: Illustrates the projected increase in the data trafficking and the the measures to meet the increase

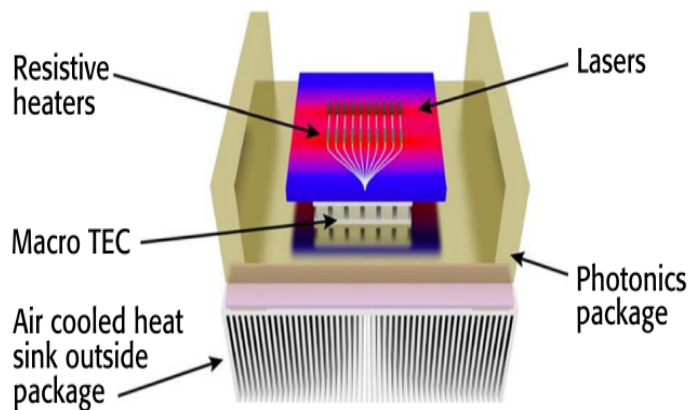


Figure 1.3: Cut away schematic of the current state-of-the-art thermal solution within a photonics integrated circuit package [9]

Figure 1.4 shows a high-level schematic of the thermally integrated photonics system. The aim of the present work is to provide a more efficient approach of temperature control by removing the large footprint, power-hungry macro-TEC and individual resistive heaters and introducing a targeted cooling/temperature control using the integrated micro-TEC's (μ -TECs). The use of μ -TECs promises several advantages including removal of parasitic thermal resistance between the heat source and thermoelectric cooling junction, direct temperature control of individual devices without the need of resistive heaters and their added power demands, reduced thermoelectric material usage and the potential for increased integration of optoelectronic components differing in operating temperature requirements as in silicon photonics.

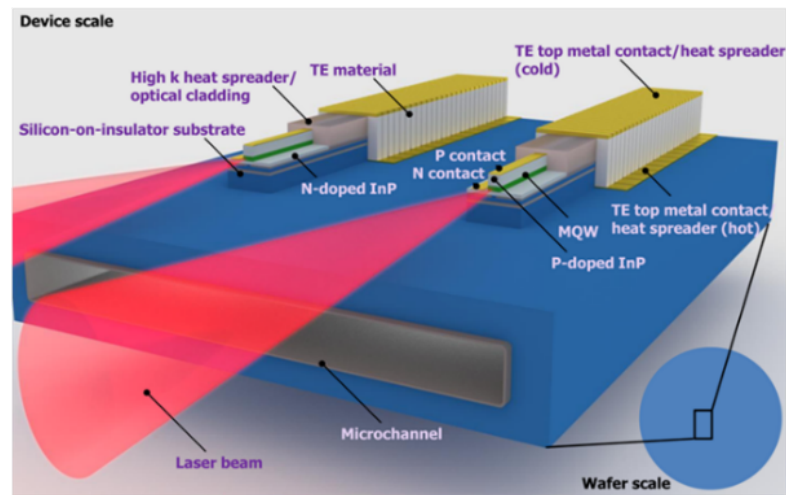


Figure 1.4: High-level schematic of the thermally integrated photonics system architecture [9]

The current state-of-the-art material is nanostructured bismuth telluride, manufactured in bulk geometries using a combination of ball milling and hot pressing. However, it is not possible to integrate these powder processing methods in a semiconductor fabrication process. Therefore, electrodeposition is the preferred fabrication technique due to its cost-effectiveness, compatibility with semiconductor fabrication and up-scalability.

1.3 Thermoelectric power generation

The recent advancements in microelectronics and MEMS technologies have made the ‘Internet of Things’ (IoT) an indispensable part of our lives that facilitates tailored fast services to enrich rural and urban lifestyle. This enables ubiquitous sensing through enumerable deployed wireless sensors nodes (WSN) that aims to integrate the physical world with the computer-based systems bringing ease in communication and computation. These versatile WSNs are widely used in industrial sensing [10], remote healthcare [11], automotive monitoring [12], surveillance [13], etc. and are a potential candidate to find their place in hitherto unexplored application. However, one of the major impediments in the path of materializing this type of smart connected environment is the perpetual powering of such billions of deployed sensor nodes. Batteries as the only power source not only add unnecessary volume and weight to such miniaturized systems mainly on wearable electronics, but also makes it impractical for recharging multiple times once they deplete their energy. However, a lot of strategies have been reported for improving the energy density of supercapacitors and batteries [14-16]. Despite these advances, batteries can hardly meet the requisites of wearable electronics. In this predicament the most attractive alternative is to scavenge energy from omnipresent ambient energy sources and assisting the energy storage devices for ultimately powering wearable

electronics [17] as shown in the Figure 1.5. Real-time autonomous powered, reliable and continuous measurements and monitoring of vital physical information such as heart rate, electrocardiograph (ECG), respiratory flow, etc. can be made possible by using wearable healthcare devices. They can be used for early-stage disease detection and long-term health monitoring. The recent growth in wearable electronics has captivated interest from both the research and commercial community. Powering such devices solely with battery requires multiple recharges, during which health monitoring can be hindered and cause inconvenience. These devices are needed to be able to work autonomously with the least human interventions. One elegant solution to this pertinent powering issue could be scavenging heat energy from the human body to power such wearable devices and reduce our sole dependence on the batteries which could pave the way for the next generation wearable health monitoring systems.

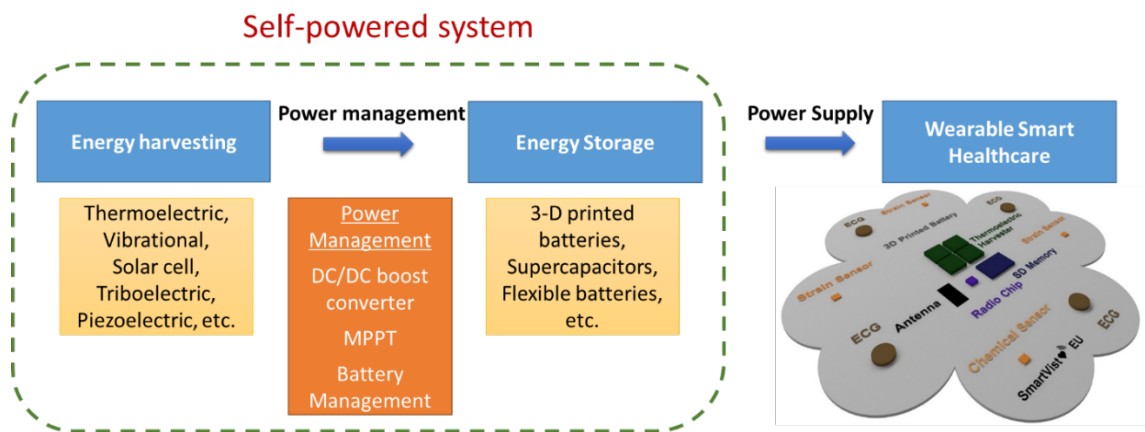


Figure 1.5: Schematic illustrating the self-powered system for powering wearable electronics

Thereby in the SmartVista project [18], the aim is to develop a smart sensor system that will be compact and unobtrusive while consuming ultra-low power. To ensure the autonomy of the smart system, it will be integrated with an energy harvesting module with a self-powered mechanism for a printable battery to prolong battery life. This is a first worldwide attempt to provide a flexible multi-modal ultra-low-power bio-signal (ECG, respiratory flow, oxygen level and temperature) monitoring device as shown in Figure 1.6. The main objective of SmartVista is to develop a smart, compact multi-sensory ECG system with several weeks of power autonomy while providing reliable measurements and continuous bio-signals monitoring. The SmartVista project targets several technology breakthroughs such as sensors, batteries, energy harvesting and system integration that will lead to a viable system design solution for developing a seamless, flexible, accurate and wearable sensor system. Such a target will allow the

investigation of the reliability and power consumption of the smart system while investigating the applicability of micro-thermoelectric generator in converting body heat into usable electricity.

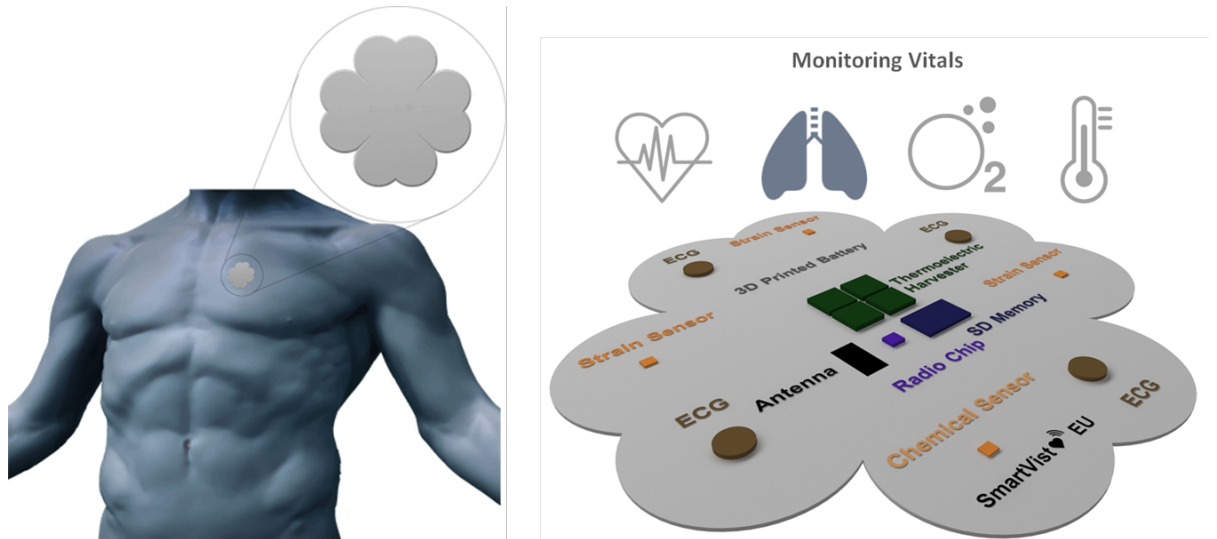


Figure 1.6: The SmartVista smart patch for monitoring vital information

The promising energy source in this context is the thermal energy that a human body generates. There has been a growing trend in the investigation and development of thermoelectric transducers that generate electricity by exploiting the thermal gradient that human body heat would offer as compared with the ambient temperature [1, 19-21]. Thermoelectric generators consist of p-type and n-type semiconductors that are connected electrically in series and thermally in parallel, which enables these materials to generate a sufficiently high number of charge carriers once the opposite junctions are subjected to a substantial temperature gradient.

In order to achieve these goals of developing μ -thermoelectric devices (μ -TEDs) for cooling and power generation applications, the whole project has been divided into three different stages, as shown in Figure 1.7. In stage one, the work was focused on the development of the best possible thermoelectric material for μ -TEDs, wherein it was mostly on the Bi-Te based alloy materials, as they have a better thermoelectric performance near room temperature region. Stage two was dedicated to designing of a efficient μ -TED, which could be feasible to be developed by the fab-compatible deposition techniques. Furthermore, in the last stage, the fabrication of the device and its testing was carried out.

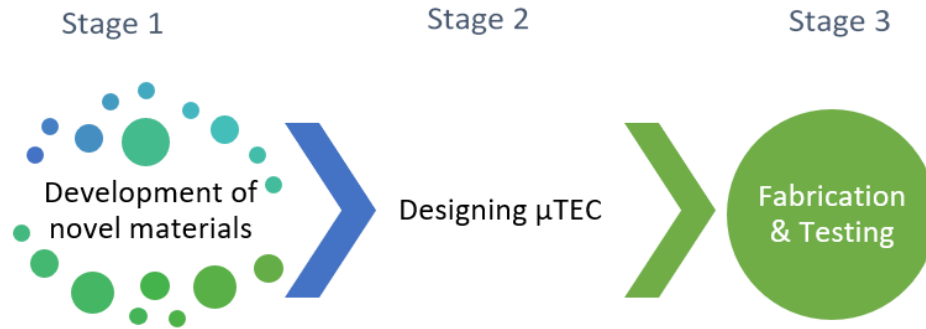


Figure 1.7: Various development stages

1.4 Research Objectives

Miniaturized thermoelectric devices have applications in both thermal management and energy harvesting. Thermal management of microelectronics and optoelectronic devices using thermoelectric (TE) coolers is an efficient way for active temperature control, where miniaturization of the devices result in generation of a high heat flux, which is difficult to manage [9, 22].

Body wearable sensors and electronics are getting immense attention with the growth in IoT and TEGs are of interest in the implementation of these self-powered wearable as it utilises the body heat and converts it into usable electrical energy. Studies that have focused on body temperature measurements have revealed that the body parts with highest temperatures are namely the forehead, back of the neck and the chest. All these body parts are capable of creating a temperature gradient of 2-10 K depending upon the ambient temperatures [23, 24].

The aim of this thesis is to study and develop new electroplated thermoelectric materials with stable and high thermoelectric material performance. Also, integration of the developed electroplated materials on a silicon substrate for the micro-device fabrication for the application of both the cooling and power generation, as explained in the motivation in the earlier section.

To fulfil the objectives, the main tasks of this research work include:

- Development of different p- and n-type thermoelectric materials using electrodeposition techniques
- Investigate the electrochemical behaviour of the associated electrolytic baths

- Characterization of the developed materials and the thermoelectric properties evaluation
- Enhancement and optimization of the developed materials using different techniques namely by additives, thermal annealing, and doping
- Integration of the developed materials on to the device using microfabrication techniques
- Investigation of cooling and power generation performance of the fabricated devices

1.5 Thesis structure

The contents of the following chapters in this thesis are given below:

- **Chapter 2** provides the basic introduction to thermoelectric materials and devices and governing equations. The large section of this chapter is dedicated to the state-of-the art literature review on the electrodeposition of thermoelectric materials for room temperature applications and micro-fabrication of state-of-the-art thermoelectric devices both for cooling and power generation applications.
- **Chapter 3** discusses the role of additives, mainly surfactant sodium do-decyl sulfate (SDS) in enhancing the thermoelectric properties of electrodeposited p-type BiSbTe material and also the role of the surfactant in decreasing the surface roughness of the deposited films which plays a crucial role in the device fabrication.
- **Chapter 4** discusses the importance of annealing in stabilizing and improving the thermoelectric properties of as-deposited thin films. Upon fine tuning the annealing parameters, the properties of the films can be varied drastically, which is investigated in detail for p-type BiSbTe based thermoelectric materials. This chapter also discusses innovative use of a Te intermediate layer helping to replenish the depleted Te during annealing. This technique eliminates the use of Te atmosphere during annealing and excessive annealing times.
- **Chapter 5** discusses the characteristic thermoelectric performance of Cu doped BiTe thin films fabricated through electrodeposition technique. In addition to this, the effect of copper incorporation and amorphization of the thermoelectric material which has been a hitherto unexplored strategy of enhancing the thermoelectric properties of the material has been demonstrated. The achieved superior carrier concentration, electrical conductivity and excellent power factor values make CuBiTe a promising n-type material for high-efficiency

thermoelectric device applications. Further stabilization of the material for application over a wide temperature range could make CuBiTe a superior n-type candidate for near room temperature thermoelectric power generation applications.

- **Chapter 6** introduces a novel Cu doped Te electrodeposited film for room temperature thermoelectric applications. A detailed structural analysis of the electrodeposited Cu-doped Te films along with an extensive investigation on the collapse of the crystal structure of the electrodeposited Te films on the addition of Cu using different characterization techniques has been performed. The inclusion of copper in the films aids in modifying the crystal structure, which leads to the amorphous nature of the films and the corresponding enhancement in the thermoelectric properties. The n-type behaviour of these deposited materials with a dramatic thermoelectric power factor of 5.6 mW/mK^2 outruns the contemporary reported thermoelectric materials. These excellent TE properties exhibited by the n-type Cu-doped Te material makes it a potential thermoelectric material for cooling and power generation for near room-temperature applications, especially in low-temperature gradient scenarios.
- **Chapter 7** successfully demonstrated and discussed the fabrication procedure of a cross-plane configuration, flip-chip bonded μ -TED. The electrodeposition of gold (Au) and indium (In) is investigated, which acts as a barrier separation layer for indium diffusion and the bonding material, respectively. The impact on the internal resistance of the device by bonding materials and the challenges faced during the flip-chip bonding of the device have been thoroughly investigated. The challenges faced during the fabrication of the μ -TED and the feasible solutions to overcome the fabrication problems have been methodically presented, finally resulting in the successful implementation of electroplated micro thermoelectric devices. As part of our second approach, we have successfully integrated the developed material for single wafer approach. Although, this approach requires a complex fabrication process, it leads to better performance of the device. The devices developed by both approaches were highly successful.
- **Chapter 8** discusses the successful fabrication of single wafer approach μ -TED. The material deposition details along with the thermoelectric device performance is evaluated using COMSOL simulations and are explained in detail. The

fabricated devices are tested for their cooling as well as the power generation performances and are discussed in detail.

- **Chapter 9** summarises the reported thesis work and suggestions for future work are discussed.

1.6 References

- [1] J. Yan, X. Liao, D. Yan, and Y. Chen, "Review of Micro Thermoelectric Generator," *Journal of Microelectromechanical Systems*, vol. 27, no. 1, pp. 1-18, 2018.
- [2] S. B. Riffat and X. Ma, "Thermoelectrics: A review of present and potential applications," (in English), *Applied Thermal Engineering*, Review vol. 23, no. 8, pp. 913-935, 2003.
- [3] D. M. Rowe, *CRC handbook of thermoelectrics*. CRC press, 1995.
- [4] L. E. Bell, "Cooling, Heating, Generating Power, and Recovering Waste Heat with Thermoelectric Systems," *Science*, vol. 321, no. 5895, pp. 1457-1461, 2008-09-12 00:00:00 2008.
- [5] G. J. Snyder and E. S. Toberer, "Complex thermoelectric materials," *Nat Mater*, 10.1038/nmat2090 vol. 7, no. 2, pp. 105-114, 02//print 2008.
- [6] R. He, G. Schierning, and K. Nielsch, "Thermoelectric Devices: A Review of Devices, Architectures, and Contact Optimization," *Advanced Materials Technologies*, vol. 3, no. 4, p. 1700256, 2018/04/01 2018.
- [7] K. V. Selvan and M. S. Mohamed Ali, "Micro-scale energy harvesting devices: Review of methodological performances in the last decade," *Renewable and Sustainable Energy Reviews*, vol. 54, pp. 1035-1047, 2016/02/01/ 2016.
- [8] J. Brodtkin, "Bandwidth explosion: As Internet uses soars, can bottlenecks be averted?," *Arstechnica*, pp. <http://arstechnica.com/business/2012/05/bandwidth-explosion-as-internet-use-soars-can-bottlenecks-be-averted/>, 2014.
- [9] R. Enright *et al.*, "A Vision for Thermally Integrated Photonics Systems," *Bell Labs Technical Journal*, vol. 19, pp. 31-45, 2014.
- [10] M. Bertocco, G. Gamba, A. Sona, and S. Vitturi, "Experimental Characterization of Wireless Sensor Networks for Industrial Applications," *IEEE Transactions on Instrumentation and Measurement*, vol. 57, no. 8, pp. 1537-1546, 2008.
- [11] H. B. Lim, D. Ma, B. Wang, Z. Kalbarczyk, R. K. Iyer, and K. L. Watkin, "A Soldier Health Monitoring System for Military Applications," in *2010 International Conference on Body Sensor Networks*, 2010, pp. 246-249.

- [12] F. Mieleve, W. Du, I. Daikh, and D. Navarro, "Wireless Sensor Networks for active control noise reduction in automotive domain," in *2011 The 14th International Symposium on Wireless Personal Multimedia Communications (WPMC)*, 2011, pp. 1-5.
- [13] C. Meesookho, S. Narayanan, and C. S. Raghavendra, "Collaborative classification applications in sensor networks," in *Sensor Array and Multichannel Signal Processing Workshop Proceedings, 2002*, 2002, pp. 370-374.
- [14] P. G. Bruce, S. A. Freunberger, L. J. Hardwick, and J.-M. Tarascon, "Li–O₂ and Li–S batteries with high energy storage," *Nature Materials*, Review Article vol. 11, p. 19, 12/15/online 2011.
- [15] X. Pu, W. Hu, and Z. L. Wang, "Toward Wearable Self-Charging Power Systems: The Integration of Energy-Harvesting and Storage Devices," *Small*, vol. 14, no. 1, p. 1702817, 2018.
- [16] S. Pan, J. Ren, X. Fang, and H. Peng, "Integration: An Effective Strategy to Develop Multifunctional Energy Storage Devices," *Advanced Energy Materials*, vol. 6, no. 4, p. 1501867, 2016/02/01 2016.
- [17] A. S. Weddell, M. Magno, G. V. Merrett, D. Brunelli, B. M. Al-Hashimi, and L. Benini, "A survey of multi-source energy harvesting systems," in *2013 Design, Automation & Test in Europe Conference & Exhibition (DATE)*, 2013, pp. 905-908.
- [18] K. M. Razeeb, C. O. Murchu, A. Todri-Sanial, F. Sebelius, I. Bose, and C. O. Dwyer, "SmartVista: Smart Autonomous Multi Modal Sensors for Vital Signs Monitoring," in *Smart Systems Integration; 13th International Conference and Exhibition on Integration Issues of Miniaturized Systems*, 10-11 April 2019 2019, pp. 1-8.
- [19] A. R. M. Siddique, S. Mahmud, and B. V. Heyst, "A review of the state of the science on wearable thermoelectric power generators (TEGs) and their existing challenges," *Renewable and Sustainable Energy Reviews*, vol. 73, pp. 730-744, 6// 2017.
- [20] L. Yang, Z.-G. Chen, M. S. Dargusch, and J. Zou, "High Performance Thermoelectric Materials: Progress and Their Applications," *Advanced Energy Materials*, vol. 8, no. 6, p. 1701797, 2018/02/01 2018.
- [21] L. Bell, "Cooling heating, generating power, and recovering waste heat with thermoelectric systems," *Science*, vol. 321, pp. 1457-1461, // 2008.

- [22] C. O'Dwyer, R. Chen, J.-H. He, J. Lee, and K. M. Razeeb, "Preface—Focus Issue on Thermoelectric Materials & Devices: Phonon Engineering, Advanced Materials and Thermal Transport," *ECS Journal of Solid State Science and Technology*, vol. 6, no. 3, pp. Y3-Y3, 2017.
- [23] F. Suarez, A. Nozariasbmarz, D. Vashaee, and M. C. Ozturk, "Designing thermoelectric generators for self-powered wearable electronics," *Energy & Environmental Science*, 10.1039/C6EE00456C vol. 9, no. 6, pp. 2099-2113, 2016.
- [24] A. S. Dahiya *et al.*, "Review—Energy Autonomous Wearable Sensors for Smart Healthcare: A Review," *Journal of The Electrochemical Society*, vol. 167, no. 3, p. 037516, 2020/01/02 2020.

Chapter 2: Electrodeposition of thermoelectric material and micro-device fabrication: State-of-the-art

2.1 Introduction

This chapter introduces the theoretical background necessary for the scope of this work along with the state-of-the-art thermoelectric materials and micro-device literature review.

2.2 Thermoelectric material theory

Thomas Seebeck was the first scientist who came across the phenomena of thermal energy conversion when he observed that different conductors or semiconductors, when connected at their ends and are subjected to temperature differences, generate electromotive force across their ends. Fig. 2.1(a) depicts an example of this effect. The p-type and n-type material together forms a thermocouple, when the two interfaces (one at the joint and the other at the free end) are subjected to different temperatures, say T_H at the hot end and T_C at the cold end, the charge carriers (electrons and holes) flow through the materials in such a fashion that gives rise to a charge gradient and hence a potential across the ends of the thermoelectric pair. This is also called the relative Seebeck electromotive force. In fact, such charge carrier diffusion may cause such electromotive force across a single thermoelectric material leg whose ends are at different temperatures which are popularly known as the absolute Seebeck electromotive force. The developed voltage (V_{out}) across the materials is directly proportional to the temperature gradient that the junctions are subjected to, which in this case is,

$$V_{out} = \alpha_{seebeck} (T_H - T_C) \quad 2.1$$

Where, $\alpha_{seebeck}$ is termed as the Seebeck coefficient, which is an intrinsic property of the thermoelectric material. This coefficient can be defined as the potential created across the ends of a thermoelectric pair when the ends are subjected to unit temperature difference. The sign of this coefficient can be positive or negative depending on the direction of the flow of the charge carriers or in other words, on the type of semiconductor/ conductor used. Conventionally the sign of this coefficient represents the potential of the cold side with respect to the hot side. In the thermocouple, if n-type semiconductors are used, then the majority carrier being electrons, when subjected to temperature difference, the electrons will flow from the hot side to the cold side. The gathering of electrons around the colder part of the semiconductor lowers the potential of that part with respect to the hotter side, and hence the sign of the Seebeck coefficient is negative in this case. On the

other hand, with the p-type semiconductors, holes being the majority carrier, the potential on the colder side gets higher than the hotter side, which makes the sign of the Seebeck coefficient positive.

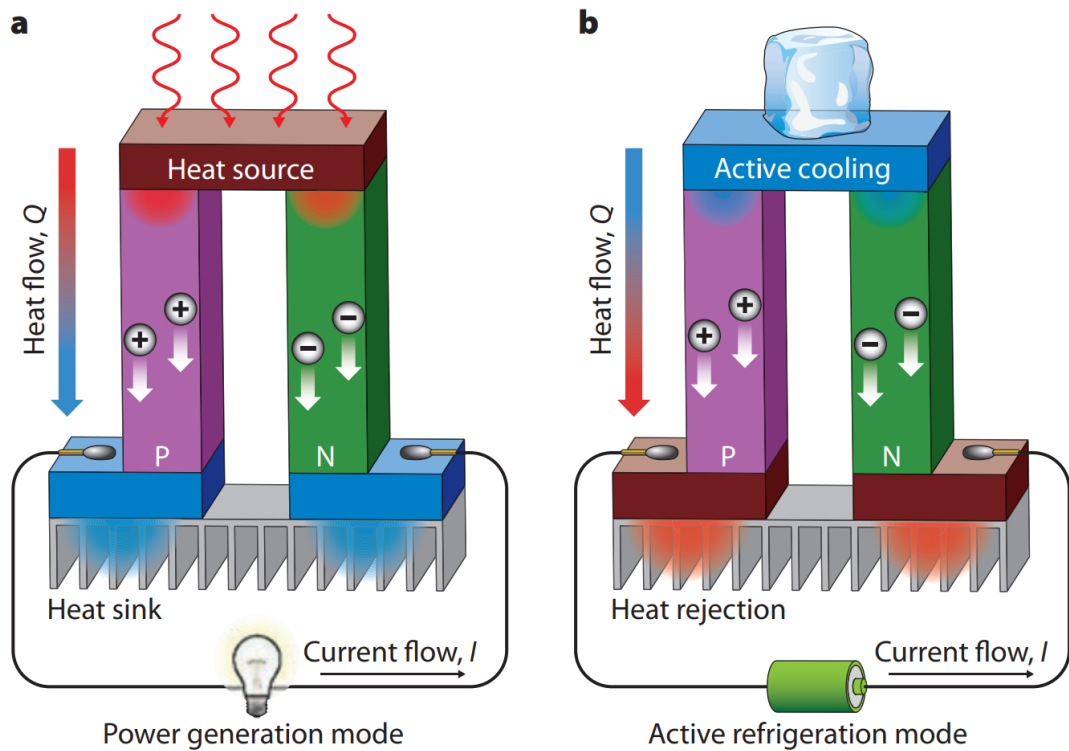


Figure 2.1: Schematic illustration of thermoelectric modules (a) power generation (Seebeck effect) and (b) refrigeration (Peltier effect) [1]

A reverse effect is also noticed in the thermoelectric generators when through external power supply a current is flowing through a thermocouple comprised of dissimilar materials, then at the joints heat is dissipated in the surroundings or heat is absorbed facilitating a cooling effect. The heat generation or absorption depends on the type of thermoelectric material used and on the direction of the current flowing through the thermal circuit (Fig. 2.1(b)). This effect is popularly called the Peltier effect, named after the scientist who first discovered this phenomenon. The heat dissipation or absorption is localized at the thermocouple junction in this case. This particular effect is associated with the entropy change of the carriers in the thermoelectric material, hence even in inhomogeneous material that offers a gradient of carrier concentration, this effect can be observed. The rate at which this heat is transported across the junction ($\frac{\Delta Q}{\Delta t}$) is proportional to the current (i) that the material is subjected to, and these two are related as-

$$\frac{\Delta Q}{\Delta t} = \Pi_{peltier} i \quad 2.2$$

Where, $\Pi_{peltier}$ is called the Peltier coefficient of the material. Depending on the direction of i , the sign of $\frac{\Delta Q}{\Delta t}$ is positive when the heat is generated and is negative when the junction absorbs heat. The Peltier coefficient rather quantifies the amount of heat generated or lost due to the flow of unit current per unit time.

Another effect that makes the thermoelectric materials so versatile is the Thompson effect. When a thermoelectric material is subjected to a temperature gradient across its junction and current is made to flow through it, then heat is generated or absorbed in the material. The rate at which this heat generation or absorption ($\frac{\Delta Q}{\Delta t}$) takes place through per unit length of the homogeneous material is proportional to the current flowing (i) through it and the temperature gradient (ΔT) that the material is subjected to. This can be expressed as-

$$\frac{\Delta Q}{\Delta t} = K_{thompson} i \Delta T \quad 2.3$$

Where, $K_{thompson}$ is termed as the Thompson coefficient. The sign of this coefficient depends on both the direction of the current flow and the temperature difference.

Figure of merit (ZT)

The dimensionless figure of merit conventionally used to compare the performance of the different thermoelectric material is expressed as-

$$ZT = \frac{\alpha_{seebeck}^2}{\rho k} T \quad 2.4$$

Where, ρ is the resistivity of the material and k is the thermal conductivity of the material, $\alpha_{seebeck}$ is the Seebeck coefficient of the material in use and T is the absolute temperature. Hence it is clear that good thermoelectric material should have a high Seebeck coefficient, and low resistivity and thermal conductivity. As these parameters are interrelated, it is difficult to optimize this by altering one of the parameters at a time. Another figure of merit to evaluate the performance of the thermoelectric materials is the Power Factor (PF), and this can be expressed as-

$$PF = \frac{\alpha_{seebeck}^2}{\rho} \quad 2.5$$

Up to this point, we have discussed briefly the figure of merit to compare the thermoelectric materials. Now we will discuss the figure of merit for the comparison of the thermoelectric devices, both as a generator and as a cooler. Considering the case of the thermoelectric energy harvesters or generators firstly, how well the associated conductor/ semiconductor converts the available thermal energy into electrical energy is evaluated on the basis of conversion efficiency (η) which can be expressed as a ratio of the usable electrical energy generated (W) to the provided heat energy (Q) to the system-

$$\eta = \frac{W}{Q} \quad 2.6$$

Let the two thermal legs as shown in Fig. 2.2 possess the following material and electrical properties

- Length of the two legs l_1 and l_2
- Area of the thermal legs A_1 and A_2
- Resistivity and thermal conductivities are ρ_1, ρ_2 and K_1, K_2 respectively

Then the overall thermal conductance κ and resistance (R) offered by the thermocouple will be-

$$R = R_1 + R_2 = \frac{\rho_1 l_1}{A_1} + \frac{\rho_2 l_2}{A_2} \quad 2.7$$

$$\kappa = \kappa_1 + \kappa_2 = \frac{K_1 A_1}{l_1} + \frac{K_2 A_2}{l_2} \quad 2.8$$

Now the Seebeck potential developed across the thermocouple is-

$$V_{out} = \alpha_{seebeck} (T_H - T_C) \quad 2.9$$

Considering a load resistance R_{load} is put across the thermocouple and the current flowing through is I , then the electrical energy delivered to the load is-

$$W = I^2 R_{load} = \frac{\alpha_{seebeck}^2 (T_H - T_C)^2}{(R + R_{load})^2} R_{load} \quad 2.10$$

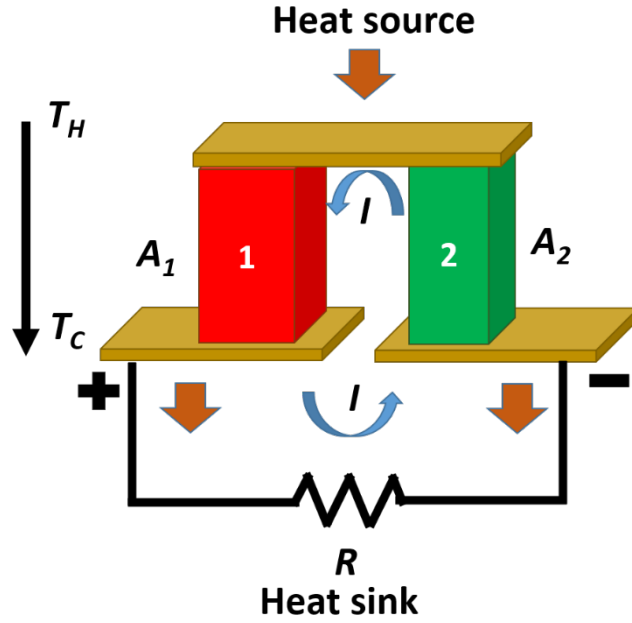


Figure 2.2: Schematic illustrating power generation model

Now considering that the hot end of the thermocouple is attached to a heat source from which the heat energy is fed to the system, then this energy can be expressed as the sum of the heat that is transported to the colder end (heat sink) of the thermocouple, the Peltier heat and the half of the Joule heating energy that feeds back to the source,

$$Q = Q_{transport} + Q_{Peltier} - \frac{1}{2} Q_{Joule} = \kappa (T_H - T_C) + \Pi_{peltier} I - \frac{1}{2} I^2 R \quad 2.11$$

$$= \kappa (T_H - T_C) + \alpha_{seebeck} T_H \frac{\alpha_{seebeck} (T_H - T_C)}{(R + R_{load})} - \frac{1}{2} R \frac{\alpha_{seebeck}^2 (T_H - T_C)^2}{(R + R_{load})^2} \quad 2.12$$

Let, $\gamma = \frac{R_{load}}{R}$, then the expression for the conversion efficiency takes the following form-

$$\eta = \frac{(T_H - T_C)}{T_H} \frac{1}{1 + \frac{\kappa R}{\alpha_{seebeck}^2} \frac{(1 + \gamma)^2}{\gamma} \frac{1}{T_H} + \frac{(T_H + T_C)}{T_H} \frac{1}{2\gamma}} \quad 2.13$$

As can be clearly seen, this efficiency depends on the electrical and material properties of the thermocouple. By optimizing different parameters, this efficiency can be maximized. From the maximum power transfer theorem, we know that for $R = R_{load}$ the delivered electrical energy maximizes. So the efficiency will be then expressed as,

$$\eta = \frac{(T_H - T_C)}{T_H} \frac{1}{1 + \frac{4 \kappa R}{\alpha_{seebeck}^2} \frac{1}{T_H} + \frac{(T_H + T_C)}{T_H} \frac{1}{2}} \quad 2.14$$

Now, as discussed above, the thermoelectric pair can also work to demonstrate the cooling effect. In this case the external power supply is required so that current flows through the thermoelectric legs. Exploiting the Peltier effect, the application of refrigeration can be implemented by making the heat energy to be transported from the heat source to the heat sink. While this effect takes place, the heat conduction and the Joule effect bring back some part of the heat energy to the source. Hence the efficiency (ξ) of such a refrigeration technique can be expressed as the ratio of the net heat energy (Q) that is transported from the heat source to the heat sink to the amount of energy that is fed (W) into the system to enable the current flowing through the thermolegs.

$$\xi = \frac{Q}{W} \quad 2.15$$

Where the net heat energy Q can be expressed as-

$$Q = Q_{peltier} - Q_{transport} - \frac{1}{2} Q_{joule} = \Pi_{peltier} I - \kappa (T_C - T_H) - \frac{1}{2} I^2 R \quad 2.16$$

On the other hand, the energy fed to the system W can be expressed as-

$$W = I^2 R + I \alpha_{seebeck} (T_C - T_H) \quad 2.17$$

Then the refrigeration efficiency takes the form,

$$\xi = \frac{\Pi_{peltier} I - \kappa (T_C - T_H) - \frac{1}{2} I^2 R}{I^2 R + I \alpha_{seebeck} (T_C - T_H)} \quad 2.18$$

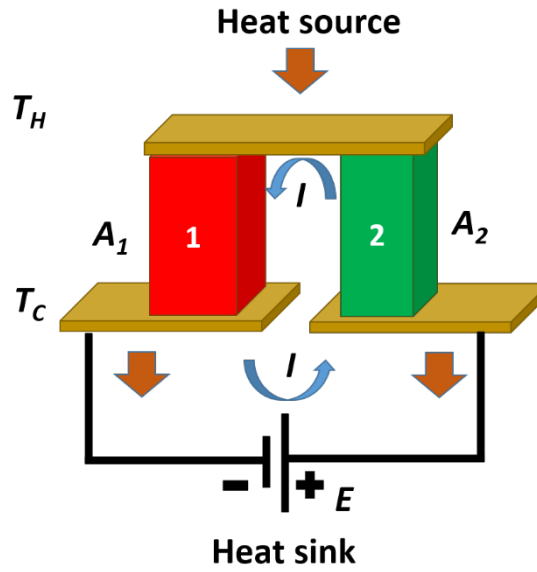


Figure 2.3: Schematic illustrating Power refrigeration model

Now to optimize this refrigeration efficiency with respect to the current flowing we perform $\frac{\partial \xi}{\partial I} = 0$ and find the value of current –

$$I = \frac{\alpha_{seebeck} (T_C - T_H)}{R \left\{ \sqrt{1 + \frac{T_C + T_H}{2} \left(\frac{\alpha_{seebeck}}{\kappa R} \right)} - 1 \right\}} \quad 2.19$$

Substituting this in the expression for refrigeration efficiency we get,

$$\xi = \frac{T_H}{T_C - T_H} \frac{\sqrt{1 + \frac{T_C + T_H}{2} \left(\frac{\alpha_{seebeck}}{\kappa R} \right)} - \frac{T_C}{T_H}}{\sqrt{1 + \frac{T_C + T_H}{2} \left(\frac{\alpha_{seebeck}}{\kappa R} \right)} + 1} \quad 2.20$$

So, we clearly see from this expression that the refrigeration efficiency is also critically dependent on the thermoelectric properties of the materials used and on the temperature of the hot and the cold junction. Using the equations stated in this section, the material as well as the device properties are evaluated.

2.3 Bismuth telluride thermoelectric material

Bismuth telluride based materials are the state-of-the-art room temperature thermoelectric materials and have been commercially used for the thermoelectric device fabrication for room temperature applications [2]. Bulk bismuth telluride based materials possess a ZT of more than 1, which makes them a potential material for room temperature applications [3-6]. Traditionally, most of the thermoelectric systems employ these bulk materials for device fabrication. However, the use of the bulk material restricts the development of

highly integrated systems due to their mechanical limitations during fabrication of micro-devices. Therefore, development of thin-film materials with comparable thermoelectric properties to bulk is very important along with micro fabrication compatibility.

Lowering the dimensionality of the materials has mainly three effects. The nano structuring of the materials can lead to a quantum confinement effect, ultimately leading to enhanced power factors due to the restricted carrier transport in few directions. Secondly, reduction of thermal conductivity of the material higher than the electrical conductivity based on the scattering lengths of the properties respectively and the third by the bringing the density of states closer to the Fermi level [7, 8].

Bismuth telluride (Bi_2Te_3) and antimony telluride (Sb_2Te_3) have similar structure sharing the same space group R-3m and rhombohedral crystal structure with a hexagonal unit cell as shown in figure 2.4. Bismuth telluride also contains heavy atoms, one of the reasons for higher thermoelectric efficiency. The crystal structure is composed of a layered structure with $\text{-Te}^{(1)}\text{-Bi- Te}^{(2)}\text{-Bi- Te}^{(1)}$ - quintuple layers (QLs) stacked on one another along the c-axis. The bonding between the atomic planes within the QLs is by strong covalent forces and partly by ionic bonding. The QL to QLs is bonded by weak van der Waals (vdW) forces. Due to the presence of weak vdW forces between QLs, the crystal can be cleaved easily along the QLs [2]. A unit cell in the hexagonal basis contains 3 QLs with a lattice constant of 3.049 nm. Due to the layered structure of Bi_2Te_3 , these are highly anisotropic with their physical properties. A variation in thermal and electrical conductivity is observed compared with in-plane and out-plane measurements with little or no significant variation in the Seebeck coefficient values [2, 9, 10].

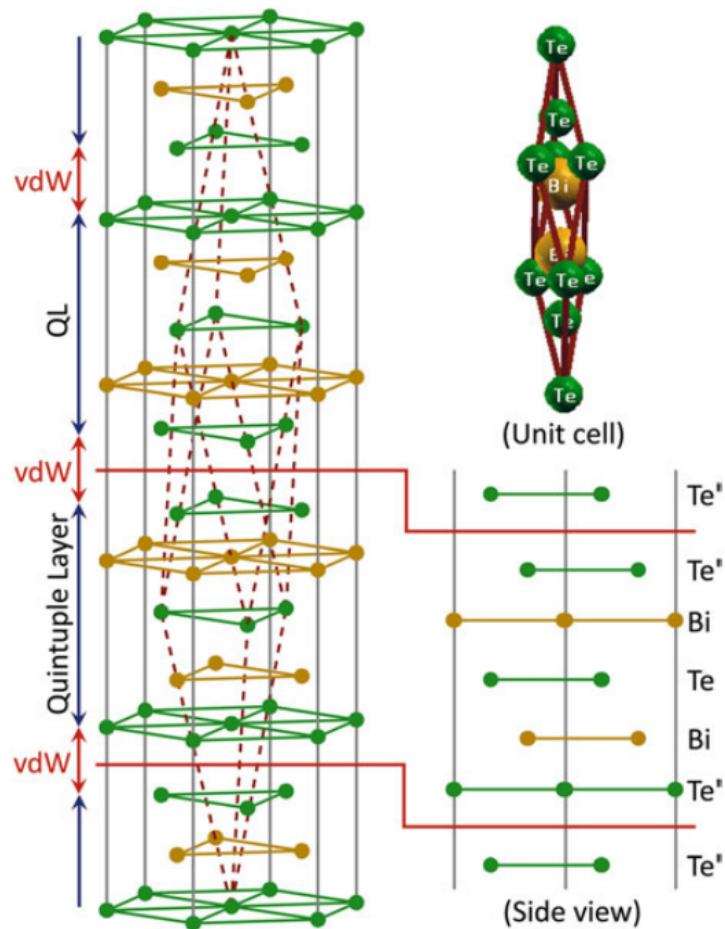


Figure 2.4: The crystal structure of bismuth telluride [5]

Bismuth telluride based room temperature thermoelectric materials are fabricated using various different techniques. These techniques can be broadly classified into two, namely the bulk material synthesis and the thin-film deposition methods. Our application is strictly confined for the material on silicon for the fabrication of the micro-thermoelectric coolers and generators fabrication. Therefore, the primary focus of the subsequent section has been devoted towards the thin-film fabrication technique.

2.4 Electrochemical Deposition

Electrodeposition has been well known for decades now for the synthesis of different semiconductor materials. The major advantage of the electrodeposition technique being its cost-effectiveness compared to dry-deposition techniques. In addition to this, the low processing temperatures play a vital role for using this technique, minimizing the inter-diffusion and undesirable chemical reactions during the depositions. Electrochemical deposition is a simple and fast method of material deposition for thin and thick material deposition with rather simple equipment. This section gives an overview of the basics of

electrochemical deposition and explains in detail the deposition techniques used for the electrodeposition of the different materials synthesized in this thesis work. The deposition methods and the parameters play a key role in influencing the composition and morphology of the deposited films [11-13].

2.4.1 Basic setup of three-electrode cell

A standard three-electrode cell setup is used most commonly for the development and analysis of most electrochemical properties of the material. The three electrodes in the cell are namely the working electrode, the counter electrode and the reference electrode, all immersed in an electrolyte solution containing positively and negatively charged cations and anions, respectively. A simple schematic of the three-electrode cell is given in figure 2.5.

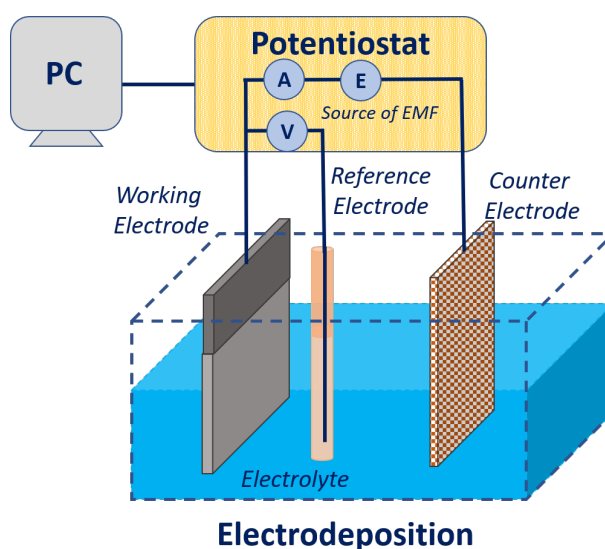


Figure 2.5: Schematic of basic three electrode cell setup

A standard reduction of the metal ion in an aqueous solution when applied with an external power supply can be given as:



Here, due to the application of external current source, the metal ion M^{x+} dissolved in the electrolyte gets deposited on the working electrode (cathode) using the above-stated reduction reaction.

In this work, three different techniques are used for analysing the electrolyte behaviour and for the reduction of material using cyclic voltammetry for analysis, followed by pulsed and constant potential deposition for the material development respectively. Brief details of these techniques are given in the following section.

2.4.2 Cyclic voltammetry

Cyclic voltammetry (CV) is a popular technique to investigate the oxidation and reduction reaction process of molecular species in an electrochemical system. This technique also is capable of transfer-initiated chemical reaction studies. The CV is recorded using a three-electrode setup with the help of a potentiostat. In this technique, the potentiostat is used to sweep the potential between the working electrode and the reference electrode until it reaches a set potential limit and once the set limit is reached, the potential is swept back in the opposite direction. Due to the aqueous electrolytes in this work, this potential sweep limit is restricted due to the hydrogen and oxygen evolution arising from the dissociation of the water molecules. This process might be repeated multiple times, depending on the requirement. During the potential sweep, the corresponding current is recorded between the working electrode and the counter electrode and is plotted against the potential as shown in figure 2.6. The plot of current vs the potential is called cyclic voltammogram. This CV measurement helps in understanding the reactions occurring in the electrolyte.

When a metal ion is reduced at the working electrode to its oxidation state, it is often deposited on the electrode surface. This is said to be a cathodic reaction due to the working electrode providing the negative current. This process takes in two steps; first the cation undergoes the mass transport from the bulk solution to the electrode and then can undergo the reduction via electron transfer process at the electrode surface. The reaction of both the stages are given below:



The reverse reaction occurs when a positive current is passed from the working electrode causing the oxidation reaction and stripping the deposited material back into the electrolyte. The associated reaction is given below:



As an example, the CV of Bi-Sb-Te from our work is shown in figure 2.6. The CV consists of three reduction/cathodic peaks and two oxidation/anodic peaks. The arrows show the direction of the sweep. At negative potential direction, the reduction peaks are observed with negative current explaining the cathodic reaction taking place on the working electrode, and after the deposition occurred on the working electrode, the deposited material is stripped out during its positive potential sweep resulting in the anodic current.

These peaks play a vital role in understanding the optimum deposition parameters for material deposition. The reduction peaks position reveals the deposition potential at which maximum reduction reactions occur for a given electrolytic composition and the corresponding peak current density is used in case of galvanostatic deposition as a starting point for an optimal current density.

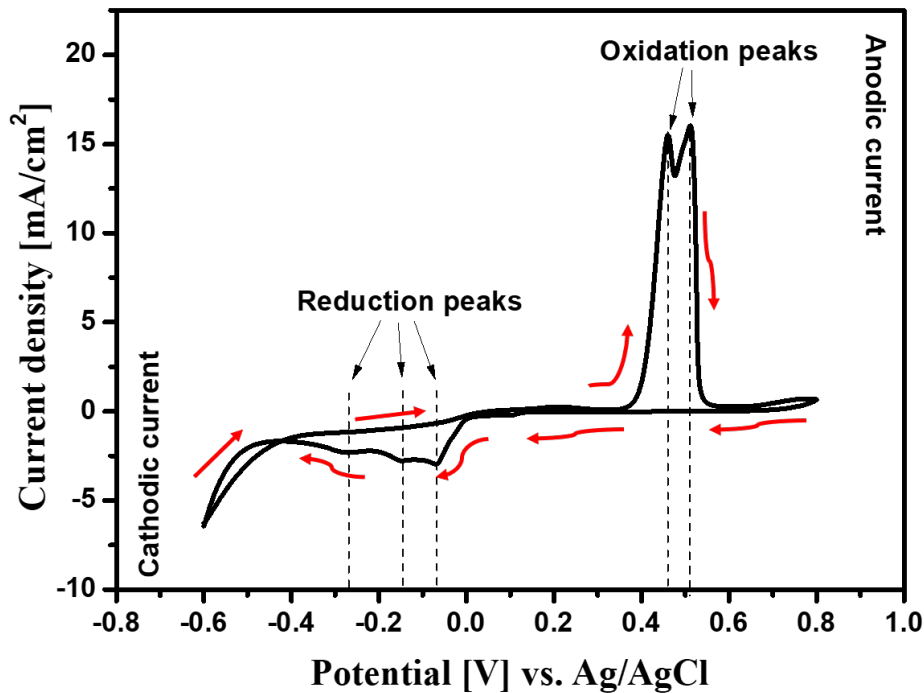


Figure 2.6: Cyclic voltammetry of Bi-Sb-Te solution vs Ag/AgCl reference electrode.

2.4.3 Pulsed Electrodeposition

Pulsed electrodeposition is used in this work for the development of p-type bismuth antimony telluride which will be explained in detail in the subsequent chapters. The pulsed deposition technique is the use of potential or current in non-constant mode but can be modulated. Typically, these pulses follow a rectangular waveform, with either both the pulses can be in one polarity or can be in bipolar. Depending upon the requirement, these pulses can be modulated in various different forms. Compared with the constant current deposition, pulsed deposition offers various advantages which can be used to enhance the film's morphological, structural and physical properties. Chandrasekar et al. [14] extensively discussed various pulsed deposition techniques and the associated theoretical aspects in the form of a review.

Pulsed deposition technique helps in achieving desired composition, denser films and the ability to control the microstructure using the pulse off. It also plays a vital role in the

reduction of film stress, and higher deposition rates can be achieved. The use of pulsed electrodeposition also reduces the use of additives in the system. Various works on pulsed electrodeposited bismuth telluride based materials have been reported in the literature [15-21].

2.4.4 Constant potential and constant current deposition

In this work both the constant potential and constant current deposition methods have been used for the deposition of bismuth telluride based materials and different interconnect materials respectively, which will be discussed further in detail in the subsequent chapters. The constant potential deposition is a simple yet widely used technique. A constant potential is supplied between the working electrode and the reference electrode for the material deposition. These potentials are usually obtained from the studies performed by CV. The constant current technique is the application of the calculated current density between the working electrode and the counter electrode. In this case, the use of the reference electrode is not required, and the current density requirements can be evaluated using the CV studies.

2.5 Electrodeposition of Bismuth Telluride

The films are generally prepared using the standard three-electrode cell as described previously. The films are deposited on the working electrode when a constant current [22] (galvanostatic deposition) or constant voltage [23, 24] (potentiometric deposition) is applied between the working and the counter electrode [25]. There are various other techniques primarily based on the above techniques such as pulsed chronopotentiometry and pulsed amperometry etc., for further refining the material deposition kinetics to achieve specific microstructure, densities and properties of the materials [15, 19, 23, 26]. The first electrodeposition of Bi₂Te₃ material was reported by Takahashi et al. in 1990s [27]. They reported the deposition of a material using potentiostatic technique using aqueous electrolyte solution consisting of HNO₃ along with the Bi and Te ions in the electrolyte with the pH of the solution in the range of 0.9 ± 0.1 . Stoichiometric Bi₂Te₃ material was achieved and was confirmed using the X-ray diffraction studies. Since then, a majority of the electrodeposited Bi₂Te₃ based materials used similar base electrolytes and are highly reported in the literature [28].

Martín-González et al. [12] reported the electrodeposition process of Bi_2Te_3 films in nitric acid baths and described the reaction, as shown below:



Along with the study of the electrodeposition process, they also reported the Pourbaix diagram for Bi_2Te_3 , which was calculated for 7.5 mM of Bi and 10 mM of Te in 1 M HNO_3 as shown in figure 2.7. Dissolution of stable tellurium in the electrolyte is challenging and from the Pourbaix diagram, it was concluded that for the HTeO_2^+ ionic species are stable at the $\text{pH} < 0$. Also, it was observed that above these pH, the dissolved Te precipitates as TeO_2 . The higher the concentration of electrolyte, the higher would be the deposition rate, which is highly favourable for industrial applications and in device fabrication technology.

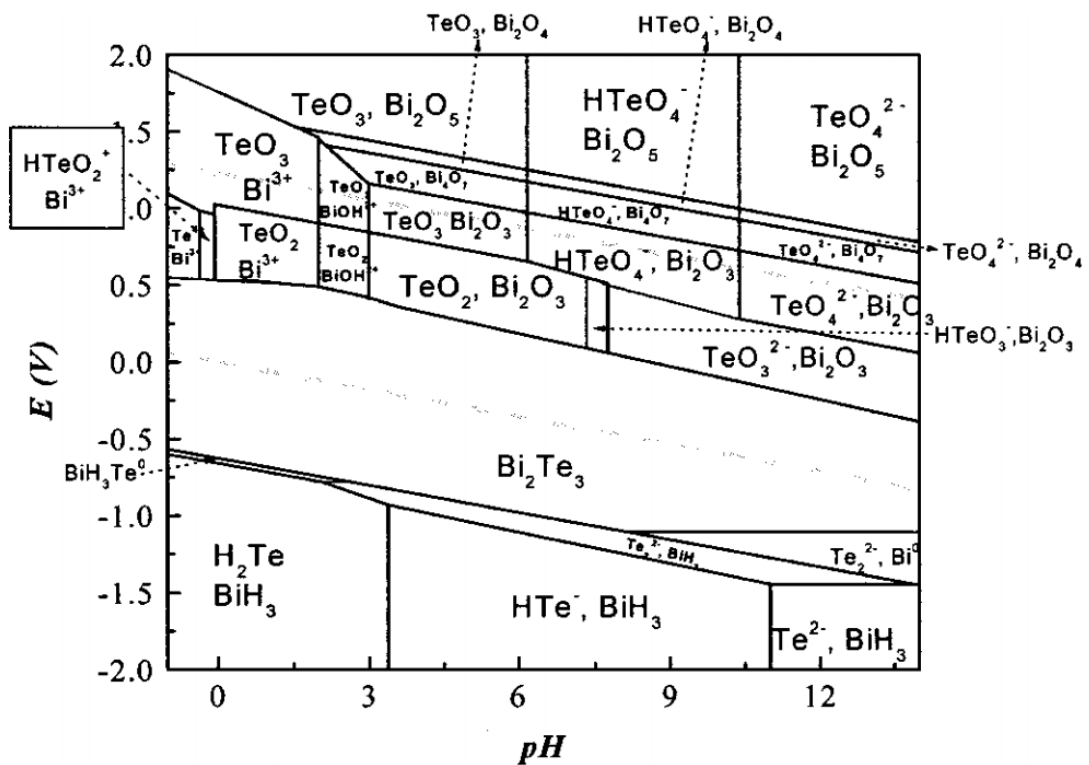


Figure 2.7: Pourbaix diagram of Bi_2Te_3 electrodeposition with 7.5 mM Bi and 10 mM Te in 1M HNO_3 in the electrolyte [12]

2.6 State-of-the-art material

This section of the chapter contains the review of the state-of-the-art electrodeposition of bismuth telluride thermoelectric compounds in detail and their advances in the thermoelectric properties. This covers the deposition of different p- and n-type

thermoelectric materials along with the results obtained by different works. Reviews on electrodeposition of bismuth telluride based materials have been extensively carried out in the literature [25, 28-31]. In this chapter, we would like to discuss the best reported materials with the highest power factors for materials developed using electrodepositions along with the best reported power factor materials deposited with other thin film techniques. An overview of the material thermoelectric properties along with their deposition techniques is given in Table 2.1.

Bismuth telluride based thermoelectric thin-film material is fabricated using different conventional techniques, namely by Chemical Vapour Deposition technique, Thermal evaporation technique, Molecular beam epitaxy (MBE), Pulse laser deposition (PLD), Magneto sputtering technique. However, these techniques have their own respective machine complexity and requirements. Moreover, these following techniques are costly and difficult to achieve the desired material due to the higher working temperature requirements along with the different vacuum conditions. In the following section, along with the electrodeposited materials we will be also discuss briefly on the different reported works on room-temperature thin films material properties deposited using these techniques, which only showcased the best thermoelectric material properties using these techniques so far.

Gary Bulman et al. [32] fabricated micro devices using p-type $\text{Bi}_2\text{Te}_3/\text{Sb}_2\text{Te}_3$ superlattice and n-type δ -doped $\text{Bi}_2\text{Te}_{3-x}\text{Se}_x$ material grown hetero-epitaxially using metalorganic chemical vapour deposition techniques. The material height used for the device pillar was $8.1 \mu\text{m}$ and for the development of n-type $\text{Bi}_2\text{Te}_{3-x}\text{Se}_x$ material, a periodic interrupted deposition was used. During the lay period, the material was dosed with Se and Te respectively which led to increase in the carrier concentration of the materials without the reduction of the mobility of the material. The material properties of both the materials along with the respective power factors are given in the Table 2.1.

Recently in 2019, Ming Tan et. al. [33] developed n-type $\text{Bi}_2\text{Te}_{2.7}\text{Se}_{0.3}$ using an externally induced electrical field to achieve controlled anisotropy of the material developed using a thermal evaporation deposition technique. This material showcased a very high ZT value of around 1.6 at room temperature region. This was due to the controlled anisotropy and inter-planar grain boundaries of the material. This was achieved using the external electric field of 20 V during the deposition. The energy filtering effect led to enhancement

of the electron mobility and a reduction in the deformation potential. The thermoelectric performance parameters are given in table 2.1.

Wang et al. [34] described the deposition of n-type Bi_2Te_3 thermoelectric films using radio frequency (RF) magnetron co-sputtering techniques. Films with a thickness of 400 nm were deposited using this technique. The Bi and Te were sputtered using a power of 10 W and 12 W respectively. Films after the deposition were annealed from 150-350 °C and studied for the morphological, structural and thermoelectric properties. The sample annealed at 300 °C showcased the best Seebeck coefficient of $-242 \mu\text{V/K}$ with a fairly high electrical conductivity resulted in a power factor of 2.1 mW/m.K^2 one of the highest reported using the technique. Chao et al. [35] developed stoichiometric Bi_2Te_3 material using an MBE technique at the temperature of 250 °C. The obtained material showcased a high thermoelectric performance with the Seebeck coefficient of $-190 \mu\text{V/K}$ and the electrical conductivity of $1.0 \times 10^5 \text{ S/m}$ resulting in a power factor of 3.61 mW/m.K^2 , which is one of the highest power factor value obtained by this technique.

Kim et al. [36] developed n-type $\text{Bi}_2\text{Te}_{3-x}\text{Se}_x$ using an electrodeposition technique, using potential-current co-adjusted pulse electrodeposition technique in order to achieve highly (110) oriented and dense films of 20-25 μm thickness. Kim et al. showcased that the well-aligned grain structures can be achieved by using a pulsed electrodeposition technique for preferred highly (110) oriented crystal structure compared to the films grown using constant potential electrodeposited films which lead to randomly oriented rhombohedral Bi_2Te_3 phase. Low-temperature annealing studies were performed for the obtained films and the film annealed at 200 °C showcased enhanced thermoelectric properties. By the use of low-temperature annealing, the uncontrolled point defects and the low crystallinity of the electrodeposited films were improved which resulted in a Seebeck coefficient of $-105 \mu\text{V/k}$ with enhanced electrical conductivity of $1.7 \times 10^5 \text{ S/m}$, enhancing the power-factor to 1.92 mW/m.K^2 .

Lei et al. [37] demonstrated a high growth rate of 100 $\mu\text{m/h}$ for Bi_2Te_3 electrodeposition of thick films on 1 cm^2 etched nickel sheets. They observed by the addition of polyvinyl alcohol (PAV) into the electrolyte, the films deposition as well as the thermoelectric performance can be enhanced. The addition of PAV helped in the uniform ion distribution on the top surface of the material growing area and also helps in reducing the surface tension of the electrolyte heading to denser films. The films were deposited using both potentiostatic electrodeposition and pulsed electrodeposition techniques. The films

deposited using pulse electrodeposition technique showcased denser, smoother films with no protrusions. Well adherent, stoichiometric, dense Bi_2Te_3 films were developed with a high Seebeck coefficient of $-200 \mu\text{V/K}$ with high electrical conductivity of $4.0 \times 10^4 \text{ S/m}$ resulting in a high power-factor of 1.6 mW/m.K^2 .

Jongbeom Na et al. [38] developed Bi_2Te_3 thin films using pulsed electrodeposition on the stainless-steel substrate and later transferred them onto a flexible adhesive film substrate for the fabrication of the flexible thermoelectric device. Bi_2Te_3 films were deposited using a precisely controlled deposition potential. It was observed that the films deposited at a potential of $+0.02\text{V}$ led to the deposition of $\text{Bi}_{2.17}\text{Te}_{2.83}$ with better thermoelectric performance. Optimized pulse deposition led to higher crystallinity along the preferred (110) direction with high electrical conductivity of the films along with smoother and dense films. Later these deposited thin films were transferred on the flexible substrates, and all the thermoelectric performance of the material were measured on the flexible substrate. The material showcased a Seebeck coefficient of $-146 \mu\text{V/K}$ with high electrical conductivity of $6.9 \times 10^4 \text{ S/m}$ resulting in a high-power factor of 1.47 mW/m.K^2 . Using this material and the PEDOT as its counter p-type material, a flexible thermoelectric device was fabricated. A device of 5 thermocouples of both n-type Bi_2Te_3 and p-type PEDOT, when subjected to a temperature gradient of 12 K , resulted in an output voltage of 5 mV .

S. Li *et al.*, [39] reported high-quality nanostructured bismuth telluride thick films deposited using an electrodeposition technique of thickness range $100 - 350 \mu\text{m}$. The Bi_2Te_3 film deposited with $200 \mu\text{m}$ thickness was used to measure the thermoelectric properties and annealed at $300 \text{ }^\circ\text{C}$ for 2 and 5 hrs in a reductive H_2 atmosphere. A significant enhancement of Seebeck value was observed due to significant improvement of the crystallinity and change in defect concentration. The Seebeck coefficient was improved from $-70 \mu\text{V/K}$ to $-130 \mu\text{V/K}$ with a measured electrical conductivity of $4.0 \times 10^4 \text{ S/m}$ resulting in a power factor of 0.68 mW/m.K^2 . Li et al. also thoroughly investigated the effect of doping on Bi_2Te_3 by using Se and Sb for the development of n- and p-type materials and performed similar annealing studies on the doped films. Although, no significant improvement in the thermoelectric performance was observed for the developed thermoelectric films but it showcased the higher potential for material properties through doping and annealing process.

J. Kim et al. [40] prepared a nanocomposite film consisting of β -Ag₂Te nano precipitates and an Ag-doped Sb₂Te₃ matrix via electrodeposition and low-temperature annealing. They observed that during annealing of the amorphous Ag-Sb-Te film, highly dense β -Ag₂Te nano precipitates of 40 nm diameter were spontaneously generated due to differences in the binding energies of the Ag-Te and Sb-Te bonds. The electronic transport properties of the resulting p-type Sb₂Te₃ film were significantly enhanced; as a result of the energy-dependent carrier filtering effect at the phase boundary between the β -Ag₂Te nano precipitates and the Sb₂Te₃ matrix. In addition, a maximum power factor of 1.87 mW/m.K² was obtained at 300 K, which is comparable to the highest values reported for the bulk.

(Bi_{1-x}Sb_x)₂Te₃ thermoelectric thin films were deposited on stainless steel substrates using an electrolyte (HClO₄ 1M and C₄H₆O₆ 0.1M) by pulse plating in order to optimize the grain growth. All samples were annealed at 200 °C for 1 h in the presence of an argon environment. The thermoelectric properties were improved without modification in the composition of the film with annealing. Frari et al. observed that smaller thickness (≤ 5) films have excellent resistivity around 150 $\mu\Omega$ -m and a power factor of around 0.19 mW/m.K² [41].

In 2012, Schumacher et al. [19] systematically optimized the p-type Sb₂Te₃ thermoelectric films by potentiostatic electrodeposition on Au and stainless steel substrates. The influence of the preparative parameters of deposition voltage, concentration, and the deposition method was investigated in a nitric acid solution. Pulsed-deposited films of Sb₂Te₃ showed improved properties, such as morphology, film composition, and thermoelectric parameters, respectively. Improvements in terms of electrical conductivity could be achieved by annealing, most likely due to a reduction of crystal defects and fine-tuning into almost perfect compositions. The power factor of the films deposited in DC mode can be improved by annealing up to about 2.5 times the initial values. However, as-deposited films made with pulsed deposition still show much higher power factors comparable to the best-reported values for electrochemically deposited Sb₂Te₃ films. In 2013, Schumacher et al. [36] did a comprehensive study of optimization of p-type BiSbTe and n-type BiSeTe films on Au and stainless-steel substrate over a wide range of deposition potentials. In this work, they studied the influence of preparative parameters such as the composition of the electrolyte bath and the deposition potential. The pulsed deposited Sb₂Te₃ had a Seebeck coefficient of +150 μ VK⁻¹ and a power factor of 1.1 mW/m.K². In this work, Christian Schumacher et al. also studied the effects of

annealing on deposited films. They observed change in film's composition and improvements in thermoelectric performance of materials in Te equilibrium atmosphere. However, they observed that the Te content reached a steady state after a particular annealing time due to the gaseous Te ambience. The samples annealed in the Te atmosphere exhibit an improvement of power factor, increases of about + 70% and observed causing maximum values of 1.32 mW/m.K^2 .

Trung et al. [42] grew a thick film of Sb_2Te_3 using pulsed electrochemical deposition. The deposited films were also annealed to enhance the thermoelectric properties. The annealing process was performed for 1 hour in N_2 ambient. Due to annealing, the Seebeck coefficient of the as-deposited Sb_2Te_3 sample increased from $140 \mu\text{VK}^{-1}$ to $170 \mu\text{VK}^{-1}$. The electrical resistivity decreased remarkably from $60 \mu\Omega\text{m}$ to $20 \mu\Omega\text{m}$ after the annealing process. They concluded that the large value of the electrical resistivity of the as-deposited film possibly is related to the high number of defects at the grain boundaries and therefore it is greatly affected by the annealing process.

In 2018, Kang et al. [43] deposited p-type Bi-Sb-Te by pulse electrodeposition. They observed the nodular followed by dendritic grain development on the top of a compact layer as the deposition proceeded. At the p-type film/substrate interface, the presence of a distinct Te-rich layer was observed. The $\text{Bi}_{0.45}\text{Sb}_{1.22}\text{Te}_{0.33}$ film is deposited via pulsed deposition with a Seebeck coefficient of $+150 \mu\text{VK}^{-1}$ and a power factor of $0.15 \text{ mWm}^{-1}\text{K}^{-2}$.

Table 2-1: List of state-of-the-art high performing thin film materials along with their fabrication technologies.

References	Material	n- /p- type	Deposition Technology	Seebeck coefficient (μVK^{-1})	Electrical conductivity (Sm^{-1})	Power- factor ($\text{mWm}^{-1}\text{K}^{-2}$)
[32]	p-type $\text{Bi}_2\text{Te}_3/\text{Sb}_2\text{Te}_3$	p- type	MOCVD	238	9.8×10^4	5.55
	n-type δ -doped $\text{Bi}_2\text{Te}_{3-x}\text{Se}_x$	n- type	MOCVD	-276	7.2×10^4	5.56
[33]	$\text{Bi}_2\text{Te}_{2.7}\text{Se}_{0.3}$	n- type	Thermal evaporation	-	-	4.50
[34]	Bi_2Te_3	n- type	Co- Sputtering	-242	3.6×10^4	2.10
[35]	Bi_2Te_3	n- type	MBE	-190	1.0×10^5	3.60
[44]	Pt $\text{Pt}_{0.060}/$ $\text{Bi}_{2.0}\text{Te}_{2.7}\text{Se}_{0.3}$	n- type	Pulsed laser deposition	-220	$*7.3 \times 10^4$	3.50
[45]	p- $\text{Bi}_{0.4}\text{Te}_{3.0}\text{Sb}_{1.6}$	p- type	Flash evaporated	254	2.4×10^4	1.59
	n- $\text{Bi}_{2.0}\text{Te}_{2.7}\text{Se}_{0.3}$	n- type		-179	6.6×10^4	2.15
[46]	Cu doped Te	n- type	ECD	-227	1.0×10^5	5.62
[47]	$\text{Bi}_2\text{Te}_{3-x}\text{Se}_x$	n- type	ECD	-105.9	1.7×10^5	1.91
[48]	Ag-doped Sb_2Te_3	p- type	ECD	*137	1×10^5	1.870

References	Material	n- /p- type	Deposition Technology	Seebeck coefficient (μVK^{-1})	Electrical conductivity (Sm^{-1})	Power- factor ($\text{mWm}^{-1}\text{K}^{-2}$)
[37]	Bi_2Te_3	n- type	ECD	-200	4.0×10^4	1.60
[38]	$\text{Bi}_{2.17}\text{Te}_{2.83}$	n- type	ECD	-146	6.9×10^4	1.47
[49]	Sb_2Te_3	p- type	ECD	*~117	1.0×10^5	1.36
[20]	$(\text{Bi}_x\text{Sb}_{1-x})_2\text{Te}_3$	p- type	ECD	182	4.0×10^4	1.32
	$\text{Bi}_2(\text{Te}_x\text{Se}_{1-x})_3$	n- type	ECD	-130	4.8×10^4	0.82
[42]	Sb_2Te_3 Pulsed- deposited	p- type	ECD	170	4.0×10^4	1.12
[50]	Bi_2Te_3	n- type	ECD	-100	*~ 7.1×10^4	0.74
[39]	Bi_2Te_3	n- type	ECD	-130	4.0×10^4	0.68
[41]	Sb_2Te_3	p- type	ECD	120	1.42×10^4	0.20
[43]	$\text{Bi}_{0.45}\text{Sb}_{1.22}\text{Te}_{3.33}$	p- type	ECD	150	6.6×10^3	0.15

2.7 State-of-the-art device

This section of the chapter will walk through the advances in the micro-thermoelectric device fabrications along the state-of-the-art works associated. This section will extensively review on the electrodeposited thermoelectric device; however, it will also give a brief overview of the other devices fabricated by different techniques.

2.7.1 Literature review on thermoelectric generator devices:

- **Figure of merit**

- Efficiency -conversion efficiency, is expressed as the ratio of the obtained output power from the device to the heat injected into the device through the hot side, as has been explained in the previous section, equation 2.6.
- Power factor -usually, the TEGs are also evaluated based on the figure of merit called the power factor. It is expressed as the power output obtained from a unit area of the TEG which is subjected to unit temperature difference.

$$\text{Power Factor} = PF = \frac{\text{Output power}}{\text{Area} \cdot (T_H - T_C)^2} \quad 2.26$$

- Voltage factor – another important figure of merit of the TEGs is the voltage factor which can be expressed as the ratio of the output voltage to the area of the TEG and the temperature difference that the opposite surface of the TEG are subjected to.

$$\text{Voltage Factor} = VF = \frac{\text{Output voltage}}{\text{Area} \cdot (T_H - T_C)} \quad 2.27$$

- **Classification of the micro-thermoelectric generators**

Depending on the direction of heat flow in the structure and the current flow, the micro thermoelectric generators (μ TEG) can be broadly classified into-

- **Vertical structures**, in which the direction of heat flow and also the current flow in the μ TEGs is in the vertical direction. In this type of device architecture, the thermal leg pairs are arranged between the heat source

and the heat sink so that the heat energy is made to flow through the substrate and the thermocouple arrangement, resulting in a large voltage across the ends of the thermocouple. The simplicity of fabrication, ease of enhancing the integration density and high output voltage [51] obtained from such device has made it one of the most popular choice for commercial applications. Hence in this thesis, the development and fabrication of such vertical thermoelectric structures on Si will be discussed.

- **Lateral structures**, in which the direction of the current flow, as well as the heat flow, is in the lateral direction. These types of structures offer planar distribution of the thermocouples, which gives more flexibility in tailoring the dimensions of the thermocouple to enhance the performance of the μ TEGs [52]. Although this technology allows for increasing the resistance of the thermocouple assembly which results in increased output voltage, the loss due to the parasitic heat flux associated with this type of structure is one of the biggest disadvantage.
- **Hybrid structures**, in which the direction of heat flow can be in the conventional vertical direction, whereas the current can flow across the lateral direction in the device. This type of device architectures combines the advantage of both the lateral and vertical architecture. The planar arrangement of the thermo-pair brings ease in altering the dimensions of each of the thermocouples that aids in improving the overall performance of the thermoelectric generator and it also offers ease in fabrication with the IC compatible technology. Unlike the lateral or in-plane structures, the heat flows across the vertical direction of the structure. There has been some effort in enhancing the efficiency of these μ TEGs by improving the path of the heat flux through introducing a metal layer on the hot and cold side to promote more efficient heat transfer or by introducing cavities around the thermocouple [53]. And the schematic of different device structure is shown in figure 2.8.

In the present work, we have focussed on the design, development and implementation

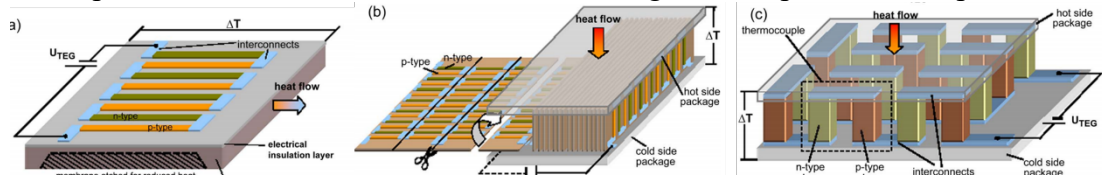


Figure 2.8: Schematic of different device structure (a) lateral (b) hybrid and (c) vertical device [54]

of a high-efficiency vertical structure type μ TEG as it offers –

- Comparatively lower contact resistance as compared to the rest of the structures.
- It restricts the parasitic heat flow.
- This type of structure also offers improved thermal contact.
- Above all the high integration density offered by the vertical arrangement of thermocouple enhances the output power substantially.

Hence, we will be looking into the different reported works on such vertical μ TEGs to understand the development of the same over time.

2.7.2 State-of-the-Art Vertical structure μ TEG

The first of the most prominent contributions in the field of development of μ TEGs was done by the Japanese company Seiko Instruments. They commercialized a thermoelectrically driven wristwatch employing Bi-Te based compounds for fabricating the thermoelectric module having an overall dimension of $2 \times 2 \times 3\text{mm}^3$ comprising of over 50 thermopairs and as shown in Fig. 2.9 [55]. They employed the hot-pressing method to enhance the structural stability of the Bi-Te compound used, which otherwise has a fragile crystal structure. The p-type and n-type pillars were formed on a different substrate, and they were finally flip-chip bonded to form the thermoelectric device to be placed inside the wristwatch as shown in Fig. 2.10.

Another important step towards the fabrication of μ TEGs with thin-film technology was the development of thermoelectric devices with V-VI compounds like Bi_2Te_3 and $(\text{Bi, Sb})_2\text{Te}_3$ by MicroPelt [56]. The unique approach of the 'two wafers' process followed by

MicroPelt gave the freedom of growing and optimizing the properties of the p-type and

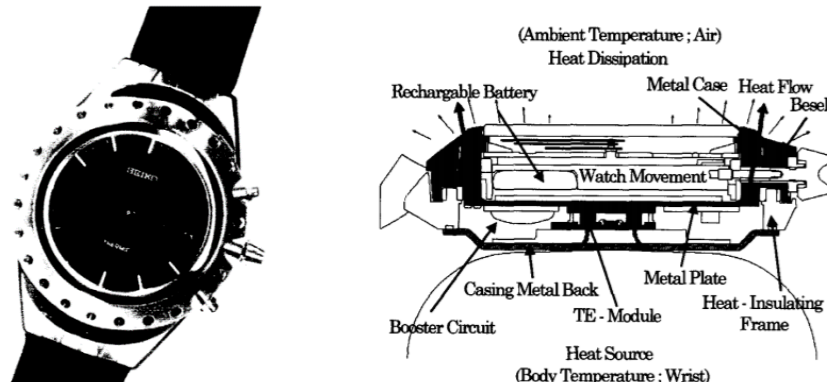


Figure 2.9: The picture of the thermoelectric watch marketed by Seiko (left), schematic of the thermoelectric powered wristwatch (right) [55].

n-type material on a separate substrate, which finally would be flip-chip bonded. The advantage of this process is that both the materials could be grown separately which reduces the chances of damaging temperature-sensitive material with high-temperature processing or treatment steps like annealing. Firstly, the bottom electrode metal and interconnecting material, as well as the contact electrodes, are grown on the separate substrates. Then individual thermoelectric material is grown, and finally the solder material is deposited on top of the thermal legs for the final flip-chip bonding process. Such an implemented μ TEG generated $0.67\mu\text{W}$ of power when the device was subjected to a temperature gradient of 5K which was delivered across a matched load resistance.

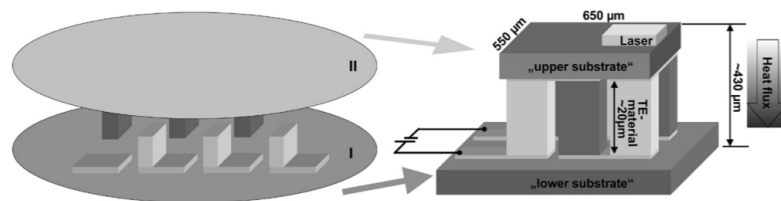


Figure 2.10: A depiction of the 'two wafers' process implemented by MicroPelt to develop micro thermoelectric devices (left), the schematic of one of the applications of the bonded thermoelectric pairs as a cooler (right)[56]

Another remarkable contribution towards the fabrication technology of the μ TEGs was from the Jet Propulsion Laboratory. They implemented the 'single wafer' process in which they employed positive photoresist to build all the required structures through relatively simple and cost-effective electrodeposition techniques [57]. As shown in Fig. 2.11, first they electrodeposited the bottom contact electrode and used positive photoresist to develop a thick spin-coated layer. Next, they opened the template and deposited the required thermoelectric material using those templates. Then a thin layer of photoresist

was spin-coated to protect the thermal legs, and the holes were opened for the deposition of the second layer of the thermal leg. Following the electrodeposition of the material, the upper contact material was deposited, and the sacrificial layers are eventually removed to get the thermoelectric module. This fabricated batch device had 126 p-type and n-type elements, each of 60 μm diameter and 20 μm height.

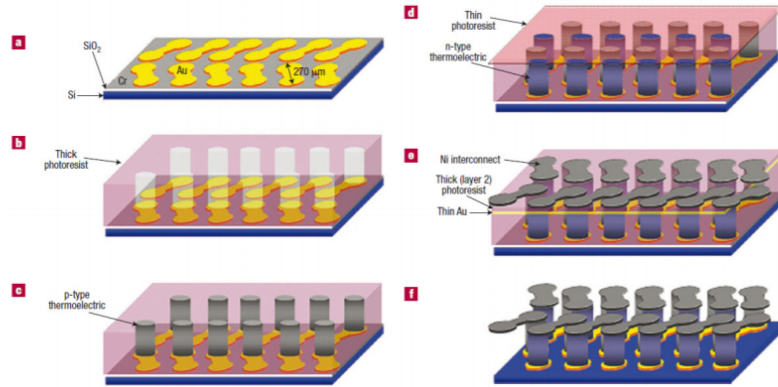


Figure 2.11: Process flow of the 'single wafer' process implemented by the Jet Propulsion Laboratory [57]

Glatz et al. developed a fabrication process of μTEGs that can be used on non-planar surfaces. They used the chemically resistant and very structurally stable photoresist SU8 for the fabrication of high aspect ratio thermopillars [58]. This photoresist is used as a sacrificial layer, and also later used as the base layer on which the thermoelectric pillars are embedded. The process flow, as shown in Fig. 2.12 begins with the deposition of electrode material which also acts as the seed layer for further deposition steps. Next, the photoresist was spin-coated and patterned to open the holes for the deposition of the p-type and the n-type thermoelectric materials. After the deposition of both thermoelectric materials, the top metal contact is established and the sacrificial layer are removed by dedicated solvents and processing steps.

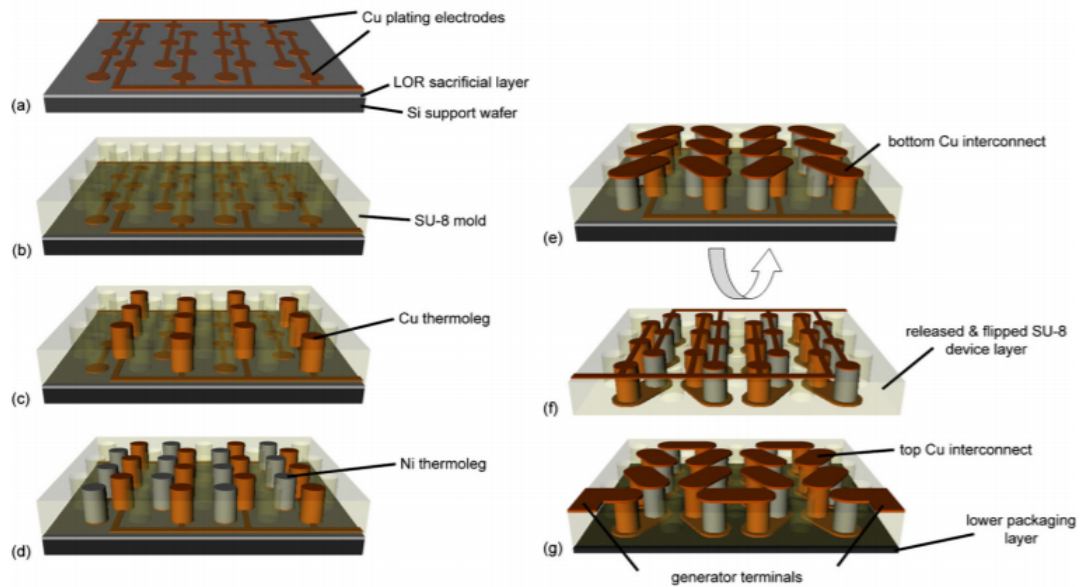


Figure 2.12: Process flow of the micro thermoelectric generator implemented by Glatz et al. [58]

A step forward in the development of miniaturized thermoelectric generators was demonstrated by Li et al. through the implementation of a high-density Si-nanowire-based thermoelectric module [59]. They exploited the excellent thermoelectric properties demonstrated by the Si nanowires and took a top-down approach to implement this chip-scale thermoelectric module. They employed conventional lithography and etching steps to realize the bundles of nanowires, and further they selected the low thermal conductivity polymer polyimide to fill the matrix of the nanowires as shown in Fig. 2.13. Such an arrangement generated a maximum output power of $0.47\mu\text{W}$ when it was subjected to a temperature difference of 70 K. Not only in microscale, this developed thermoelectric generator made itself a potential candidate to be used in wide range of applications where microwatt levels of power are required from a nanoscale footprint.

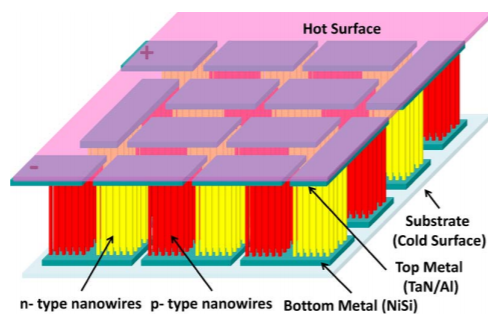


Figure 2.13: Schematic of the high density arrangement of Si-nanowires in chip-scale thermoelectric generator [59].

Kim et al. proposed another way of fabricating a cross-plane μ TEG using the flip-chip technique to bond the substrate layer with the top electrodes that are deposited on a separate layer of the substrate [60]. They fabricated 242 thermocouples having $20\mu\text{m}$ height, producing the overall volume of $5\times 5\text{ mm}^2$. The fabrication process as depicted in Fig. 2.14 shows the technique of using positive photoresist to make an opening for the deposition of the Bi-Te and Sb-Te thermoelectric materials. These electrodeposited thin films demonstrated a Seebeck coefficient of $-59\ \mu\text{V/K}$ and $485\ \mu\text{V/K}$ respectively. The thermocouple legs are polished to get a smooth top surface that aids in facilitating the flip-chip bonding. Another substrate layer consisting of patterned Sn bumps were finally flip-chip bonded to implement the final device. Subjected to a temperature difference of 22.3K , this device generated output power of $5.9\mu\text{W}$.

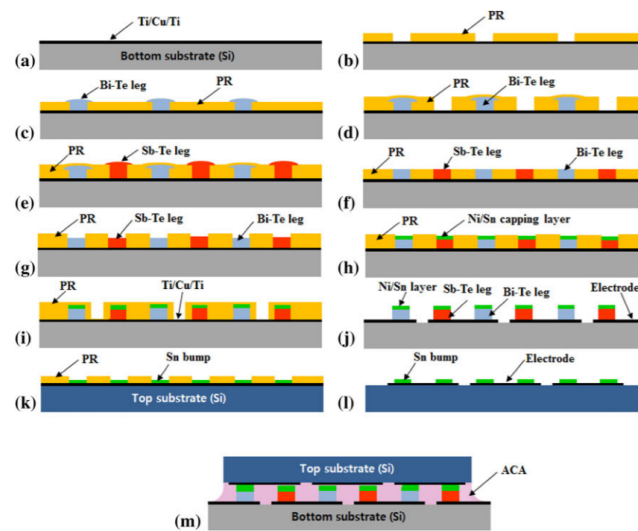


Figure 2.14: Process flow of the fabrication of cross-plane μ TEG as proposed and implemented by Kim et al. [60]

Over the past decade, significant research and industrial interest have been drawn towards the enhancement of the performance of the integrated micro thermoelectric generators. Along with novel integration techniques, substantial effort has also been put forward in optimizing the contact and the resistance due to connectors to further boost the efficiency of these μ TEGs. Zhang et al. demonstrated an electroplated cross-plane μ TEG comprising of 127 thermoelectric pillars embedded in SU8 resist layer [61]. They used Bi_2Te_3 and Sb_2Te_3 as the n-type and p-type thermoelectric material respectively, deposited with pulsed electroplating employing the standard three-electrode deposition process. In order to fabricate the device, they sputtered and patterned a Cr/Au layer as the bottom connector of the thermoelectric pillars. An Au layer was further electrodeposited to form the connectors. As shown in Fig. 2.15, next they formed the SU8 matrix and patterned the

holes for the electrodeposition of the previously mentioned n-type and p-type thermoelectric materials successively. Ni has been used as the material to form the top connector. The electrodeposited top and bottom connectors reduced the parasitic resistances and this in turn aided in enhancing the performance of the fabricated μ TEG. They achieved the remarkable power density of $9.2\text{mW}/\text{cm}^2$ when the device was subjected to a temperature difference of 52.5K .

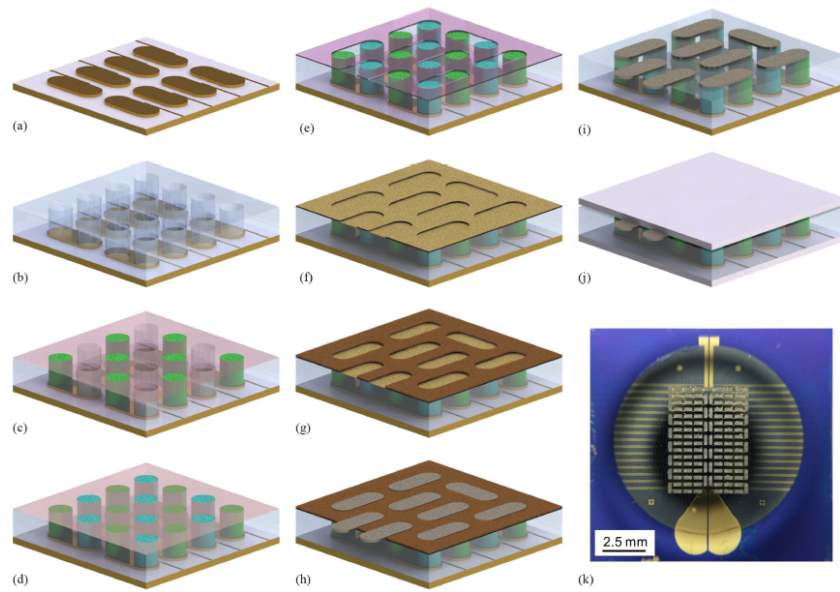


Figure 2.15: Process flow of the bottom-up approach undertaken to fabricate the high power density micro thermoelectric generator [61]

Owing to the versatility that the μ TEGs offer, they are used in a wide range of applications as sustainable power source, one of them being as the power source for low-power demanding wearable sensor and electronics applications. Dunham et al. presented the design, fabrication and intricate characterization of the fabricated μ TEGs that consisted of physical vapour deposited n-type and p-type thermocouples [62]. One of the potential obstacles in the characterization of such a miniaturized device is the in-situ measurement of the actual temperature gradient that the generator is subjected to. The various parasitic effects at the interface hinder such measurements. In this work, they used infrared microscopy for the accurate measurement of this temperature gradient along with the thermal resistance measurement of the device. The compact device yielded an output power of 1mW from a temperature gradient of 7.3K , making it a potential candidate for powering the wearable sensors as a replacement of energy-limited batteries.

Li et al. reported the fabrication of a high-density micro thermoelectric cooler that comprised of 5000 thermal pillars per cm^2 area [63]. This particular device demonstrated

very high reliability along with remarkably high response times, which outruns many of the reported micro thermoelectric coolers. The fabrication technology behind the implementation of this devices, could be employed for the fabrication of μ TEGs as well. As shown in Fig. 2.16, they employed a conventional lithography process along with electrochemical deposition for the fabrication of high-density thermoelectric modules. They used BiTeSe and pure Te as the n-type and p-type thermoelectric material respectively. A novel approach to reduce the contact resistivity was presented in this work. Following each step of electrodeposition, they plated a thin layer of Au before the next layer of electrodeposition, which reduced the resistivity, contact resistance and also reduced the probability of thermal oxidation of the thermocouple.

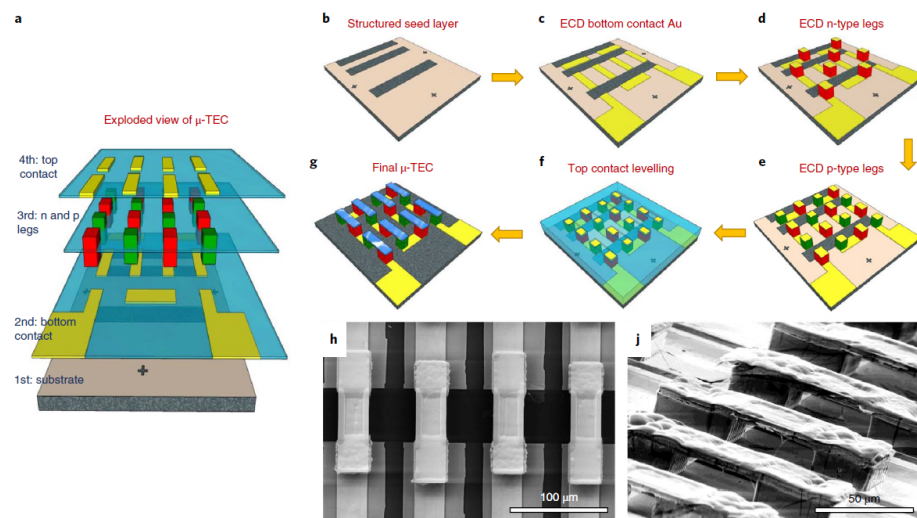


Figure 2.16: Schematic of the fabrication process of the micro thermoelectric coolers with rapid response time. [63]

2.8 References

- [1] J.-F. Li, W.-S. Liu, L.-D. Zhao, and M. Zhou, "High-performance nanostructured thermoelectric materials," *NPG Asia Mater*, vol. 2, pp. 152-158, 10/21/online 2010.
- [2] D. E. Rowe, Burkov, A., Kishimoto, K., Ravich, Y., Fedorov, M., Ktitorov, S., Anatyshuk, L., Slack, G., Burke, E., Haringa, J., Han, S., Koyanagi, T., Nagao, K., Studd, R., Trimmer, D., Bennett, G., Hall, W. (Ed.), Borshchevsky, A., Cassart, M., Redstall, R., Hartman, R., Stordeur, M., Vining, C., Birkholz, U., Cobble, M., Min, G., Woodbury, H., Emin, D., Pollock, D., Taylor, R., Scherrer, S., Scherrer, H., Beaudry, B., Matsuura, K., Kajikawa, T., Skrabek, E., Gschneidner, Jr., K., Fano, V., McNaughton, A., Levinson, L., Issi, J., Goldsmid, H., Buist, R., Nishida, I., Bhandari, C., Vedernikov, M., Stockholm, J., Matsubara,

- K., Ohta, T., Zaitsev, V., Uemura, K., Aselage, T., Mondt, J., Cook, B., Kuznetsov, V., Vandersande, J., Marlow, R., Scoville, N. (1995). CRC Handbook of Thermoelectrics. Boca Raton: CRC Press., "CRC Handbook of Thermoelectrics," 1995.
- [3] G. J. Snyder and E. S. Toberer, "Complex thermoelectric materials," *Nat Mater*, 10.1038/nmat2090 vol. 7, no. 2, pp. 105-114, 02//print 2008.
- [4] L. Bell, "Cooling heating, generating power, and recovering waste heat with thermoelectric systems," *Science*, vol. 321, pp. 1457-1461, // 2008.
- [5] I. T. Witting *et al.*, "The Thermoelectric Properties of Bismuth Telluride," *Advanced Electronic Materials*, vol. 5, no. 6, p. 1800904, 2019/06/01 2019.
- [6] L.-D. Zhao, V. P. Dravid, and M. G. Kanatzidis, "The panoramic approach to high performance thermoelectrics," *Energy Environ. Sci.*, vol. 7, no. 1, pp. 251-268, 2014.
- [7] M. S. Dresselhaus *et al.*, "New Directions for Low-Dimensional Thermoelectric Materials," *Advanced Materials*, vol. 19, no. 8, pp. 1043-1053, 2007.
- [8] Z.-G. Chen, G. Han, L. Yang, L. Cheng, and J. Zou, "Nanostructured thermoelectric materials: Current research and future challenge," *Progress in Natural Science: Materials International*, vol. 22, no. 6, pp. 535-549, 12// 2012.
- [9] J. S. G. S. Nolas, and H. J. Goldsmid, "Thermoelectrics," Springer Series in *Material Science*, 2001.
- [10] H. Kaibe, Y. Tanaka, M. Sakata, and I. Nishida, "Anisotropic galvanomagnetic and thermoelectric properties of n-type Bi₂Te₃ single crystal with the composition of a useful thermoelectric cooling material," *Journal of Physics and Chemistry of Solids*, vol. 50, no. 9, pp. 945-950, 1989/01/01/ 1989.
- [11] M. Datta and D. Landolt, "Fundamental aspects and applications of electrochemical microfabrication," *Electrochimica Acta*, vol. 45, no. 15, pp. 2535-2558, 2000/05/03/ 2000.
- [12] M. S. Martín-González, A. L. Prieto, R. Gronsky, T. Sands, and A. M. Stacy, "Insights into the Electrodeposition of Bi₂Te₃" *Journal of The Electrochemical Society*, vol. 149, no. 11, p. C546, 2002.
- [13] F. Nasirpouri, "An Overview to Electrochemistry," in *Electrodeposition of Nanostructured Materials*, F. Nasirpouri, Ed. Cham: Springer International Publishing, 2017, pp. 43-73.

- [14] M. S. Chandrasekar and M. Pushpavanam, "Pulse and pulse reverse plating—Conceptual, advantages and applications," *Electrochimica Acta*, vol. 53, no. 8, pp. 3313-3322, 2008/03/10/ 2008.
- [15] S. Diliberto, V. Richoux, N. Stein, and C. Boulanger, "Influence of pulsed electrodeposition on stoichiometry and thermoelectric properties of bismuth telluride films," *physica status solidi (a)*, vol. 205, no. 10, pp. 2340-2344, 2008.
- [16] Y. Ma, E. Ahlberg, Y. Sun, B. B. Iversen, and A. E. C. Palmqvist, "Thermoelectric properties of thin films of bismuth telluride electrochemically deposited on stainless steel substrates," (in English), *Electrochimica Acta*, vol. 56, no. 11, pp. 4216-4223, Apr 15 2011.
- [17] V. Richoux, S. Diliberto, and C. Boulanger, "Pulsed Electroplating: a Derivate Form of Electrodeposition for Improvement of $(\text{Bi}_{1-x}\text{Sb}_x)_2\text{Te}_3$ Thin Films," *Journal of Electronic Materials*, vol. 39, no. 9, pp. 1914-1919, 2010// 2010.
- [18] V. Richoux, S. Diliberto, C. Boulanger, and J. M. Lecuire, "Pulsed electrodeposition of bismuth telluride films: Influence of pulse parameters over nucleation and morphology," *Electrochimica Acta*, vol. 52, no. 9, pp. 3053-3060, 2007/02/15/ 2007.
- [19] C. Schumacher *et al.*, "Optimization of Electrodeposited p-Doped Sb_2Te_3 Thermoelectric Films by Millisecond Potentiostatic Pulses," *Advanced Energy Materials*, vol. 2, no. 3, pp. 345-352, 2012.
- [20] C. Schumacher *et al.*, "Optimizations of Pulsed Plated p and n-type Bi_2Te_3 -Based Ternary Compounds by Annealing in Different Ambient Atmospheres," *Advanced Energy Materials*, vol. 3, no. 1, pp. 95-104, 2013.
- [21] A. Zhou *et al.*, "Enhancing the Thermoelectric Properties of the Electroplated Bi_2Te_3 Films by Tuning the Pulse Off-to-on Ratio," *Electrochimica Acta*, vol. 178, pp. 217-224, 10/1/ 2015.
- [22] S. Li *et al.*, "Fabrication of Nanostructured Thermoelectric Bismuth Telluride Thick Films by Electrochemical Deposition," *Chemistry of Materials*, vol. 18, no. 16, pp. 3627-3633, 2006/08/01 2006.
- [23] C. V. Manzano *et al.*, "Thermoelectric properties of Bi_2Te_3 films by constant and pulsed electrodeposition," *Journal of Solid State Electrochemistry*, journal article vol. 17, no. 7, pp. 2071-2078, 2013.
- [24] Y. Ma, E. Ahlberg, Y. Sun, B. B. Iversen, and A. E. C. Palmqvist, "Thermoelectric Characteristics of Electrochemically Deposited Bi_2Te_3 and Sb_2Te_3 Thin Films of

- Relevance to Multilayer Preparation," *Journal of the Electrochemical Society*, vol. 159, no. 2, pp. D50-D58, 2012 2012.
- [25] F. Xiao, C. Hangarter, B. Yoo, Y. Rheem, K.-H. Lee, and N. V. Myung, "Recent progress in electrodeposition of thermoelectric thin films and nanostructures," *Electrochimica Acta*, vol. 53, no. 28, pp. 8103-8117, 2008/11/30/ 2008.
- [26] A. J. Zhou *et al.*, "Enhancing the Thermoelectric Properties of the Electroplated Bi₂Te₃ Films by Tuning the Pulse Off-to-on Ratio," *Electrochimica Acta*, vol. 178, pp. 217-224, Oct 2015.
- [27] M. Takahashi, Y. Katou, K. Nagata, and S. Furuta, "The composition and conductivity of electrodeposited Bi/Te alloy films," *Thin Solid Films*, vol. 240, no. 1, pp. 70-72, 1994/03/15/ 1994.
- [28] C. Boulanger, "Thermoelectric Material Electroplating: a Historical Review," *Journal of Electronic Materials*, vol. 39, no. 9, pp. 1818-1827, 2010// 2010.
- [29] R. Rostek, N. Stein, and C. Boulanger, "A review of electroplating for V–VI thermoelectric films: from synthesis to device integration," *Journal of Materials Research*, vol. 30, no. 17, pp. 2518-2543, 2015.
- [30] H. Alam and S. Ramakrishna, "A review on the enhancement of figure of merit from bulk to nano-thermoelectric materials," *Nano Energy*, vol. 2, no. 2, pp. 190-212, 3// 2013.
- [31] C. V. Manzano and M. Martin-Gonzalez, "Electrodeposition of V-VI Nanowires and Their Thermoelectric Properties," (in English), *Frontiers in Chemistry*, Review vol. 7, no. 516, 2019-August-06 2019.
- [32] G. Bulman *et al.*, "Superlattice-based thin-film thermoelectric modules with high cooling fluxes," Article vol. 7, p. 10302, 01/13/online 2016.
- [33] M. Tan *et al.*, "Anisotropy Control–Induced Unique Anisotropic Thermoelectric Performance in the n-Type Bi₂Te_{2.7}Se_{0.3} Thin Films," *Small Methods*, vol. 3, no. 11, p. 1900582, 2019/11/01 2019.
- [34] X. Wang, H. He, N. Wang, and L. Miao, "Effects of annealing temperature on thermoelectric properties of Bi₂Te₃ films prepared by co-sputtering," *Applied Surface Science*, vol. 276, pp. 539-542, 2013/07/01/ 2013.
- [35] S. Cho, Y. Kim, A. DiVenere, G. K. Wong, J. B. Ketterson, and J. R. Meyer, "Antisite defects of thin films," *Applied Physics Letters*, vol. 75, no. 10, pp. 1401-1403, 1999/09/06 1999.
- [36] J. Kim, K. H. Lee, S. W. Kim, and J.-H. Lim, "Potential-current co-adjusted pulse electrodeposition for highly (110)-oriented Bi₂Te_{3-x}Se_x films," *Journal of Alloys*

- and Compounds*, vol. 787, pp. 767-771, 2019/05/30/ 2019, doi: <https://doi.org/10.1016/j.jallcom.2019.01.301>.
- [37] C. Lei, M. R. Burton, and I. S. Nandhakumar, "Facile production of thermoelectric bismuth telluride thick films in the presence of polyvinyl alcohol," *Physical Chemistry Chemical Physics*, 10.1039/C6CP02360F vol. 18, no. 21, pp. 14164-14167, 2016.
- [38] J. Na, Y. Kim, T. Park, C. Park, and E. Kim, "Preparation of Bismuth Telluride Films with High Thermoelectric Power Factor," *ACS Applied Materials & Interfaces*, vol. 8, no. 47, pp. 32392-32400, 2016/11/30 2016.
- [39] S. Li *et al.*, "Effects of Annealing and Doping on Nanostructured Bismuth Telluride Thick Films," *Chemistry of Materials*, vol. 20, no. 13, pp. 4403-4410, 2008/07/01 2008.
- [40] J. Kim, K. H. Lee, S.-D. Kim, J.-H. Lim, and N. Myung, "Simple and effective fabrication of Sb_2Te_3 films embedded with Ag_2Te nanoprecipitates for enhanced thermoelectric performance," *Journal of Materials Chemistry A*, 10.1039/C7TA09013G vol. 6, no. 2, pp. 349-356, 2018.
- [41] D. D. Frari, S. Diliberto, N. Stein, C. Boulanger, and J.-M. Lecuire, "Pulsed electrodeposition of $(\text{Bi}_{1-x}\text{Sb}_x)_2\text{Te}_3$ thermoelectric thin films," *Journal of Applied Electrochemistry*, vol. 36, no. 4, pp. 449-454, 2006/04/01 2006.
- [42] N. H. Trung, K. Sakamoto, N. V. Toan, and T. Ono, "Synthesis and evaluation of thick films of electrochemically deposited Bi_2Te_3 and Sb_2Te_3 thermoelectric materials," *Materials*, vol. 10, no. 2, p. 154, 2017.
- [43] W.-S. Kang, W.-C. Chou, W.-J. Li, T.-H. Shen, and C.-S. Lin, "Electrodeposition of Bi_2Te_3 -based p and n-type ternary thermoelectric compounds in chloride baths," *Thin Solid Films*, vol. 660, pp. 108-119, 2018.
- [44] T. Sun *et al.*, "Enhanced thermoelectric properties of n-type $\text{Bi}_2\text{Te}_{2.7}\text{Se}_{0.3}$ thin films through the introduction of Pt nano-inclusions by pulsed laser deposition," *Nano Energy*, vol. 8, pp. 223-230, 2014/09/01/ 2014.
- [45] M. Takashiri, T. Shirakawa, K. Miyazaki, and H. Tsukamoto, "Fabrication and characterization of bismuth–telluride-based alloy thin film thermoelectric generators by flash evaporation method," *Sensors and Actuators A: Physical*, vol. 138, no. 2, pp. 329-334, 8/26/ 2007.
- [46] S. Lal, K. M. Razeeb, and D. Gautam, "Enhanced Thermoelectric Properties of Electrodeposited Cu-Doped Te Films," *ACS Applied Energy Materials*, vol. 3, no. 4, pp. 3262-3268, 2020/04/27 2020.

- [47] J. Kim, K. H. Lee, S. W. Kim, and J.-H. Lim, "Potential-current co-adjusted pulse electrodeposition for highly (110)-oriented $\text{Bi}_2\text{Te}_{3-x}\text{Se}_x$ films," *Journal of Alloys and Compounds*, vol. 787, pp. 767-771, 2019/05/30/ 2019.
- [48] J. Kim, K. H. Lee, S.-D. Kim, J.-H. Lim, and N. V. Myung, "Simple and effective fabrication of Sb_2Te_3 films embedded with Ag_2Te nanoprecipitates for enhanced thermoelectric performance," *Journal of Materials Chemistry A*, vol. 6, no. 2, pp. 349-356, 2018.
- [49] N. Hatsuta, D. Takemori, and M. Takashiri, "Effect of thermal annealing on the structural and thermoelectric properties of electrodeposited antimony telluride thin films," *Journal of Alloys and Compounds*, vol. 685, pp. 147-152, 11/15/ 2016.
- [50] P. Heo, K. Hagiwara, R. Ichino, and M. Okido, "Electrodeposition and Thermoelectric Characterization of Bi_2Te_3 ," *Journal of The Electrochemical Society*, vol. 153, no. 4, p. C213, 2006.
- [51] V. Leonov, "Thermoelectric Energy Harvesting of Human Body Heat for Wearable Sensors," *IEEE Sensors Journal*, vol. 13, no. 6, pp. 2284-2291, 2013.
- [52] S. Qing, A. Rezaia, L. A. Rosendahl, A. A. Enkeshafi, and X. Gou, "Characteristics and parametric analysis of a novel flexible ink-based thermoelectric generator for human body sensor," *Energy Conversion and Management*, vol. 156, pp. 655-665, 2018/01/15/ 2018.
- [53] S. M. Yang, T. Lee, and C. A. Jeng, "Development of a thermoelectric energy harvester with thermal isolation cavity by standard CMOS process," *Sensors and Actuators A: Physical*, vol. 153, no. 2, pp. 244-250, 2009/08/03/ 2009.
- [54] W. Glatz, E. Schwyter, L. Durrer, and C. Hierold, "Bi₂Te₃-Based flexible micro thermoelectric generator with optimized design," *Journal of Microelectromechanical Systems*, vol. 18, no. 3, pp. 763-772, 2009, doi: 10.1109/JMEMS.2009.2021104.
- [55] M. Kishi *et al.*, "Micro thermoelectric modules and their application to wristwatches as an energy source," in *Eighteenth International Conference on Thermoelectrics. Proceedings, ICT'99 (Cat. No.99TH8407)*, 1999, pp. 301-307.
- [56] H. Bottner *et al.*, "New thermoelectric components using microsystem technologies," *Microelectromechanical Systems, Journal of*, vol. 13, pp. 414-420, 07/01 2004.
- [57] G. J. Snyder, J. R. Lim, C.-K. Huang, and J.-P. Fleurial, "Thermoelectric microdevice fabricated by a MEMS-like electrochemical process," *Nature Materials*, vol. 2, no. 8, pp. 528-531, 2003/08/01 2003.

- [58] W. Glatz, S. Muntwyler, and C. Hierold, "Optimization and fabrication of thick flexible polymer based micro thermoelectric generator," *Sensors and Actuators A: Physical*, vol. 132, no. 1, pp. 337-345, 2006/11/08/ 2006.
- [59] Y. Li, K. Buddharaju, B. C. Tinh, N. Singh, and S. J. Lee, "Improved Vertical Silicon Nanowire Based Thermoelectric Power Generator With Polyimide Filling," *IEEE Electron Device Letters*, vol. 33, no. 5, pp. 715-717, 2012.
- [60] M. Kim and T.-S. Oh, "Thermoelectric Power Generation Characteristics of a Thin-Film Device Consisting of Electrodeposited n-Bi₂Te₃ and p-Sb₂Te₃ Thin-Film Legs," *Journal of Electronic Materials*, vol. 42, 09/01 2013.
- [61] W. Zhang, J. Yang, and D. Xu, "A High Power Density Micro-Thermoelectric Generator Fabricated by an Integrated Bottom-Up Approach," *Journal of Microelectromechanical Systems*, vol. 25, no. 4, pp. 744-749, 2016.
- [62] M. T. Dunham *et al.*, "Experimental Characterization of Microfabricated Thermoelectric Energy Harvesters for Smart Sensor and Wearable Applications," *Advanced Materials Technologies*, vol. 3, no. 6, p. 1700383, 2018/06/01 2018.
- [63] G. Li *et al.*, "Integrated microthermoelectric coolers with rapid response time and high device reliability," *Nature Electronics*, vol. 1, no. 10, pp. 555-561, 2018/10/01 2018.

Chapter 3: The impact of the surfactant sodium dodecyl sulfate on the microstructure and thermoelectric properties of p-type $(\text{Sb}_{1-x}\text{Bi}_x)_2\text{Te}_3$ electrodeposited films

Chapter based on the publication journal article:

ECS Journal of Solid State Science and Technology, volume 6, issue 3, N3017-N3021
(2017)

Swatchith Lal, Devendraprakash Gautam and Kafil M. Razeeb

Tyndall National Institute, University College Cork, Lee Maltings, Cork T12 R5CP,
Ireland

3.1 Abstract

This work reports on the synthesis of p-type $(\text{Sb}_{1-x}\text{Bi}_x)_2\text{Te}_3$ thin films using pulsed electrodeposition with and without the presence of an anionic surfactant, sodium dodecyl sulfate (SDS). The effect of SDS on the morphology of the films was investigated, and it was found that films with SDS in the electrolyte were smooth and denser as compared to the films without SDS. Post-deposition annealing of the films resulted in preferential crystal orientation. The Seebeck coefficient showed an improvement of 49% for the films deposited with SDS, which improved the overall power factor of the films by 143%.

3.2 Introduction

Data traffic is projected to increase sharply (40-80× by 2020) and this is driving an increase in network complexity and the requirement for scalable optoelectronic integration [1]. A major bottleneck to this large-scale integration is thermal management. Active photonic devices generate extremely high heat flux levels ($\sim 10 \text{ kW/cm}^2$) that must be efficiently removed to maintain performance and reliability; furthermore, active photonic devices must be controlled at temperature precision better than $\pm 0.1^\circ\text{C}$. Today's thermal technology is at the limit and cannot scale with growth in the network [2].

Current state-of-the-art thermal design of photonic integrated circuits (PICs) is unable to meet the challenge in data traffic over the coming years. Today's PICs employ macro thermoelectric cooler (TEC) that are inefficient in thermal management of the device. Micro-TEC integrated directly on the laser can more efficiently manage thermal cooling of the device. The aim of TIPS project [2] is to develop novel p and n type thermoelectric materials, and to design and develop a micro-thermoelectric cooler ($\mu\text{-TEC}$), integrated

around the PIC, which can effectively remove heat from the photonic system. As a part of this work, we have been trying to enhance the structural and thermoelectric (TE) properties of bismuth telluride based materials. Binary semiconductor bismuth telluride based materials have been extensively studied, and applied in thermoelectric generators (TEG) and thermoelectric coolers (TEC) devices because of their unique properties, which exhibit better figure of merit (ZT) near room temperature regime [3-6].

The efficiency of the thermoelectric films are evaluated in terms of dimensionless figure of merit ZT , which can be expressed as,

$$ZT = \frac{S^2 \sigma}{\kappa} T$$

where S , σ , T and κ are the Seebeck coefficient, the electrical conductivity, the absolute temperature and the thermal conductivity respectively. Therefore, for superior thermoelectric properties, ZT should be high, for which the Seebeck coefficient and the electrical conductivity must be high and the thermal conductivity should be low [7, 8]. Two strategies are generally used to enhance the thermoelectric efficiency of the materials, (1) to minimize the thermal conductivity and/or (2) to enhance the power factor (PF). In the present work we focused on improving the PF of the materials, where $PF = S^2 \sigma$.

Electrochemical deposition is extensively used for the synthesis of the device fabrication due to suitability of the technique for its cost effectiveness, up-scalability and ease of controlling film properties such as composition, crystallinity and morphology [9, 10].

In the fabrication of micro-thermoelectric devices, one of the challenges to overcome is to reduce the roughness of the films. The electrodeposited Bi Te based materials are dendritic and rough [11, 12]. Thereby, the focus of the present work is to reduce the morphological defects and produce smoother films, without sacrificing the Seebeck coefficient. Here, we studied the addition of a surfactant that modifies the interfacial tension between the solution and the electrode which enables the ease of escape to the gas bubbles from the electrode surface, due to which the formation of pinholes and pitting can be eliminated [13]. Researchers have been working to improve these properties by the addition of surfactant. In order to make the films homogeneous and smooth, different surfactants have been used namely sodium ligninsulfonate (SLS) [14, 15], cetyltrimethylammonium bromide CTAB [16, 17], ethylene-glycol [18], polyvinylpyrrolidone (PVP), and sodium dodecyl sulfate (SDS) [19]. However, most of

the reported works are done on n-type Bi_2Te_3 . There has been only one paper in the literature that reported on improving the homogeneity of electroplated p-type $\text{Bi}_{0.5}\text{Sb}_{1.5}\text{Te}_3$ by using surfactants [20]. It was shown that the addition of sodium ligninsulfonate improved the homogeneity of the films without changing the crystallographic orientation of the films and also improved the Seebeck coefficient as compared to films without any surfactant. Thereby, in the present work we demonstrate smooth and dense films of p-type bismuth antimony telluride (Bi-Sb-Te) synthesized by pulsed electrodeposited using SDS as a surfactant. Pulsed plating is an advanced form of electrodeposition compared to the conventional potentiostatic or galvanostatic deposition. It has several advantages such as synthesis of uniform films with fine grains and low porosity, better and crack free adhesion and reduction in the surface roughness[11]. Furthermore, we investigated and compared morphology, crystallinity, composition and the thermoelectric properties of the electrodeposited films with and without SDS after annealing for 1 h at 350 °C in N_2 atmosphere.

3.3 Experimental

Bismuth (III) nitrate pentahydrate (ACS reagent $\geq 98.0\%$), antimony (III) oxide, tellurium (powder ~ 200 mesh, 99.8% trace metals basis), sodium dodecyl sulfate (SDS) (BioReagent $\geq 99.5\%$), tartaric acid (ACS reagent $\geq 99.5\%$), nitric acid (ACS reagent $\geq 69\%$) and dimethyl sulfoxide (ACS reagent $\geq 99.9\%$) were used for the experiments as received.

In preparing solution (A), 15mM of tellurium (Te) was put into 25 mL of 1 M HNO_3 and was heated at ~ 45 °C to dissolve Te completely and 5 mM $\text{Bi}(\text{NO}_3)_3 \cdot 5\text{H}_2\text{O}$ was added to the solution. Solution (B) was prepared using 5 mM Sb_2O_3 in 25 mL of 0.2 M tartaric acid and was heated at ~ 45 °C for proper dissolution. Two solutions A and B were mixed and 50 mL of dimethyl sulfoxide (DMSO) was added to the mixed solutions. The whole solution was maintained at 1:1 ratio of DI water and DMSO. SDS was added at different concentrations ranging from 0.2 mM to 2.0 mM in the solution while stirring.

Experiments were carried out in a three-electrode setup at room temperature. The electrodeposition potential was controlled by CHI600 series electrochemical analyzer/workstation. The reference electrode was Ag/AgCl. A platinized titanium mesh was used as the counter electrode. In order to determine the reduction potentials, cyclic voltammetry (CV) was performed between the fixed potentials of -0.6 V and 0.8 V vs Ag/AgCl at a scan rate of 10 mV/s. Films were deposited by triple pulse amperometry

technique on a square (32 mm × 32 mm) Si/SiO₂ substrate, having 20 nm Au layer on the top of 10 nm Ti layer. No magnetic stirring was used and all the depositions were performed at ambient room temperature of 25 °C. The substrates were cleaned with ethanol and then with deionized (DI) water in an ultrasonic bath and finally dried by blowing nitrogen at ambient temperature before deposition. The films deposited with and without SDS were annealed at 350 °C for 1 h in N₂ atmosphere at a ramp rate of 5 K/min in order to enhance their thermoelectric properties.

X-ray diffraction patterns (XRD) were measured by X-Ray diffractometer Pan analytical X'pert pro, using Cu K_α radiation at a voltage of 40 kV and a current of 40 mA. The morphology and elemental composition of the obtained films were analyzed using a scanning electron microscope (SEM) Quanta FEG 450 at an accelerating voltage of 15 kV, coupled with an energy dispersive spectrometer (EDS).

Electrical properties were measured using a four point probe measurement system (Jandel RM300). Laboratory built Seebeck-measurement system was used to measure the Seebeck coefficient of the electrodeposited films. The temperature gradient (ΔT) was established along the ends of the film using commercially available thermoelectric coolers. The thermovoltage produced due to the temperature difference was measured using a high impedance electrometer. Temperatures of the hot and cold ends were measured using two separate thermocouples. The samples were measured for Seebeck coefficient at different ΔT values from 2-10 °C. Necessary calibrations were done to ensure the accuracy of the system.

3.4 Results and Discussion

In order to determine the appropriate reduction potential range and to investigate the underlying electrochemical reaction, cyclic voltammograms (CVs) were recorded, using gold as a working electrode immersed in an electrolyte containing Bi⁺³, SbO⁺ and HTeO₂⁺ ions with and without the presence of SDS in the electrolyte. Figure 3.1(a) shows the voltammograms of the solutions with and without SDS measured on the standard gold electrode of 1 mm radius with a scan rate of 10 mV/s. Both the CVs reveal three cathodic peaks at potentials of -0.07, -0.15 and -0.27 V vs. Ag/AgCl, which may be attributed to the reduction of Bi, Te and Sb, respectively [20]. Different concentrations of SDS ranging from 0.2 to 2 mM were analyzed and no significant change was observed in the CVs as can be seen in Figure 3.S1 of the supplementary information (SI) section and illustrated for 0.8 mM SDS in Figure 3.1 (a). Based on these studies, the reduction potentials were

fixed for the deposition of the films using triple pulse amperometry technique as shown in Figure 3.1(b), where the chosen pulse potentials were $V_1 = -80$ mV for a duration of 10 ms, $V_2 = -50$ mV for a duration 50 ms and $V_3 = -300$ mV for a duration of 10 ms. The total duration of deposition of the films was fixed to 3600 s and the film thickness obtained was approximately $2.0 \mu\text{m}$ with this deposition time.

As a preliminary characterization, in order to observe the morphological change, SEM images were taken of the films without and with various concentration of SDS. It was observed that from 0.8 mM concentration of SDS, films started to change from fibrous to granular morphology and thereby further studies were focused on 0.8 mM SDS samples where 0.4 mM SDS films were also used for a better understanding.

The SEM image in Figure 3.2(a) shows the surface morphology of the electrodeposited Bi-Sb-Te thin films without SDS. The film shows a fibrous dendritic structure, which is

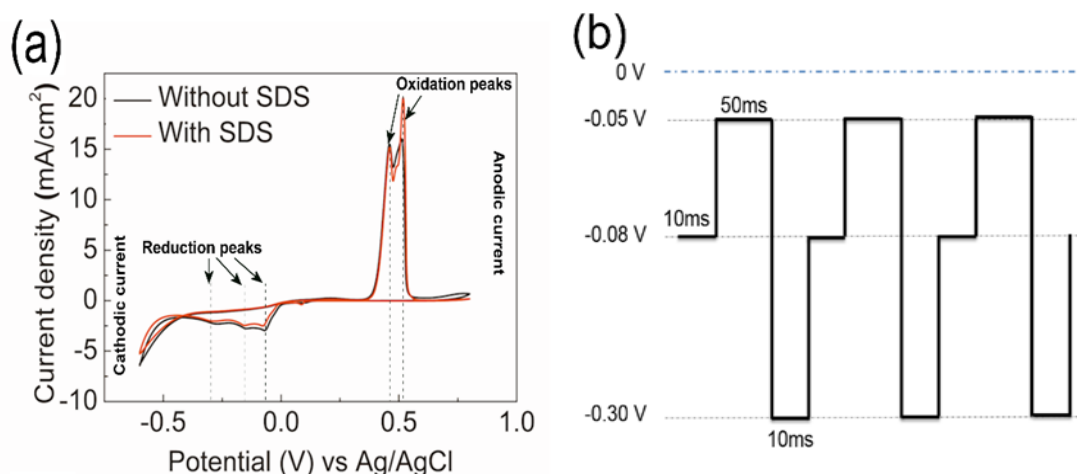


Figure 3.1: (a) Cyclic voltammograms of gold working electrode without and with 0.8 mM SDS. All the voltammograms were recorded at room temperature at a scan rate of 10 mVs^{-1} (b) Schematic of triple pulse deposition potentials.

rough and porous. For the 0.4 mM SDS film (Figure 3.2(b)), no major change in the morphology is observed. However, the SEM of 0.8 mM film in Figure 3.2(c) shows a granular structure, which reveals that in the presence of 0.8 mM SDS the morphology changed drastically and the films became denser. The density of the films was calculated from the weight of the deposit and total volume of the film. It was found that the films with 0.8 mM SDS have an average density of 6.11 g/cm^3 as compared to 5.64 g/cm^3 for the films without SDS. The cross-sectional images of the films are shown in Figure 3.3, where Figure 3.3(a) shows the film without SDS, which is rough and indicates rough

deposition with a high porosity. Whereas, the film with 0.8 mM SDS shows significant improvement in terms of uniformity and smooth profile as can be seen in Figure 3.3(b).

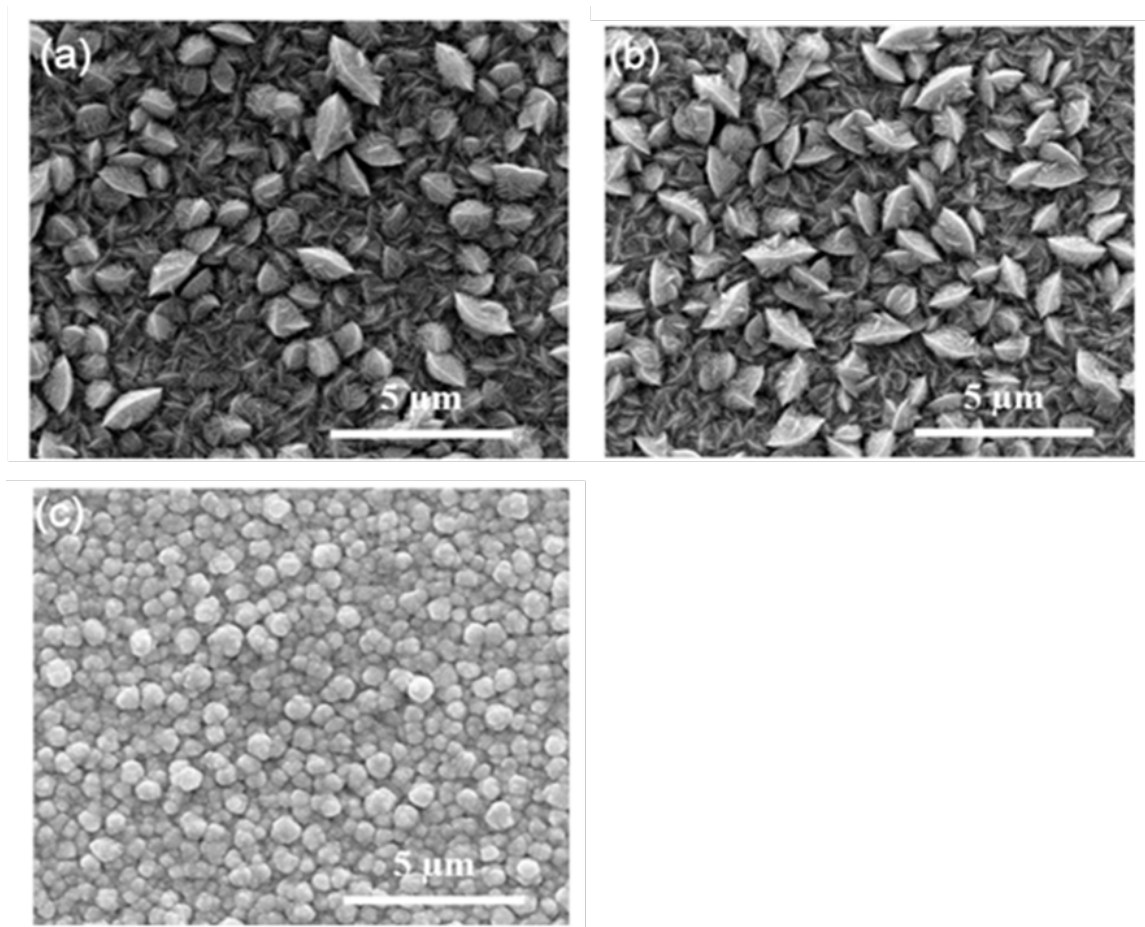


Figure 3.2: (a) SEM images of as-deposited samples (a) without SDS (b) 0.4 mM SDS and (c) 0.8 mM SDS.

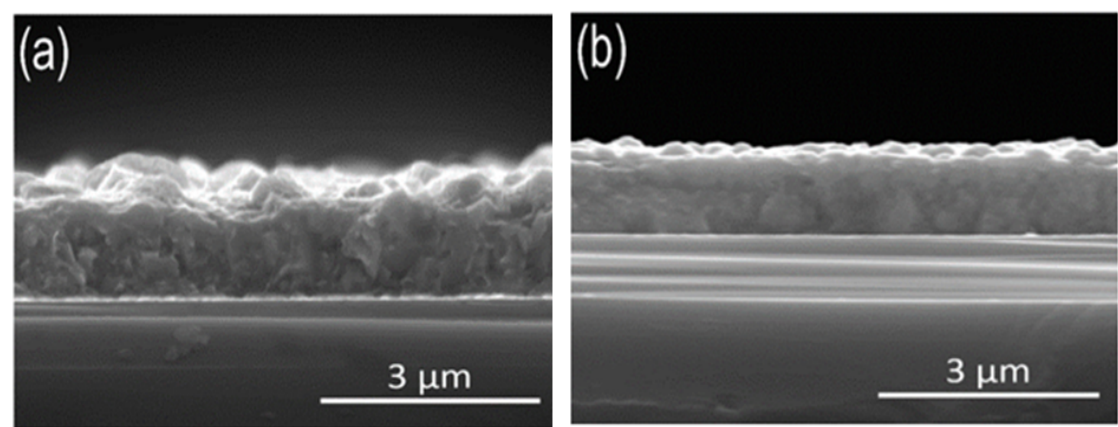


Figure 3.3: Cross-sectional images of with and without SDS (a) without SDS (b) with 0.8 mM SDS.

Chapter 3

The composition of the films was determined by EDX analysis. Table 3.1 shows the atomic percentages of different constituents and a comparison between the films with and without surfactant of different concentrations. Due to the addition of SDS in the electrolyte, bismuth and tellurium contents in the films increased and antimony content decreased. Both of the films with and without SDS were annealed at 350 °C for 1 h. It was observed that the tellurium content starts depleting when annealed at 350 °C for both films, which may be due to the evaporation of tellurium at high temperatures. Table 3.2 exhibits the analysed composition of the films before and after annealing with different concentrations of SDS.

Table 3-1: Atomic composition of Bi-Sb-Te films with different concentrations of SDS in electrolyte and change in the composition after annealing.

Concentration of SDS (mM)	Film composition (%)			Film composition (%) Annealed at 350 °C		
	Sb	Te	Bi	Sb	Te	Bi
0	20.49	61.34	18.18	21.78	59.81	18.42
0.4	18.99	62.23	18.78	20.47	60.09	19.45
0.8	13.59	64.92	21.50	15.28	61.80	22.93

Table 3-2: Composition of Bi-Sb-Te films with different concentrations of SDS before and after annealing.

Concentration of SDS (mM)	As-deposited	Annealed at 350 °C
0.0	$(\text{Sb}_{1.02}\text{Bi}_{0.91})_2\text{Te}_{3.07}$	$(\text{Sb}_{1.09}\text{Bi}_{0.92})_2\text{Te}_{3.00}$
0.4	$(\text{Sb}_{0.95}\text{Bi}_{0.94})_2\text{Te}_{3.11}$	$(\text{Sb}_{1.02}\text{Bi}_{0.97})_2\text{Te}_{3.00}$
0.8	$(\text{Sb}_{0.68}\text{Bi}_{1.10})_2\text{Te}_{3.25}$	$(\text{Sb}_{0.76}\text{Bi}_{1.15})_2\text{Te}_{3.09}$

Table 3-3: Average crystallite size of films prepared with different concentrations of SDS.

Samples	Crystallite size (nm)	
	As-deposited	After annealing
0.0 mM SDS	13.5	27.7
0.4 mM SDS	14.5	27.1
0.8 mM SDS	17.6	31.6

Figure 3.4(a) shows the XRD patterns of the films electrodeposited without SDS and with 0.4 and 0.8 mM SDS. All the films have a rhombohedral crystal structure of $(\text{Sb}_{1-x}\text{Bi}_x)_2\text{Te}_3$ (ICSD PDF card (72-1835)). The (015) was the preferred orientation detected at $2\theta \sim 27.6$ for all the films. From the XRD, it can be observed that the (110) peak present in films without SDS and 0.4 mM SDS while it is absent in 0.8 mM SDS films. With 0.8 mM SDS concentration, (015) peak becomes more intense. XRD studies reveal that the SDS impacts the growth of (110) peak and it gradually wanes and diminishes for films of the case of 0.8 mM SDS (see Figure 3.4(a)). On annealing the films become more crystalline with (015) peak still stays as a prominent peak. (110) peak is observed in 0.8 mM SDS sample after annealing along with some more peaks as shown in Figure 3.4(b). AuTe_2 peak was observed after annealing, which may be due to the reaction of Au from the seed layer with tellurium from the film at elevated temperatures to form AuTe_2 . The average crystallite size of the as-deposited films was measured from the XRD data using the Debye-Scherrer formula and is shown in Table 3.3. It was observed that the average crystallite size increases with the addition of SDS from 13.5 nm to 17.6 nm. This observation relates that the SDS concentration has a direct impact on the crystallite size. On annealing, it further increases where the average crystallite size of the annealed films without SDS was 27.7 nm and 31.6 nm for the films with 0.8 mM SDS. One of the probable reasons for the change in the microstructure of the films from rough to granular structure (see Figures 3.2 and 3.3) could result from the anisotropy in adsorption stability of SDS molecules in the electrolyte. The SDS molecule tends to adsorb along (110) plane thereby lowering its surface energy and hindering growth along this direction in agreement with the XRD data shown in Figure 3.4(a), where (110) peak intensity gradually decreases with increasing SDS concentration. The decrease in the surface

projections and surface energy leads to smoother microstructure. Similar observation was seen on electrodeposited CuInSe_2 on Mo substrate [21].

Figure 3.5(a) shows the Seebeck coefficient of the samples deposited with and without SDS before and after annealing. The Seebeck coefficient of the as-deposited sample without SDS was $-27.22 \mu\text{V/K}$, which on annealing increased to $60.85 \mu\text{V/K}$ indicating not only the increment in the absolute value of the Seebeck coefficient but also the nature of the charge carriers change from n -type electron to p -type holes. However, for 0.8 mM SDS thin films the Seebeck coefficient of as-deposited samples showed a value of $12.22 \mu\text{V/K}$, which on annealing increased to $90.5 \mu\text{V/K}$ that is almost 49% higher than the values obtained from the films without SDS. The thermoelectric properties and electrical conductivities of the annealed Bi-Sb-Te thin films are shown in Figure 3.5(b).

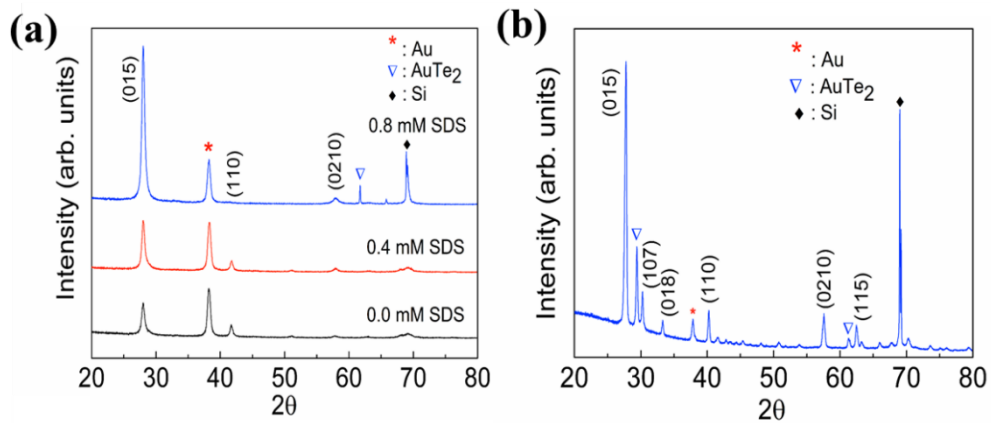


Figure 3.2:(a) XRD of as-deposited films with different concentrations of SDS, (b) Annealed 0.8 mM SDS.

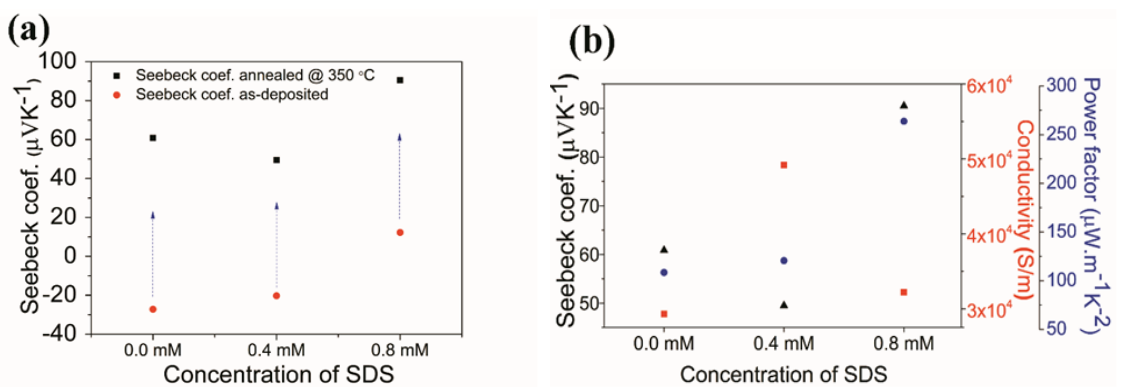


Figure 3.3:(a) Seebeck measurement of as-deposited films with different concentrations of SDS and their comparison with values obtained post-annealing; (b) Electrical and thermoelectric properties of annealed films deposited with different concentration.

There has been no drastic change observed in the electrical conductivities of films with different concentrations of SDS. The electrical conductivities of the films are in the order of 10^4 S/m with an optimum value of $5 \times 10^4 \text{ S/m}$ observed for 0.4 mM SDS. Annealing

decreases the conductivity of the films compared to as-deposited films, and this may be due to decrease in the tellurium content in the films. Electrical conductivity measurements before and after annealing the films of different concentrations can be seen in Figure 3.8. Currently, there is no unambiguous understanding on the enhancement of the Seebeck coefficient with SDS. One of the probable hypotheses[22, 23] could be due to the role of Te in the film. As exhibited in Table 3.1, the content of Te in as-deposited with SDS is reasonably high compared to without SDS samples. Annealing the film results in Te depletion, however, the absolute value of Te remains higher compared to films without SDS (see Table 3.1). Thus, the Seebeck coefficient of films without SDS is lower than compared to 0.8 mM SDS. The power factor of the films without SDS was $108.48 \mu\text{W}\cdot\text{m}^{-1}\text{K}^{-2}$, which on addition of 0.4 mM SDS raised to $120.55 \mu\text{W}\cdot\text{m}^{-1}\text{K}^{-2}$ and with 0.8 mM SDS concentration in the electrolyte, films exhibited a power factor of $263.72 \mu\text{W}\cdot\text{m}^{-1}\text{K}^{-2}$ which is 143% higher than the power factor of without SDS films. Further work is needed to investigate in detail the impact of SDS on the thermoelectric properties.

3.5 Conclusions

This study demonstrates that the surfactant SDS improved the quality and surface smoothness of p-type $(\text{Sb}_{1-x}\text{Bi}_x)_2\text{Te}_3$ films. SEM images reveal that the SDS contributes in reducing the surface roughness and the films obtained were compact, overcoming the porous nature of the films without SDS. XRD studies revealed the growth of the average crystallite size with the increasing concentration of SDS. Furthermore, the films deposited with surfactant showed a Seebeck coefficient value of $90.5 \mu\text{V}/\text{K}$ post annealing, which is 49% higher as compared to the film without surfactant. Due to which, a power factor of $263.72 \mu\text{W}/\text{mK}^2$ was achieved, which is more than twice of the value for the films deposited without SDS.

3.6 References

- [1] J. Brodtkin, "Bandwidth explosion: As Internet uses soars, can bottlenecks be averted?," *Arstechnica*, pp. <http://arstechnica.com/business/2012/05/bandwidth-explosion-as-internet-use-soars-can-bottlenecks-be-averted/>, 2014.
- [2] R. Enright *et al.*, "A Vision for Thermally Integrated Photonics Systems," *Bell Labs Technical Journal*, vol. 19, pp. 31-45, 2014.
- [3] R. Rostek, N. Stein, and C. Boulanger, "A review of electroplating for V-VI thermoelectric films: from synthesis to device integration," *Journal of Materials Research*, vol. 30, no. 17, pp. 2518-2543, Sep 2015.

- [4] R. Venkatasubramanian, E. Siivola, T. Colpitts, and B. O'Quinn, "Thin-film thermoelectric devices with high room-temperature figures of merit," (in English), *Nature*, Article vol. 413, no. 6856, pp. 597-602, 2001.
- [5] F. J. Disalvo, "Thermoelectric cooling and power generation," (in English), *Science*, Review vol. 285, no. 5428, pp. 703-706, 1999.
- [6] L. E. Bell, "Cooling, Heating, Generating Power, and Recovering Waste Heat with Thermoelectric Systems," *Science*, vol. 321, no. 5895, pp. 1457-1461, 2008-09-12 00:00:00 2008.
- [7] X. Zhang and L.-D. Zhao, "Thermoelectric materials: Energy conversion between heat and electricity," *Journal of Materiomics*, vol. 1, no. 2, pp. 92-105, 6// 2015.
- [8] G. J. Snyder and E. S. Toberer, "Complex thermoelectric materials," *Nat Mater*, 10.1038/nmat2090 vol. 7, no. 2, pp. 105-114, 02//print 2008.
- [9] C. Boulanger, "Thermoelectric Material Electroplating: a Historical Review," *Journal of Electronic Materials*, vol. 39, no. 9, pp. 1818-1827, 2010// 2010.
- [10] F. Xiao, C. Hangarter, B. Yoo, Y. Rheem, K.-H. Lee, and N. V. Myung, "Recent progress in electrodeposition of thermoelectric thin films and nanostructures," *Electrochimica Acta*, vol. 53, no. 28, pp. 8103-8117, 2008.
- [11] D. D. Frari, S. Diliberto, N. Stein, C. Boulanger, and J.-M. Lecuire, "Pulsed electrodeposition of $(\text{Bi}_{1-x}\text{Sb}_x)_2\text{Te}_3$ thermoelectric thin films," *Journal of Applied Electrochemistry*, vol. 36, no. 4, pp. 449-454, 2006/04/01 2006.
- [12] F. Li and W. Wang, "Electrodeposition of $\text{Bi}_x\text{Sb}_{2-x}\text{Te}_y$ thermoelectric thin films from nitric acid and hydrochloric acid systems," *Applied Surface Science*, vol. 255, no. 7, pp. 4225-4231, 1/15/ 2009.
- [13] R. Vittal, H. Gomathi, and K.-J. Kim, "Beneficial role of surfactants in electrochemistry and in the modification of electrodes," *Advances in Colloid and Interface Science*, vol. 119, no. 1, pp. 55-68, 1/31/ 2006.
- [14] O. Caballero-Calero *et al.*, "Improvement of Bismuth Telluride electrodeposited films by the addition of Sodium Lignosulfonate," *Electrochimica Acta*, vol. 123, pp. 117-126, 2014/03/20/ 2014.
- [15] A. J. Naylor, E. Koukharenko, I. S. Nandhakumar, and N. M. White, "Surfactant-Mediated Electrodeposition of Bismuth Telluride Films and Its Effect on Microstructural Properties," *Langmuir*, vol. 28, no. 22, pp. 8296-8299, 2012/06/05 2012.
- [16] Y. Song *et al.*, "Electrodeposition of thermoelectric Bi_2Te_3 thin films with added surfactant," *Current Applied Physics*, vol. 15, no. 3, pp. 261-264, 3// 2015.

- [17] I.-J. Yoo *et al.*, "Thermoelectric characteristics of Sb_2Te_3 thin films formed via surfactant-assisted electrodeposition," *Journal of Materials Chemistry A*, 10.1039/C3TA01631E vol. 1, no. 17, pp. 5430-5435, 2013.
- [18] M. Wu, H. P. Nguyen, R. J. M. Vullers, P. M. Vereecken, K. Binnemans, and J. Fransaer, "Electrodeposition of Bismuth Telluride Thermoelectric Films from Chloride-Free Ethylene Glycol Solutions," *Journal of The Electrochemical Society*, vol. 160, no. 4, pp. D196-D201, January 1, 2013 2013.
- [19] K. Chiranjit, M. Mousumi, K. Kajari, G. Saibal, B. Dipali, and G. Shyamaprosad, "Effect of different surfactants and thicknesses on electrodeposited films of bismuth telluride and its thermoelectric performance," *Materials Research Express*, vol. 2, no. 10, p. 106403, 2015.
- [20] J. Kuleshova *et al.*, "Optimization of the Electrodeposition Process of High-Performance Bismuth Antimony Telluride Compounds for Thermoelectric Applications," *Langmuir*, vol. 26, no. 22, pp. 16980-16985, 2010/11/16 2010.
- [21] P.-K. Hung, H.-G. Cai, K.-C. Huang, and M.-P. Houn, "Effect of Sodium Dodecyl Sulfate on Surface Roughness and Nucleation Mechanisms of Electrodeposited CuInSe_2 Films," *Journal of The Electrochemical Society*, vol. 160, no. 1, pp. D1-D5, January 1, 2013 2013.
- [22] K. M. R. a. D. Gautam, "Alloy System with Enhanced Seebeck Coefficient and Process for Making Same," vol. U.S. Serial No. 62/240,197, 2015.
- [23] E. D. D. Gautam, and K. M. Razeeb, "Innovative method to enhance Seebeck coefficient of annealed p-type $(\text{Sb}_{1-x}\text{Bi}_x)_2\text{Te}_3$," *Adv. Energy Mater.*, To be communicated soon.

3.7 Supplementary material

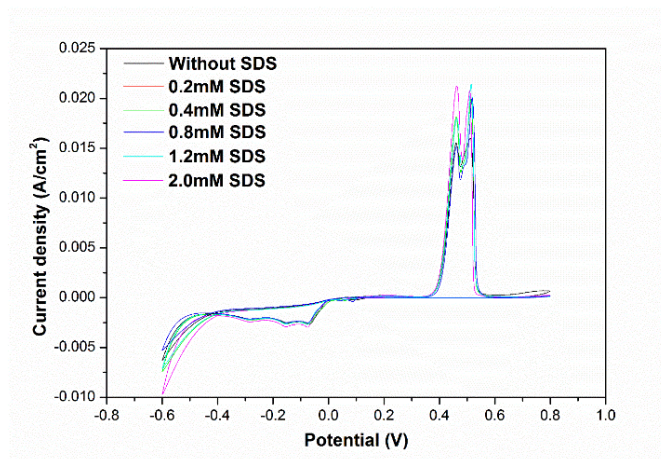


Figure 3.4: Cyclic voltammograms of gold working electrode without and with different concentrations of SDS. All the voltammograms were recorded at room temperature at a scan rate of 10 mVs⁻¹.

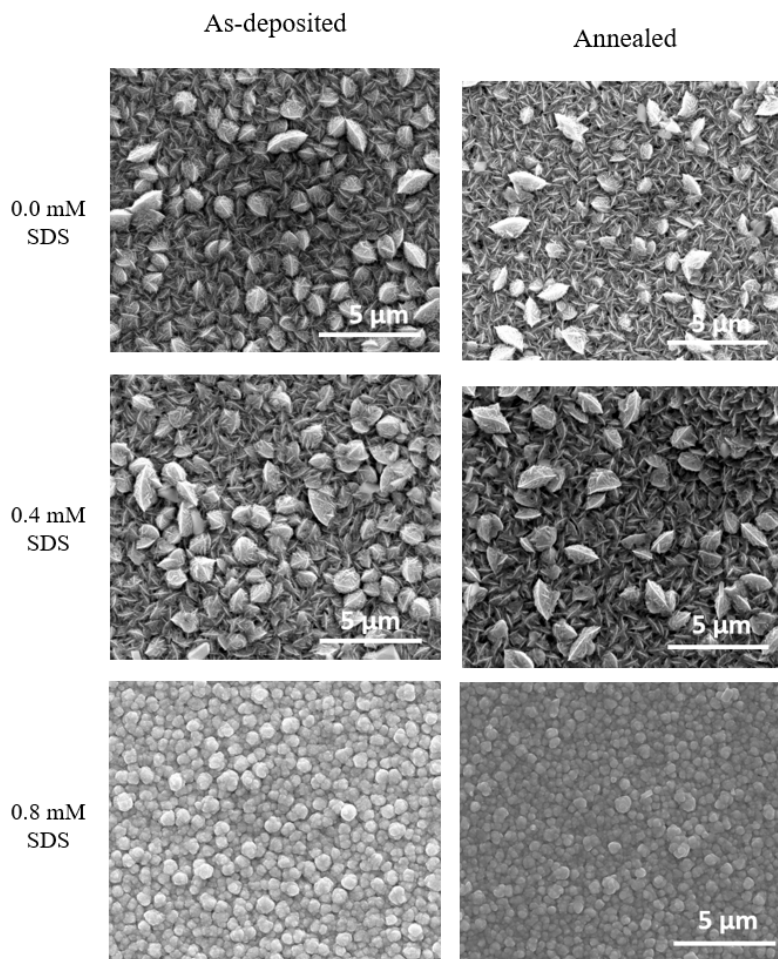


Figure 3.5: SEM images of with different concentrations of SDS, as-deposited and annealed at 350 °C.

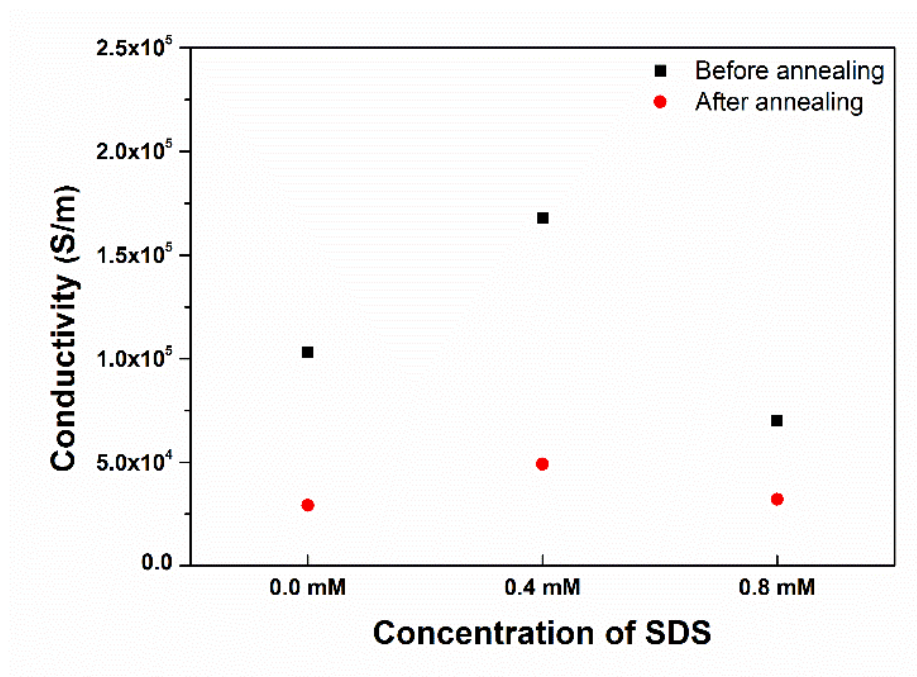


Figure 3.8: Electrical conductivities of the films before and after annealing with different concentrations of SDS.

Chapter 4: Optimization of annealing conditions to enhance thermoelectric performance of electrodeposited p-type BiSbTe thin films

Chapter based on the publication journal article:

APL Materials 7, 031102 (2019)

Swatchith Lal, Devendraprakash Gautam and Kafil M. Razeeb

Tyndall National Institute, University College Cork, Lee Maltings, Cork T12 R5CP, Ireland

4.1 Abstract

In this work, we report the optimization of annealing process to improve the thermoelectric properties of pulse electrodeposited bismuth antimony telluride (Bi-Sb-Te) films by varying the annealing time-temperature profile. The innovative approach of sandwiched Te in between the Bi-Sb-Te layers aids in compensating the loss of tellurium during the annealing of BiSbTe thin films. An optimized Seebeck coefficient of $90.5 \mu\text{V/K}$ along with a power factor of $240 \mu\text{W/mK}^2$ is achieved for samples annealed at 350°C for 1 h under N_2 atmosphere with controlled heating and cooling rates. These improvements are attributed to a significant decrease in the carrier concentration as substantiated by the Hall measurements and to the increase in the crystallite size at the elevated temperatures as indicated by the XRD data. A comprehensive study on the annealing parameters reveals that the Seebeck coefficient and the electrical conductivity are considerably more sensitive to the annealing temperature than compared to the annealing time.

4.2 Introduction

Bismuth telluride based materials still dominate in thermoelectric (TE) properties for room temperature applications. Bulk materials have been extensively studied [1-3]. However, they cannot be used in miniaturized thermoelectric devices due to integration and processing constraints. Thin film thermoelectric materials can be used for such applications [4-6]. Various thin film deposition techniques have been reported, such as metal organic chemical vapour deposition (MOCVD)[7], electrochemical deposition[8], molecular beam epitaxy (MBE)[9], pulsed laser deposition[10] and thermal evaporation[11]. Among different deposition techniques, electrochemical deposition

attracts attention due to its ease of deposition and industrial scalability [8, 12]. In addition, due to its selective deposition over a patterned structure, the wastage of material is minimized and hence becomes cost-effective. Also, the ability to tune material's stoichiometry makes the electrochemical technique potentially advantageous to be employed for the deposition of TE thin films. However, the TE properties, in particular, the Seebeck coefficient of bulk materials are superior compared to the electrodeposited materials. This can be attributed to the high carrier concentrations of electrodeposited films in comparison to predicted carrier concentration by common antistructure model [13]. Various approaches, mainly using additives [14] and doping [15] have been applied to enhance the TE properties of electrodeposited thin films. Annealing is an alternative route to further enhance the TE properties of electrochemically deposited thin films. Annealing passivates defects resulting in the decrease of structural and point defects and thereby reduces the defect density and the carrier concentration in the materials and hence, improving the Seebeck coefficient.

Interdependent relation between the Seebeck coefficient, the carrier concentration, mobility, and the electrical conductivity can be expressed by these equations:

$$S = \frac{8\pi^2 k_b^2}{3eh^2} \cdot m^* T \left(\frac{\pi}{3n}\right)^{2/3} \quad 4.1$$

$$\frac{1}{\rho} = e \cdot n \cdot \mu \quad 4.2$$

Where, m^* is the effective mass, k_b is the Boltzmann constant, e is the electron charge, h is the Planck constant, n is the charge carrier concentration, μ is the mobility of charge carrier, ρ is the electrical resistivity and T is the absolute temperature[1]. From the above relation, it can be seen that a decrease in the carrier concentration not only increases the Seebeck coefficient, but also decreases the electrical conductivity. Therefore, an optimization is required, which in this work has been studied by optimizing the annealing parameters, namely the annealing temperature-time profile.

The deposition of stoichiometric ternary BiSbTe alloy thin films is challenging compared to the binary material. One of the significant problems associated with the annealing of bismuth telluride alloy thin films is the evaporation of tellurium (Te) at elevated temperatures due to its high vapour pressure and thereby impacting on the composition and the TE properties of thin films[16, 17]. To circumvent the loss of Te during annealing and to maintain the films composition, they are usually annealed in the Te atmosphere for long annealing time of about 60 h [18]. This makes the process environmentally

unfriendly, cumbersome and industrially not scalable. Most of the annealing studies reported in the literature are on binary n-type bismuth telluride materials [17, 19-23] and few on p-type ternary material [18], but all are investigated in the Te atmosphere. Building-up on our previous work of using an encapsulated Te layer between p-type BiSbTe film [16], here we study the effect of annealing parameters on the TE properties of electrodeposited p-type BiSbTe films. The experiments are performed at various annealing temperatures and times in the N₂ atmosphere. The impact of annealing temperature-time profile on the microstructure and TE properties is investigated in detail.

4.3 Experimental

Thin films of p-type BiSbTe were deposited potentiostatically on a square (32 mm × 32 mm) Si/SiO₂ substrate, where SiO₂ layer of 1 μm was thermally grown. On top of it, titanium (Ti) layer of 10 nm and gold (Au) layer of 20 nm was deposited, which acts as a metal seed layer for electrochemical deposition. Depositions were performed at room temperature using the triple pulse amperometry technique in a three-electrode conventional setup. The electrodeposition potentials were controlled by a CHI600 series electrochemical analyser/work station. Ag/AgCl reference electrode was used with a Pt mesh as a counter electrode. Prior to the deposition, all the substrates were cleaned with Isopropanol (IPA) and then with deionized (DI) water followed by drying with N₂ jet at ambient temperature.

Bismuth (III) nitrate pentahydrate (ACS reagent ≥ 98.0%), antimony (III) oxide, tellurium (powder □200mesh, 99.8% trace metals basis), tartaric acid (ACS reagent ≥ 99.5%), nitric acid (ACS reagent ≥ 69%) and dimethyl sulfoxide (ACS reagent ≥ 99.9%) were used for the experiments as received.

Dissolving Te powder and antimony oxide (Sb₂O₃) is nontrivial due to surface TeO₂ that dissolves only in strong HNO₃ medium and Sb₂O₃ having lower solubility in an aqueous solution. Therefore, two separate solutions were made in order to dissolve the salts and combined at a later stage to form a stable electrolyte.

In preparing solution (A), 15mM of Te was put into 25 mL of 1 M HNO₃ and was heated at ~45 °C to dissolve Te completely and 5 mM Bi(NO₃)₃.5H₂O was added to the solution. Solution (B) was prepared using 10 mM Sb₂O₃ in 25 mL of 0.2 M tartaric acid and was heated at ~45 °C for proper dissolution. Both solutions A and B were mixed and 50 mL

of dimethyl sulfoxide (DMSO) was added to the mixed solutions. The whole solution was maintained at 1:1 (v/v) ratio of DI water and DMSO.

In order to evaluate the reduction potential of the dissolved species, cyclic voltammetry (CV) studies were performed within the fixed potentials of -0.6 V and 0.8 V vs. Ag/AgCl at a scan rate of 10 mV/s. Optimised pulse design was used for deposition using the triple pulse amperometry technique for an overall duration of 2 h leading to two layers of BiSbTe films. Pure Te layer was deposited in between BiSbTe layers using an electrolyte with 15 mM Te in 1 M nitric acid. Pulse deposition technique has various advantages over conventional potentiometric deposition such as uniform and adhesive films, low porosity, fine-grained structure, reduced surface roughness, improved morphology and stoichiometry of the films [24-26]. The overall deposition gave a film thickness of ~2 μm . Subsequently, the films were cleaned with IPA and DI water and dried under N_2 flow at ambient temperatures.

The structural characterization of thin films was performed using a scanning electron microscopy (SEM), and the composition was determined with energy dispersive X-ray spectroscopy (EDX) attached to the SEM. All the SEM analyses were done on the Quanta FEG 450 at an accelerating voltage of 20 kV at 20 Kx magnification. X-ray diffraction patterns (XRD) were recorded using a Pan analytical X'pert pro, with $\text{Cu K}\alpha$ radiation ($\alpha=1.5406 \text{ \AA}$) at a voltage of 40 kV and a current of 40 mA. Electrical resistivity and Hall measurements were performed using an in-line four-point probe measurement system (Jandel RM300) and in Hall arrangement for the Hall coefficient (Lakeshore model 8404) to independently measure the sheet resistivity of the samples. Seebeck coefficient of the electrodeposited thin films was measured using a laboratory built system.

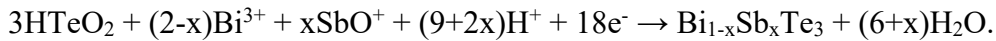
Seebeck coefficient for all samples was evaluated in the in-plane configuration by establishing a temperature gradient (ΔT) along the length of the sample through commercially available thermoelectric coolers at the two ends of the sample. The thermovoltage was measured in the range of $\Delta T \approx 2\text{-}10 \text{ }^\circ\text{C}$. Two separate thermocouples situated at the ends of the sample recorded the temperatures. Seebeck coefficient was evaluated from the slope of the thermovoltage against ΔT . Seebeck coefficient was calculated with the intact seed layer.

The thermal treatment of the electrodeposited films was performed under controlled flow of N_2 atmosphere in rapid thermal annealing (RTA) system for a different time duration ranging from 15 minutes–1 h and at different temperatures ranging from 250–400 $^\circ\text{C}$. The

samples were heated from room temperature to the desired annealing temperature in a controlled heating and cooling rate of 20 K/min and kept at that temperature for set time duration. Three sets of samples were prepared to ensure the reproducibility of the properties.

4.4 Results and Discussion

The deposition mechanism of ternary alloys from the electrolytic bath solution is more complex than the deposition of binary materials. Thus, fine optimization of plating parameters is required for controlled film composition. The electrolyte constitutes with Bi^{3+} , SbO^+ and HTeO^+ ions[27]. In order to understand the deposition potentials of the constituents, cyclic voltammograms (CVs) were recorded, using standard Au working electrode of 1 mm radius and with a scan rate of 10 mV/s. As shown in Fig. 4.1, CV reveals three cathodic peak potentials at -0.07, -0.15 and -0.27 V vs. Ag/AgCl and two anodic peaks at 0.46 and 0.51 V vs. Ag/AgCl. These reduction peaks can be attributed to Bi, Te and Sb, respectively [28]. The deposition of the desired composition of $(\text{Bi}_{1-x}\text{Sb}_x)\text{Te}_3$ can be described as[20]



Based on the CV studies, the deposition potentials were fixed as optimized in our previous work[14]. Triple pulse amperometry was used at potentials $V_1 = -80$ mV for a duration of 10 ms, $V_2 = -50$ mV for a duration of 20 ms and $V_3 = -250$ mV for a duration of 50 ms. The films were deposited for a duration of 2 h in order to attain a thickness of 2 μm .

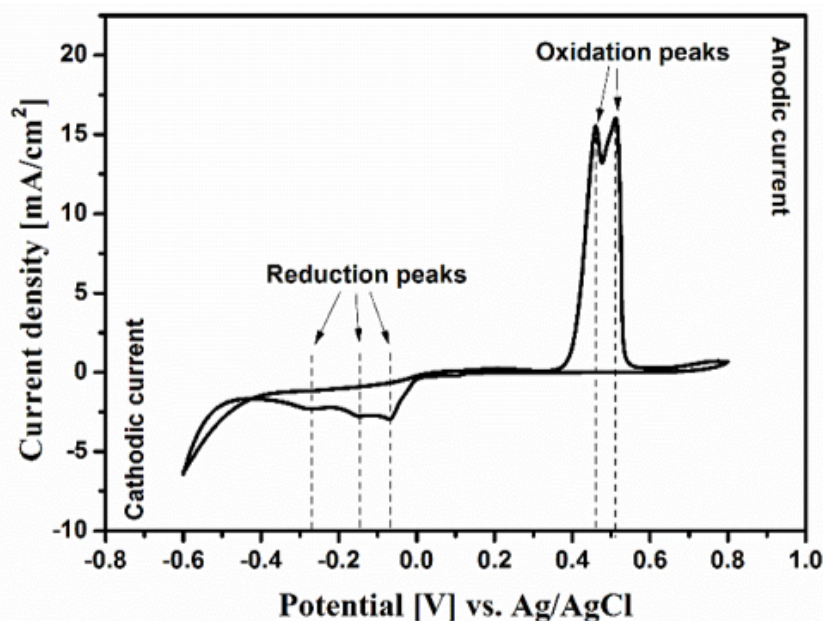


Figure 4.1: Cyclic voltammogram recorded on a gold working electrode in the electrolyte containing $0.005M Bi^{3+}$, $0.010M SbO^+$, $0.015M HTeO_2^+$, and $1M HNO_3$. The CV's are recorded at room temperature at a scan rate of 10 mV/s .

4.4.1 Effect of annealing temperature on TE properties

Due to the high vapour pressure of Te and considerable evaporation at elevated temperatures, these samples were annealed in the temperature range of 250 to 400 °C with a step of 50 °C for the time duration of 1 h. In order to understand the effect of annealing temperature on the microstructure, micrographs were recorded using SEM. Figure 4.2 shows the micrograph of as-deposited and annealed films. The microstructures of the films changed drastically with the increasing annealing temperatures. The dendritic and fluffy structure of the as-deposited films collapses as the annealing temperature is increased and gets modified to dense films. At the high annealing temperature of 350 °C and 400 °C, we observed a porous network in the films, which is due to the loss of Te at these temperatures. In order to understand the effect of thermal treatment on these films, the composition was analyzed using EDX analysis and is depicted in Table 4-1. It is interesting to observe that, there has been no significant change in the composition of the films on annealing even though there has been a strong modification in the microstructure. This observation can be ascribed to the depletion of excess Te that is sandwiched between p-BiSbTe layer during annealing and thereby resulting in the stoichiometric films.

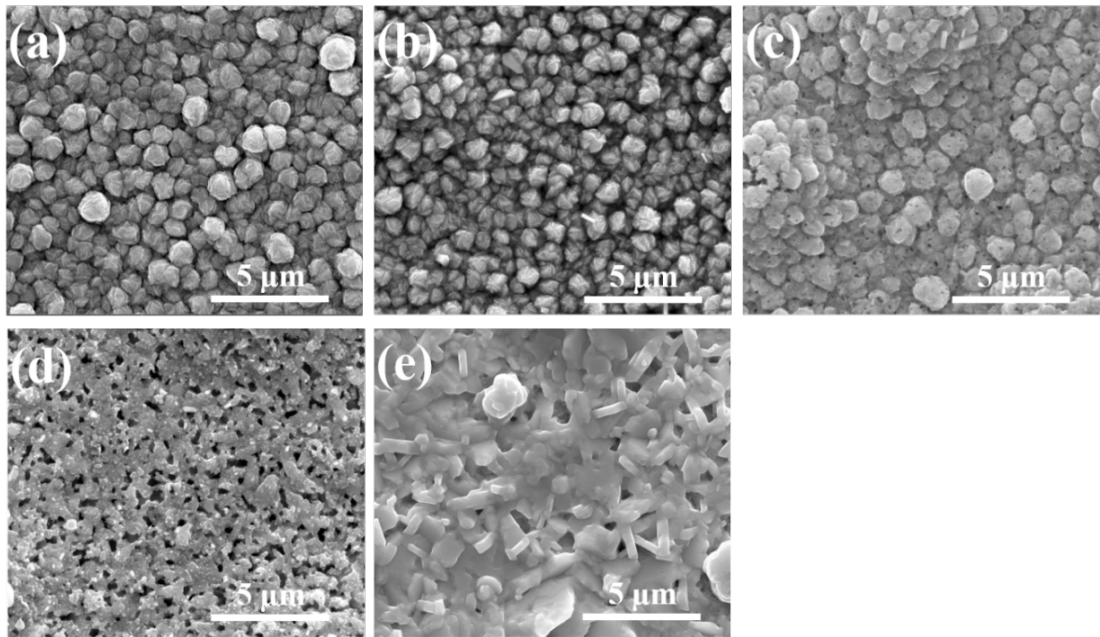


Figure 4.2: SEM images of (a) as-deposited samples and samples annealed at (b) 250 °C, (c) 300 °C, (d) 350 °C, and (e) 400 °C.

Table 4-1: Atomic composition of Bi-Sb-Te as-deposited films and films annealed at different annealing temperatures.

Annealing temperature (°C)	Film composition (at. %)		
	Sb	Te	Bi
As-deposited	24.05	60.11	15.84
250	24.10	59.69	16.21
300	24.69	58.96	16.35
350	23.36	59.68	16.96
400	21.86	60.04	18.13

Figure 4.3 shows the XRD patterns of the as-deposited and the films annealed at different temperatures. Standard references for $(\text{Sb}_{0.5}\text{Bi}_{0.5})_2\text{Te}_3$, Au, AuTe_2 , Si are obtained from ICSD PDF card (72-1835, 02-1095, 85-1309, 01-0787), respectively. All the films have a rhombohedral crystal structure of $(\text{Sb}_{1-x}\text{Bi}_x)_2\text{Te}_3$, with (015) being the prominent peak. However, some small peaks with different orientation were observed after annealing at different temperatures. AuTe_2 peak was observed for the films annealed at 400 °C, indicating the formation of a new phase due to the diffusion and reaction of Te with Au, forming AuTe_2 . The Au and Si peak observed in the XRD patterns are from the seed layer. The average crystallite size was calculated using the Debye-Scherrer formula and presented in Table II. There is a significant increase in the crystallite size of annealed

films as compared to as-deposited films (see Table 4-2). The size increases as the annealing temperature are raised to 250 °C. After that, there has been little or no change in the crystallite size. However, an increase in the intensity of (015) peak with increasing annealing temperature signifying the growth in (015) crystalline orientation in the film (see Fig. 4.3). Also, the micrographs reveal that the grain size increases with the increasing annealing temperature as shown in Fig. 4.2. The annealed films tend to form large and dense grains with increased connectivity in-between the grains. This can be attributed to change in the crystallite size between the as-deposited and annealed films.

Table 4-2:Crystallite size of films annealed at different annealing temperatures.

Annealing temperature (°C)	Crystallite size (nm)
As-deposited	11.55
250	37.20
300	35.61
325	35.61
350	37.16
375	37.16
400	35.61

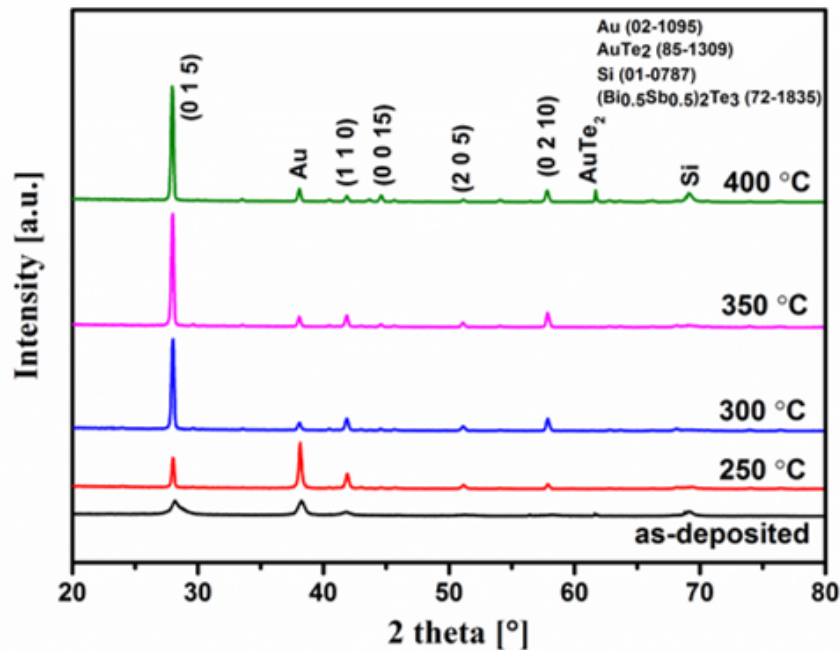


Figure 4.3: XRD patterns of the as-deposited and the annealed BiSbTe films. The annealing temperatures are mentioned in the pattern.

Thermoelectric properties, namely the Seebeck coefficient, the electrical conductivity and the power factor were measured and calculated for the as-deposited and annealed

samples at different temperatures as shown in Figs. 4.4 (a) and 4.4 (b). The Seebeck coefficient of films increased with the annealing temperatures and the maximum Seebeck coefficient was observed for the samples annealed at 350 °C. On further increment of the temperature, the Seebeck coefficient of the film decreased. The electrical conductivity of the as-deposited films is an order of magnitude higher compared to the annealed film. In order to understand this, Hall measurements of the films were performed. Figure 4.5 shows the Hall measurements of the as-deposited and annealed samples. The carrier concentration of the as-deposited film is 1.58×10^{21} carriers/cm³, which is more than an order of magnitude higher compared to the annealed films, which is around $2-6 \times 10^{19}$ carriers/cm³ (see Fig. 4.5). This reduction in the carrier concentrations of the annealed films resulted in reduced electrical conductivity and a simultaneous increase in the Seebeck coefficient. The mobility of the as-deposited films is measured to be 8.9 cm²/V.s, which increased upon annealing of films. This increase in the mobility of charge carriers with the annealing can be interrelated to the structural transformations as revealed through micrographs in Fig. 4.2. With annealing, the films become denser and get connected to adjacent grains and as an outcome the mobility of the annealed films increases, as shown in Fig. 4.5. In addition, with annealing crystallinity of thin films was improved resulting in an increase of the average grain size and minimization of grain boundaries that leads to higher mobility. The mobility of the charge carriers is observed to increase with the annealing temperature from ~ 30 cm²/V.s for the film annealed at 250 °C to ~ 125 cm²/V.s for films annealed at 400 °C. A slight drop in the mobility of charge carriers is observed for films annealed at 350 °C, and this reduction may be due to the porosity in the film, resulted from the Te evaporation (see Fig. 4.2(d)). Upon further increase in the temperature, the microstructure further collapses and become dense forming interconnected grains; this led to an increase in the mobility (Fig. 4.2(e)). This increase in the mobility and no drastic changes in the carrier concentration for the annealed films have led to a gradual and slight increment in the electrical conductivity of the annealed films from 250 °C to 400 °C. The electrical conductivities of the films were measured using the in-line four-point probe measurement system, which was also used to cross-check the conductivity values obtained from the Hall measurements. The values from both the measurement techniques are almost the same, ensuring that the obtained data are correct and are within the error limits of the measurements. As stated in the earlier section, three different set of samples were deposited and annealed. The variation in their Seebeck coefficient values are plotted with error bars in Fig. 4.4(a). It can be noticed from

the figure that the error bars depict the spread in the measured Seebeck coefficient values, which reduces and become significantly low at around 350 °C showing higher stability in the Seebeck coefficient values for 350 °C annealed thin films.

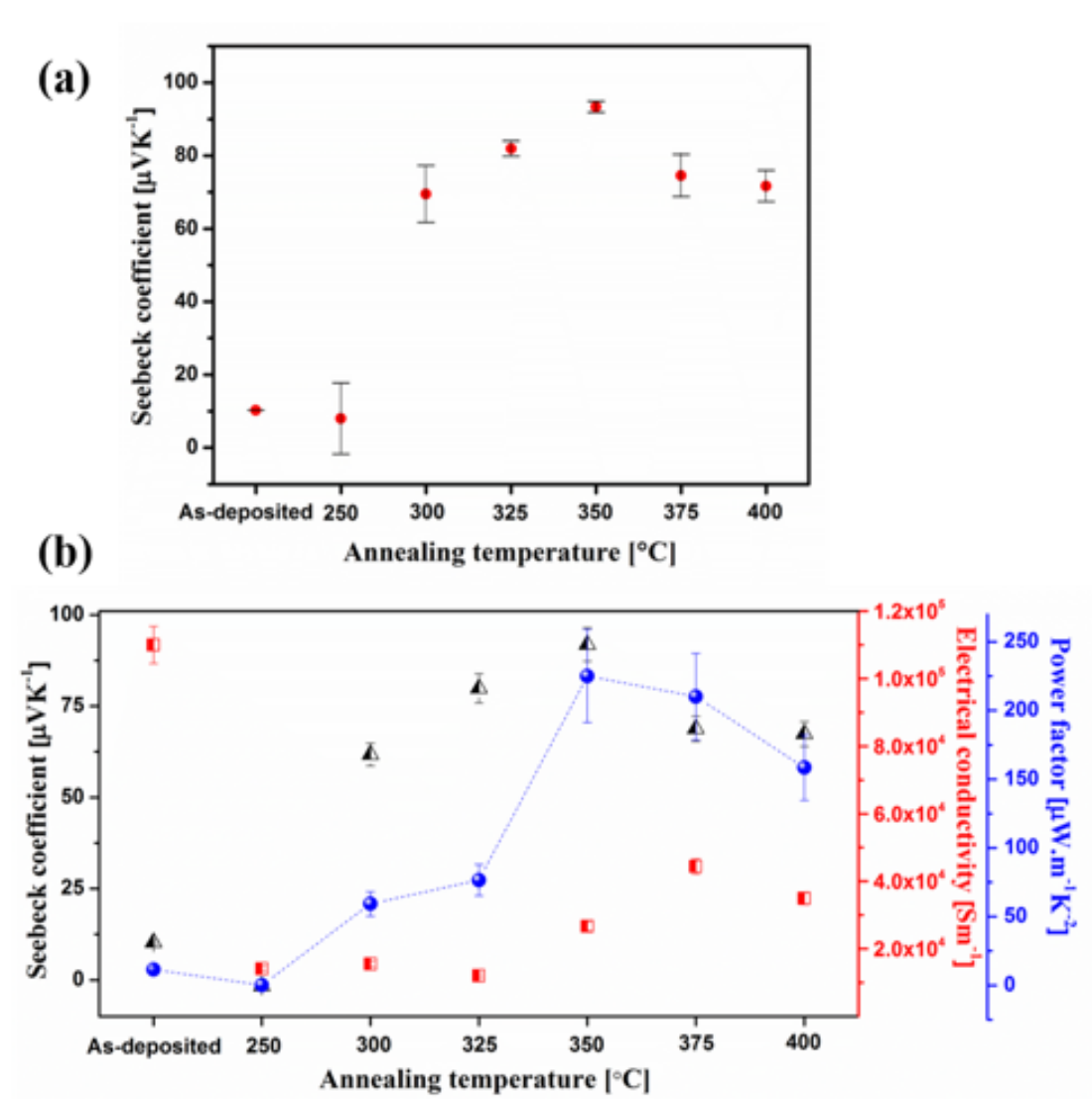


Figure 4.4: (a) Seebeck coefficient of BiSbTe films annealed at different temperatures for 1 h with the error bars. (b) Seebeck coefficient, electrical conductivity, and calculated power-factor of asdeposited and annealed films.

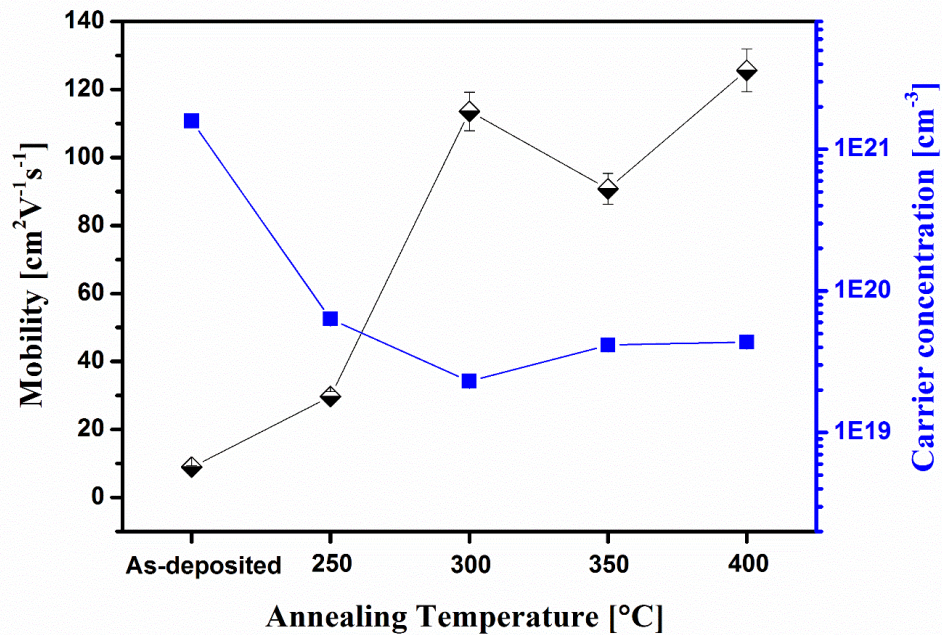


Figure 4.5: Carrier mobility and carrier concentration of BiSbTe thin films as a function of the annealing temperature.

The power factor of all the films was calculated and plotted as shown in Fig. 4.4(b). The power factor of the as-deposited films was $11 \mu\text{W}/\text{mK}^2$, which increased for the annealed films and a maximum power factor of $225 \mu\text{W}/\text{mK}^2$ was obtained for the films annealed at $350 \text{ }^\circ\text{C}$ for a duration of 1 h in N_2 atmosphere. The power factor of the annealed films increased due to increment in both the Seebeck coefficient and the electrical conductivity of the annealed films. This shows the role of annealing parameters in fine-tuning the individual thermoelectric properties of the electrodeposited films.

4.4.2 Effect of annealing time of TE properties

To further understand the effect of annealing time on the TE performance of the films, samples were annealed at $350 \text{ }^\circ\text{C}$ for different duration of time from 15 minutes to 1 h. The $350 \text{ }^\circ\text{C}$ annealing temperature was chosen for further analysis as the maximum power factor was attained at this temperature. Figure 4.6 shows the micrographs of films annealed for different annealing times. From the micrographs, it can be observed that there is no specific change in the microstructure of the films annealed for different duration of time except the porosity of the films, which tend to increase with increasing annealing times. The as-deposited films are dendritic and fluffy in nature, which on annealing at $350 \text{ }^\circ\text{C}$ for 15 minutes become granulated and crystalline, but a porous network appears at the same time. The porosity in the films is increased with increasing annealing time from 15 minutes to 1 h. Even though an increase in the porosity is

observed, which can be attributed to the Te evaporation, the composition of all the films has no significant change as tabulated in Table III. This can be ascribed to the sandwich Te layer in the films, which replenishes Te content during annealing of the films.

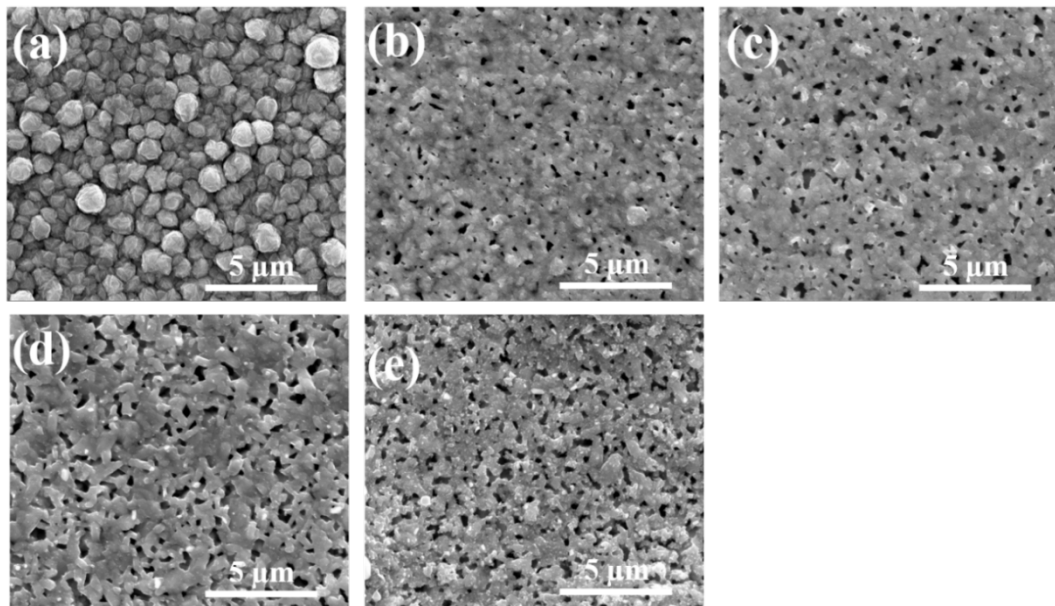
To understand the impact of annealing time on the crystallinity of the films, the XRD patterns were recorded for the films with increasing time of thermal treatment. Figure 4.7 shows the XRD patterns of the as-deposited and films annealed with annealing time varied from 15- 60 minutes. Table IV shows the calculated average crystallite size of different films. All the films had (015) peak as the prominent peak similar to earlier samples with different annealing temperatures. In comparison with the as-deposited sample, the (015) peak for the annealed film is sharp and higher in intensity with the increase in crystallite size. The emergence of other small peaks confirms that the annealed films are polycrystalline. The Au peak observed in the XRD patterns is from the seed layer. It is noteworthy to mention that the crystallite size of the as-deposited films was 11.55 nm, which on annealing at 350 °C for 15 minutes increased to 38.85 nm. But further increase in the annealing time had no significant effect on the crystallite size. However, from the micrographs, it can be seen that the grain-size tend to enhance with increasing annealing time and also made the films more porous. This shows that the duration of annealing has no noticeable effect on the crystallite size of the material and the temperature of annealing controls the crystallite size.

Table 4-3: Atomic composition of Bi-Sb-Te as-deposited films and films annealed at 350 °C for different annealing time.

Annealing time (minutes)	Film composition (at. %)		
	Sb	Te	Bi
As-deposited	24.05	60.11	15.84
15	22.91	59.87	17.21
30	22.95	59.40	17.14
45	23.17	59.48	17.34
60	23.36	59.68	16.96

Table 4-4: Crystallite size of films annealed at 350 °C for different annealing time.

Annealing time (minutes)	Crystallite size (nm)
As-deposited	11.55
15	38.85
30	37.16
45	37.16
60	37.16

**Figure 4.6: SEM images of (a) as-deposited samples and samples annealed at 350 °C for a duration of (b) 15 min, (c) 30 min, (d) 45 min, and (e) 60 min.**

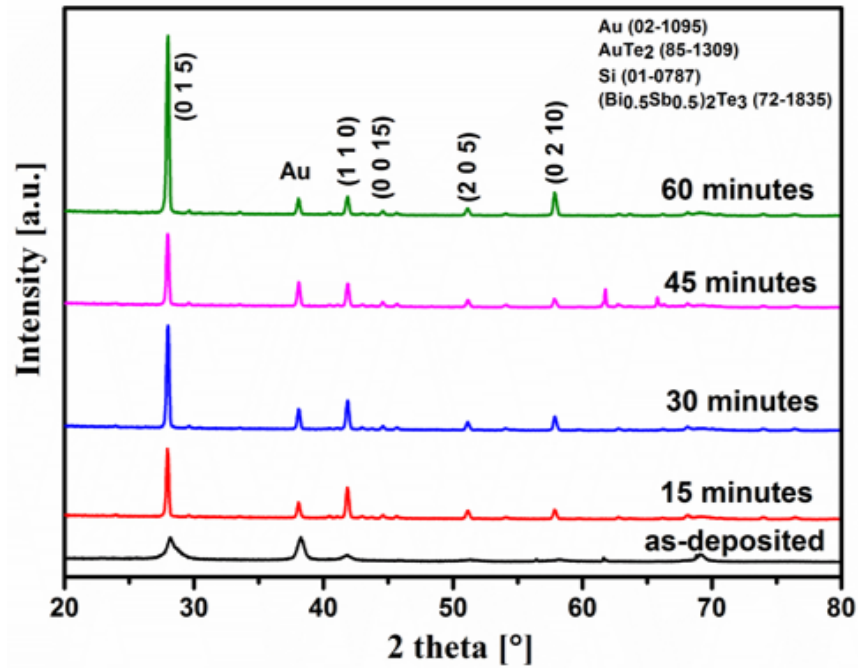


Figure 4.7: XRD patterns of BiSbTe films annealed at 350 °C for different annealing time.

The Seebeck coefficient and the electrical conductivity were measured for the as-deposited and the films annealed at 350 °C for different duration of time and plotted as shown in Fig. 4.8. The Seebeck coefficient of the annealed films varied slightly with increasing annealing time, whereas the electrical conductivity exhibits an optimum for films annealed for 45 minutes as seen in Fig. 4.8. In order to understand this change in the Seebeck coefficient and the electrical conductivity, Hall study was performed on the samples and the results are plotted in Fig. 4.9.

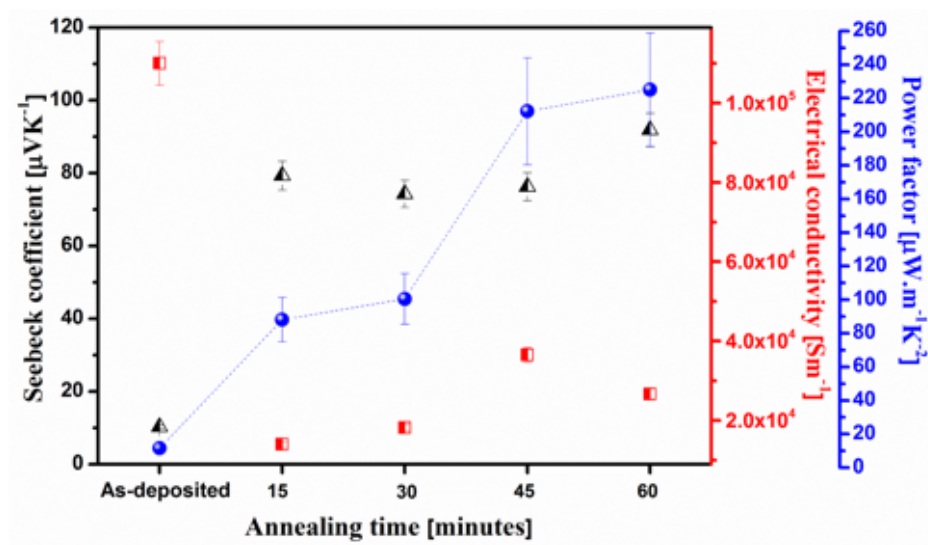


Figure 4.8: Thermoelectric properties of BiSbTe films annealed at 350 °C for different annealing times.

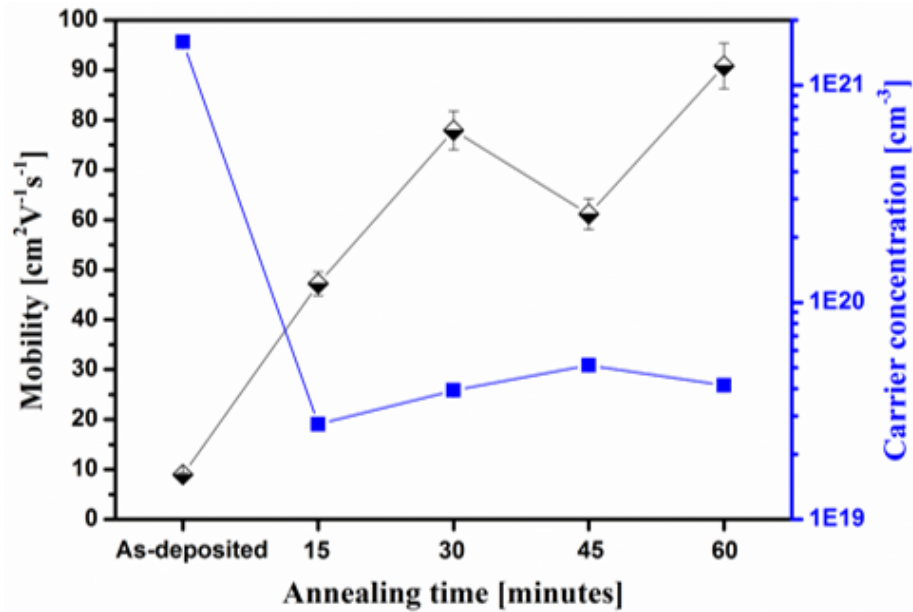


Figure 4.9: Mobility and carrier concentration as a function of the annealing time of BiSbTe films annealed at 350 °C.

The carrier concentration of the annealed films compared to as-deposited films reduced by more than an order of magnitude as discussed in the earlier section of the work. It is noticeable that even small change in the carrier concentration of the annealed films is directly reflected in the change of measured Seebeck coefficient. The Seebeck coefficient of the film annealed at 350 °C for 15 minutes was 79.3 $\mu\text{V}/\text{K}$, which increased to 90.5 $\mu\text{V}/\text{K}$ for the film annealed for 1 h. Although the change is not significant but when coupled with the electrical conductivity of film, it has a strong impact on the power factor of the films. The increase in the mobility from 8.9 $\text{cm}^2/\text{V}\cdot\text{s}$ for the as-deposited film to 90.7 $\text{cm}^2/\text{V}\cdot\text{s}$ for films annealed at 350 °C for 1 h had an impact on increasing the electrical conductivity of the films. With the increase in annealing time from 15 minutes to 1h, the mobility of the charge carriers increased even though there was no significant change in the carrier concentration. This insignificant change in carrier concentration of the films with increasing annealing time might be due to the fact that defect density stabilization has already reached at this particular temperature, and increasing the annealing time only changes the microstructure further with better grain connectivity. This leads to an increase in mobility as shown in Fig. 4.9, and consequently to the increase in electrical conductivity as shown in Fig. 4.8. This increase in the electrical conductivity of the annealed films with no significant change in the carrier concentration led to an increase in the overall power factor of the films. With the maximum power factor of 225 $\mu\text{W}/\text{mK}^2$ for the film annealed for 1 h at 350 °C.

4.5 Conclusion

This study signifies the importance of annealing parameters, such as temperature and time, on the thermoelectric properties of electrodeposited p-type BiSbTe films. The inclusion of a Te layer in-between BiSbTe layers prevents the loss of tellurium at elevated temperatures maintaining the stoichiometry of the deposited films regardless of the annealing conditions.

The microstructure evaluation studies depict the densification and interconnected nature of the films with different annealing parameters. It demonstrates the control over the carrier concentration and the mobility by tuning the annealing parameters. The Seebeck coefficient values of the annealed films increase with the annealing temperature leading to an optimum value of 90.5 $\mu\text{V}/\text{K}$ when annealed at 350 °C for 1 h duration in N_2 atmosphere under controlled heating and cooling rates. The maximum power factor of 225 $\mu\text{W}/\text{mK}^2$ is achieved for the same annealing conditions as above but decreases beyond that temperature. No substantial change in the Seebeck coefficient is observed with increasing annealing time. However, due to an increase in the mobility of the carriers with increasing annealing time, the electrical conductivity gradually rises. This result in a maximum power factor for thin films annealed for 1 hour.

4.6 References

- [1] G. J. Snyder and E. S. Toberer, "Complex thermoelectric materials," *Nat Mater*, 10.1038/nmat2090 vol. 7, no. 2, pp. 105-114, 02//print 2008.
- [2] J. He, M. G. Kanatzidis, and V. P. Dravid, "High performance bulk thermoelectrics via a panoscopic approach," *Materials Today*, vol. 16, no. 5, pp. 166-176, 2013/05/01/ 2013.
- [3] L.-D. Zhao, V. P. Dravid, and M. G. Kanatzidis, "The panoscopic approach to high performance thermoelectrics," *Energy Environ. Sci.*, vol. 7, no. 1, pp. 251-268, 2014.
- [4] L. E. Bell, "Cooling, Heating, Generating Power, and Recovering Waste Heat with Thermoelectric Systems," *Science*, vol. 321, no. 5895, pp. 1457-1461, 2008-09-12 00:00:00 2008.
- [5] R. Venkatasubramanian, "Thin-film thermoelectric devices with high room-temperature figures of merit," *Nature*, vol. 413, pp. 597-602, // 2001.

- [6] B. Habbe and J. Nurnus, "Thin film thermoelectrics today and tomorrow," *Electron. Cooling*, vol. 17, pp. 24-31, // 2011.
- [7] A. Giani, A. Boulouz, F. Pascal-Delannoy, A. Foucaran, E. Charles, and A. Boyer, "Growth of Bi₂Te₃ and Sb₂Te₃ thin films by MOCVD," *Materials Science and Engineering B: Solid-State Materials for Advanced Technology*, Article vol. 64, no. 1, pp. 19-24, 1999.
- [8] C. Boulanger, "Thermoelectric Material Electroplating: a Historical Review," *Journal of Electronic Materials*, vol. 39, no. 9, pp. 1818-1827, 2010// 2010.
- [9] T. C. Harman, P. J. Taylor, M. P. Walsh, and B. E. LaForge, "Quantum dot superlattice thermoelectric materials and devices," (in English), *Science*, Article vol. 297, no. 5590, pp. 2229-2232, 2002.
- [10] A. Li Bassi *et al.*, "Thermoelectric properties of Bi-Te films with controlled structure and morphology," *Journal of Applied Physics*, vol. 105, no. 12, p. 124307, 2009/06/15 2009.
- [11] J.-M. Lin, Y.-C. Chen, and C.-P. Lin, "Annealing Effect on the Thermoelectric Properties of Bi₂Te₃ Thin Films Prepared by Thermal Evaporation Method," *Journal of Nanomaterials*, vol. 2013, p. 6, 2013, Art. no. 201017.
- [12] F. Xiao, C. Hangarter, B. Yoo, Y. Rheem, K.-H. Lee, and N. V. Myung, "Recent progress in electrodeposition of thermoelectric thin films and nanostructures," *Electrochimica Acta*, vol. 53, no. 28, pp. 8103-8117, 2008/11/30/ 2008.
- [13] K. Tittes *et al.*, "Electrochemical deposition of Bi₂Te₃ for thermoelectric microdevices," *Journal of Solid State Electrochemistry*, vol. 7, no. 10, pp. 714-723, 2003/10/01 2003.
- [14] S. Lal, D. Gautam, and K. M. Razeeb, "The Impact of Surfactant Sodium Dodecyl Sulfate on the Microstructure and Thermoelectric Properties of p-type (Sb_{1-x}Bi_x)₂Te₃ Electrodeposited Films," *ECS Journal of Solid State Science and Technology*, vol. 6, no. 3, pp. N3017-N3021, January 1, 2017 2017.
- [15] R. Rostek, N. Stein, and C. Boulanger, "A review of electroplating for V-VI thermoelectric films: from synthesis to device integration," *Journal of Materials Research*, vol. 30, no. 17, pp. 2518-2543, 2015.
- [16] K. M. R. a. D. Gautam, "Alloy System with Enhanced Seebeck Coefficient and Process for Making Same," vol. U.S. Serial No. 62/240,197, 2015.
- [17] R. Rostek, V. Sklyarenko, and P. Woias, "Influence of vapor annealing on the thermoelectric properties of electrodeposited Bi₂Te₃," (in English), *Journal of*

- Materials Research*, 10.1557/jmr.2011.141 vol. 26, no. 15, pp. 1785-1790, Aug 2011.
- [18] C. Schumacher *et al.*, "Optimizations of Pulsed Plated p and n-type Bi₂Te₃-Based Ternary Compounds by Annealing in Different Ambient Atmospheres," *Advanced Energy Materials*, vol. 3, no. 1, pp. 95-104, 2013.
- [19] N. G. Stoltz and G. J. Snyder, "Effects of annealing electrodeposited bismuth telluride films," in *Thermoelectrics, 2002. Proceedings ICT '02. Twenty-First International Conference on*, 2002, pp. 28-30.
- [20] S. Li *et al.*, "Effects of Annealing and Doping on Nanostructured Bismuth Telluride Thick Films," *Chemistry of Materials*, vol. 20, no. 13, pp. 4403-4410, 2008/07/01 2008.
- [21] M. M. Rashid, K. H. Cho, and G.-S. Chung, "Rapid thermal annealing effects on the microstructure and the thermoelectric properties of electrodeposited Bi₂Te₃ film," *Applied Surface Science*, vol. 279, pp. 23-30, 8/15/ 2013.
- [22] D. M. Lee, C. H. Lim, D. C. Cho, Y. S. Lee, and C. H. Lee, "Effects of annealing on the thermoelectric and microstructural properties of deformed n-type Bi₂Te₃-based compounds," *Journal of Electronic Materials*, vol. 35, no. 2, p. 360, 2006// 2006.
- [23] S. Kamolmad, S. Aparporn, and S. Rachsak, "Effects of annealing temperature on the structural, mechanical and electrical properties of flexible bismuth telluride thin films prepared by high-pressure RF magnetron sputtering," *Advances in Natural Sciences: Nanoscience and Nanotechnology*, vol. 8, no. 3, p. 035002, 2017.
- [24] V. Richoux, S. Diliberto, and C. Boulanger, "Pulsed Electroplating: a Derivate Form of Electrodeposition for Improvement of (Bi_{1-x}Sb_x)₂Te₃ Thin Films," *Journal of Electronic Materials*, vol. 39, no. 9, pp. 1914-1919, 2010// 2010.
- [25] V. Richoux, S. Diliberto, C. Boulanger, and J. M. Lecuire, "Pulsed electrodeposition of bismuth telluride films: Influence of pulse parameters over nucleation and morphology," *Electrochimica Acta*, vol. 52, no. 9, pp. 3053-3060, 2007/02/15/ 2007.
- [26] S. Diliberto, V. Richoux, N. Stein, and C. Boulanger, "Influence of pulsed electrodeposition on stoichiometry and thermoelectric properties of bismuth telluride films," *physica status solidi (a)*, vol. 205, no. 10, pp. 2340-2344, 2008.
- [27] X. Li, E. Koukharenko, I. S. Nandhakumar, J. Tudor, S. P. Beeby, and N. M. White, "High density p-type Bi_{0.5}Sb_{1.5}Te₃ nanowires by electrochemical

templating through ion-track lithography," *Physical Chemistry Chemical Physics*, 10.1039/B818040G vol. 11, no. 18, pp. 3584-3590, 2009.

- [28] J. Kuleshova *et al.*, "Optimization of the Electrodeposition Process of High-Performance Bismuth Antimony Telluride Compounds for Thermoelectric Applications," *Langmuir*, vol. 26, no. 22, pp. 16980-16985, 2010/11/16 2010.

Chapter 5: Amorphous framework in electrodeposited CuBiTe thermoelectric Thin-films with High Room Temperature performance

Chapter based on the journal article submitted to:

Advanced Electronic Materials

N. Padmanathan[#], Swatchith Lal[#], Devendraprakash Gautam and Kafil M. Razeeb

Tyndall National Institute, University College Cork, Lee Maltings, Cork T12 R5CP,
Ireland

[#]These authors contributed equally to this work.

5.1 Abstract

Bismuth telluride based alloys are the most efficient thermoelectric materials near room temperature and widely used in commercial thermoelectric devices. Nevertheless, its thermoelectric performance is needed to be improved further for wide-scale implementation either as a thermoelectric generator or cooler. Here we propose a simultaneous co-deposition of CuBiTe thin films and their phase transition strategy via traditional electrodeposition process. With just 13 atom % Cu doping, crystalline-to-amorphous phase transformation resulted for the electroplated CuBiTe alloy. A close look of the alloy composition revealed spikes-shaped nanocrystalline Bi₂Te₃ embedded in the CuBiTe amorphous matrix. Our result shows an exceptionally high power factor (3.02 mW m⁻¹K⁻²), which comes from the enhanced Seebeck coefficient (-275 μV K⁻¹) and high electrical conductivity (3.99 × 10⁴ S m⁻¹) of CuBiTe films. Therefore, it can be suggested that the adopted new strategy to form a unique nano-crystallite-embedded amorphous frame-work provide a new platform to develop a next-generation high-performance thermoelectric materials with extraordinary power factor.

5.2 Introduction

The recent advancements in wireless sensor networks (WSNs) have the potential to realise the ‘Internet of Things’ (IoT) and aiming to integrate the physical world with the computer-based systems. These versatile WSNs have been widely used in industrial communications [1], remote healthcare [2], automotive monitoring [3], surveillance [4], etc. and is a potential candidate to find its place in the hitherto unexplored application. However, one of the major impediments in the path of materializing this type of smart connected environment is the perpetual powering of such billions of deployed sensor

nodes. Batteries as the only power source not only add unnecessary volume and weight to such miniaturized system and also need to recharge or replacement once its energy depleted. A lot of new strategies have been adopted to enhance the battery performance; however the current battery technologies not able to meet the requisites of advanced microelectronics technologies. In this predicament, the most attractive alternative is to scavenge energy from omnipresent ambient energy sources and assisting the energy storage devices for ultimately powering the microelectronics system [5, 6].

A thermoelectric generator is well-suited in extending the life of the battery and eventually replaces the battery of these wireless sensors if there is a large temperature differential exists. Conversely, these thermoelectric devices can be used in niche cooling applications, for example, to maintain stable temperatures in lasers and optical detectors.[7-10] Therefore, Thermoelectric (TE) devices entail highly efficient thermoelectric materials and their in-depth understanding of the electron and phonon transport phenomenon. The performance of thermoelectric material is determined by its figure of merit, $zT = S^2\sigma T/k$, where S is the Seebeck coefficient, σ is the electrical conductivity, k is the thermal conductivity and T is the absolute temperature.[7, 8] Usually, two strategies are followed to improve the zT of the thermoelectric materials. First one is to find new materials with ultra-low thermal conductivity, and the later for the development of low-dimensional systems for improved power factor ($PF = S^2\sigma$).[11-13] The primary focus of this work is to enhance the power factor of the material by tailoring the internal microstructure using doping process.

Until now, Bi_2Te_3 based alloys have been demonstrated as the best near room temperature thermoelectric materials [14-17] where zT values of these alloys reaching to greater than unity for both n-type and p-type conduction.[17, 18] To utilize these materials for widespread applications of a thermoelectric device, a minimum zT of 4 should be achieved, which remains a formidable challenge[18]. The problem is that the three parameters in zT (S , σ , and k) are independent.[18] However, these interdependent transport parameters (Seebeck coefficient, electrical conductivity) can be optimised through chemical doping or alloying the crystal structure by tuning the mobility, effective mass and concentration of the charge carriers through modification of the electronic band structure near the Fermi level, whereas the thermal conductivity ($k = k_e + k_L$), specifically the lattice thermal conductivity (k_L) can be reduced through phonon scattering at the interfaces by forming multi-scale defect formation and nanostructuring .[19-21]

To date, many of these strategies are adopted to enhance the zT by tuning the Bi_2Te_3 structure through alloying,[22-24] superlattice formation,[25] varying the composition or defects level,[26-30] and by designing a hybrid architecture nanocomposite, which facilitates the simultaneous optimization of the electrical and the thermal transport properties.[31] Recently, enhancement of power factor ($S^2\sigma$) was observed for TE materials, (e.g. Bi_2Te_3 , GeTe , PbTe , SnTe etc.) by introducing an energy-barrier in the layered structure. This is mainly due to the carrier filtering effect by introducing conducting nanophase at the interface to act as phase boundaries.[23] The nanophases that formed in the thin films are believed to be the effect of the metal-induced crystallization of the dopant metals.[32] However, control over the nanophases and their transport properties are still challenging through a desirable choice of dopant and efficient method for thin film deposition. Among various methods reported earlier, including atomic layer deposition,[33] molecular beam epitaxy,[34, 35] arc-melting[36] etc., electrodeposition is one of the most versatile fabrication methods owing to its simple operation at low temperature, low cost, high deposition rate with flexibility to design a material with tunable properties.[37] Following the traditional electrodeposition process, the simultaneous co-deposition greatly influence on their structure and composition of metallic alloys. So far two kind of co-deposition mechanism has been observed such as normal and anomalous to form the metallic alloys.[38]

The electrical and thermal properties of Bi_2Te_3 thin films mainly depend on their compositions and stoichiometry. Alternatively, these fundamental thermoelectric features can be tuned by adding different amount of extra atoms in the Bi_2Te_3 crystal structure. The extra atoms play a key role and should be co-deposited stably with Bi and Te to control their composition and crystallinity; therefore, it is important to select the appropriate element. Because of its small electrode potential difference (30 – 50 mV) from Bi, Cu atom can be co-deposit over a wide range of potential/current density without depolarization effect [Abner Brenner, Thesis]. [39, 40] Until now, the effect of Cu doping in the $\text{Bi}_2\text{Te}_3/\text{Bi}_2\text{Se}_3$ have been reported by different groups including Cu-intercalation, Cu-electro-deposition etc., and showed enhancement in the thermoelectric properties.[32, 40-45] Recently, Chen et al. have found that the formation of Cu clusters is due to migration from quintuple layers with ageing.[46] Matthew R. Burton et al showed extremely high thermoelectric performance ($S = -390\mu\text{VK}^{-1}$) in electrochemically copper-doped bismuth tellurium selenide thin films.[47] The general hypothesis accepted for the Cu place in the Bi_2Te_3 is being the replacement of Bi position. In reality, there are unusual

structural changes also been caused by Cu addition in Bi_2Te_3 such as crystal symmetry disorder, phase transformation, change in microstructure, and elemental composition. However, the qualitative structural analysis of Cu occupation in the layered structure is not yet reported, in particularly for thin films. Meanwhile, few amorphous metallic alloys based thermoelectric materials have also been reported in the literature [48-50] and recently Cu ion liquid-like thermoelectrics have received considerable attention. [51] However, most of these reported materials are bulk powder-sintered materials that possess better thermoelectric performance at high temperatures ($zT = 1.5 @ 1000\text{ }^\circ\text{C}$). [52] Thereby, a truly high-performance material working at near room temperature and can be fabricated using silicon-fab compatible techniques for volume production is remain unexplored.

In this work, we have evaluated the room temperature phase transformation and microstructural changes of CuBiTe films with Cu addition by simultaneous electrocodeposition technique. The detailed structural changes and the thermoelectric properties of CuBiTe films are systematically investigated for different Cu concentration. In the light of the structural and the thermoelectric data, we evaluate the possible occupation of Cu in the CuBiTe ternary alloy thin films. Finally, we propose electrochemically deposited CuBiTe ternary alloy with embedded Bi_2Te_3 nanocrystals as a potential thermoelectric material with the highest power factor of $3.02\text{ mW m}^{-1}\text{K}^{-2}$ for room temperature applications.

5.3 Experimental

5.3.1 Electrodeposition of CuBiTe

The electrodeposition mechanism of the CuBiTe is investigated using cyclic voltammetry (CV). The CV experiments are conducted in a conventional three-electrode cell with a CHI660C potentiostat. The reference electrode is a Ag/AgCl/KCl (3M) electrode, the counter electrode is a pure graphite plate electrode, with Si/SiO_2 ($\sim 1\text{ }\mu\text{m}$)/ Ti/Au (10/20 nm) substrate ($32 \times 32\text{ mm}^2$) as the working electrode. The substrates are cleaned with deionized (DI) water and then dried under flowing N_2 . The electrolytes are prepared by dissolving adequate quantities of the precursors to give CuCl_2 (0 mM, 0.5 mM, 1 mM, 1.5 mM, 2 mM and 4 mM), $\text{Bi}(\text{NO}_3)_3$ (2 mM), TeO_2 (4 mM), HNO_3 (1 M) and NH_4Cl (0.5 M) as a stabilizing agent. The cyclic voltammograms are carried out at a sweep rate of 10 mV s^{-1} , with the potential scanned first in the negative (cathodic) direction. All the films are electrodeposited at a constant potential of -0.050 V for 2 h at

the room temperature. After electrodeposition, the substrate is removed from the electrolyte and rinsed with DI water and dried under flowing N₂.

5.3.2 Material Characterization

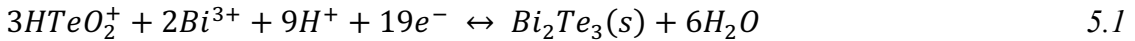
The phase structure in CuBiTe thin films is characterized using X-ray diffraction technique (XRD Philips PW3710-MPD diffractometer) with the CuK_α radiation ($\lambda=1.54$ Å). The sample morphologies are examined by a field emission scanning electron microscope (FEI QUANTA 650 HRSEM) with an attached energy dispersive X-ray spectrometer (EDX Oxford Instruments INCA energy system). For the TEM analysis, a thin film lamella of 600 nm width and 40-50 nm thickness is cut using a focused ion beam (FIB) and fixed on the Mo grid. The microstructure analysis is performed on a transmission electron microscope (JEOL HRTEM-2100) at 200 kV. The Raman spectra are recorded using the Horiba LabRAM HR Evolution Raman Spectrometer Via confocal Raman Microscope at 632.8 nm excitation. The surface and depth profiles of X-ray photoelectron spectra (XPS) are measured using a Kratos Ultra DLD spectrometer with the Al K_α radiation (1486.6 eV). The carbon 1s peak is used as a reference to calibrate the binding energies of the other core level spectra. The electrical resistivity of the samples is measured by a DC-current four-point probe method using Jandel RM-3000, while the Seebeck coefficient is determined using a laboratory-built system from the slope of the thermo-voltage versus the temperature gradient. Further information on the Seebeck coefficient measurements are given in Supplementary Information (SI). The in-plane electrical conductivity, the carrier concentration (n) and the Hall mobility (μ_H) are measured at room temperature using four-probe van der Pauw geometry using 10×10 mm² samples. For Hall measurements, 1.7 T AC magnetic field is applied using a Lake Shore's fully integrated Hall measurements systems (HMS) (LakeShore 8400).

5.4 Results and Discussion

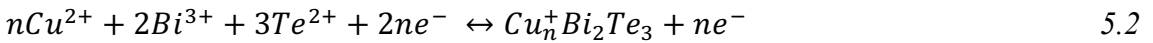
5.4.1 Cyclic voltammetry

A typical cyclic voltammogram (CV) for BiTe and CuBiTe are shown in Figure 5.1(a), which is acquired using standard Au working electrode of 1 mm radius and with a scan rate of 10 mV s⁻¹. For binary Bi-Te solution containing 2 mM Bi(NO₃)₃, 4 mM TeO₂, 1 M HNO₃ and 0.5 M NH₄Cl, the CV shows only one reduction peak at -0.045 V, which involves the co-deposition of BiTe compounds on the substrate. When the potential sweeps in the positive direction, two anodic peaks are visible between 0 to 0.2 V and at 0.340 V, which may correspond to the stripping of Bi(III) and Te(IV) from BiTe

compound. The simultaneous reduction reaction of both Bi and Te are expressed by the following chemical reaction as reported earlier:[37]



The CV of ternary Cu-Bi-Te system, which contains an appropriate quantity of $CuCl_2$ (0.5 mM, 1.5 mM and 4 mM) in addition to the fixed $Bi(NO_3)_3$ (2 mM), TeO_2 (4 mM), HNO_3 (1 M) and NH_4Cl (0.5 M) exhibit some distinct features from the binary $BiTe$. On the anodic sweeps, three peaks were visible at 0.2, 0.340, and 0.4 V and can be assigned to the oxidation of $Bi(0)$ to $Bi(III)$, $Te(0)$ to $Te(IV)$ and $Cu(0)$ to $Cu(II)$, respectively. Due to the complex electrolyte system, it is difficult to propose actual chemical reaction for the ternary $CuBiTe$ formation, and it is assumed as follows:[42]



During the negative sweep, there is considerable changes have been observed for binary and ternary alloys. In Bi-Te mixed solution, current density starts to increase from -0.030 V and then reached diffusion limiting current region at -0.045 V. For ternary system, the deposition potential shifted in the more positive direction than the binary system. As shown in Figure 5.1(a) the co-deposition of $CuBiTe$ starts at -0.016, -0.005 and -0.013 V for 0.5 mM, 1.5 mM and 4 mM $CuCl_2$ mixed solution baths respectively. This confirms that the co-deposition of Cu, Bi and Te occur around this potential as will be confirmed by EDS composition analysis in the following paragraph.

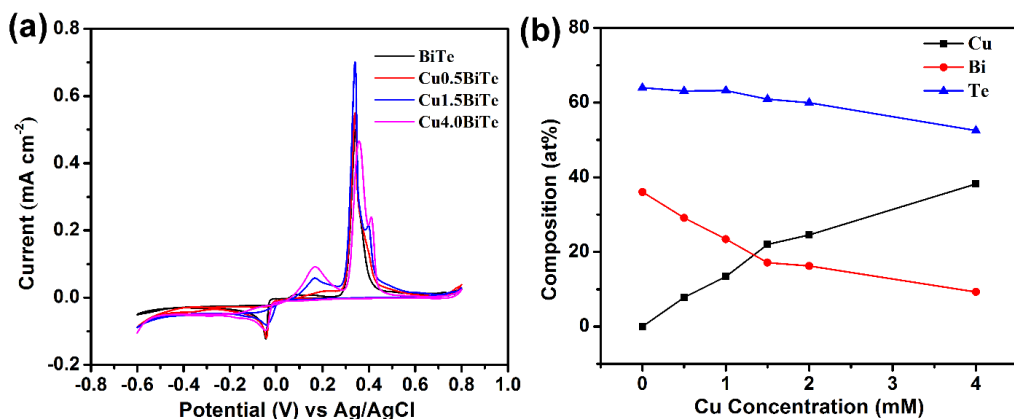


Figure 5.1: (a) Cyclic voltammograms of $BiTe$ and Cu added $BiTe$ bath measured at 10 mV s^{-1} and (b) Elemental composition of electrodeposited thin films with respect to Cu concentration in the bath solution.

Typical thickness of the binary and ternary films along with the elemental composition analysis by EDS is presented in Table 1 of the SI. The co-deposition of the elements in the ternary $CuBiTe$ system is supported by the measured atomic composition of the thin films. From Fig. 5.1(b) it can be seen that the composition of films is changing

with the addition of copper. Only small variation was observed in the 'Te' composition, implying that the inclusion of Cu plays a little role on Te content. However, after Cu1.0, there is a slight decrease in Te content. In contrast, there is a drastic change in Bi composition in the presence of Cu in the ternary system. Since the formation of CuBiTe ternary alloy produces a negative Gibbs energy thus promote the deposition of less noble metal [Cu = -0.09] at a high rate than the other components in the bath. [52] Therefore, Cu deposits much higher than the Bi and leads to high Cu:Bi ratio in the ternary alloys. It can be realized that a possible co-deposition mechanism could be anomalous, which reduce the composition of Bi in the film when increasing the Cu concentration. [38, 53, 54] Therefore deposition of Bi inhibited in the presence of Cu as observed in the EDS data analysis. However, further investigations are needed to understand the anomalous co-deposition phenomenon in the complicated ternary alloy system.

5.4.2 Morphology and Phase Analysis

Figure 5.2(a-f) shows the SEM images of electrodeposited Bi₂Te₃ and CuBiTe alloys thin films. As-deposited Bi₂Te₃ binary alloy (Fig 5.2(a)) shows the wire-like morphology with uniform distribution of bismuth and tellurium. When 0.5 mM Cu is added, the deposited film morphology changed to microscale wire-like hierarchical surface with many branches. On further increasing the Cu concentration to ≥ 1 mM, wire-like morphology disappears, and unevenly smooth film with precipitates are observed as shown in Fig. 5.2(c-f). From the TEM images, we can see the only amorphous structure without any crystalline features as depicted in Figure 5.S2(a-c). Interestingly, the HRTEM images showed in Figure 5.3(a-c) evidences the presence of nano-crystallites within the amorphous framework. The calculated d-spacing value (3.2 Å) and the corresponding plane (0 1 5) indicate the crystallites are none other than Bi₂Te₃. The observed dot spots with diffused rings in the selected area diffraction (SAED) pattern further support the presence of Bi₂Te₃ nano-crystals. Noticeably, at 4 mM of Cu there are no visible precipitates found in the TEM analysis and results in the complete reformation of amorphous CuBiTe alloy.

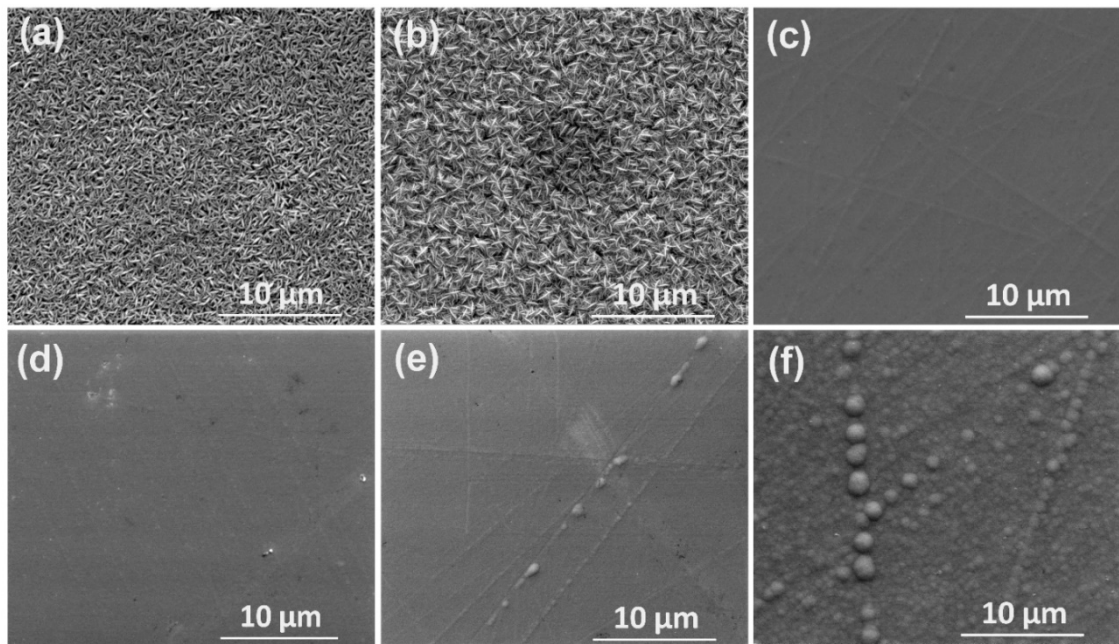


Figure 5.2: (a-f) SEM images of Bi_2Te_3 and Cu-added Bi_2Te_3 thin films (a) Bi_2Te_3 , (b) $\text{Cu}_{0.5}\text{BiTe}$, (c) $\text{Cu}_{1.0}\text{BiTe}$, (d) $\text{Cu}_{1.5}\text{BiTe}$, (e) $\text{Cu}_{2.0}\text{BiTe}$, and (f) $\text{Cu}_{4.0}\text{BiTe}$.

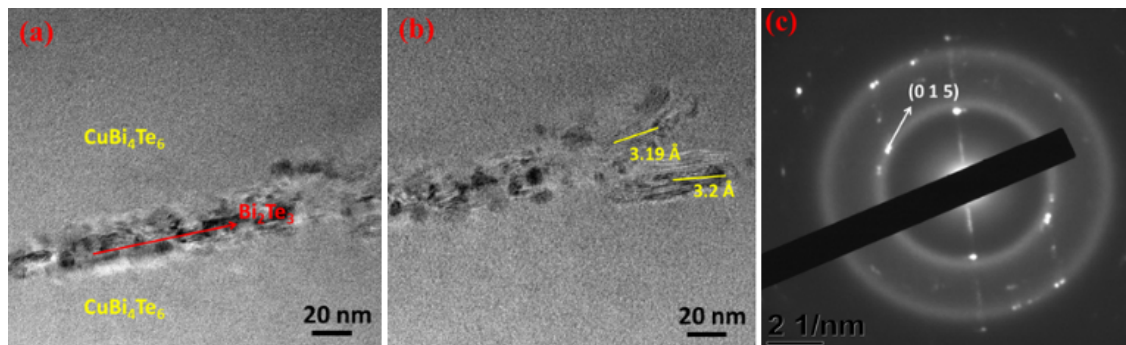


Figure 5.3: (a-c) HRTEM images of $\text{Cu}_{1.0}\text{BiTe}$ thin films and the corresponding SAED pattern.

To further study the effect of Cu inclusion, x-ray diffraction is carried out on all the samples. Figure 5.4 displays the typical XRD patterns for the as-deposited binary and ternary thin films. Diffraction peaks of (015) and (110) are found for the as-deposited Bi_2Te_3 sample, confirming film's crystallinity. With the exception of the peaks from the substrate, all the diffraction peaks can be indexed to rhombohedral Bi_2Te_3 (JCPDSfile # 01-089-2009, $a = 4.386 \text{ \AA}$, $c = 30.497 \text{ \AA}$)[55]. The crystalline Bi_2Te_3 is strongly oriented in the (110) direction and as compared to (015) direction, as shown in Fig. 5.4. The pattern exhibits different full width at half maximum of (110) and (105), indicating larger average crystallite size in (110) orientation, indicating the growth of Bi_2Te_3 with multiple branches along the main direction with hierarchical surface morphology.[56] There is no

evidence for any other phases in the XRD pattern for the binary system. However, in the ternary system, only (015) orientation is observed, while (110) peak is diminished at a lower concentration of Cu (0.5 mM), representing the degradation in the crystallinity of Bi_2Te_3 alloy thin films. When the Cu concentration is further increased to 1 mM, the material becomes completely amorphous with patterns manifesting an amorphous hump. It demonstrates a high degree of lattice distortion in the system, which lead to the crystal symmetry breakage.[57] Thus, the addition of Cu after a certain concentration range can effectively reduce the crystallinity with the emergence of amorphous state in CuBiTe alloy films. However, when the Cu concentration is high (4 mM), the phase segregation is visible with negligible intensity in the XRD pattern. All the XRD peaks indexed as (200), (106), (109) and (209) are matched to Cu_{2-x}Te phase (JCPDS # 10-0421) with a hexagonal structure.

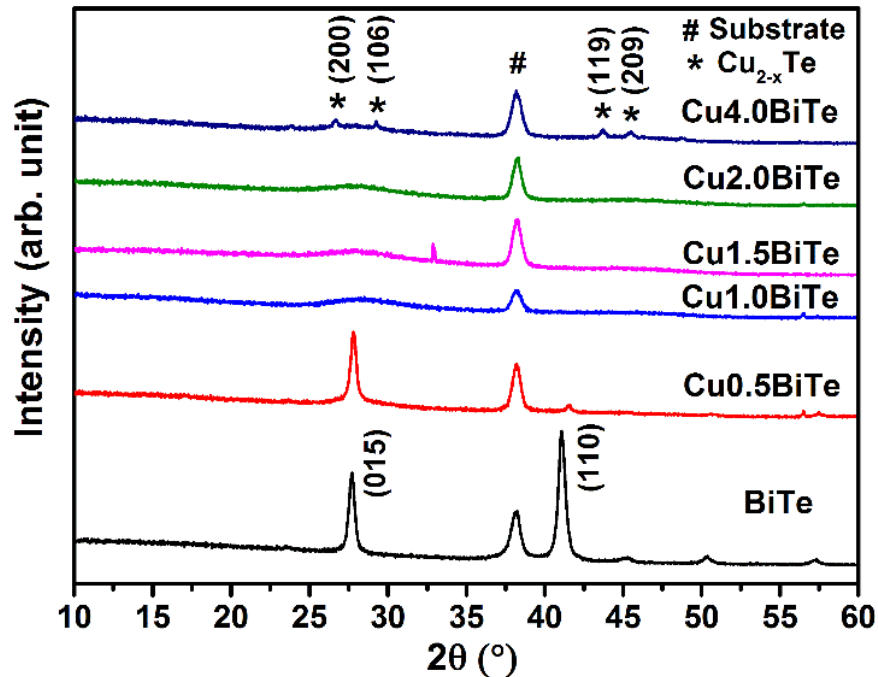


Figure 5.4: XRD patterns of as deposited Bi_2Te_3 thin films with and without addition of copper.

5.4.3 Raman Analysis

The Raman spectra of pristine Bi_2Te_3 and CuBiTe thin films are shown in Figure 5.5. The reproducibility of the Raman spectra is discussed in Figure 5.S3 in the SI. It is well established that the primitive unit cell of Bi_2Te_3 contains five atoms in accordance with the chemical formula. Generally, bulk Bi_2Te_3 has 15 dynamical modes at $q = 0$, 3 of which are acoustic modes and 12 are the optical modes. These 12 optical phonon modes are known to be 2 A_{1g} , 2 E_g , 2 E_u , and 2 A_{1u} . Among them, the A_{1g} and A_{1u} vibration modes

are along the out-of-plane direction, whereas the E_g modes are along the in-plane direction.[58] The de-convoluted Raman peaks are presented on the Figure 5.S4 in the SI. In Figure 5.5, for binary Bi_2Te_3 , the optical phonon modes at 60.2 (A_{1g}^1) and 99.8 cm^{-1} (E_g^2) can be identified. However, discrepancies are observed when compared to the bulk samples.[55] Here, E_{g1} mode (~ 40 cm^{-1}) is missing and the sample exhibits three additional bands at 89.9 cm^{-1} , 115.2 cm^{-1} and 137.2 cm^{-1} , which can be assigned to the respective E_1 , A_1 and E_2 active modes of Te rich BiTe.[58, 59] These peaks may be originated from native defects including antisite defects (Bi_{Te}), structural defects (Bi_3Te_4) and excess Te phase decomposed by Raman laser, which leads to strong Te Raman features.[60] The existence of native defects are associated with the stoichiometry of Bi atoms in Bi_2Te_3 . The addition of Cu in Bi_2Te_3 system shows similar Raman spectra as pristine Bi_2Te_3 . However, variation in the relative peak intensity when Cu is added as well as a shift in the peak positions at the highest concentration of Cu are observed, which indicates that the Cu is disturbing the Bi_2Te_3 layer structure by replacing Bi as evident from the EDX analysis. It is worth mentioning that the Raman peaks are shifted to higher wavenumber with more Cu incorporation, though it is not consistent. This may be due to the different occupation state of smaller Cu atoms in Bi_2Te_3 lattices at high concentration, where significant variation/ change in the chemical bonds can happen and ultimately results the structural disorder.[61] Noticeably, the A_{1g}^1 (60.2 cm^{-1}) and E_g^2 (99.8 cm^{-1}) active modes disappear for CuBiTe films due to the formation of ternary alloy, which may be due to the breaking of the crystal symmetry of Bi_2Te_3 through the addition of a high amount of Cu. Thereby, further crystallization of Bi_2Te_3 falls down with the increasing Cu concentration for up to 1 mM samples and showed amorphous phase in the XRD pattern. The shift (> 7 cm^{-1}) in the Raman peak for 4 mM Cu concentration sample further approve the chemical composition change from CuBiTe to the formation of Cu_{2-x}Te solid solution.

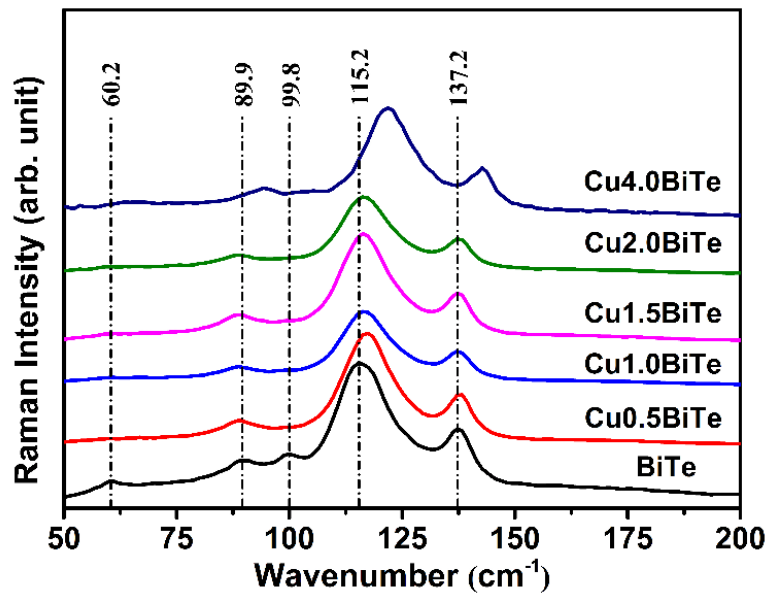


Figure 5.5: Raman spectra of pristine Bi_2Te_3 and CuBiTe thin films.

5.4.4 XPS Analysis

X-ray photoelectron spectroscopy (XPS) could provide quantitative and direct analysis on the oxidation state of the elements, stoichiometry and allow to study the electron transfer by probing the chemical shift of the electronic structure of the elements involved. Figure 5.6(a-c) shows the core level XPS signals of Bi, Te and Cu for the as-deposited pure and Cu added BiTe thin films. The survey spectrum of both binary and ternary systems shown in Figure 5.5 demonstrates that the samples are composed of bismuth, tellurium, copper and a certain amount of oxygen. The presence of O1s peak in the spectra indicates surface oxidation, which generally takes place after the sample is exposed to the atmosphere.[62] The core level $\text{Bi}4f$ XPS spectra shown in Fig.5.6(a) designates that the peaks are de-convoluted into two peaks at binding energy 158.9 eV and 164.2 eV, which corresponds to $\text{Bi}4f_{7/2}$ and $\text{Bi}4f_{5/2}$ spin-orbit splitting of Bi_2O_3 . [63] It can be clearly seen, that the peaks at 157.3 eV and 162.6 eV are from the $\text{Bi}4f$, denoting the presence of Bi in 3+ state. Moreover, the addition of Cu into BiTe matrix resulted in a decrease in the intensity of $\text{Bi}4f$ peaks (Bi_2O_3), which slightly shifted (0.2 eV) towards low energy regime. These measured shifts are quite low and within the energy resolution of the XPS instrument and thereby can be confirmed that the result of the addition of Cu does not affect the binding energies of the binary alloy at the surface.[64] However, the existence of high-intensity Bi_2O_3 peak can be resulted from the easy surface oxidation nature of binary and ternary bismuth chalcogenides upon exposing to atmosphere.[62] As a consequence, it is essential for the films to be stored under an inert atmosphere to avoid

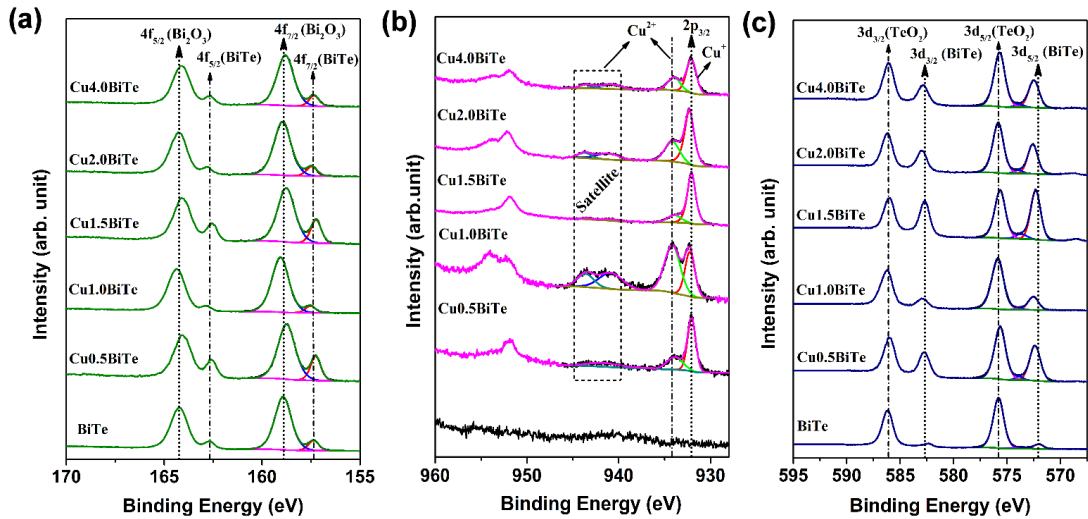


Figure 5.6: The core level XPS signals of Bi4f (a), Cu2p (b) and Te3d (c) for the as-deposited pure and Cu added BiTe thin films at film surfaces.

surface oxidation. The Cu2p XPS spectra for ternary systems are shown in Fig.5.6(b). With the 19.7 eV spin-orbit separation, two distinct peaks positioned at 932.1 eV and 951.8 eV can be assigned to $\text{Cu}2p_{3/2}$ and $\text{Cu}2p_{1/2}$ respectively.[65] Moreover, the prominent peak at 932.1 eV is related to Cu^+ intercalation or diffusion into the interstitial position of Bi_2Te_3 layered structure.[66] The peaks of Cu2p confirm the dual oxidation ($\text{Cu}^+/\text{Cu}^{2+}$) states of Cu, with a different ratio. It is very hard to distinguish the two states of Cu in the XPS spectra. The prominent way to define the characteristic Cu^{2+} state is a satellite peak and it should appear at ~940 eV.[67] In Fig.5.6(b), Cu2p spectra have the satellite peak at 940 – 943 eV regime for all the ternary alloys indicates the multi oxidation states of Cu. This may be attributed either to available 3d conduction states in the CuBiTe , which allows for the taking on of multiple oxidation states or due to atmospheric exposure triggered oxidation.[68] Worth mentioning, 1 mM Cu added Bi_2Te_3 system have the highest $\text{Cu}^+/\text{Cu}^{2+}$ ratio of 0.98, signifying that two states of Cu has been equally distributed in the alloy. Further increase in Cu concentration showed a ratio of 1.25, 1.15 and 1.1 for 1.5, 2, and 4 mM copper concentration respectively. Fig. 5.6(c) depicts the core level XPS spectra of Te3d spin-orbit splitting and exhibits strong peaks at a binding energy of 586.2 and 575.8 eV, which are in good agreement for $\text{Te}3d_{3/2}$ and $\text{Te}3d_{5/2}$ due to surface oxide layer of TeO_2 . There is two peaks at binding energy 572.0 and 582.5 eV, which can be attributed to actual $\text{Te}3d_{5/2}$ and $\text{Te}3d_{3/2}$ split related to Bi-Te layers.[63] The oxide layer was resulting from air oxidation of Bi_2Te_3 surface. The surface oxidation of this electrodeposited ternary CuBiTe was further supported with the XPS depth profile studies on 1 mM Cu concentration sample. The depth profile confirmed surface oxidation for few tens of nm and showed in Fig. 5.S6. Subsequently, the overall

XPS result confirms that the as deposited films consist of Bi_2Te_3 and CuBiTe without any detectable residual secondary phases excluding Cu_{2-x}Te solid solution at higher Cu (4 mM) concentration.

5.4.5 Thermoelectric Studies

In order to evaluate these electrodeposited bismuth telluride and copper bismuth telluride films as thermoelectric materials, their thermoelectric transport properties are investigated as a function of Cu concentration as shown in Figure 5.7. From Fig. 5.7(a), it can be seen that the room temperature electrical conductivities (σ) are in the order of 10^5 S m^{-1} for both binary and ternary alloys. For comparison, the electrical conductivity is measured using a conventional four-probe technique, which follows the same trend and in agreement with the Hall data. However, to keep the consistency, we used the electrical conductivities determined by Hall measurement for the thermoelectric analysis. While adding the Cu into Bi_2Te_3 binary system, the σ decreases from $1.2 \times 10^5 \text{ S m}^{-1}$ to $(0.2 - 0.4) \times 10^5 \text{ S m}^{-1}$ range. The high electrical conductivity for binary Bi_2Te_3 could be contributed from the desired (110) orientation and high Te content with reasonable crystallinity of the film.[69] With the addition of Cu; there is a collapse of the crystal structure (Fig. 5.2), which leads to the crystallinity loss and decreases the electrical conductivity significantly.[70] This can be further explained through the variation in the carrier density and the mobility of the system due to the addition of Cu as obtained from the Hall measurements. The carrier mobility of a semiconductor is directly related to its electrical conductivity by the relation:[14]

$$\sigma = ne\mu \quad 5.3$$

where, n is the carrier concentration (cm^{-3}), e is the charge of an electron ($1.602 \times 10^{-19} \text{ C}$) and μ is the electron mobility ($\text{cm}^2\text{V}^{-1}\text{s}^{-1}$). Figure 5.7(b) shows the change in carrier concentration (n) and the Hall mobility (μ_H) as a function of Cu concentration. The as-deposited Bi_2Te_3 film shows high p-type carrier concentration ($1.7 \times 10^{21} \text{ cm}^{-3}$) with maximum mobility of $4.38 \text{ cm}^2 \text{ V}^{-1} \text{ s}^{-1}$. Clearly, by the addition of Cu concentration into the films, a sudden fall in the mobility and carrier concentration can be observed for the film with 0.5 mM Cu. However, with further increase in the Cu concentration in the films, carrier concentration increases and a sudden increase in mobility for the sample with 1 mM Cu concentration are also observed. Upon further increase in Cu concentration, decrease in mobility is observed for the rest of the samples. It is noteworthy that the sample with 1 mM Cu concentration has optimum carrier concentration with higher

mobility values compared to other higher Cu concentrations, resulting in higher electrical conductivity ($3.99 \times 10^4 \text{ S m}^{-1}$) of the sample. When Cu amount further increases, a certain amount of Cu replaces the Bi atom and start to change the chemical composition by compensating holes, thereby density of states near Fermi level decreases. Due to the low density of states, the corresponding carrier mobility is somewhat low for higher Cu concentration samples.[71] Furthermore, the carrier type has been changed from p-type as-deposited sample to n-type for 0.5 mM Cu and their concentration decreases at low Cu content and follows the increasing trend with increasing Cu concentration. At low Cu concentration (7.77 at.% for 0.5 mM sample), the available p-type carriers are compensated by excess n-type carriers created due to Cu inclusion and showed n-type characteristics. More Cu in the BiTe system during co-deposition, act as a donor, increasing the free electron density and thereby decreasing the hole concentration, which exist in the pristine Bi_2Te_3 . [42] By the addition of Cu, there may be a shift in the Fermi level from the upper edge of the valence band to the conduction band, which leads the p to n crossover conductivity in CuBiTe at room temperature. The Fermi level can move further up and lies above the lower edge of the conduction band with increasing Cu concentration. Hence, the p-type carrier concentration reaches its minimum and n-type carrier concentration rise accordingly.

Fig. 5.7(c) displays the variation of Seebeck coefficient (S) and power factor as a function of Cu addition. As expected, Bi_2Te_3 exhibit positive S value representing p-type thermoelectric response of the material. With ~8 at.% Cu into the BiTe system; the Seebeck coefficient becomes negative suggesting that the majority carriers are electrons due to Cu plays a donor role in the CuBiTe system. The room temperature Seebeck coefficient varies accordingly with the carrier concentration as discussed above and can be related with the following Mott relationship:[72, 73]

$$S = \frac{8\pi^2 k_B^2}{3eh^2} m^* T (\pi/3n)^{2/3} \quad 5.4$$

Where S is the Seebeck coefficient, k_B is the Boltzmann's constant, e is the electronic charge, h is the Planck constant, m^* is the density of states effective mass, T is the absolute temperature and n is the carrier concentration. With low Cu content, the S value is low then rapidly increases for 1 mM Cu and then falls down for higher Cu (1.5 to 2 mM) concentrations. This observation can be related to the carrier concentration, since there is often an optimal value of charge carrier density at which the Seebeck coefficient is maximum.[73] Higher carrier concentration would result in a lower Seebeck coefficient,

which is also supported by our electrical conductivity measurements.[74] Typically, the absolute Seebeck coefficient increases abruptly from -34.9 to $-275 \mu\text{V K}^{-1}$ for 1 mM Cu, and start to decreases again -220 , -216.4 and $-133.6 \mu\text{V K}^{-1}$ for 1.5, 2.0, and 4.0 mM Cu concentration, respectively. It is worth noting that the 1.5 and 2 mM Cu concentration exhibit nearly similar Seebeck coefficient, which agrees well with their carrier concentration and electrical conductivity. This may cause a greater increase in carrier density and result in a reduction of Seebeck coefficient. The abrupt increase of Seebeck coefficient at room temperature for 1 mM Cu can be explained by the optimal value of carrier concentration, increase in local density of states near Fermi level and structural change.[58,59]

The power factor is an important thermoelectric parameter, which can be calculated using the Seebeck coefficient and electrical conductivity ($PF = S^2\sigma$).[73] Figure 5.7(c) shows the power factors for the electrodeposited Bi_2Te_3 films with different amount of Cu at room temperature. Interestingly, a maximum power factor of $3.02 \text{ mW m}^{-1}\text{K}^{-2}$ is obtained for 1 mM Cu added Bi_2Te_3 thin film owing to its good electrical conductivity of $3.99 \times 10^4 \text{ S m}^{-1}$ and a maximum Seebeck coefficient of $-275 \mu\text{V K}^{-1}$. The samples which showed similar Seebeck coefficients (-220 and $-216.42 \mu\text{V K}^{-1}$), exhibit a bit lower power factor of 1.52 and $1.47 \text{ mW m}^{-1}\text{K}^{-2}$, respectively. The estimated Seebeck and power factor values are much higher than the various electrochemically deposited thermoelectric thin films reported so far and are presented in Table 2 in the SI. Furthermore, this values are well correlated to the reported power factor of $\text{Cu}_x\text{Bi}_2\text{Te}_{2.7}\text{Se}_{0.3}$ ($PF = 3.15 \text{ mWm}^{-1}\text{K}^{-2}$) bulk sample. [75] Considerably, low power factor was obtained when compared to the result ($5.3 \text{ mWm}^{-1}\text{K}^{-2}$) reported for $\text{Cu}_x\text{Bi}_2(\text{Te}_{0.9}\text{Se}_{0.1})_3$ and may be due to the limited donor contribution from the Cu induced amorphous framework.[44, 76] This indicates that the addition of Cu greatly tunes the power factor and 1 mM Cu sample could be a better choice for further improvement of power factor and ultimately, the figure of merit (zT).

This extraordinary power factor of our electrochemically co-deposited CuBiTe ternary alloy is due to the pronounced enhancement of its Seebeck coefficient and the nominal electrical conductivity due to the formation of ternary CuBiTe systems, which reorganize an original layered structure to a new amorphous framework. Therefore, this approach will give a new strategy to further enhance the desirable power-factor of Bi_2Te_3 thin films by reducing their crystallinity at near room temperature. However, caution should be needed for high-temperature thermoelectric applications. Further study related

to the structural stability of these materials at medium-high temperature regime is in

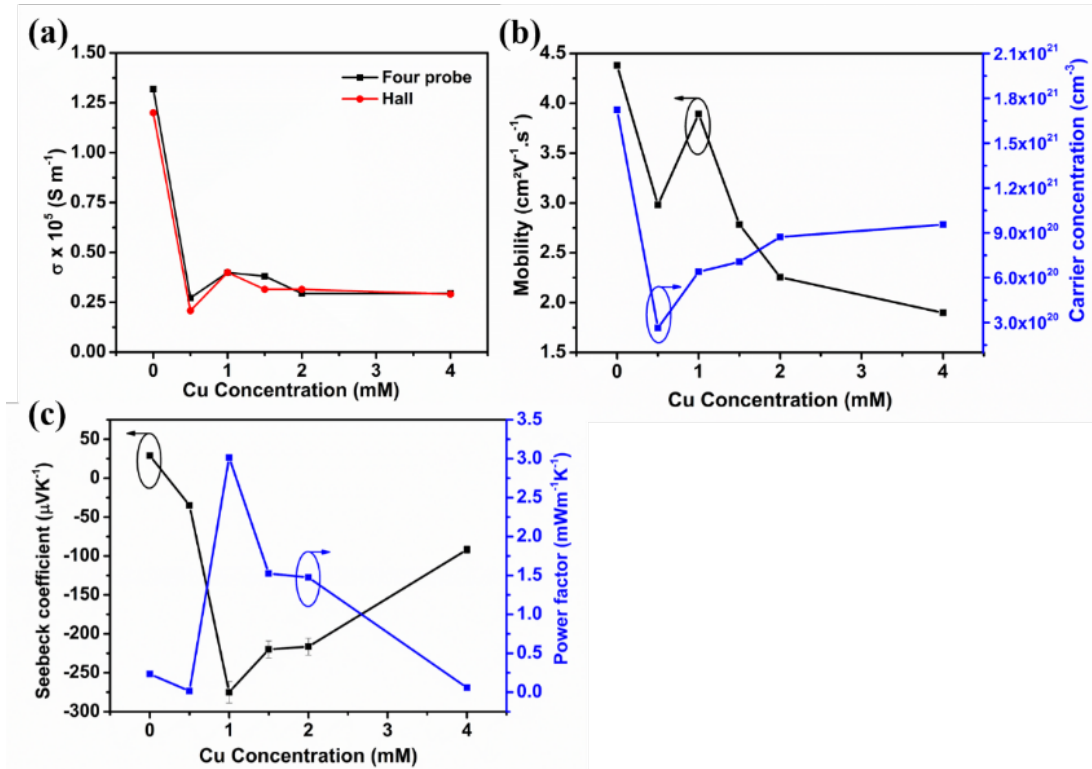


Figure 5.7: (a) Electrical conductivity of as deposited pure Bi_2Te_3 and CuBiTe at different Cu concentration measured at two conventional techniques, (b) The correlation between Hall mobility and carrier concentration of the films with respect Cu concentration and measured Seebeck and calculated power factor variation of the film with Cu content.

progress.

5.4.6 Structure Property Relation

Bi_2Te_3 doped with transition metals are well known high-performance thermoelectric materials with an enhanced figure of merit ($ZT \sim 1$) at elevated temperatures. Particularly, the addition of Cu into Bi_2Te_3 layered structure is being studied extensively in order to improve the thermoelectric properties of the system in the realm of thin films.[40, 47, 77-79] Studies showed that the Cu addition could influence the electrical conductivity, Hall coefficient and thermal power due to the dopant induced structural defects.[40, 41] However, few research focused on the structure and position of the Cu within the Bi_2Te_3 layers, there has been no studies done on electrodeposited CuBiTe materials explaining the destruction of the crystal symmetry and enhancement of thermoelectric properties. With the proposed Cu substitution at the Bi site, due to the valence of the Cu^{++} it could act as an acceptor doping. The observed negative Seebeck coefficient and n-type carriers can be correlated with the possibility of incorporation of Cu into the compound which increases the electrical conductivity to further extent. Originally, the as-deposited Bi_2Te_3 exhibits a high concentration of holes, hence it should require a high amount of Cu to

crossover the p to n-type conductivity. From the composition analysis, it is evident that >7 at. % of Cu is present in the BiTe system, which shows dominant n-type carriers for all the CuBiTe ternary alloys.

From XRD analysis, it is clearly visible that there is a strong distortion in the crystal structure for CuBiTe samples. The crystallinity of Bi₂Te₃ falls down with increased Cu concentration, where samples deposited from 1 – 2 mM Cu concentrations clearly evidences the amorphous nature. A closer study of this amorphous phase by STEM reveals Bi₂Te₃ nanocrystals embedded in the system for samples fabricated from 1 mM Cu concentration. Here, the possible mechanism for Cu addition is either 1) Cu sits in the van der Waals gap and chemical exfoliation happens during Bi₂Te₃ quintuples formation or 2) Cu replaces Bi and interacts with Te (2) layer. Both the mechanisms can distort the crystallinity of the CuBiTe ternary system and leads towards amorphization with embedded Bi₂Te₃ nanocrystals. Recently, it has been observed that the addition of an excess amount of Cu atoms into Bi₂Te₃ favours the formation of Cu clusters.[68] Since, our bath contains excess Te²⁻ and Cu²⁺ ions, it should readily form the Cu_{2-x}Te secondary phase during electrodeposition. At high Cu concentration, the emergence of the Cu_{2-x}Te phase segregation is noticeable (Fig. 5.4), which is due to the excess Cu reacts with Te to form the secondary phase within the host matrix. However, there is no direct evidence for the presence of Cu_{2-x}Te at low Cu (1 mM) concentrations. Thereby, it can be suggested that Cu_{2-x}Te does not play any major role in the observed thermoelectric transport properties. The anomalous variation in the electrical conductivity and carrier concentration may be due to the Cu ion substitution and acts as a donor impurity, thus increase the amount of carrier. As evidenced from the HRTEM, presence of few layers of crystalline Bi₂Te₃ within the amorphous framework could be a charge transport channel in the CuBiTe amorphous matrix. These nanocrystalline Bi₂Te₃ may play a key role to abruptly increase the carrier mobility at 1 mM Cu added BiTe films.[80] Additionally, this ultra-thin Bi₂Te₃ nanocrystals in the amorphous matrix may act as an energy barrier for carriers and phonon scattering center.[81] With further increase of Cu concentration, Cu_{2-x}Te secondary phase is formed, which limit the carrier mobility by the formation of new phases and thereby, low electrical transport properties are observed. Therefore, further investigation on stability and temperature-dependent thermoelectric studies are required to stabilize the materials for its application in future micro-thermoelectric devices and the work is in progress.

5.5 Conclusion

In summary, we have studied the thermoelectric characteristic performance of Cu doped BiTe thin films fabricated through electrodeposition technique. To our surprise, the crystallinity of Bi₂Te₃ binary system collapsed with the addition of >7 at.% Cu and transformed the material into amorphous. Interestingly, when the Cu-level 13 at.% in BiTe, the carrier mobility increased abruptly and delivered the highest power-factor of 3.02 mWm⁻¹K⁻². The observed superior carrier concentration, electrical conductivity and excellent power factor values, demonstrating a new strategy in emerging high-efficiency room temperature thermoelectric materials by simple electrodeposition technique that CuBiTe can be a promising n-type material for high-efficiency thermoelectric device applications. Further stabilization of the material for application over a wide temperature range could make CuBiTe a superior n-type candidate for near room temperature thermoelectric power generation applications.

5.6 References

- [1] M. Bertocco, G. Gamba, A. Sona, and S. Vitturi, "Experimental Characterization of Wireless Sensor Networks for Industrial Applications," *IEEE Transactions on Instrumentation and Measurement*, vol. 57, no. 8, pp. 1537-1546, 2008.
- [2] H. B. Lim, D. Ma, B. Wang, Z. Kalbarczyk, R. K. Iyer, and K. L. Watkin, "A Soldier Health Monitoring System for Military Applications," in *2010 International Conference on Body Sensor Networks*, 2010, pp. 246-249.
- [3] F. Mieleville, W. Du, I. Daikh, and D. Navarro, "Wireless Sensor Networks for active control noise reduction in automotive domain," in *2011 The 14th International Symposium on Wireless Personal Multimedia Communications (WPMC)*, 2011, pp. 1-5.
- [4] C. Meesookho, S. Narayanan, and C. S. Raghavendra, "Collaborative classification applications in sensor networks," in *Sensor Array and Multichannel Signal Processing Workshop Proceedings, 2002*, 2002, pp. 370-374.
- [5] A. S. Weddell, M. Magno, G. V. Merrett, D. Brunelli, B. M. Al-Hashimi, and L. Benini, "A survey of multi-source energy harvesting systems," in *2013 Design, Automation & Test in Europe Conference & Exhibition (DATE)*, 2013, pp. 905-908.
- [6] A. S. Dahiya *et al.*, "Review—Energy Autonomous Wearable Sensors for Smart Healthcare: A Review," *Journal of The Electrochemical Society*, vol. 167, no. 3, p. 037516, 2020/01/02 2020.

- [7] L. E. Bell, "Cooling, Heating, Generating Power, and Recovering Waste Heat with Thermoelectric Systems," *Science*, vol. 321, no. 5895, pp. 1457-1461, 2008.
- [8] J.-F. Li, W.-S. Liu, L.-D. Zhao, and M. Zhou, "High-performance nanostructured thermoelectric materials," *Npg Asia Materials*, Review vol. 2, p. 152, 10/01/online 2010.
- [9] S. Lal, D. Gautam, and K. M. Razeeb, "Fabrication of micro-thermoelectric devices for power generation and the thermal management of photonic devices," *Journal of Micromechanics and Microengineering*, vol. 29, no. 6, p. 065015, 2019/05/10 2019.
- [10] S. Ortega *et al.*, "Bottom-up engineering of thermoelectric nanomaterials and devices from solution-processed nanoparticle building blocks," *Chemical Society Reviews*, 10.1039/C6CS00567E vol. 46, no. 12, pp. 3510-3528, 2017.
- [11] B. C. Sales, D. Mandrus, and R. K. Williams, "Filled Skutterudite Antimonides: A New Class of Thermoelectric Materials," *Science*, vol. 272, no. 5266, p. 1325, 1996.
- [12] R. Venkatasubramanian, E. Siivola, T. Colpitts, and B. O'Quinn, "Thin-film thermoelectric devices with high room-temperature figures of merit," *Nature*, vol. 413, 2001.
- [13] L. D. Hicks and M. S. Dresselhaus, "Effect of quantum-well structures on the thermoelectric figure of merit," (in English), *Physical Review B*, Article vol. 47, no. 19, pp. 12727-12731, 1993.
- [14] H. J. Goldsmid, "The Electrical Conductivity and Thermoelectric Power of Bismuth Telluride," *Proceedings of the Physical Society*, vol. 71, no. 4, p. 633, 1958.
- [15] H. J. Goldsmid and R. W. Douglas, "The use of semiconductors in thermoelectric refrigeration," *British Journal of Applied Physics*, vol. 5, no. 11, p. 386, 1954.
- [16] S. K. Mishra, S. Satpathy, and O. Jepsen, "Electronic structure and thermoelectric properties of bismuth telluride and bismuth selenide," *Journal of Physics: Condensed Matter*, vol. 9, no. 2, p. 461, 1997.
- [17] B. Poudel *et al.*, "High-Thermoelectric Performance of Nanostructured Bismuth Antimony Telluride Bulk Alloys," *Science*, vol. 320, no. 5876, pp. 634-638, 2008.
- [18] F. J. DiSalvo, "Thermoelectric Cooling and Power Generation," *Science*, 10.1126/science.285.5428.703 vol. 285, no. 5428, p. 703, 1999.

- [19] A. Nag and V. Shubha, "Oxide Thermoelectric Materials: A Structure–Property Relationship," *Journal of Electronic Materials*, journal article vol. 43, no. 4, pp. 962-977, April 01 2014.
- [20] O. Appel and Y. Gelbstein, "A Comparison Between the Effects of Sb and Bi Doping on the Thermoelectric Properties of the $\text{Ti}_{0.3}\text{Zr}_{0.35}\text{Hf}_{0.35}\text{NiSn}$ Half-Heusler Alloy," *Journal of Electronic Materials*, vol. 43, no. 6, pp. 1976-1982, 2014/06/01 2014.
- [21] S. Lal, D. Gautam, and K. M. Razeeb, "Optimization of annealing conditions to enhance thermoelectric performance of electrodeposited p-type BiSbTe thin films," *APL Materials*, vol. 7, no. 3, p. 031102, 2019/03/01 2019.
- [22] Y. Pan and J.-F. Li, "Thermoelectric performance enhancement in n-type $\text{Bi}_2(\text{TeSe})_3$ alloys owing to nanoscale inhomogeneity combined with a spark plasma-textured microstructure," *Npg Asia Materials*, Original Article vol. 8, p. e275, 06/03/online 2016.
- [23] J. Kim, K. H. Lee, S.-D. Kim, J.-H. Lim, and N. Myung, "Simple and effective fabrication of Sb_2Te_3 films embedded with Ag_2Te nanoprecipitates for enhanced thermoelectric performance," *Journal of Materials Chemistry A*, 10.1039/C7TA09013G vol. 6, no. 2, pp. 349-356, 2018.
- [24] I. Cohen, M. Kaller, G. Komisarchik, D. Fuks, and Y. Gelbstein, "Enhancement of the thermoelectric properties of n-type PbTe by Na and Cl co-doping," *Journal of Materials Chemistry C*, 10.1039/C5TC01781E vol. 3, no. 37, pp. 9559-9564, 2015.
- [25] H. Böttner, G. Chen, and R. Venkatasubramanian, "Aspects of Thin-Film Superlattice Thermoelectric Materials, Devices, and Applications," *MRS Bulletin*, vol. 31, no. 3, pp. 211-217, 2011.
- [26] L. Hu *et al.*, "Enhancement in thermoelectric performance of bismuth telluride based alloys by multi-scale microstructural effects," *Journal of Materials Chemistry*, 10.1039/C2JM32916F vol. 22, no. 32, pp. 16484-16490, 2012.
- [27] C. V. Manzano *et al.*, "Anisotropic Effects on the Thermoelectric Properties of Highly Oriented Electrodeposited Bi_2Te_3 Films," *Scientific Reports*, Article vol. 6, p. 19129, 01/18/online 2016.
- [28] R. Zhai, L. Hu, H. Wu, Z. Xu, T.-J. Zhu, and X.-B. Zhao, "Enhancing Thermoelectric Performance of n-Type Hot Deformed Bismuth-Telluride-Based Solid Solutions by Nonstoichiometry-Mediated Intrinsic Point Defects," *ACS*

- Applied Materials & Interfaces*, vol. 9, no. 34, pp. 28577-28585, 2017/08/30 2017.
- [29] E. Hazan, N. Madar, M. Parag, V. Casian, O. Ben-Yehuda, and Y. Gelbstein, "Effective Electronic Mechanisms for Optimizing the Thermoelectric Properties of GeTe-Rich Alloys," *Advanced Electronic Materials*, vol. 1, no. 11, p. 1500228, 2015/11/01 2015.
- [30] G. M. Guttman, D. Dadon, and Y. Gelbstein, "Electronic tuning of the transport properties of off-stoichiometric $\text{Pb}_x\text{Sn}_{1-x}\text{Te}$ thermoelectric alloys by Bi_2Te_3 doping," *Journal of Applied Physics*, vol. 118, no. 6, p. 065102, 2015/08/14 2015.
- [31] Y. Zheng *et al.*, "Designing hybrid architectures for advanced thermoelectric materials," *Materials Chemistry Frontiers*, 10.1039/C7QM00306D vol. 1, no. 12, pp. 2457-2473, 2017.
- [32] A. E. Mohd Tamidi and Y. Sasajima, "The Relationship between Nanocluster Precipitation and Thermal Conductivity in Si/Ge Amorphous Multilayer Films: Effects of Cu Addition," *Journal of Nanomaterials*, vol. 2016, p. 7, 2016, Art. no. 8017814.
- [33] T. Sarnet *et al.*, "Atomic Layer Deposition and Characterization of Bi_2Te_3 Thin Films," *The Journal of Physical Chemistry A*, vol. 119, no. 11, pp. 2298-2306, 2015/03/19 2015.
- [34] J. Kampmeier, S. Borisova, L. Plucinski, M. Luysberg, G. Mussler, and D. Grützmacher, "Suppressing Twin Domains in Molecular Beam Epitaxy Grown Bi_2Te_3 Topological Insulator Thin Films," *Crystal Growth & Design*, vol. 15, no. 1, pp. 390-394, 2015/01/07 2015.
- [35] Z. Zeng *et al.*, "Molecular beam epitaxial growth of Bi_2Te_3 and Sb_2Te_3 topological insulators on GaAs (111) substrates: a potential route to fabricate topological insulator p-n junction," *AIP Advances*, vol. 3, no. 7, p. 072112, 2013.
- [36] Y. Sadia, Z. Aminov, D. Mogilyansky, and Y. Gelbstein, "Texture anisotropy of higher manganese silicide following arc-melting and hot-pressing," *Intermetallics*, vol. 68, pp. 71-77, 2016/01/01/ 2016.
- [37] W. Töllner, S. Bäbller, N. Peranio, E. Pippel, O. Eibl, and K. Nielsch, "Electrodeposition of Bi_2Te_3 -Based Thin Films and Nanowires," in *Thermoelectric Bi_2Te_3 Nanomaterials*: Wiley-VCH Verlag GmbH & Co. KGaA, 2015, pp. 11-32.
- [38] M. B. Porto, V. d. L. Bellia, T. C. d. M. Nepel, F. L. Moreira, and A. F. d. A. Neto, "The influence of anomalous codeposition on few coating alloys properties,"

- Journal of Materials Research and Technology*, vol. 8, no. 5, pp. 4547-4555, 2019/09/01/ 2019.
- [39] Y. Pengzhan, F. Hong, and C. Dongyong, "Thermoelectric Properties of Ternary Alloy $\text{Ag}_{0.405}\text{Sb}_{0.532}\text{Te}$ Prepared by Spark Plasma Sintering," *Rare Metal Materials and Engineering*, vol. 39, no. 4, pp. 570-573, 2010/04/01/ 2010.
- [40] Z.-L. Wang, T. Onda, and Z.-C. Chen, "Effect of Cu doping on microstructure and thermoelectric properties of $\text{Bi}_2\text{Te}_{2.85}\text{Se}_{0.15}$ bulk materials," *Scripta Materialia*, vol. 146, pp. 119-122, 2018/03/15/ 2018.
- [41] J. Bludská, I. Jakubec, Č. Drašar, P. Lošťák, and J. Horák, "Structural defects in Cu-doped Bi_2Te_3 single crystals," *Philosophical Magazine*, vol. 87, no. 2, pp. 325-335, 2007/01/11 2007.
- [42] J. Bludská, S. Karamazov, J. Navrátil, I. Jakubec, and J. Horák, "Copper intercalation into Bi_2Te_3 single crystals," *Solid State Ionics*, vol. 171, no. 3, pp. 251-259, 2004/07/30/ 2004.
- [43] J. L. Cui, "Thermoelectric performance of quaternary Cu–Bi–Sb–Te alloys prepared by cold pressing," *Journal of Alloys and Compounds*, vol. 415, no. 1, pp. 216-219, 2006/05/18/ 2006.
- [44] H. J. Yu *et al.*, "Effects of Cu addition on band gap energy, density of state effective mass and charge transport properties in Bi_2Te_3 composites," *RSC Advances*, 10.1039/C4RA07134D vol. 4, no. 82, pp. 43811-43814, 2014.
- [45] J. Zhang, J. Sun, Y. Li, F. Shi, and Y. Cui, "Electrochemical Control of Copper Intercalation into Nanoscale Bi_2Se_3 ," *Nano Letters*, vol. 17, no. 3, pp. 1741-1747, 2017/03/08 2017.
- [46] T. Chen *et al.*, "Topological transport and atomic tunnelling–clustering dynamics for aged Cu-doped Bi_2Te_3 crystals," *Nature Communications*, Article vol. 5, p. 5022, 09/23/online 2014.
- [47] M. R. Burton, A. J. Naylor, and I. S. Nandhakumar, "Electrochemically copper-doped bismuth tellurium selenide thin films," *Electrochemistry Communications*, vol. 97, pp. 56-59, 2018/12/01/ 2018.
- [48] Y. Zhou *et al.*, "Thermoelectric Properties of Amorphous Zr-Ni-Sn Thin Films Deposited by Magnetron Sputtering," *Journal of Electronic Materials*, vol. 44, no. 6, pp. 1957-1962, 2015/06/01 2015.
- [49] C. Ju, X. M. Cheng, and X. S. Miao, "Amorphization and amorphous stability of Bi_2Te_3 chalcogenide films," *Applied Physics Letters*, vol. 100, no. 14, p. 142114, 2012.

- [50] M. He, Y. Zhao, B. Wang, Q. Xi, J. Zhou, and Z. Liang, "3D Printing Fabrication of Amorphous Thermoelectric Materials with Ultralow Thermal Conductivity," vol. 11, no. 44, pp. 5889-5894, 2015.
- [51] H. Liu *et al.*, "Copper ion liquid-like thermoelectrics," *Nature Materials*, vol. 11, p. 422, 03/11/online 2012.
- [52] T. Ishizaki, D. Yata, and A. Fuwa, "Electrodeposition of a Copper-Tellurium Compound under Diffusion-Limiting Control," *MATERIALS TRANSACTIONS*, vol. 44, no. 8, pp. 1583-1587, 2003.
- [53] H. Wada, Y. Nishisaka, R. Ichino, and M. Okido, "Bi-Cu film deposition in aqueous solutions," *Transactions of Nonferrous Metals Society of China*, vol. 19, no. 4, pp. 791-794, 2009/08/01/ 2009.
- [54] D. Gupta, A. C. Nayak, J. Mazher, R. Sengar, K. P. Joshi, and R. K. Pandey, "In-situ atomic force microscopic study of reverse pulse plated Cu/Co-Ni-Cu films," *Journal of Materials Science*, vol. 39, no. 5, pp. 1615-1620, 2004/03/01 2004.
- [55] Y. Zhao, R. W. Hughes, Z. Su, W. Zhou, and D. H. Gregory, "One-Step Synthesis of Bismuth Telluride Nanosheets of a Few Quintuple Layers in Thickness," *Angewandte Chemie International Edition*, vol. 50, no. 44, pp. 10397-10401, 2011.
- [56] L. Cao, Y. Deng, H. Gao, Y. Wang, X. Chen, and Z. Zhu, "Towards high refrigeration capability: the controllable structure of hierarchical Bi_{0.5}Sb_{1.5}Te₃ flakes on a metal electrode," *Physical Chemistry Chemical Physics*, 10.1039/C4CP05386A vol. 17, no. 10, pp. 6809-6818, 2015.
- [57] K. M. F. Shahil, M. Z. Hossain, D. Teweldebrhan, and A. A. Balandin, "Crystal symmetry breaking in few-quintuple Bi₂Te₃ films: Applications in nanometrology of topological insulators," *Applied Physics Letters*, vol. 96, no. 15, p. 153103, 2010.
- [58] W. Richter and C. R. Becker, "A Raman and far-infrared investigation of phonons in the rhombohedral V2–VI3 compounds Bi₂Te₃, Bi₂Se₃, Sb₂Te₃ and Bi₂(Te_{1-x}Se_x)₃ (0 < x < 1), (Bi_{1-y}Sb_y)₂Te₃ (0 < y < 1)," *physica status solidi (b)*, vol. 84, no. 2, pp. 619-628, 1977.
- [59] V. Wagner, G. Dolling, B. M. Powell, and G. Landweher, "Lattice vibrations of Bi₂Te₃," *physica status solidi (b)*, vol. 85, no. 1, pp. 311-317, 1978.
- [60] J. Yuan *et al.*, "Raman Spectroscopy of Two-Dimensional Bi₂Te_xSe_{3-x} Platelets Produced by Solvothermal Method," *Materials*, vol. 8, no. 8, p. 5007, 2015.

- [61] S. Liu, N. Peng, Y. Bai, D. Ma, F. Ma, and K. Xu, "Fabrication of Cu-Doped Bi_2Te_3 Nanoplates and Their Thermoelectric Properties," *Journal of Electronic Materials*, journal article vol. 46, no. 5, pp. 2697-2704, May 01 2017.
- [62] H. Bando, K. Koizumi, Y. Oikawa, K. Daikohara, V. A. Kulbachinskii, and H. Ozaki, "The time-dependent process of oxidation of the surface of Bi_2Te_3 studied by x-ray photoelectron spectroscopy," *Journal of Physics: Condensed Matter*, vol. 12, no. 26, p. 5607, 2000.
- [63] M. Loor, G. Bendt, U. Hagemann, C. Wolper, W. Assenmacher, and S. Schulz, "Synthesis of Bi_2Te_3 and $(\text{Bi}_x\text{Sb}_{1-x})_2\text{Te}_3$ nanoparticles using the novel IL $[\text{C4mim}]_3[\text{Bi3I12}]$," *Dalton Transactions*, 10.1039/C6DT02361D vol. 45, no. 39, pp. 15326-15335, 2016.
- [64] Y. Zhao and C. Burda, "Chemical Synthesis of $\text{Bi}_{0.5}\text{Sb}_{1.5}\text{Te}_3$ Nanocrystals and Their Surface Oxidation Properties," *ACS Applied Materials & Interfaces*, vol. 1, no. 6, pp. 1259-1263, 2009/06/24 2009.
- [65] D. C. Frost, A. Ishitani, and C. A. McDowell, "X-ray photoelectron spectroscopy of copper compounds," *Molecular Physics*, vol. 24, no. 4, pp. 861-877, 1972/10/01 1972.
- [66] G. Chhatrasal, S. Raghunandan, M. Iram, K. D. Malay, and K. K. Kamal, "Exploring the doping effects of copper on thermoelectric properties of lead selenide," *Journal of Physics D: Applied Physics*, vol. 49, no. 28, p. 285104, 2016.
- [67] J. Yao *et al.*, "Thermoelectric properties of p-type CuInSe_2 chalcopyrites enhanced by introduction of manganese," *Physical Review B*, vol. 84, no. 7, p. 075203, 08/08/ 2011.
- [68] B. Leedahl *et al.*, "Bulk vs. Surface Structure of 3d Metal Impurities in Topological Insulator Bi_2Te_3 ," *Scientific Reports*, vol. 7, no. 1, p. 5758, 2017/07/18 2017.
- [69] M. Oh, S.-j. Jeon, H. Jeon, S. Hyun, and H.-j. Lee, "A Study on Sputtered Bi-Te Thermoelectric Films with Various Compositions: Microstructure Evolution and the Effects on Thermoelectric and Electrical Properties," *Journal of Electronic Materials*, journal article vol. 41, no. 1, pp. 60-66, January 01 2012.
- [70] W.-L. Wang, C. C. Wan, Y.-Y. Wang, and C.-H. Lan, "The Effect of Heat Treatment on Electrodeposited Bi_2Te_3 Thin Films for Thermoelectric Applications," *ECS Transactions*, vol. 35, no. 21, pp. 69-76, October 11, 2011 2011.

- [71] Devender *et al.*, "Harnessing Topological Band Effects in Bismuth Telluride Selenide for Large Enhancements in Thermoelectric Properties through Isovalent Doping," *Advanced Materials*, vol. 28, no. 30, pp. 6436-6441, 2016.
- [72] M. Cutler, J. F. Leavy, and R. L. Fitzpatrick, "Electronic Transport in Semimetallic Cerium Sulfide," *Physical Review*, vol. 133, no. 4A, pp. A1143-A1152, 02/17/ 1964.
- [73] G. J. Snyder and E. S. Toberer, "Complex thermoelectric materials," *Nature Materials*, Review Article vol. 7, p. 105, 02/01/online 2008.
- [74] C.-L. Chen *et al.*, "Fabrication and Characterization of Electrodeposited Bismuth Telluride Films and Nanowires," *The Journal of Physical Chemistry C*, vol. 114, no. 8, pp. 3385-3389, 2010/03/04 2010.
- [75] W.-S. Liu *et al.*, "Thermoelectric Property Studies on Cu-Doped n-type $\text{Cu}_x\text{Bi}_2\text{Te}_{2.7}\text{Se}_{0.3}$ Nanocomposites," *Advanced Energy Materials*, vol. 1, no. 4, pp. 577-587, 2011.
- [76] S. Wang, H. Li, R. Lu, G. Zheng, and X. Tang, "Metal nanoparticle decorated n-type Bi_2Te_3 -based materials with enhanced thermoelectric performances," *Nanotechnology*, vol. 24, no. 28, p. 285702, 2013/06/20 2013.
- [77] Z.-L. Wang, Y. Yokoyama, T. Onda, Y. Adachi, and Z.-C. Chen, "Improved Thermoelectric Properties of Hot-Extruded Bi-Te-Se Bulk Materials with Cu Doping and Property Predictions via Machine Learning," *Advanced Electronic Materials*, vol. 5, no. 6, p. 1900079, 2019/06/01 2019.
- [78] S. Lal, K. M. Razeeb, and D. Gautam, "Enhanced Thermoelectric Properties of Electrodeposited Cu-Doped Te Films," *ACS Applied Energy Materials*, vol. 3, no. 4, pp. 3262-3268, 2020/04/27 2020.
- [79] F. Hao *et al.*, "Roles of Cu in the Enhanced Thermoelectric Properties in $\text{Bi}_{0.5}\text{Sb}_{1.5}\text{Te}_3$," *Materials*, vol. 10, no. 3, 2017.
- [80] F. K. Aleskerov, K. S. Kakhramanov, and S. S. Kakhramanov, "Percolation effect in copper- and nickel-doped Bi_2Te_3 crystals," *Inorganic Materials*, journal article vol. 48, no. 5, pp. 456-461, May 01 2012.
- [81] E. Lee *et al.*, "Thermoelectric transport properties of cu nanoprecipitates embedded $\text{Bi}_2\text{Te}_{2.7}\text{Se}_{0.3}$," *J. Nanomaterials*, vol. 16, no. 1, pp. 115-115, 2015.

5.7 Supplementary material

The Seebeck coefficient measurements

The schematic of the Seebeck measurement setup is shown in Figure 5.S1. The Seebeck coefficient of all samples was evaluated in the in-plane configuration by establishing a temperature gradient (ΔT) along the length of the sample through commercially available Peltier modules at the two ends of the sample as shown in Figure 5.S1.

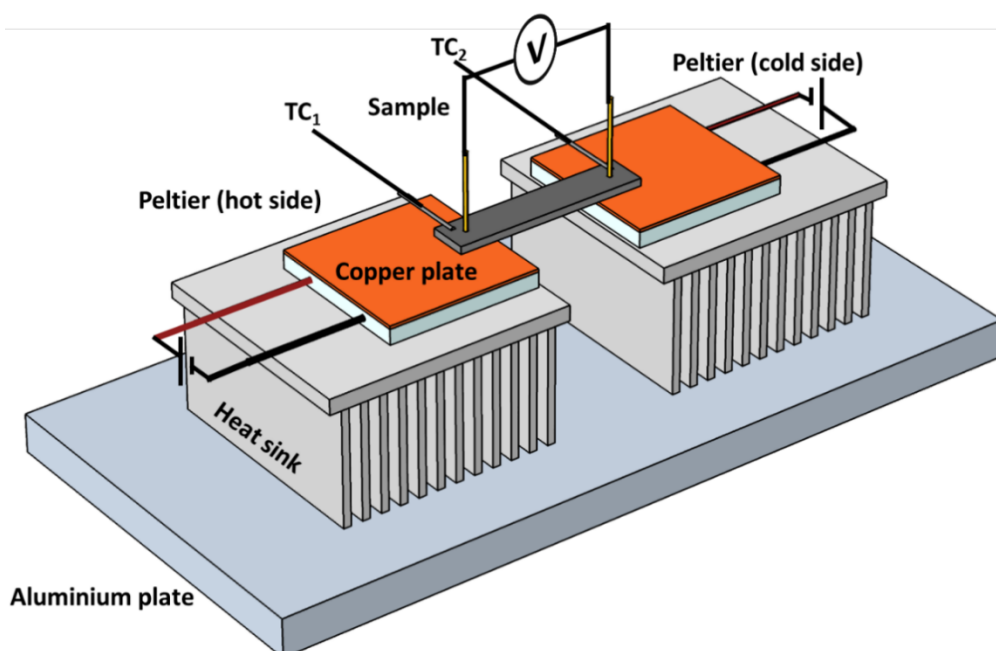


Figure 5.S1: Schematic of the Seebeck coefficient measurement system of thin films.

Two separate thermocouples (Type K) situated at the ends of the sample recorded the temperatures (TC_1 and TC_2). The thermocouples were in direct contact with the sample ensuring minimal thermal losses. The temperature gradient between both the ends was measured using a thermocouple reader. The temperature of the cold was kept at a fixed temperature for e.g. at room temperature (298 K), and a temperature gradient of 2 to 10 K was created by increasing the temperature of the Peltier module on the hot side.

The sample was placed on the Peltier module and to ensure proper thermal contact of the sample with the Peltier modules, boron nitride-based commercial thermal interface materials was used between the sample and the Peltier module. The voltage readings were taken by a spring-loaded flat and spherical ended gold microprobe ensuring a good

electrical contact with the thermoelectric film without cracking, stressing and damaging the films.

Similar setups are well known and have been reported in the literature for near room temperature Seebeck coefficient measurement of the thermoelectric materials.

The thermovoltage was measured in the range of $\Delta T \rightarrow 2-10$ K using a high impedance voltmeter. Two different runs of increasing and decreasing ΔT were performed to ensure the measurements obtained are stable and correct. In run-1 the ΔT was increased from 2 K to 10 K with an interval of 2 K for every thermovoltage measurement. The measured data were recorded only when both the temperature gradient and the thermovoltage depict stable value thereby minimizing the measurement errors. In run-2 the ΔT was decreased back from 10 K to 2 K. All the obtained thermovoltage data are plotted against ΔT . The thermovoltage dependence on the temperature gradient depicts a linear behaviour. The Seebeck coefficient is determined from the slope of the curve.

Table 1. The average film thickness and the elemental composition of the electrodeposited films.

Sample	Average Film Thickness	At% - Bi	At% - Te	At% - Cu
BiTe	1.2 μm	36.04 \pm 2	63.96 \pm 2	0
Cu0.5BiTe	1.6 μm	29.11 \pm 0.1	63.12 \pm 0.1	7.77 \pm 0.1
Cu1.0BiTe	1.85 μm	23.4 \pm 0.5	63.19 \pm 0.5	13.4 \pm 0.5
Cu1.5BiTe	1.85 μm	17.11 \pm 1	60.9 \pm 1	21.99 \pm 1
Cu2.0BiTe	1.85 μm	16.24 \pm 0.5	59.95 \pm 0.5	24.57 \pm 0.5
Cu4.0BiTe	1.6 μm	9.29 \pm 0.9	52.49 \pm 0.9	38.22 \pm 0.9

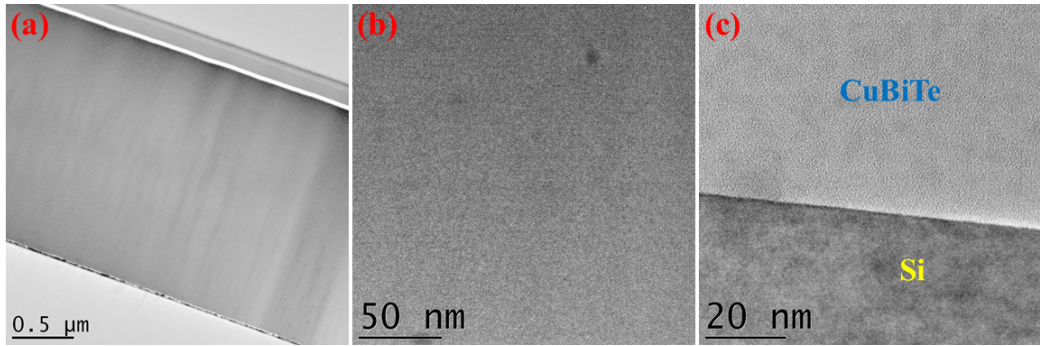


Figure 5.S2: (a-c) TEM images of Cu_{1.0}BiTe thin films at different resolutions.

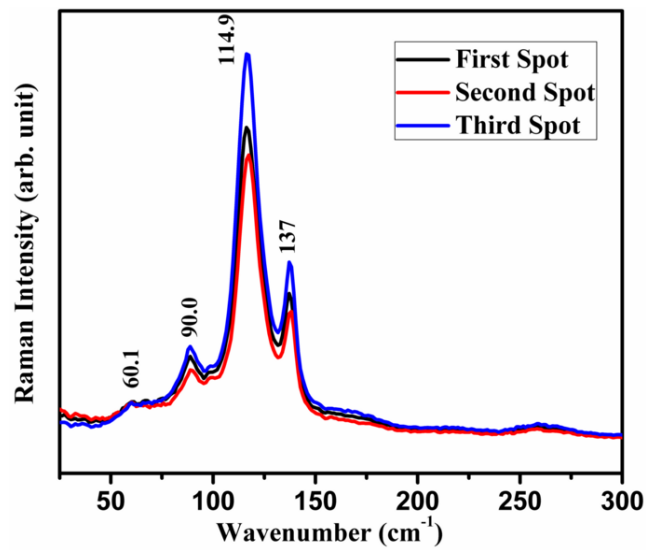


Figure 5.S3: Raman spectra of CuBiTe thin film with 1 mM Cu measured at different points on the film surface.

In order to confirm the reproducibility, the spectra were taken at three different spots on the film. We observed the difference in the intensity between different spots as shown in Fig. 5.S3. The intensity variation could result from the varying thickness of the film over the surface of the substrate.

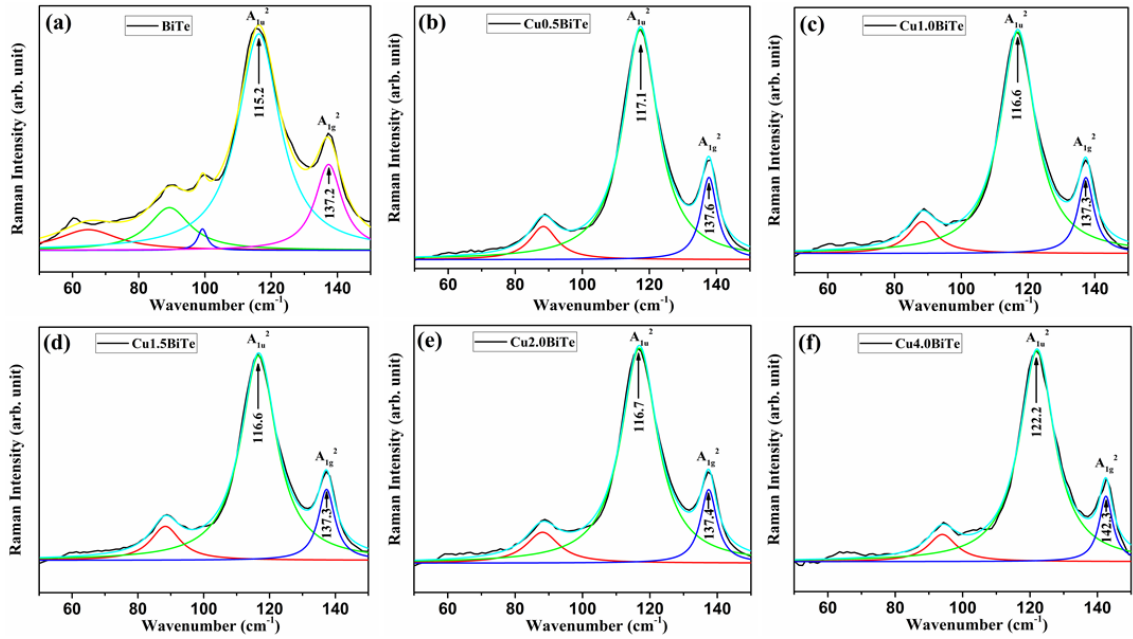


Figure 5.S4: (a-f) De-convoluted Raman A_{1u}^2 and A_{1g}^2 for both pure and Cu added Bi_2Te_3 thin films.

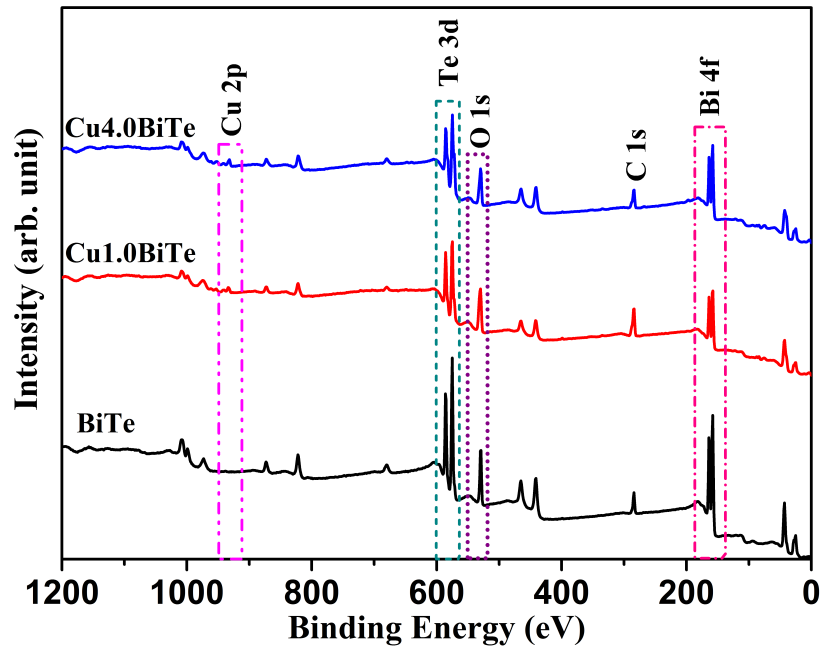


Figure 5.S5: XPS survey spectrum of pure Bi_2Te_3 and $CuBiTe_3$ with 1 mM and 4 mM Cu addition.

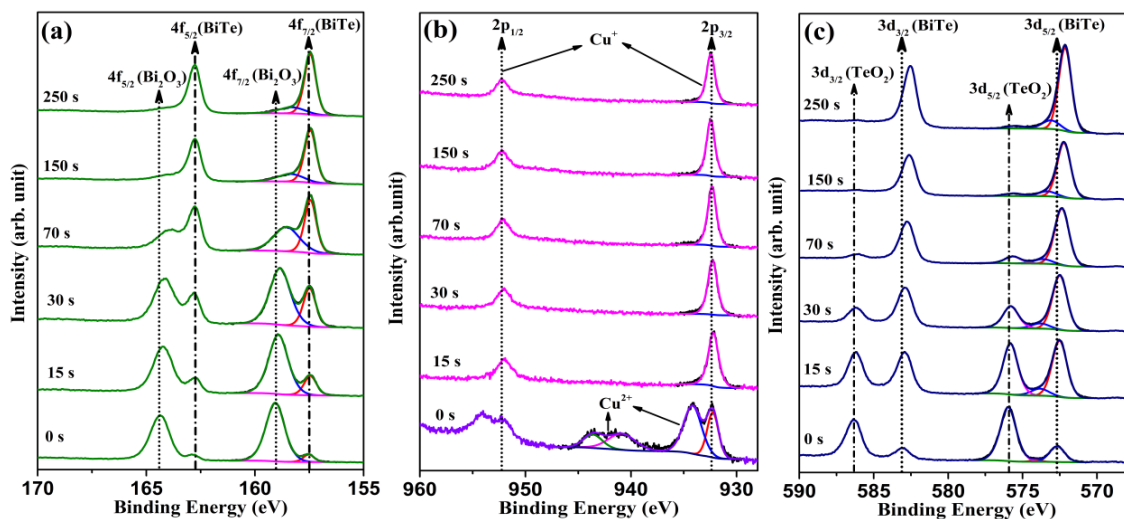


Figure 5.S6: The core level XPS signals of Bi4f (a), Cu2p (b) and Te3d (c) for Cu_{1.0}BiTe thin films at different etching time.

Chapter 6: Enhanced thermoelectric properties of electrodeposited Cu-doped Te films

Chapter based on the publication journal article:

ACS Applied Energy Materials 3(4): 3262-3268.

Swatchith Lal, Kafil M. Razeeb* and Devendraprakash Gautam*

Tyndall National Institute, University College Cork, Lee Maltings, Cork T12 R5CP, Ireland

6.1 Abstract

Bismuth telluride based alloys are the best known thermoelectric materials in the room-temperature regime. Here, we report on the enhanced thermoelectric properties of electrodeposited copper doped tellurium films as n-type thermoelectric material for near room temperature applications. With increase of the copper content in the films, we observe an enhancement of the thermoelectric properties. Thereby, we investigate the role of copper in modifying the crystal structure, which leads to the amorphous nature of the films and the corresponding enhancement in the thermoelectric properties. The electrodeposited copper doped tellurium films exhibit a high Seebeck coefficient of $-227 \mu\text{V}/\text{K}$, resulting to a power factor of $5.6 \text{ mW}/\text{mK}^2$, which is a promising power factor observed for the electrodeposited thermoelectric materials and can be a favourable n-type thermoelectric material for device applications.

6.2 Introduction

The advancement in electronics and the constant drive for miniaturization has given rise to a highly integrated system but opened-up the challenge of managing the thermal budget of these integrated systems. Simultaneously, in the era of IoT [1-4] low power consuming wireless sensor nodes (typically in range of milli to micro watts) that enables to create a more smart and responsive environment are required. Typically, batteries employed to power-up these sensor nodes fail and need to be replaced after a limited time, which adds up to the cost [3, 5]. Therefore, power generation from abundant waste heat through thermoelectric (TE) materials is receiving huge attention by researchers both in academia and industry [6, 7]. A TE device can transform thermal energy into electricity using the “Seebeck effect” and conversely to enable cooling or heating using the “Peltier effect”. Microscale TE devices have huge advantages over macroscopic devices. The apparent

advantage is the smaller size, which allows integration into compact smaller systems. Due to the use of small structures, the integration density increases, thereby significantly increasing the number of thermocouples in the device leading to high power outputs, especially for small temperature differences [8, 9]. The present state of the art micro-thermoelectric generators (μ TEG) are mainly fabricated using silicon fabrication technology and micro-electromechanical systems (MEMS) compatible techniques. These techniques are the basis of many rapidly growing technologies because they combine miniaturised sensors and actuators with electronics resulting in a substantial reduction in the device cost [10, 11].

Another challenge to address is to synthesize highly efficient thermoelectric material. Bi_2Te_3 based thermoelectric materials still dominate the room temperature applications [12-15]. However, copper-based TE materials such as copper selenide,[16] copper sulphide [17, 18] and copper telluride [19] are getting renewed attention [20] as they exhibit excellent TE efficiency. It is worth mentioning that all these copper-based TE materials are bulk materials exhibiting a p-type behaviour, and their working temperature are around $\sim 700\text{-}900\text{ K}$ [20]. So far, all Cu-based thermoelectric materials reported in the literature demonstrated high TE performance at the high-temperature regime. Here, we report the development of Cu doped Te films for thermoelectric applications near room temperature. We synthesize Cu doped Te films using electrodeposition and characterise structural and TE properties of the as-deposited materials. The role of Cu on the crystal structure of the Te film and its effect on the thermoelectric properties are discussed in detail. The excellent thermoelectric properties exhibited by Cu doped Te films can lead to a potential thermoelectric material for power generation in near room temperature applications, specifically for low differential temperature scenarios.

A great deal of work in enhancing the ZT of the material has been carried out and reported in the literature over the last decade [21-25]. The maximum power density of a thermoelectric device is closely associated with the power factor of the thermoelectric materials. Higher power factors lead to larger output power densities for a given working condition [26, 27]. Developing thermoelectric materials with high power factor is crucially important for real-time applications. Here, we also report the extraordinary power factor exhibited by Cu doped Te film for room-temperature application which is at par with the highest power factor reported for thin-film thermoelectric material developed by electrodeposition so far [28-30].

6.3 Experimental

All the depositions were performed at room temperature from an electrolyte containing 1 M nitric acid, 15 mM pure tellurium powder and 2 mM copper (II) sulphate pentahydrate. In order to prepare the solution, tellurium was first dissolved in 1 M nitric acid and heated at 40 °C while stirring. Copper (II) sulphate pentahydrate was separately dissolved in de-ionised (DI) water. Both the solutions were mixed at a later stage while stirring to form the final solution. Cyclic voltammetry (CV) was performed using a standard gold electrode with respect to Ag/AgCl reference electrode at a sweep rate of 10 mV s⁻¹. Platinised titanium mesh was used as the counter electrode. The thermoelectric films were electrodeposited on Si/SiO₂ substrate, having 20 nm of gold (Au) layer on top of 10 nm titanium (Ti) adhesion layer. All the depositions were performed for 1 hour at room temperature by applying different deposition potentials (-50 to -250 mV). The deposition area of the sample was fixed to 9 cm². All the samples were rinsed using DI water and with isopropanol and again with DI water, before drying under nitrogen jet.

Morphology of the films was observed using scanning electron microscopy (SEM) (Quanta FEG 450) and the composition was determined with the energy-dispersive X-ray spectroscopy (EDS) attached to the SEM. The crystal orientation of the electrodeposited samples was studied using X-ray diffraction system (Pan analytical X'pert pro) with Cu K_α radiation ($\alpha=1.5406 \text{ \AA}$) at a voltage of 40 kV and a current of 40 mA. The Raman spectra of the samples were recorded with the Renishaw (RA100) inVia confocal Raman microscope at 514.5 nm excitation.

The electrical transport and Hall properties were measured in the Van-der-Pauw arrangement at room temperature under a magnetic field of 1.7 T on 10×10 mm² thin film samples by using a Hall Kit (Lakeshore model 8404). The Hall measurements are of above 99% accuracy. For the Seebeck coefficient measurements; a laboratory built system was used. All the measurements were done in the in-plane orientation with different temperature gradients (ΔT), established along the ends of the samples using commercially available Peltier modules. The thermovoltage of the sample was measured over a range of ΔT values (2-10 °C), where the temperature was monitored using two separate thermocouples situated on either end of the sample. The Seebeck coefficient was determined from the slope of the thermovoltage versus the temperature gradient. The measurement error is no more than 5% for this setup. Further details on the Seebeck coefficient measurements are provided in the Supporting Information section. The presence of Au seed layer underneath the deposited film and its impact on the

thermoelectric and electrical property measurements of the film has been taken into consideration. However, telluride-based chalcogenides, such as BiTe alloys demonstrate anisotropic behaviour with respect to thermal/electrical properties [31, 32]. Hence, we think that it might be possible that the in-plane electrical resistivity is different compared to the cross-plane resistivity of the deposited material. The electrical resistivity was measured using an in-line four-point probe measurement system (Jandel RM3000), which was also used to cross-check the sheet resistance values obtained from the Hall measurements. The electrical conductivity values from both the techniques were almost the same, within an error of 4%.

6.4 Results and Discussion

6.4.1 Electrochemical Deposition

Electrolytic behaviour of different baths was investigated using CV to understand the reduction mechanism of the electrolyte with Cu and Te ions. Three separate baths were prepared, the first bath with 2 mM copper (II) sulphate pentahydrate dissolved in 200 ml DI water. The second bath consisting of 15 mM tellurium in 1 M nitric acid and the third bath with 2 mM copper (II) sulphate and 15 mM of tellurium in 1 M nitric acid. All the CV's were recorded using the standard gold electrode with respect to the Ag/AgCl reference electrode. Figure 6.1 shows the recorded CV's of the prepared baths. The CV from pure Cu bath depicts two cathodic and two anodic peaks, representing different reduction and oxidation states of Cu. One small and a broad reduction peaks are observed, with maximum current density at -40 mV and -217 mV respectively. The former peak is due to the reduction of Cu^{2+} to Cu^{1+} , and the latter is due to the reduction of Cu^{1+} to metallic Cu^0 [33-35]. The two oxidation peaks correspond to Cu^{1+} and Cu^{2+} respectively.



Dissolution of Te in the nitric acid gives rise to HTeO_2^+ ions, and the recorded CV of the bath has a single broad reduction peak with peak current at -180 mV resulting in the reduction of Te as depicted in equation (6.3) and single oxidation peak at 510 mV.



The CV recorded for the solution with 2 mM Cu and 15 mM Te in 1 M HNO_3 , revealed a single broad peak at less negative potentials, with the maximum cathodic current at -70 mV as depicted in Figure 6.1. The CV also reveals the oxidation peak at 510 mV and

an overlapping shoulder peak corresponding to the oxidation of Te and Cu respectively.

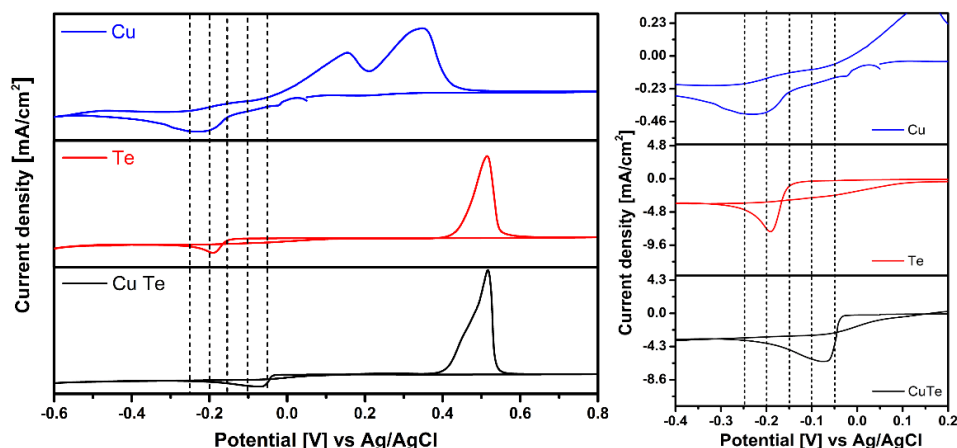


Figure 6.1: Cyclic voltammogram recorded on a standard gold working electrode in the Cu, Te, CuTe electrolyte and magnified image of reduction peaks (right).

Five different potentials were selected in order to understand the role of the deposition potential on the stoichiometry of the films. All the films were deposited at a constant potential ranging from -50 to -250 mV with an interval of -50 mV.

The elemental composition of the films deposited at different potentials is shown in Figure 6.2(a). The composition of the films varied with different deposition potentials as depicted in the figure. The film deposited at -50 mV led to maximum Cu percentage in the films of 16.06%. Moreover, with an increase in the deposition potentials, Cu content tends to decrease to 6.45% for the films deposited at -150 mV. On further increasing the deposition potential (at -200 mV), Cu content increases and reaches to 11.94%. However, deposition at -250 mV resulted in a decrease in the Cu percentage as observed from EDS studies. This can be attributed to the Cu^{1+} reduction at a lower potential, leading to a higher Cu content in the films. Similarly, the reduction of Cu^{2+} ions to Cu is prominent at -200 mV, increasing the Cu reduction kinetics, thereby resulting in higher Cu content. However, Te maintains to be at significantly higher atomic percentages in the deposited films due to the higher ion concentration (15 mM) in the bath as compared to Cu with 2 mM concentration and due to higher reduction current of Te as can be observed in Figure 6.1.

Figure 6.2(b) shows the detrimental effect on the deposition rate with increase in the Cu content in the films. The films with less Cu have a higher deposition rate as compared to the films with the higher atomic percentage of Cu. This shows that the Cu content in the film hinders the kinetics of the film growth, resulting in a decrease in the deposition rates.

This can be due to the formation of higher nucleation site of Cu hindering the deposition of Te.

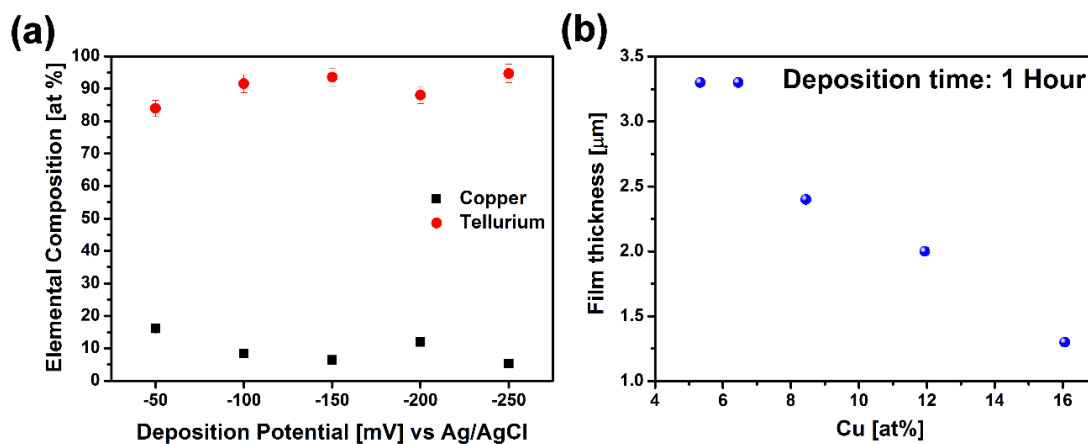


Figure 6.2: (a) Elemental composition of films at different deposition potentials and (b) The thickness of electrodeposited films with different Cu%.

6.4.2 Structural Properties

The micrographs of the films deposited at different deposition potentials were recorded as shown in Figure 6.3. From the micrographs, we can see that there is no significant microstructure, revealing smooth and dense films. The films deposited at -100 mV, -150 mV and -250 mV, which also tend to have a Cu at. % of 8.44, 6.45 and 5.33, respectively have a solid and visibly flat structure. However, there is no structure observed for the other films deposited at -50 and -200 mV that have a higher Cu content of 16.06% and 11.94% as compared to the films deposited at other potentials. This study reveals that the Cu percentage in the films has a significant impact on the microstructure. To investigate further, a through TEM analysis was performed on the sample with maximum Cu content at multiple places. TEM showed a highly amorphous structure with no crystallite features, as shown in Figure 6.3(f). The selected area diffraction (SAED) rings further confirms that the films are amorphous as can be seen in Figure 6.3(f) inset. However, very few places in the sample showcased nano-features with no specific shapes. SAED was performed on these features. As expected these features tend to be crystalline, and this is due to the presence of Cu_{2-x}Te phase, confirmed using SAED as shown in the inset of Figure 6.3(g). In order to further investigate, X-ray diffraction (XRD) patterns of the films with increasing Cu at. % are plotted as shown in Figure 6.4.

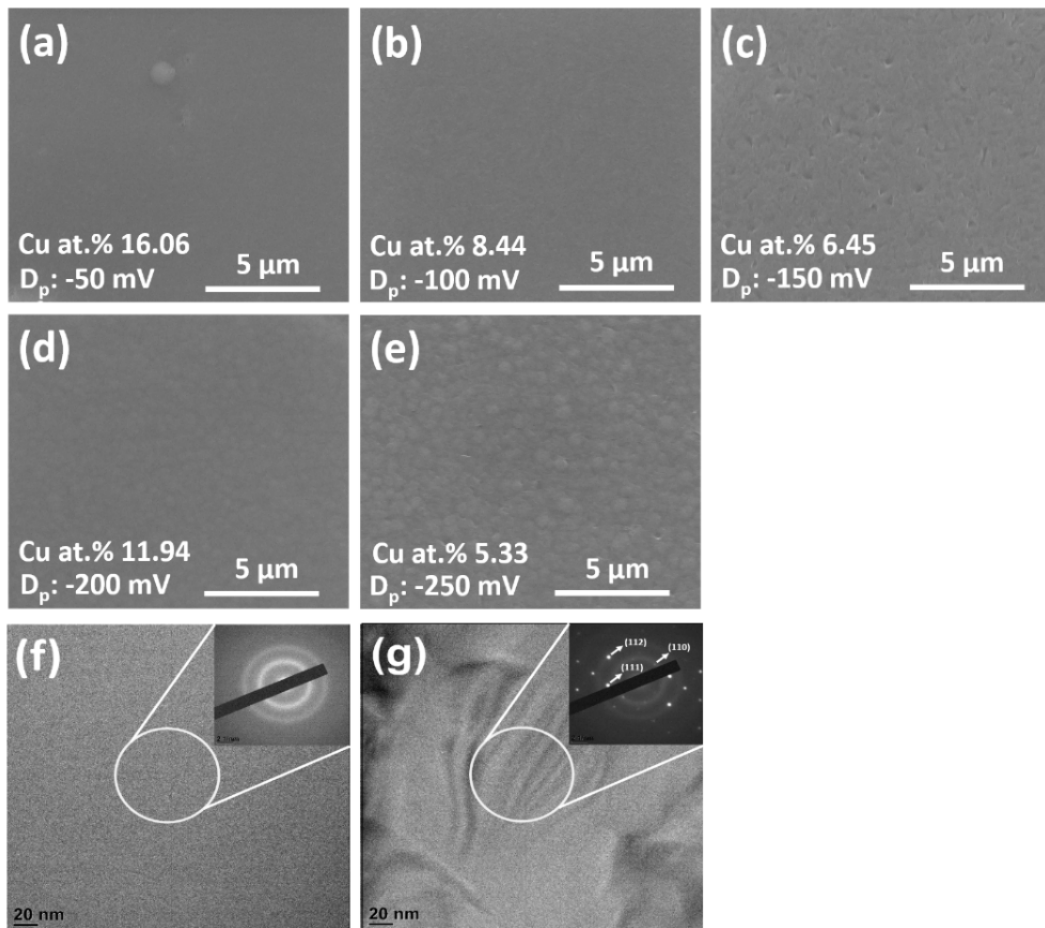


Figure 6.3: SEM and TEM micrographs of Cu doped Te films (a) -50 mV, (b) -100 mV, (c) -150 mV, (d) -200 mV, (e) -250 mV, (f) TEM image of the film deposited at -50 mV with SAED inset and (g) TEM image of the film deposited at -50 mV showing nano features along with SAED inset.

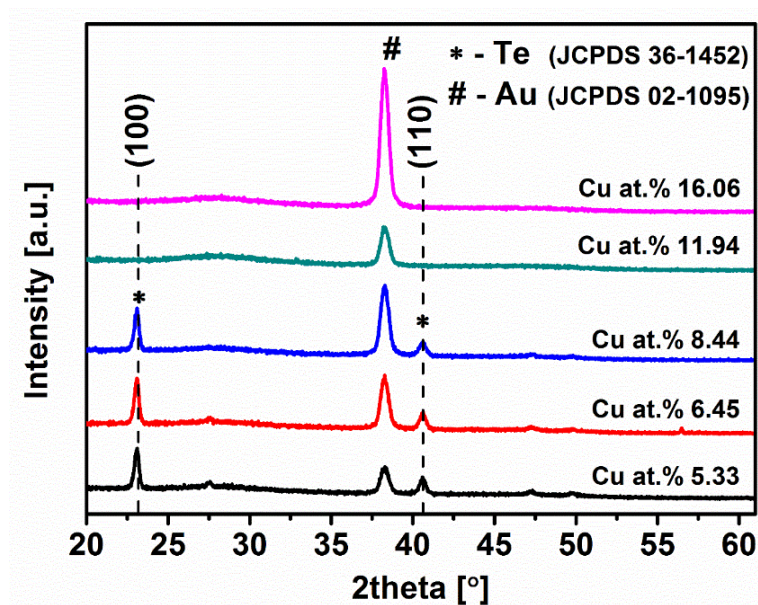


Figure 6.4: X-ray diffraction patterns of the deposited films with increasing Cu at. % in the films.

Table 6-1: Average crystallite size of the films with increasing Cu% in the films.

Copper [at. %]	Deposition potential [mV]	Average crystallite size [nm]	
		(100)	(110)
5.33	-250	26.45	20.10
6.45	-150	26.45	19.66
8.44	-100	25.65	17.01
11.94	-200	Amorphous	Amorphous
16.06	-50	Amorphous	Amorphous

Diffraction peaks of (100) and (110) are found for the films with Cu at.% < 11.94, and the observed diffraction peaks are indexed to a trigonal phase of tellurium (JCPDS 36-1452). The (100) diffraction peak located at $2\theta = 23.09^\circ$, is the prominent peak for the films with Cu at.% of 5.33%, 6.45% and 8.44%, and the peak at $2\theta = 40.60^\circ$ corresponds to the (110) crystallographic orientation. The Au diffraction peak (111) at $2\theta = 38.25^\circ$ originates due to the Au seed layer used for the electrodeposition of the films. Even though the EDS shows a substantial presence of Cu in the films, the XRD patterns show no pattern of either elemental Cu or CuTe phases. However, with an increase in the Cu percentage above 8.44% in the film, the crystal structure drastically collapsed as no diffraction peaks are observed for the films, and changing the films from crystalline to amorphous. The average crystallite size of different orientations was calculated using the Debye-Scherrer equation and shown in Table 6-1. With increase of the Cu content in the films until 8.44%, no major change in the average crystallite size is observed for the peak with (100) orientation. However, the crystallite size evaluated using (110) orientation decreased with an increase of Cu percentage in the film and finally the films became amorphous.

Raman spectra were recorded using a Renishaw (RA100) with an excitation wavelength of 514 nm at 50 \times magnification at different positions on the films. The Lorentzian function was used to fit the spectra and to obtain the peak value. The spectra were recorded at different spots of the films to ensure the reproducibility. There was no change in the peak positions with measurements done at different spots on the films, except a nominal difference in the intensities. The Raman spectra were recorded for different

concentrations of Cu in Te films as shown in Figure 6.5. Three prominent Raman peaks are observed at $\sim 92 \text{ cm}^{-1}$, $\sim 122 \text{ cm}^{-1}$ and 140 cm^{-1} . The Raman spectra for the Cu-doped Te films matches with the spectrum of Te thin films [150]. However, the spectra do not match with Cu_{2-x}Te films [151, 152], confirming no Cu_{2-x}Te phase formation and is in agreement with our XRD data. The characteristic vibrational modes of different Te films from the literature and the films deposited in the present work are tabulated in Table 6-2.

Table 6-2: Tellurium vibrational modes measured in comparison with the data published in the literature.

Sample	Vibrational modes (cm^{-1})			Reference
	E^1	A^1	E^2	
Cu doped Te film	92	121.4	139.9	This work
Te cluster	93	123	142	[37]
1-D Te	94	122	142	[39]
Te film	88	117	137	[40]
Te film	91.3	119.7	139.5	[36]

As observed from Table 6-2, the Raman shift of tellurium films grown with different techniques has a spread in the recorded data. The most intense peak is located at $\sim 122 \text{ cm}^{-1}$, which can be attributed to A^1 mode, corresponding to the chain expansion mode where each atom moves in the basal plane [39, 41]. Meanwhile, there exist two degenerate E modes, which separate into predominately bond-bending and bond-stretching types. E^1 mode at $\sim 92 \text{ cm}^{-1}$ is caused by a-axis rotation, and E^2 mode at $\sim 140 \text{ cm}^{-1}$ is attributed to asymmetric stretching mainly along the c-axis [41] as depicted in Figure 6.5. In order to study the effect of Cu addition in Te films, the shift in the Raman peaks is plotted with respect to the Cu concentration in the films (Figure 6.5(b)). With the addition of Cu, the prominent A^1 peak moves to higher Raman shift, till the Cu concentration reaches 8.44% and does not change for 11.94% Cu sample. In-between these Cu concentrations, there is a transformation from the crystalline to amorphous phase as observed from the XRD data (see Figure 6.4). Further addition of Cu in the films reduces the Raman peak shift. A similar trend is followed by all other vibration modes, as can be seen in Figure 6.5(b). This shift to a higher frequency of Raman peak positions for Cu doped samples (as compared to pure Te) shows that Cu interacts with the Te chemical bonds, which finally results in collapsing of the crystal structure. From our XRD studies, it is clear that the addition of Cu distorts the crystal structure and after a particular concentration, the

crystallinity diminishes with films getting amorphous. However, the mechanism of how Cu initiate and participate in the crystal distortion and finally collapsing the crystal structure without forming any separate phase with Te is still not clear. Nevertheless, this amorphous nature of the material has a significant impact on the thermoelectric properties as discussed in the subsequent section.

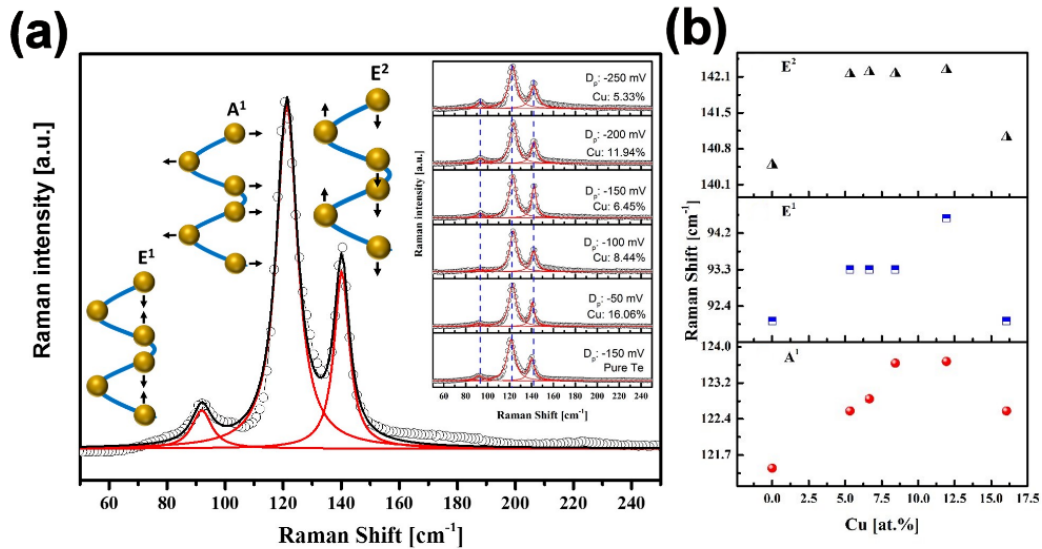


Figure 6.5: (a) Room temperature Raman scattering spectra of films without and with increasing Cu % in the films and (b) Raman spectra peak shift of A¹, E¹ and E² peaks.

6.4.3 Thermoelectric Properties

The thermoelectric properties of the electrodeposited films are investigated as a function of Cu concentration. Figure 6.6(a) shows the Seebeck coefficient and the electrical conductivities with respect to Cu at% in the films. As discussed in the previous section, Cu content in the film changes with the deposition potentials. This change in Cu content has a direct impact on the thermoelectric properties of the electrodeposited films. The Seebeck coefficient of the films decreased with increase in the Cu content in the films except for the films deposited at -50 mV, which also tend to have maximum Cu content in the films. The film with the maximum Cu content of 16.06 at.% has a Seebeck coefficient of -227 μ V/K.

The electrical conductivity of the films increased with increase of the Cu concentration in the films as shown in Figure 6.6(a). Addition of Cu enhances the electrical conductivity of the electrodeposited films with the maximum conductivity achieved by films with 16.06 at.% of Cu. In order to understand the impact of Cu content on thermoelectric properties of the films, electronic transport properties, carrier concentration and mobility were measured using a Hall probe. All the measured Hall voltages were negative in sign,

indicating electrons as the majority charge carriers and confirming the negative Seebeck coefficient. Interdependent relation between the Seebeck coefficient, the carrier densities, the mobility and the electrical conductivity can be expressed by the following equations:

$$S = \frac{8\pi^2 k_b^2}{3eh^2} \cdot m^* T \left(\frac{\pi}{3n}\right)^{\frac{2}{3}} \quad (4)$$

$$\frac{1}{\rho} = e \cdot n \cdot \mu \quad (5)$$

where n is the carrier density, k_b is the Boltzmann constant, e is the electron charge, h is the Planck constant, m^* is the charge carrier effective mass and μ is the mobility [14]. Electrical resistivity (ρ) of the film can be decreased with high carrier concentrations as well as with an increase in the carrier mobility as expressed in Eq. 5.

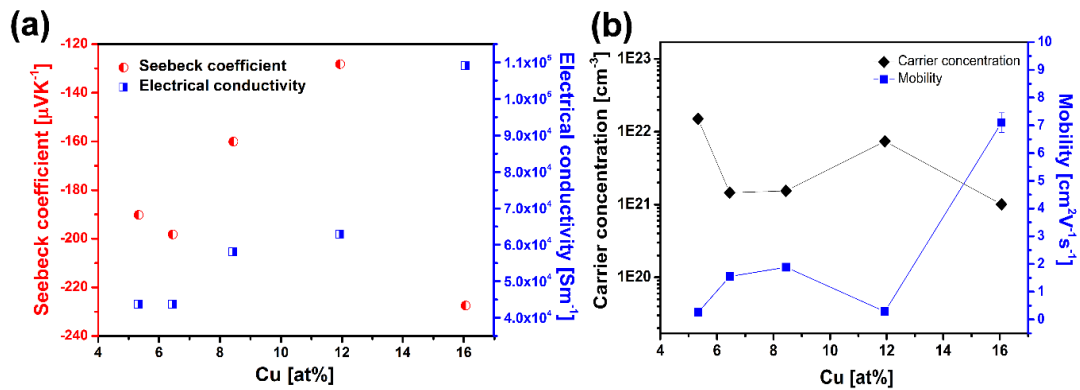


Figure 6.6: (a) Thermoelectric properties of electrodeposited Cu doped Te films with different Cu content in the films and (b) Mobility and carrier concentration as a function of Cu percentage in the films.

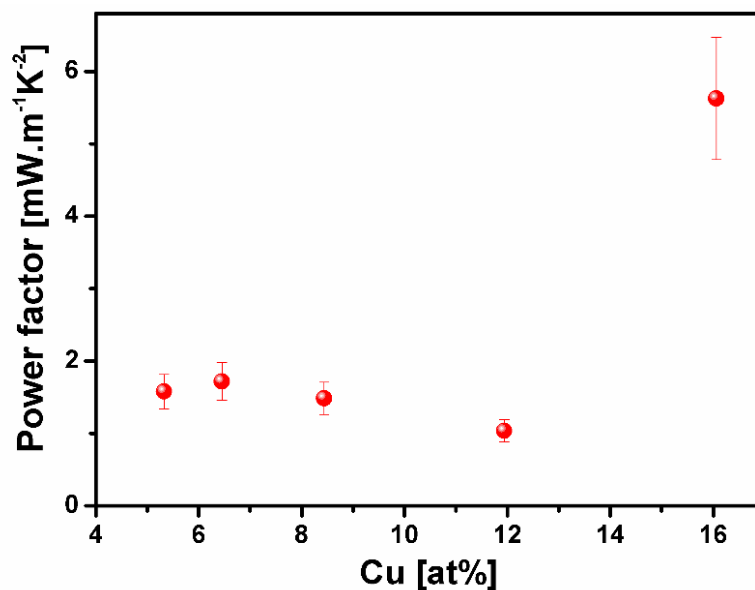


Figure 6.7: The calculated power factor of the films with different Cu% in the films.

The change in the carrier concentrations and the mobility of the films can be directly correlated with the Seebeck and electrical conductivities of the films with different Cu concentrations. Figure 6.6(b) shows carrier concentration and mobility as a function of Cu concentration in the films. The mobility of the films initially increases from 0.25 – 1.8 $\text{cm}^2\text{V}^{-1}\text{s}^{-1}$ for the films with 5.33 to 8.44% Cu. On further increase in the Cu content, at which the crystallinity of the films collapses, a sudden decrease in the mobility to 0.28 $\text{cm}^2\text{V}^{-1}\text{s}^{-1}$ can be observed for the films with 11.94% Cu content. This decrease in mobility might have a direct relation with the collapse in crystallinity of the films. However, a further increase in Cu content (16.06%) resulted in maximum mobility of 7.1 $\text{cm}^2\text{V}^{-1}\text{s}^{-1}$. The presence of nano-crystalline features in the sample with Cu content of 16.06 at. % as observed in the TEM analysis shown in the Figure 6.3(g) might be the reason for an increase in the mobility, which ultimately increased the overall electrical conductivity of the sample. On the other hand, the charge carrier concentration of the films does not show any drastic change as a function of Cu content in the films and stays within the range of 10^{21} - 10^{22} cm^{-3} . The film with maximum Cu content exhibits the lowest charge concentrations, which leads to high Seebeck coefficient values for the films.

The overall increase in the Seebeck coefficient and the electrical conductivity resulted in high power factors of Cu doped Te films at room temperature. The films with the Cu content of ~5 – 12 at. % have a power factor of ~1-1.7 mW/mK^2 and the film with a high percentage of Cu showed a maximum power factor of 5.6 mW/mK^2 as shown in Figure 6.7, which is highest power factor obtained for an electrodeposited near-room temperature thermoelectric material. In comparison with thermoelectric materials synthesized using other deposition techniques, the obtained power factor of the Cu doped Te electrodeposited films stands out not only with Bi-Te based thermoelectric materials but also with the CrN thin films which have shown promising thermoelectric performance near room-temperature recently.[30, 42] Further investigation on the temperature dependence of the thermoelectric properties of the deposited films are required to evaluate its application in future micro-thermoelectric devices for wider temperature range applications

6.5 Conclusion

Cu-doped Te films with varying Cu content were electrodeposited using different reduction potentials. Reduction of Cu, Te and CuTe were studied using cyclic voltammetry. The Cu content has a significant impact on the structure of the electrodeposited films as well as on its thermoelectric performance. Increase of the

Cu content over a certain range tends to destroy the crystallinity of the films and eventually making them amorphous. The as-deposited films show an n-type behaviour with a maximum Seebeck coefficient of $-227 \mu\text{V/K}$ resulting in a power factor of 5.6 mW/mK^2 , which is one of the most promising power factor values as compared to the reported contemporary electrodeposited room-temperature thermoelectric material.

6.6 References

- [1] L. Du, G. Shi, and J. Zhao, "Review of micro magnetic generator," *Sens Transducers*, vol. 176, pp. 1-12, 2014.
- [2] B. H. Calhoun *et al.*, "Design considerations for ultra-low energy wireless microsensor nodes," *IEEE Transactions on Computers*, vol. 54, no. 6, pp. 727-740, 2005.
- [3] M. Haras and T. Skotnicki, "Thermoelectricity for IoT – A review," *Nano Energy*, vol. 54, pp. 461-476, 2018/12/01/ 2018.
- [4] J. M. Rabaey *et al.*, "PicoRadios for wireless sensor networks: the next challenge in ultra-low power design," in *2002 IEEE International Solid-State Circuits Conference. Digest of Technical Papers (Cat. No.02CH37315)*, 2002, vol. 1, pp. 200-201 vol.1.
- [5] D. P. Arnold, "Review of Microscale Magnetic Power Generation," *IEEE Transactions on Magnetics*, vol. 43, no. 11, pp. 3940-3951, 2007.
- [6] K. V. Selvan and M. S. Mohamed Ali, "Micro-scale energy harvesting devices: Review of methodological performances in the last decade," *Renewable and Sustainable Energy Reviews*, vol. 54, pp. 1035-1047, 2016/02/01/ 2016.
- [7] A. S. Dahiya *et al.*, "Review—Energy Autonomous Wearable Sensors for Smart Healthcare: A Review," *Journal of The Electrochemical Society*, vol. 167, no. 3, January 1, 2020 2020.
- [8] J. P. Fleurial *et al.*, "Thick-film thermoelectric microdevices," in *Thermoelectrics, 1999. Eighteenth International Conference on*, 1999, pp. 294-300.
- [9] S. Lal, D. Gautam, and K. M. Razeeb, "Fabrication of micro-thermoelectric devices for power generation and the thermal management of photonic devices," *Journal of Micromechanics and Microengineering*, vol. 29, no. 6, p. 065015, 2019/05/10 2019.

- [10] G. J. Snyder, J. R. Lim, C.-K. Huang, and J.-P. Fleurial, "Thermoelectric microdevice fabricated by a MEMS-like electrochemical process," *Nat Mater*, 10.1038/nmat943 vol. 2, no. 8, pp. 528-531, 08//print 2003.
- [11] M. T. Dunham, M. T. Barako, S. LeBlanc, M. Asheghi, B. Chen, and K. E. Goodson, "Power density optimization for micro thermoelectric generators," *Energy*, vol. 93, pp. 2006-2017, 2015/12/15/ 2015.
- [12] I. T. Witting *et al.*, "The Thermoelectric Properties of Bismuth Telluride," *Advanced Electronic Materials*, vol. 5, no. 6, p. 1800904, 2019/06/01 2019.
- [13] S. Lal, D. Gautam, and K. M. Razeeb, "Optimization of annealing conditions to enhance thermoelectric performance of electrodeposited p-type BiSbTe thin films," *APL Materials*, vol. 7, no. 3, p. 031102, 2019/03/01 2019.
- [14] G. J. Snyder and E. S. Toberer, "Complex thermoelectric materials," *Nat Mater*, 10.1038/nmat2090 vol. 7, no. 2, pp. 105-114, 02//print 2008.
- [15] J. R. Sootsman, D. Y. Chung, and M. G. Kanatzidis, "New and old concepts in thermoelectric materials," *Angew Chem Int Ed Engl*, vol. 48, no. 46, pp. 8616-39, 2009.
- [16] H. Liu *et al.*, "Ultrahigh Thermoelectric Performance by Electron and Phonon Critical Scattering in $\text{Cu}_2\text{Se}_{1-x}\text{I}_x$," *Advanced Materials*, vol. 25, no. 45, pp. 6607-6612, 2013.
- [17] Z.-H. Ge, B.-P. Zhang, Y.-X. Chen, Z.-X. Yu, Y. Liu, and J.-F. Li, "Synthesis and transport property of $\text{Cu}_{1.8}\text{S}$ as a promising thermoelectric compound," *Chemical Communications*, 10.1039/C1CC16368J vol. 47, no. 47, pp. 12697-12699, 2011.
- [18] Y. He *et al.*, "High Thermoelectric Performance in Non-Toxic Earth-Abundant Copper Sulfide," *Advanced Materials*, vol. 26, no. 23, pp. 3974-3978, 2014.
- [19] Y. He, T. Zhang, X. Shi, S.-H. Wei, and L. Chen, "High thermoelectric performance in copper telluride," *Npg Asia Materials*, Original Article vol. 7, p. e210, 08/14/online 2015.
- [20] P. Qiu, X. Shi, and L. Chen, "Cu-based thermoelectric materials," *Energy Storage Materials*, vol. 3, no. Supplement C, pp. 85-97, 2016/04/01/ 2016.
- [21] G. J. Snyder and E. S. Toberer, "Complex thermoelectric materials," *Nature Mater*, vol. 7, 2008.
- [22] Y. Pei, X. Shi, A. Lalonde, H. Wang, L. Chen, and G. J. Snyder, "Convergence of electronic bands for high performance bulk thermoelectrics," (in English), *Nature*, Article vol. 473, no. 7345, pp. 66-69, 2011.

- [23] B. Hinterleitner *et al.*, "Thermoelectric performance of a metastable thin-film Heusler alloy," *Nature*, vol. 576, no. 7785, pp. 85-90, 2019/12/01 2019.
- [24] L.-D. Zhao, V. P. Dravid, and M. G. Kanatzidis, "The panoramic approach to high performance thermoelectrics," *Energy Environ. Sci.*, vol. 7, no. 1, pp. 251-268, 2014.
- [25] L. Yang, Z.-G. Chen, M. S. Dargusch, and J. Zou, "High Performance Thermoelectric Materials: Progress and Their Applications," *Advanced Energy Materials*, vol. 8, no. 6, p. 1701797, 2018/02/01 2018.
- [26] R. He, G. Schierning, and K. Nielsch, "Thermoelectric Devices: A Review of Devices, Architectures, and Contact Optimization," *Advanced Materials Technologies*, vol. 3, no. 4, p. 1700256, 2018/04/01 2018.
- [27] W. Liu, H. S. Kim, Q. Jie, and Z. Ren, "Importance of high power factor in thermoelectric materials for power generation application: A perspective," *Scripta Materialia*, vol. 111, pp. 3-9, 2016.
- [28] N. Hatsuta, D. Takemori, and M. Takashiri, "Effect of thermal annealing on the structural and thermoelectric properties of electrodeposited antimony telluride thin films," *Journal of Alloys and Compounds*, vol. 685, pp. 147-152, 11/15/ 2016.
- [29] J. Zhou *et al.*, "Transferable and flexible thermoelectric thin films based on elemental tellurium with a large power factor," *Applied Physics Letters*, vol. 112, no. 24, p. 243904, 2018/06/11 2018.
- [30] M. A. Gharavi *et al.*, "Microstructure and thermoelectric properties of CrN and CrN/Cr₂N thin films," *Journal of Physics D: Applied Physics*, vol. 51, no. 35, p. 355302, 2018/08/02 2018.
- [31] C. V. Manzano *et al.*, "Anisotropic Effects on the Thermoelectric Properties of Highly Oriented Electrodeposited Bi₍₂₎Te₍₃₎ Films," *Scientific Reports*, vol. 6, p. 19129, 01/18
- [32] X. Yan *et al.*, "Experimental Studies on Anisotropic Thermoelectric Properties and Structures of n-Type Bi₂Te_{2.7}Se_{0.3}," *Nano Letters*, vol. 10, no. 9, pp. 3373-3378, 2010/09/08 2010.
- [33] M. A. Pasquale, L. M. Gassa, and A. J. Arvia, "Copper electrodeposition from an acidic plating bath containing accelerating and inhibiting organic additives," *Electrochimica Acta*, vol. 53, no. 20, pp. 5891-5904, 2008/08/20/ 2008.
- [34] C. Gabrielli, P. Moçotéguy, H. Perrot, D. Nieto-Sanz, and A. Zdunek, "An investigation of copper interconnect deposition bath ageing by electrochemical

- impedance spectroscopy," *Journal of Applied Electrochemistry*, vol. 38, no. 4, pp. 457-468, 2008/04/01 2008.
- [35] J. Vazquez-Arenas, R. Cruz, and L. H. Mendoza-Huizar, "The role of temperature in copper electrocrystallization in ammonia–chloride solutions," *Electrochimica Acta*, vol. 52, no. 3, pp. 892-903, 2006/11/12/ 2006.
- [36] B. H. Torrie, "Raman spectrum of tellurium," *Solid State Communications*, vol. 8, no. 22, pp. 1899-1901, 1970/11/15/ 1970.
- [37] J. U. Salmón-Gamboa, A. H. Barajas-Aguilar, L. I. Ruiz-Ortega, A. M. Garay-Tapia, and S. J. Jiménez-Sandoval, "Vibrational and electrical properties of Cu_{2-x}Te films: experimental data and first principle calculations," *Scientific Reports*, vol. 8, no. 1, p. 8093, 2018/05/25 2018.
- [38] S. S. Dhasade, S. H. Han, and V. J. Fulari, "A nanostructured copper telluride thin film grown at room temperature by an electrodeposition method," *Journal of Semiconductors*, vol. 33, no. 9, p. 093002, 2012.
- [39] Y. Du *et al.*, "One-Dimensional van der Waals Material Tellurium: Raman Spectroscopy under Strain and Magneto-Transport," *Nano Letters*, vol. 17, no. 6, pp. 3965-3973, 2017/06/14 2017.
- [40] R.-F. Carlos *et al.*, "The fingerprint of Te-rich and stoichiometric Bi_2Te_3 nanowires by Raman spectroscopy," *Nanotechnology*, vol. 27, no. 7, p. 075706, 2016.
- [41] R. M. Martin, G. Lucovsky, and K. Helliwell, "Intermolecular bonding and lattice dynamics of Se and Te," *Physical Review B*, vol. 13, no. 4, pp. 1383-1395, 02/15/ 1976.
- [42] J. Yan, X. Liao, D. Yan, and Y. Chen, "Review of Micro Thermoelectric Generator," *Journal of Microelectromechanical Systems*, vol. 27, no. 1, pp. 1-18, 2018.

6.7 Supplementary material

A. The Seebeck coefficient measurements:

The schematic of the Seebeck measurement setup is shown in Figure 6.S1. The Seebeck coefficient of all samples was evaluated in the in-plane configuration by establishing a temperature gradient (ΔT) along the length of the sample through commercially available Peltier modules at the two ends of the sample as shown in Figure 6.S1.

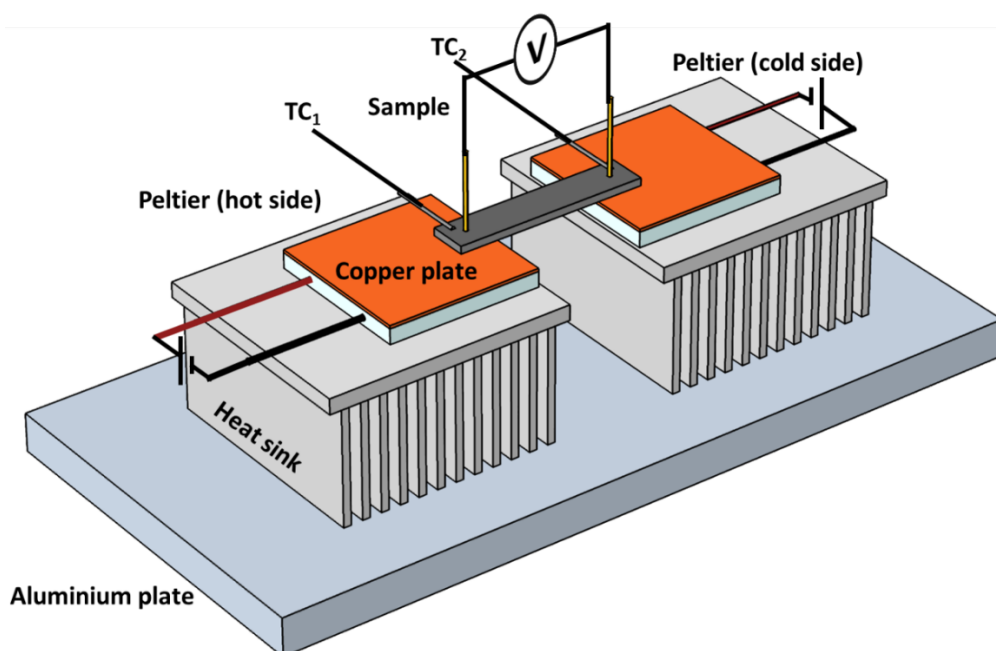


Figure 6.S1: Schematic of the Seebeck coefficient measurement system of thin films.

Two separate thermocouples (Type K) situated at the ends of the sample recorded the temperatures (TC_1 and TC_2). The thermocouples were in direct contact with the sample ensuring minimal thermal losses. The temperature gradient between both the ends was measured using a thermocouple reader. The temperature of the cold was kept at a fixed temperature for e.g. at room temperature (298 K), and a temperature gradient of 2 to 10 K was created by increasing the temperature of the Peltier module on the hot side.

The sample was placed on the Peltier module and to ensure proper thermal contact of the sample with the Peltier modules, boron nitride-based commercial thermal interface materials was used between the sample and the Peltier module. The voltage readings were taken by a spring-loaded flat and spherical ended gold microprobes ensuring a good electrical contact with the thermoelectric film without cracking, stressing and damaging the films.

Chapter 6

Similar setups are well known and have been reported in the literature for near room temperature Seebeck coefficient measurement of the thermoelectric materials¹⁻³.

The thermovoltage was measured in the range of $\Delta T \rightarrow 2-10$ K using a high impedance voltmeter. Two different runs of increasing and decreasing ΔT were performed to ensure the measurements obtained are stable and correct. In run-1 the ΔT was increased from 2 K to 10 K with an interval of 2 K for every thermovoltage measurement. The measured data were recorded only when both the temperature gradient and the thermovoltage depict stable value thereby minimizing the measurement errors. In run-2 the ΔT was decreased back from 10 K to 2 K. All the obtained thermovoltage data are plotted against ΔT . The thermovoltage dependence on the temperature gradient depicts a linear behaviour. The Seebeck coefficient is determined from the slope of the curve. The reported Seebeck coefficient in the manuscript is an average of the values calculated from run-1 and run-2.

The thermovoltage measured for samples deposited using different deposition potentials have been plotted against the ΔT . The slope of the curves corresponding to runs-1 & 2 has been calculated and shown in Figure 6.S2. The plot depicts a linear behaviour over the measured temperature gradient. The sample with the optimized Seebeck coefficient was re-measured after eight months. It exhibits the same Seebeck coefficient for the films within the measurement errors thereby indicating that the thermoelectric properties of Cu-doped Te thin films are reproducible and stable as a function of time.

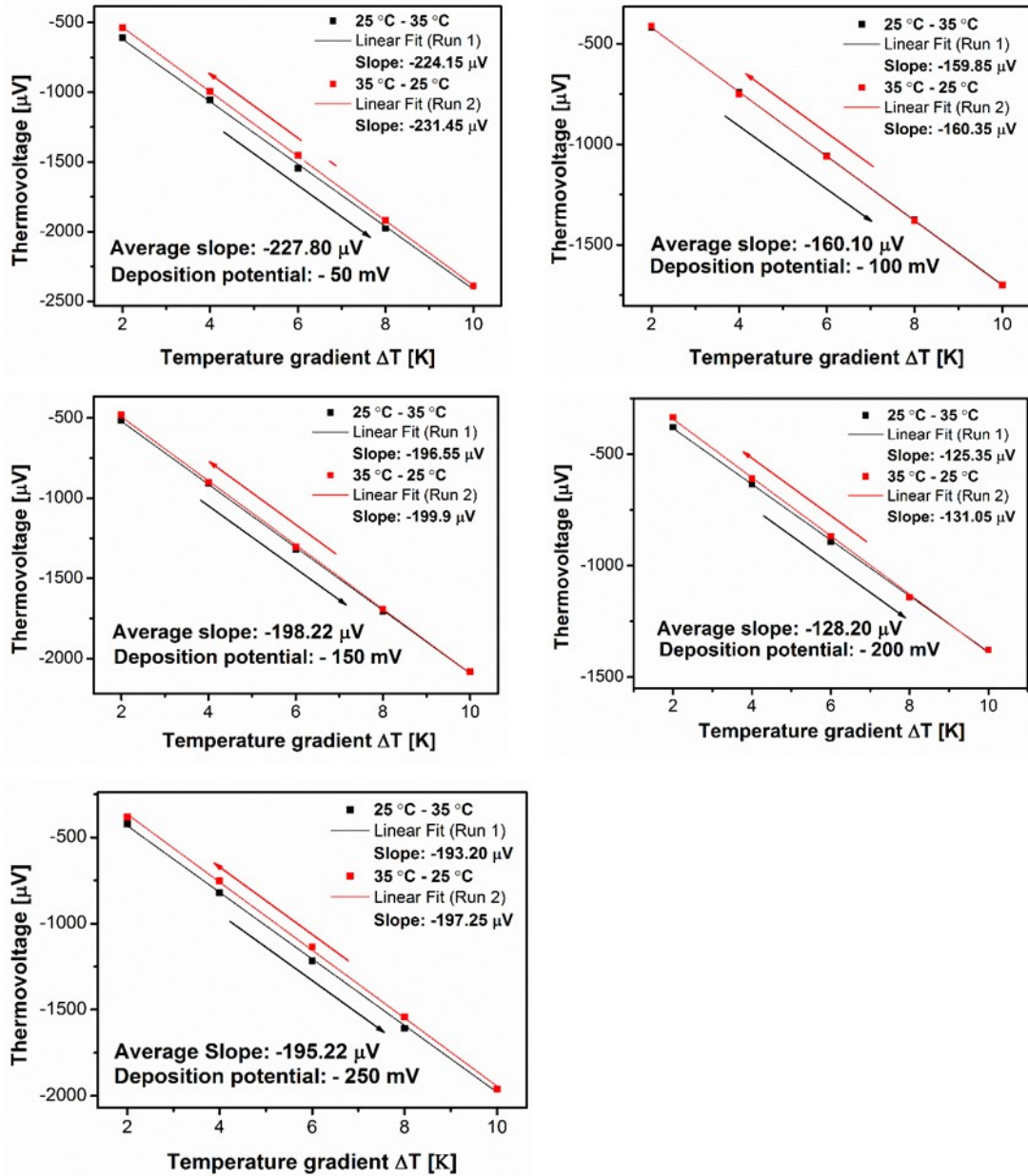


Figure 6.S2: Measured thermovoltage data as a function of the temperature gradient ΔT .
The slope of the curve corresponding to runs-1 and 2 is shown in the inset.

B. Stability of Thermoelectric Film:

Re-measured the Seebeck coefficient of our films eight months after the film deposition. The film was stored in the normal atmosphere for eight months. The behaviour of the thermovoltage against the temperature gradient is shown in Figure 6.S3. The average Seebeck coefficient for the optimized sample deposited at -50 mV deposition potential has been re-measured and the obtained value ($-236.97 \mu\text{V/K}$) is in excellent agreement with the previous value ($-227.8 \mu\text{V/K}$) within the error of the measurements indicating the stability of thin film under room temperature.

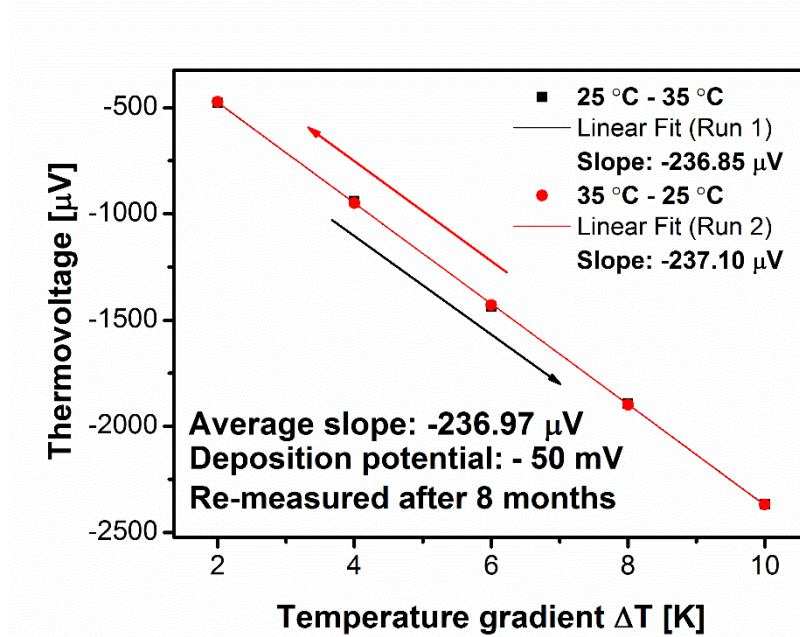


Figure 6.S3: Re-measured thermovoltage of the sample deposited at -50 mV and plotted against temperature gradient (ΔT), eight months after the deposition.

C. Roughness measurements

AFM characterization has been performed on -50 mV and -200 mV deposited samples, which exhibited the maximum and minimum power factor, respectively. The measurements were performed on the sample using contact mode at the room temperature in the ambient atmosphere. The scan area for the roughness measurements was $10 \times 10 \mu m^2$. Scans were performed on different places on the sample surface. The data were processed by using Nanoscope analysis software.

The RMS roughness, along with the sample details, is tabulated in Table 1 and the 2-d and 3-D images of the AFM measurements are shown in Figure 6.S4. This information has also been included in the supporting information document.

Table 1: Roughness measurements on the Cu doped Te electrodeposited thermoelectric films

Sample	Deposition potential	RMS roughness
Cu doped Te films	-50 mV	6.50 nm
Cu doped Te films	-200 mV	4.96 nm

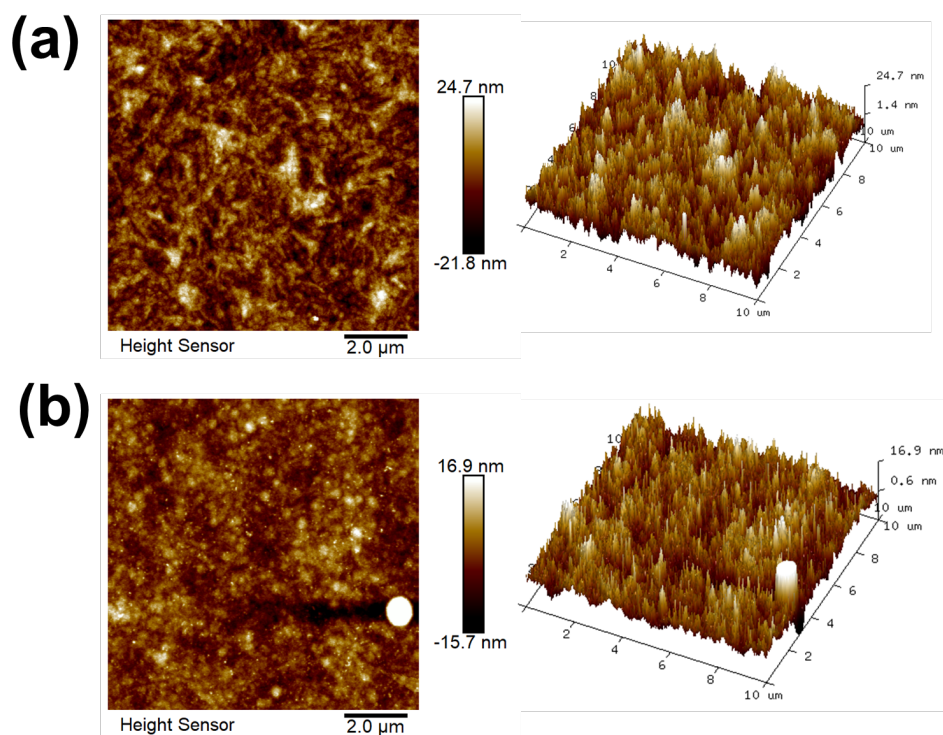


Figure 6.S4: 2-D and 3-D AFM image of Cu doped Te film deposited at (a) -50mV and (b) -200 mV deposition potential for 1-hour duration respectively.

D. Reproducibility of Cu doped Te films

Figure 6.S5 demonstrates and compares the structural and the thermoelectric properties of the old -50 mV deposited sample (which also tend to show maximum power factor) with the recently deposited film using a freshly prepared electrolytic bath. Figure 6.S5 (a) compares the cyclic voltammograms (CV) of the old and the new electrolytic baths prepared at different times. Both the electrolytic baths recorded a similar CV with the same maximum cathodic and anodic peak position. The CV's were recorded on the standard gold electrode and both the CV tend to show the similar reduction peak currents. The film was deposited at -50 mV for 1 hour. The microstructure of the deposited film is depicted in Figure 6.S5 (b) and (c). Figure 6.S5 (b) exhibits the micrograph of old Cu-doped Te films, which shows no specific microstructure. Similar microstructure features has been observed for the recent deposited thin films, as shown in Figure 6.S5 (c). The Cu at.% of both the deposited materials are given as the inset. It can be observed that the Cu at.% measured using EDS are almost the same taking into account the instrumental error. Figure 6.S5 (d) shows the XRD diffractograms of the old and the recent deposited film. Both the deposited materials exhibit single crystalline peak arising from the Au seed layer on which the materials has been electrodeposited. A hump can be observed signifying the amorphous nature of the Cu-doped Te films. It should be noted that no other peak corresponding to Cu, Te or CuTe were recorded in the diffractogram. The intensity has been normalised to compare both

the diffractograms. It can be seen from Figure 6.S5 (d), both patterns tend to superimpose each other indicating an amorphous nature of both the electrodeposited Cu-doped Te films. Finally, the thermoelectric properties were evaluated for the recently sample. Multiple samples were prepared and measured for the Seebeck coefficient and the electrical conductivity. Out of which the sample with the maximum calculated power factor and the minimum power factor have been reported in the Table as shown in Figure 6.S5 (e). The reported Seebeck coefficient and the corresponding electrical conductivity of the sample deposited at -50 mV for 1 hour in the main manuscript is $-227 \mu\text{V/K}$ and $1.09 \times 10^5 \text{ S/m}$, which constitutes to a calculated power factor of 5.62 mW/mK^2 . The electrical conductivity values of the recent prepared samples are almost the same compared to the old samples as shown in the Table S5 (e). The Seebeck coefficient of the new samples are $-223 \mu\text{V/K}$ and $-235 \mu\text{V/K}$, which individually constitutes a calculated power factor of 5.32 mW/mK^2 and 5.88 mW/mK^2 , respectively. The reported power factor of the old sample falls in between these values and within the error of the measurement of the individual parameters.

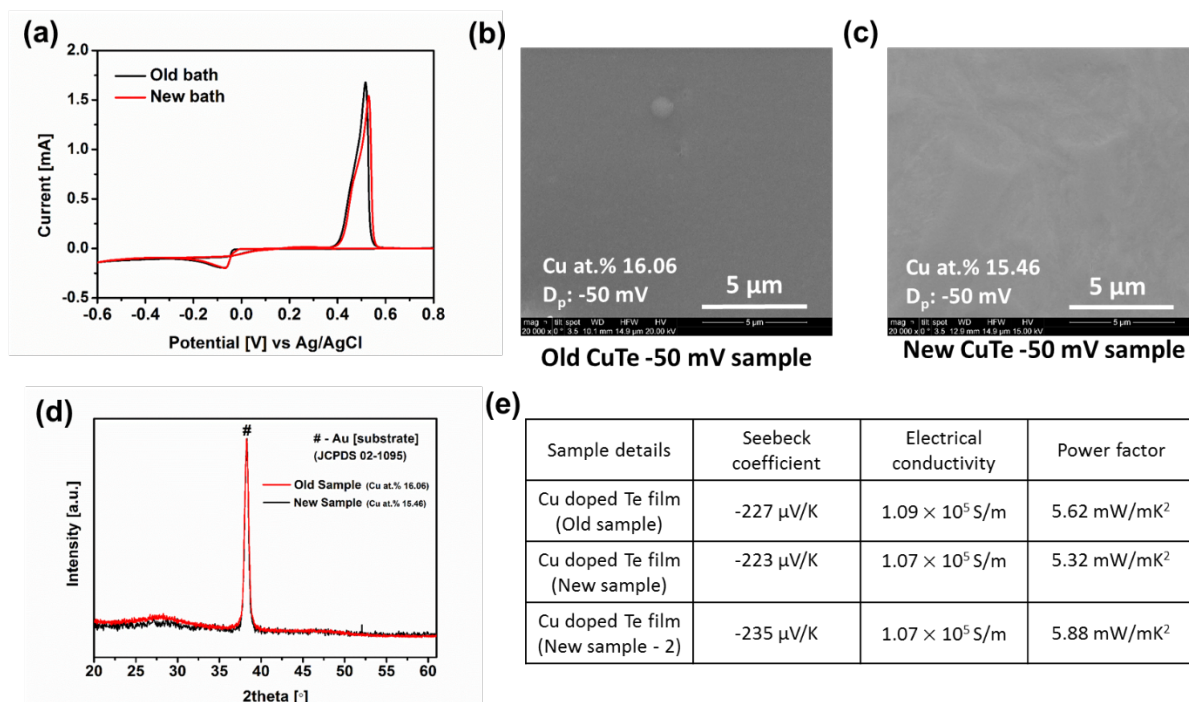


Figure 6.S5: (a) Cyclic voltammogram of old and the new electrolytic baths prepared and scanned at 10 mV s^{-1} (b) SEM image of old sample deposited at -50 mV for 1-hour duration along with its Cu at. %, (c) SEM image of new sample deposited at -50 mV for 1-hour duration along with its Cu at. %, (d) XRD diffractograms of old and new -50 mV deposited samples and (e) comparison of the Seebeck coefficient, electrical conductivity along with the calculated power factor of old and the new deposited films.

References:

1. Borup, K. A.; de Boor, J.; Wang, H.; Drymiotis, F.; Gascoin, F.; Shi, X.; Chen, L.; Fedorov, M. I.; Müller, E.; Iversen, B. B.; Snyder, G. J., Measuring thermoelectric transport properties of materials. *Energy & Environmental Science* **2015**, 8 (2), 423-435.
2. Loureiro, J.; Neves, N.; Barros, R.; Mateus, T.; Santos, R.; Filonovich, S.; Reparaz, S.; Sotomayor-Torres, C. M.; Wyczisk, F.; Divay, L.; Martins, R.; Ferreira, I., Transparent aluminium zinc oxide thin films with enhanced thermoelectric properties. *Journal of Materials Chemistry A* **2014**, 2 (18), 6649-6655.
3. Iwanaga, S.; Toberer, E. S.; LaLonde, A.; Snyder, G. J., A high temperature apparatus for measurement of the Seebeck coefficient. *Review of Scientific Instruments* **2011**, 82 (6), 063905.

Chapter 7: Fabrication of micro-thermoelectric devices for power generation and the thermal management of photonic devices

Chapter based on the publication journal article:

Journal of Micromechanics and Microengineering 29 (6), 065015 (2019)

Swatchith Lal, Devendraprakash Gautam and Kafil M. Razeeb

Tyndall National Institute, University College Cork, Lee Maltings, Cork T12 R5CP,
Ireland

7.1 Abstract

This work demonstrates and discusses the fabrication of cross-plane configured micro thermoelectric devices for the power generation and thermal management of the photonic devices. The device is fabricated using a cost-effective electrodeposition technique on the silicon wafer with 210 pairs of the electrodeposited p-type BiTe and n-type CuTe pillars. The complete device is fabricated using the flip-chip bonding technique. Our focus in this work is on the challenges in the device fabrication and the solutions employed to overcome the obstacles thereby successfully fabricating the micro thermoelectric device.

7.2 Introduction

Thermal management of optoelectronics devices is challenging as the device miniaturization generate high heat flux, which makes it difficult to manage the optoelectronic chip within a desired temperature range [1, 2]. One of the solutions to efficiently manage the thermal load of the optoelectronic chip is to use an integrated thermoelectric cooler (TEC) on the chip. Micro TEC (μ TEC) offers a wide range of advantages like the small size, quiet operation and reliability [3] compared to the conventional cooling techniques such as fluidics and macro TEC. In addition, μ TEC offers precise onsite cooling and high cooling densities due to smaller thermoelectric length, which is very much required for the thermal management of optoelectronic devices [4]. Similarly, the same device can be applied for converting waste heat into usable electricity, when there is a temperature differential. A thermoelectric cooling/ generation can be achieved by applying current/ temperature gradient through single or series of thermoelectric pairs comprising p- and n-type thermoelectric (TE) materials, which are placed electrically in series and thermally in parallel configuration [5-7]. These portable and highly integrated thermoelectric device (TED) are attractive for energy harvesting

applications. By miniaturization of these devices and by increasing the density of the thermocouples in the device should lead to high power outputs especially for small temperature differences [8].

Bismuth telluride (Bi-Te) based alloy materials have been extensively studied due to their relatively high thermoelectric efficiency near room temperature regime for the fabrication of thermoelectric devices [9-12]. Different approaches and techniques have been employed to fabricate TE devices in the literature [12, 13]. We employed electrodeposition in the synthesis of thermoelectric materials and devices due to its suitability in terms of cost-effectiveness, up-scalability, and ease of controlling material properties such as composition, crystallinity, and morphology [14-16]. Moreover, because of its compatibility with microelectronic processing techniques, electrodeposition can be used to fabricate micro-thermoelectric device (μ TED) directly on the wafer for the thermal management of photonics/ electronic devices and for power generation.

The thermoelectric device can be broadly classified by its heat flow as in-plane or cross-plane device [13]. Compared to the in-plane, cross-plane setup devices are more advantageous due to their high packing density, low-electrical resistances and improved thermal contacts [12]. However, connecting top contacts in a cross-plane device using the flip-chip bonding process is challenging, which makes the fabrication of cross-plane devices an arduous task.

Previous reports in the literature have demonstrated different approaches to microdevice fabrication, using various material deposition techniques. Most of the works have been demonstrated using single substrate approach, wherein, both the p- and n-type materials are deposited on the single substrate, subsequently etching the bottom interconnects and growing the top interconnects [13, 16]. However, plating two different materials on the same substrate is a complex process involving more number of process steps, thereby adding further to the device cost. Depositing top contacts is always a difficult task, as the use of multiple photoresist layers is involved, and this makes the whole fabrication more complex. In order to address this issue, previous reports in the literature used flip-chip bonding using different solder materials [17, 18]. Fabricating the top interconnects using a different substrate is comparatively an easy process employing the use of bonding material. The bonding material acts as an electrical interconnection material between the thermoelectric leg and the top contact material. There has been a report in the literature for device fabrication using two-substrates, where p- and n-type thermoelectric legs were deposited on two different substrates and bonded in the final stage using a bonding

material [19]. However, it should be noted that the materials were deposited using the sputtering method.

In this work, we demonstrate and discuss the fabrication procedure of cross-plane configuration, flip-chip bonded μ TED. The device is fabricated using electrodeposition for depositing TE material having 210 leg pairs. P-type BiTe and n-type CuTe pillars are deposited, and the properties of the deposited materials are discussed. Further details can be found in our previous studies [20-22]. We also discuss the electrodeposition of gold (*Au*) and indium (*In*), which acts as a barrier separation layer for indium diffusion and the bonding material respectively. The impact on the internal resistance of the device by bonding materials and the challenges faced during the flip-chip bonding of the device are discussed. It should be mentioned that such difficulties faced in the fabrication process are not analyzed and reported in the literature. Therefore, in the present work, we discuss various issues faced during the fabrication of the μ TED and suggest feasible solutions to overcome the fabrication problems, thereby resulting in the successful manufacturing of electroplated micro thermoelectric devices.

7.3 Experimental Procedure

7.3.1 Thermoelectric pillars deposition

7.3.1.1 p-type Bi_2Te_3

All the electrochemical depositions during the device fabrication were performed using a CHI600 series electrochemical analyzer/workstation. P-type BiTe pillars of 10 μm thickness were electrodeposited using nitric acid based solution containing 5 mM $\text{Bi}(\text{NO}_3)_3 \cdot 5\text{H}_2\text{O}$, and 15 mM Te. Te and $\text{Bi}(\text{NO}_3)_3 \cdot 5\text{H}_2\text{O}$ were successfully dissolved in 1 M HNO_3 acid. The depositions were performed on Si/SiO₂ substrate with thermally grown oxide having 200 nm of *Au* layer on 20 nm of Titanium (Ti). Platinized titanium mesh was used as the counter electrode and Ag/AgCl as the reference electrode. The pillars were deposited at a constant potential of -40 mV at room temperature without stirring. The deposition rate of BiTe in the patterned features was approximately 15 $\mu\text{m}/\text{h}$. The scanning electron microscopy (SEM) [Quanta FEG 450] image of the electrodeposited pillar is shown in Figure 7.1(a) along with the elemental composition of the deposited TE pillar obtained using energy dispersive spectrometer (EDS) coupled with the SEM.

7.3.1.2 n-type CuTe

Copper-based thermoelectric materials have not been integrated into a thermoelectric device so far. However, previously Cu pillars have been proposed in the fabrication of the micro thermoelectric device [17]. We report for the first time the use of n-type copper telluride based thermoelectric material in a device, adopting and developing from our previous work [22]. CuTe pillars were electrodeposited using a solution containing 1 M nitric acid, 15 mM pure Te powder and 2 mM copper (II) sulfate pentahydrate. In order to prepare the electrolytic solution, Te was first dissolved in 1 M HNO₃ acid at a temperature of 40 °C while stirring. Copper (II) sulfate pentahydrate, being readily dissolvable in water was separately dissolved in de-ionized (DI) water. Both the solutions were mixed at the later stage while stirring to form the final solution. The depositions were performed using a three-electrode setup at the room temperature. Platinized titanium mesh was used as the counter electrode and Ag/AgCl as a reference electrode. A constant potential of -50 mV was applied to deposit CuTe, which gave better thermoelectric properties obtained from our previous work [20]. The deposition rate of CuTe in the patterned features was approximately 8 μm/h. The SEM image along with the elemental composition is depicted in Figure 7.1(b).

7.3.2 The separation layer and bonding material deposition

For the electrodeposition of *Au*, a commercial *Au* bath (Doduco) was used. *Au* was electroplated at a constant current density of 0.02 mA/mm² on both the seed layer and the TE materials to serve two different purposes: (1) to increase the thickness of the interconnect material in order to minimize the electrical resistance of the interconnecting material and (2) to act as a barrier separation layer between the BiTe alloy material and the *In* bonding metal. All *Au* depositions were performed at 40 °C, which gave a smooth deposition without stirring.

Commercial *In* bath was used (Indium corp.) to electroplate *In* using the galvanostatic technique with *In* sheet as a counter electrode. The *In* sheet was thoroughly cleaned before the electrodeposition, using acetone followed by IPA. All the *In* depositions were performed at the room temperature without stirring. *In* was deposited on top of the thermoelectric pillars at a constant current density of 0.05 mA/mm². Simultaneously, *In* was deposited on the *Au* interconnect material. The resulting electroplating of *In* was rough with larger grain size as shown in Figure 7.1(c).

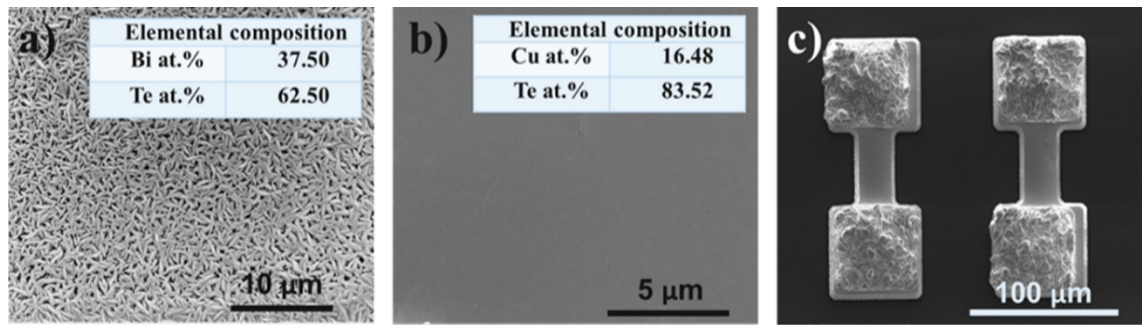


Figure 7.1: SEM image of electrodeposited pillars along with respective elemental compositions of (a) BiTe, (b) CuTe (c) In bump electrodeposited on top of electrodeposited Au interconnect material.

7.4 Fabrication

The μ TED device was fabricated on the 4" $\langle 100 \rangle$ Si wafers with $1\mu\text{m}$ of thermally grown SiO_2 as an insulation layer. A seed layer of $\text{Ti}/\text{Au} - 20/200\text{nm}$ was grown using e-beam evaporation on the SiO_2/Si substrate. In order to increase the thickness of the interconnect material, the seed layer was patterned by photolithography using photoresist AZ-9260. This particular photoresist is well known for its stability at very low pH and higher resist thickness. Therefore, AZ-9260 photoresist has been used throughout the device fabrication. Au layer of $3\mu\text{m}$ was selectively electroplated to increase the interconnect thickness, which will subsequently lower the interconnect resistance between the thermoelectric legs as shown in Figure 7.2.

Additionally, this electroplated Au will act as a seed layer for electroplating of TE material. The photoresist was stripped out after the electroplating of Au and the wafer was thoroughly cleaned using Acetone and IPA. Then the wafer was exposed to O_2 -plasma for 5 minutes at 50 W, to ensure complete removal of resist residue left on the rough electroplated gold. The wafer was then dried on a hotplate at 110°C for 5 minutes as a pretreatment for the subsequent photolithographic processes. A fresh layer of photoresist AZ-9260 was spun in order to achieve a uniform thickness of $15\mu\text{m}$ for electroplating of TE material. The soft-bake was performed for 5 minutes at 110°C on a leveled hotplate ensuring the uniformity of the resist. All the baking temperatures were achieved using low ramp rates. After the soft-bake, the wafer was kept at the room temperature for 15 minutes for rehydration before UV exposure. Exposure was done using a mask aligner (MA6) at an intensity of $10\text{ mW}/\text{cm}^2$. The exposed features were developed using AZ-400K developer and then thoroughly rinsed under DI water. The wafer was further exposed under O_2 -plasma for 5 minutes at 50 W to remove the residual resist on the electrodeposited Au. The O_2 -plasma etching also enhances the hydrophilic nature of the

photoresist and assists in reducing trapping of air bubbles inside the patterned features, which might hinder the growth of the thermoelectric material during electrodeposition. CuTe was deposited as n-type thermoelectric material for the device fabrication. A squared thermopile of size $50 \times 50 \mu\text{m}^2$ was electrodeposited and the deposition time was managed so that a thickness of $10 \mu\text{m}$ can be achieved. A higher thickness of the thermopiles is possible with a greater thickness of the photoresist and longer deposition time. After the electrodeposition of TE material, the wafer was thoroughly cleaned under DI water, before it was used for further depositions. Before growing *In* as a bonding material on the thermopile, a thin layer of 200 nm Au was electrodeposited on top of the thermopile using the same wafer immediately after TE material deposition. This thin layer of sandwiched *Au* in-between TE material and *In* bonding material acts as a barrier separation layer in terms of suppressing the inter-diffusion of *In* into the TE material. Also, this reduces the number of photolithographic steps, which in turn decreases the overall fabrication cost. Similar work showing the barrier nature of *Au* and *Ti* was discussed by Lin et al. [23]. An *In* layer of $3 \mu\text{m}$ thickness was electrodeposited at constant current as explained in the previous section. As the electrodeposited *In* was usually rough and prone to oxidation at elevated temperatures during the bonding process, a thin layer of *Au* of about 50 nm was again deposited to prevent the oxidation of the underlying *In* layer. After this, the supporting photo-resist was removed using acetone and cleaned by isopropanol followed by DI water and dried under nitrogen jet. As the freestanding TE pillars with *Au* and *In* were without structural support, the wafers were handled with utmost care. The photoresist was spun again, to achieve a resist thickness of around $15 \mu\text{m}$, similar to n-type thermopile, thereby covering and protecting the electrodeposited n-type TE thermopiles. The p-type openings were developed after exposing in the UV light using the mask aligner as described above. All the necessary steps were followed to ensure the verticality of the side walls and removal of the resist residue on the electrodeposited *Au*. P-type BiTe materials were electroplated as explained in the experimental section using a constant potential of -40 mV to achieve a thickness of $10 \mu\text{m}$ (equal to the n-type material) and followed by the electrodeposition of *Au*, *In* and again *Au* in a similar fashion to the previous deposition on the n-type thermopile. The photoresist was removed using acetone, and both the p- and n-type pillars were free standing. The photoresist was spun and exposed on the wafers with p and n-type pillars. The photoresist covers both the pillars and the interconnection, leaving the rest of *Au* seed layer to be etched. The *Au* layer was chemically etched using potassium iodide based

solution. The 20 nm of Ti was etched using HF-based solution. After the *Au/Ti* etching, the photoresist was stripped off and the wafer was thoroughly cleaned and exposed under O₂-plasma for 5 minutes as the topography of the pillars was rough due to the rough *In* electrodeposition and the probability of photoresist adhering on to the pillars was very high. Which could lead to a deleterious electrically resistive layer during flip-chip bonding.

In order to connect the p and n-type TE pillars electrically in series, the flip-chip bonding approach was used. Therefore, another wafer which will act as the interconnect material along with the bonding material has to be fabricated. A new Si/SiO₂ wafer with 20 nm of Ti and 200 nm of *Au* was spun with the AZ-9260 photoresist and patterned for the top-interconnect material. *Au* was electrodeposited as a top interconnect material with a thickness of 3 μm, similar to that of wafer 1. In order to make *In-In* bonding possible, *In* metal has to be electroplated as the bonding material. A fresh layer of photoresist was spun on the electrodeposited *Au* covering the interconnect *Au* region and exposing the area where the pillars are expected to bond. *In* layer of 3 μm was electroplated on these exposed areas in a similar way used earlier to deposit *In* on the pillars. Following that, the photoresist was stripped out, and all the cleaning procedures were undertaken. The excess seed layer was chemically wet etched similar to the wafer 1 as shown in Figure 7.2.

Prior to the bonding, both the wafers were diced into individual dies. The bonding was performed using a FineTech flip-chip bonder by aligning both the bottom and the top interconnect chips in such a way that the pillars form a daisy chain. The challenges and difficulties faced in the fabrication of the device and the proposed feasible solution employed will be discussed in the subsequent section.

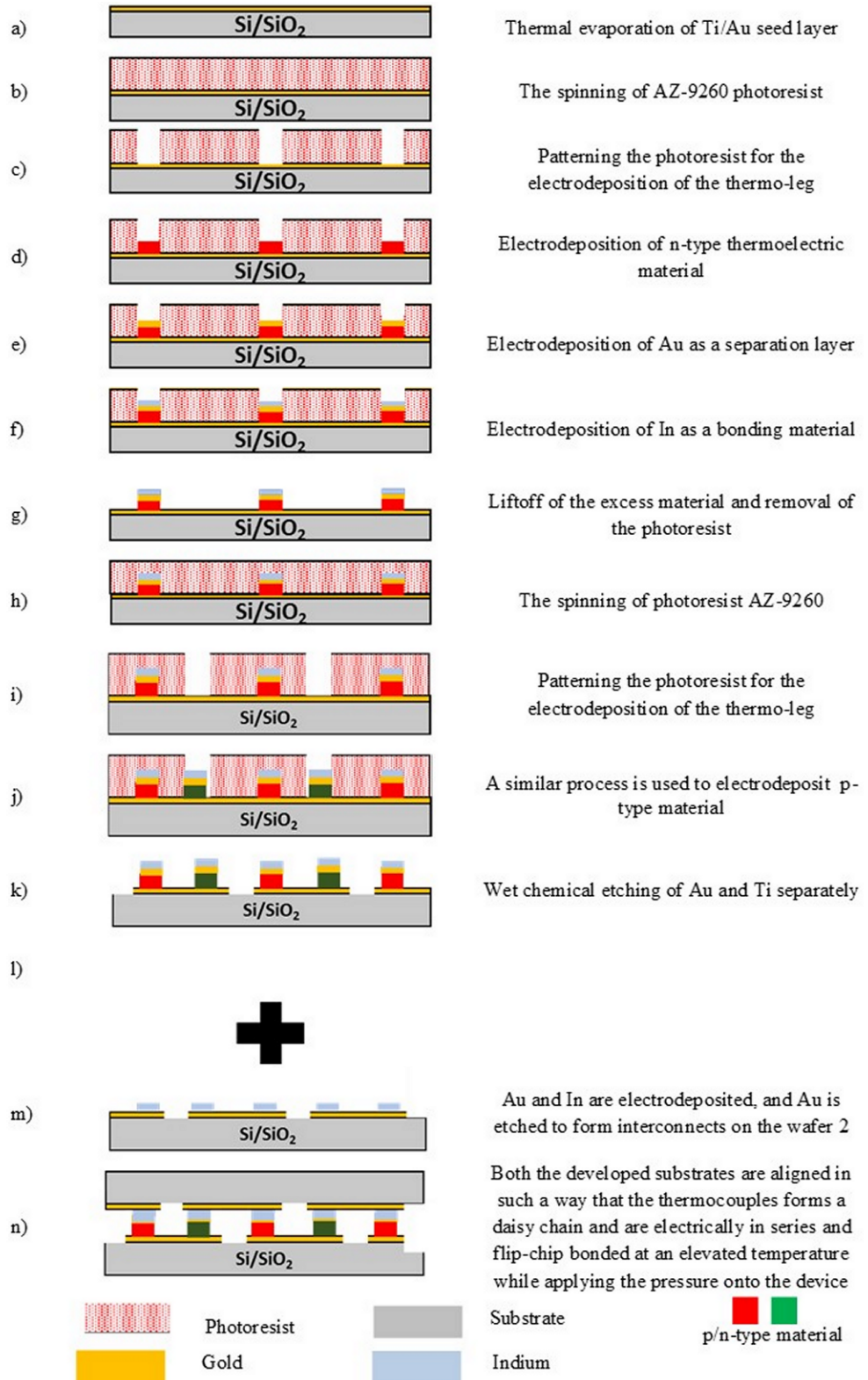


Figure 7.2: Schematic illustration of device fabrication process [24]

7.5 Results and Discussion

7.5.1 Challenges and feasible solutions

This section of the paper will discuss the different fabrication difficulties and the applied feasible solution.

Au with 200 nm thickness and 20 nm of Ti were grown on a Si/SiO₂ wafer to act as a seed layer for the electrochemical deposition of the thermoelectric pillars. However, the adhesion between the thin layer and the deposited TE pillars were not strong enough to structurally hold the pillars in place as shown in Figure 7.3. This was due to the photoresist residue still left on the *Au* seed layer, and the induced stress due to the formation of AuTe from the interaction between the Au seed layer and Te from the electrodeposited materials, which can play a role in the detachment of the pillars from the seed layer. The polymer residue at the electrochemically active seed regions were removed by optimizing the photo-lithographic process, mainly by increasing the development time during lithography and exposing the developed wafer to O₂-plasma to ensure the complete removal of the photoresist. Also, this process increases the hydrophilic nature of the photoresist, which helps in the free flow of the electrolyte into the patterns and reduces the air bubble trapping inside the patterns, resulting in the homogeneous growth of the pillars during electrodeposition.

The stress from the electrodeposited pillars may lead to the delamination of the pillars along with the seed layer. In order to address this issue, the seed layer thickness was increased from 200 nm to 3 μm using the selective electrodeposition of *Au*. As the electrodeposited *Au* has higher roughness than the evaporated *Au*, this further increased the adhesion of pillars on the *Au*. With the increased interconnect material thickness,

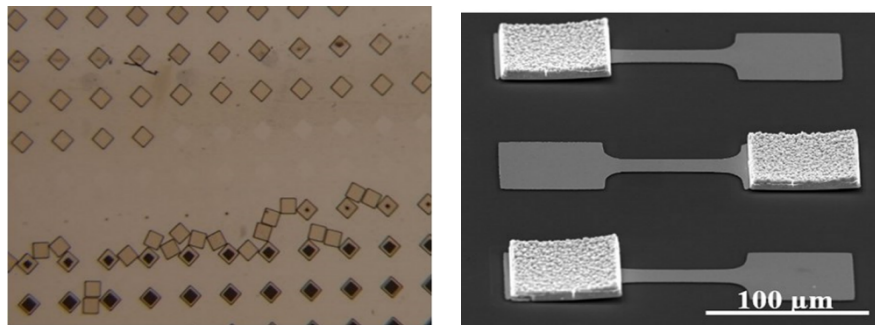


Figure 7.3: Images show non-adherence of pillars to the seed and delamination of pillars.

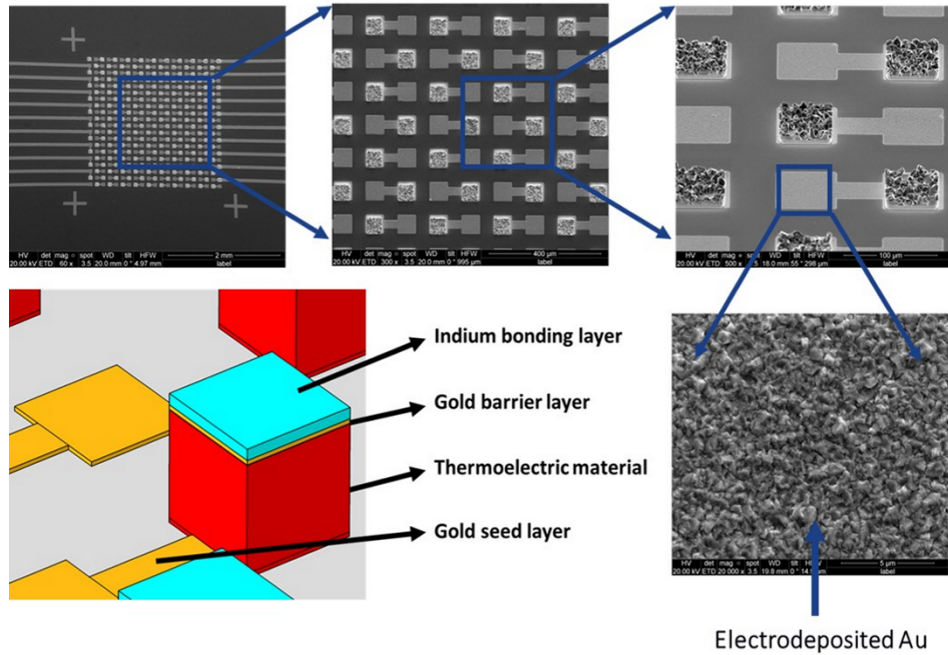


Figure 7.4: Schematic of sequential electrodeposited materials on the Au seed. [24]

the TE materials, the barrier separation layer, and the bonding materials were electrodeposited on the patterned substrate as shown in Figure 7.4. The individual thicknesses of the electrochemically deposited materials are listed in Table 1.

Table 7-1: Individual material thickness of electrochemically deposited materials.

Material	Thickness
Interconnect material	3 μm
TE material thickness	10 μm
Indium thickness	3 μm
Barrier separation thickness	200 nm

However, there were issues during the electroplating of the thermoelectric materials, which led to electrically disconnected structures after the bonding. This issue was due to the difference in height of the electrochemically deposited pillars across the wafer. Figure 7.5 depicts the height difference of the thermoelectric pillars across each die on a wafer. The pillar heights of the TE materials need to be consistent for proper flip-chip bonding. The electroplated pillars were higher at the edges and at the corners compared to the pillars situated at the center of the wafer [25]. This is due to the so-called edge effects

where the current density is higher at the edges than in the middle, resulting in faster growth of the pillars at the edge area of the wafer. This height variation resulted in insufficient or no contact during the bonding process. The bonding process becomes more challenging when the pillar density is higher and cannot be neglected. Figure 7.6(a) shows the SEM image of an edge pillar after bonding where the top die was removed in order to analyze the bonding process. It can be seen from the image that the edge pillars were cracked and it appears that pillars are structurally not stable enough to take the bonding force. This was due to the dissimilar (higher in this case) height of the edge pillar, which took the entire load during bonding as the pillars from the central position did not share the bonding loads, leading to the fracture of the edge pillars. Therefore, it is imperative to address the die co-planarity or uniformity, which can be calculated according to equation (1), where H_{\max} and H_{\min} are the maximum and minimum heights of the pillars, respectively. The uniformity percentage should be less than 5% for good reliability [26], which is widely accepted in both the industrial and scientific community.

$$\text{Uniformity (\%)} = \frac{1}{2} \left(\frac{H_{\max} - H_{\min}}{H_{\text{Avg}}} \right) \times 100 \quad 7.1$$



Figure 7.5: Schematic sketch of the non-uniformity in the electrodeposited pillar height.

In order to improve the uniformity, we have worked on different approaches. In particular, the use of additives in the electrolytic bath can help to achieve a uniform growth across the substrate. Levelers are preferentially attracted to the regions of higher current density, where they suppress the electroplating rate and create a more uniform array of pillars. However, it should be mentioned that this approach can influence the TE properties of the pillars. To reduce the complexity, we have taken an alternative approach to address this issue by increasing the thickness of the bonding material, which can compensate the height differences across the pillars. We selected *In* as a bonding material, as *In* metal is malleable and can deform easily acquiring the required shape at the applied bonding temperature and the bonding force. However, the risk of overflow of *In* will always be an issue as shown in Figure 7.6(b). This overflow of *In* can be minimized by

the optimization of the *In* height and the bonding forces during the flip-chip bonding of the device.

The SEM image in Figure 7.6(b) depicts *In* acting as a bonding material on the second bonding wafer with the overflowed *In* metal around the pillars. We can also observe the non-adherence nature of *In* with the *Au*. We assume that this can be due to a thin layer of InO_2 formation over the *In* bumps, which restricts the formation of *Au-In* bonding. To address this issue, a thin layer of 50 nm of *Au* is electrodeposited over the *In* bumps to protect the *In* from oxidation during the flip-chip bonding process at the elevated temperature. As explained in the experimental section, *In* bumps were electrodeposited on both the wafers. This leads to an *In-In* bonding during the bonding process. The optimized bonding parameters are listed in Table 2.

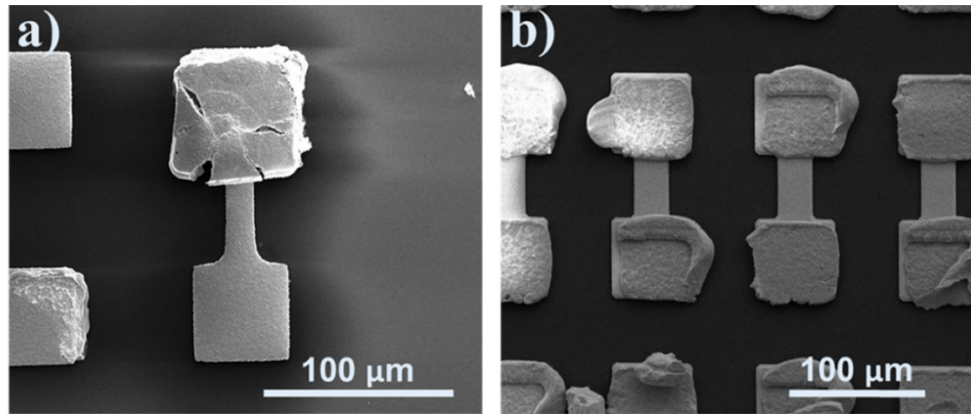


Figure 7.6: The SEM image of (a) an edge pillar after applying a bonding force, (b) electrodeposited *In* bumps after bond forces are applied.

Table 7-2: Bonding parameters used in the flip-chip bonding process.

Bonding parameters	Values
Bonding force	250-500 gf
Temperature	160 – 200 °C
Atmosphere	Nitrogen
Time	60-120 s

7.5.2 Structural and electrical characterization

This section discusses the structural and initial electrical characterizations of the fabricated micro thermoelectric device. After addressing and overcoming various challenges, the device was fabricated by flip-chip bonding. The bonding was performed at a temperature of 200 °C for 60 s with 300 gf under a continuous nitrogen flow in order

to minimize the oxide formation at the elevated temperatures. The heating and cooling rates during the bonding were set at 5 °C/sec. A fully processed, μ -thermoelectric device consists of 210 pairs of p- and n-type TE pillars, connected thermally in parallel and electrically in series as shown in Figure 7.7. The images were taken using a Nordson Dage Diamond XD7600NT, X-ray Imaging system. The images reveal the underlying top view features through the top silicon substrate. A perfect alignment of both the dies to form an electrical contact of the device and the formation of the daisy chain can be seen in Figure 7.7. However, a slight overflow of the *In* metal is visible near the edges of pillars, which is significant. Even though there seems to be an overflow of *In* in the pillars at the edges, there has been no visible contact with immediate pillars in the vicinity, which might be deleterious as it will short-circuit the entire device. In order to thoroughly investigate the overflow of *In*, cross-sectional images were recorded.

Figure 7.8 shows the vertical cross-sectional SEM image of the flip-chip bonded device ensuring the bond formation. The gap between the top and the bottom substrates is approximately 20 μm . The *In* bonding material holding the *Au* interconnect metal and the thermoelectric pillar forms an electrical contact between both the materials. The image is taken at the edge pillar, where the possibility of overflowing *In* is maximum due to the height difference of the pillars. From the SEM images, a slight overflow of *In* can be clearly observed as anticipated due to excess *In* owing to the pillar height differences across the substrate. However, this overflowed *In* does not short-circuit the connection as observed from Figure 7.8. Additionally, the *In* bond formed at the center pillars is perfect without any overflow suggesting an optimized bonding force applied.

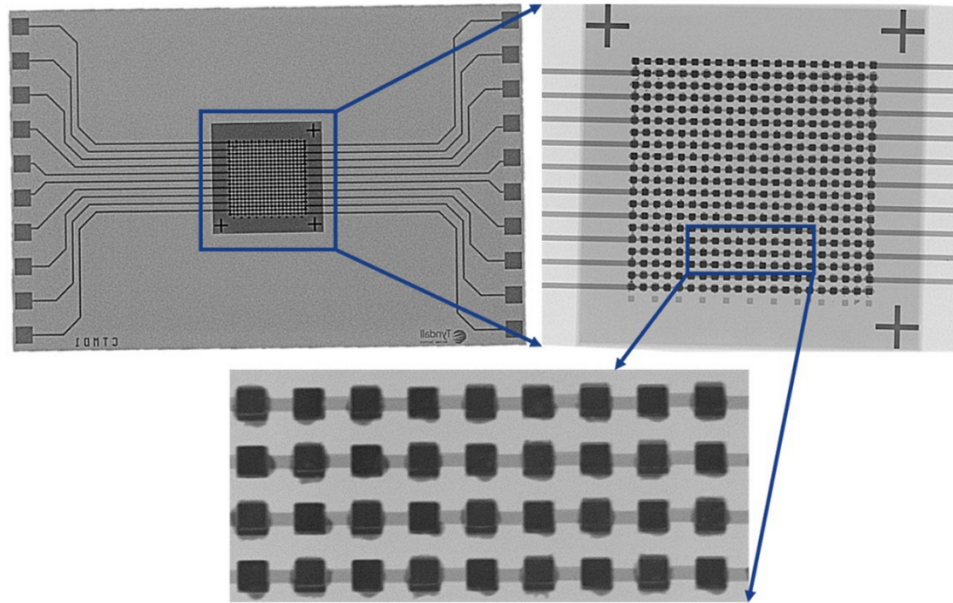


Figure 7.7: Images of the device using Nordson Dage Diamond XD7600NT X-ray Imaging system.

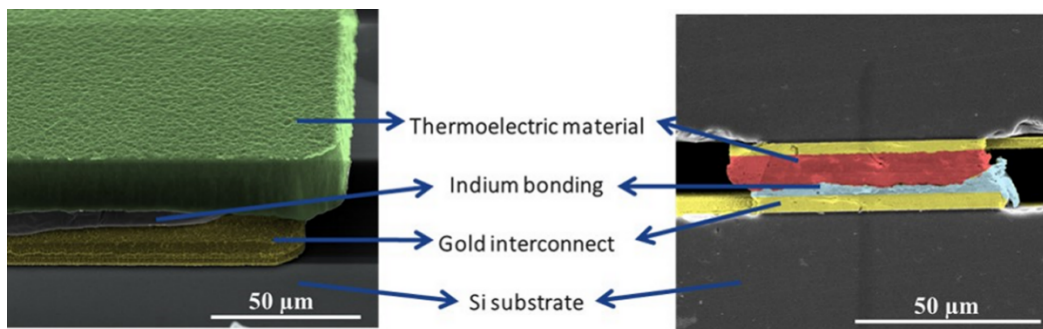


Figure 7.8: SEM images of the flip-chip bonded device using FineTech flip-chip bonder.

Measuring the overall resistance of the fabricated thermoelectric device ensures that all the contacts are formed after the flip-chip bonding. The device was designed in such a way that the electrical resistance can be measured for every 22 pairs. The electrical resistance of the device with respect to the number of pillars is plotted in Figure 7.9. Also, the resistance of single thermoelectric pair was calculated using the materials property in order to estimate the contact resistances formed during the bonding of the materials. The internal resistance of the thermoelectric pillar pair R_d is the sum of the material resistance (R_p+R_n), interconnect material resistance (R_{Au}) and the interfacial resistance of the flip-chip bonded joints ($R_{Au}+R_{In}$) as shown in Figure 7.10(a). The photograph of a flip-chip bonded device is shown in Figure 7.10(b). The material resistance (R_p+R_n) comprises of the resistance from the CuTe and the BiTe pillars, interconnect material resistance (R_{Au}) is the electrical resistance from the electrodeposited Au and the interfacial resistance ($R_{Au}+R_{In}$) corresponds to the resistance by the In-Au joint after the bonding.

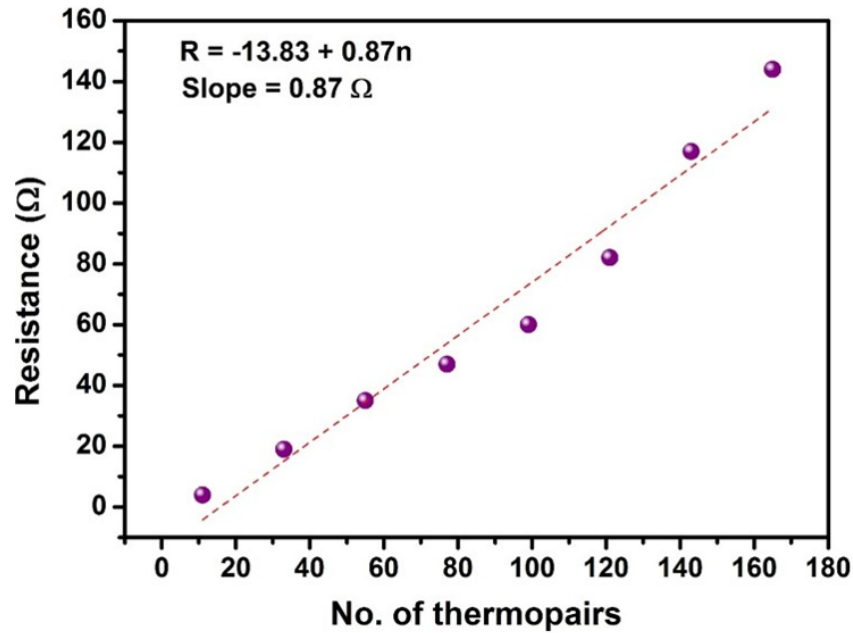


Figure 7.9: Measured electrical resistance of the flip-chip bonded device.

The average measured electrical resistance of a single thermoelectric pair is 0.87Ω deduced from the electrical resistance measured on the complete device after performing a linear fit on the obtained values. The deviation of the measured resistances in the plot arises from the change in the distance of the Au pads from the pillars to the measuring pads. The measuring pad itself adds resistance during the measurements, and this resistance will be high for a longer bond pad compared to the shorter pad (see Figure 7.7). The decrease in the resistance measured can only be seen when the measurements are done using the shorted bond pads as seen in Figure 7.9. This ensures that the measured electrical resistance is same throughout the device and confirms the homogeneous bond formation over the complete device. The calculated resistance of a thermoelectric pair using material properties is 0.45Ω , which is 48% lower than the measured value. This higher measured value is due to the contact resistances $[3R_{Au} + 2(R_{Au} + R_{In})]$ between the p-n leg pairs.

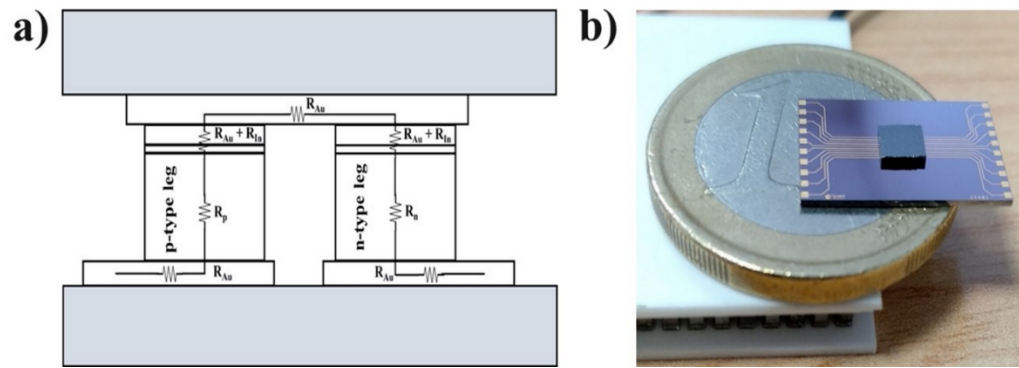


Figure 7.10: a) The schematic of internal resistances of thermoelectric pillar pair, b) Flip-chip bonded μ -TED device.

In order to check the functionality of the thermoelectric device, two thermocouples were attached at the top and bottom of the device. A temperature gradient was created using two commercially available Peltier coolers placed over and under the device. A voltage of 90 mV was measured for a temperature difference of 10 K from 60 active TE pairs. This measurement when extrapolated for a complete device using 210 TE pairs, projects a voltage generation of about 315 mV, which indicates a contribution of 143.1 μ V/K from each TE pair. This Seebeck coefficient value is, however, lower than the values of individual p and n-type TE films. The lower values compared to the individual materials might stem from the thermal losses at the device interface and not accurate temperature determination in the micro-thermoelectric device in addition to the interfacial electrical losses. However, the calculations were done assuming a negligible thermal loss in the substrate and at the interface between the thermoelectric material and the interconnect material. Further work is required to precisely analyze the device and evaluate the reasons for the measured lower values of the overall device voltage. Additionally, the complete device characterization over a range of temperature interval has to be measured in future.

7.6 Conclusion

A micro-thermoelectric device with 210 pairs of thermopiles was fabricated using the flip-chip bonding that are connected electrically in series and thermally in parallel on the silicon substrate. Here, we demonstrate and discuss the challenges encountered during the fabrication of a thermoelectric device using flip-chip bonding approach and the solutions employed to overcome these challenges to minimize the processing steps, which leads to the reduction of overall fabrication cost. Different problems, namely adherence issues, delamination, bonding, edge effects, and structural stability are discussed. Cross-sectional characterization reveals that the overflow of In bonding metal does not short-

circuit the device. The electrical resistance of the complete device with 210 pairs of thermocouples was about 182.7Ω , which gives an average electrical resistance of 0.87Ω for individual thermoelectric pair. The resistance of a single thermopile is higher than the calculated value using material properties, which is due to the contact resistance of the bonding materials. A thermoelectric voltage of about 90 mV is generated when the device with 60 active thermopile pairs was subjected to a temperature gradient of 10 K. Future studies will analyze and evaluate the device performance including the complete thermoelectric characterization.

7.7 References

- [1] R. Enright *et al.*, "A Vision for Thermally Integrated Photonics Systems," *Bell Labs Technical Journal*, vol. 19, pp. 31-45, 2014.
- [2] C. O'Dwyer, R. Chen, J.-H. He, J. Lee, and K. M. Razeeb, "Preface—Focus Issue on Thermoelectric Materials & Devices: Phonon Engineering, Advanced Materials and Thermal Transport," *ECS Journal of Solid State Science and Technology*, vol. 6, no. 3, pp. Y3-Y3, 2017.
- [3] L. E. Bell, "Cooling, Heating, Generating Power, and Recovering Waste Heat with Thermoelectric Systems," *Science*, vol. 321, no. 5895, pp. 1457-1461, 2008-09-12 00:00:00 2008.
- [4] J. P. Fleurial *et al.*, "Thermoelectric microcoolers for thermal management applications," in *Thermoelectrics, 1997. Proceedings ICT '97. XVI International Conference on*, 1997, pp. 641-645.
- [5] I. Chowdhury *et al.*, "On-chip cooling by superlattice-based thin-film thermoelectrics," (in English), *Nature Nanotechnology*, Article vol. 4, no. 4, pp. 235-238, 2009.
- [6] R. Venkatasubramanian, E. Siivola, T. Colpitts, and B. O'Quinn, "Thin-film thermoelectric devices with high room-temperature figures of merit," *Nature*, vol. 413, 2001.
- [7] D. E. Rowe, Burkov, A., Kishimoto, K., Ravich, Y., Fedorov, M., Ktitorov, S., Anatyshuk, L., Slack, G., Burke, E., Haringa, J., Han, S., Koyanagi, T., Nagao, K., Studd, R., Trimmer, D., Bennett, G., Hall, W. (Ed.), Borshchevsky, A., Cassart, M., Redstall, R., Hartman, R., Stordeur, M., Vining, C., Birkholz, U., Cobble, M., Min, G., Woodbury, H., Emin, D., Pollock, D., Taylor, R., Scherrer, S., Scherrer, H., Beaudry, B., Matsuura, K., Kajikawa, T., Skrabek, E., Gschneidner, Jr., K., Fano, V., McNaughton, A., Levinson, L., Issi, J., Goldsmid,

- H., Buist, R., Nishida, I., Bhandari, C., Vedernikov, M., Stockholm, J., Matsubara, K., Ohta, T., Zaitsev, V., Uemura, K., Aselage, T., Mondt, J., Cook, B., Kuznetsov, V., Vandersande, J., Marlow, R., Scoville, N. (1995). CRC Handbook of Thermoelectrics. Boca Raton: CRC Press., "CRC Handbook of Thermoelectrics," 1995.
- [8] J. P. Fleurial *et al.*, "Thick-film thermoelectric microdevices," in *Thermoelectrics, 1999. Eighteenth International Conference on*, 1999, pp. 294-300.
- [9] G. J. Snyder and E. S. Toberer, "Complex thermoelectric materials," *Nat Mater*, 10.1038/nmat2090 vol. 7, no. 2, pp. 105-114, 02//print 2008.
- [10] C. Schumacher *et al.*, "Optimizations of Pulsed Plated p and n-type Bi₂Te₃-Based Ternary Compounds by Annealing in Different Ambient Atmospheres," *Advanced Energy Materials*, vol. 3, no. 1, pp. 95-104, 2013.
- [11] C. Boulanger, "Thermoelectric Material Electroplating: a Historical Review," *Journal of Electronic Materials*, vol. 39, no. 9, pp. 1818-1827, 2010// 2010.
- [12] R. Rostek, N. Stein, and C. Boulanger, "A review of electroplating for V–VI thermoelectric films: from synthesis to device integration," *Journal of Materials Research*, vol. 30, no. 17, pp. 2518-2543, 2015.
- [13] W. Glatz, E. Schwyter, L. Durrer, and C. Hierold, Bi₂Te₃-Based Flexible Micro Thermoelectric Generator With Optimized Design," *Journal of Microelectromechanical Systems*, vol. 18, no. 3, pp. 763-772, 2009.
- [14] W. Glatz, S. Muntwyler, and C. Hierold, "Optimization and fabrication of thick flexible polymer based micro thermoelectric generator," *Sensors and Actuators A: Physical*, vol. 132, no. 1, pp. 337-345, 2006/11/08/ 2006.
- [15] W. Glatz, L. Durrer, E. Schwyter, and C. Hierold, "Novel mixed method for the electrochemical deposition of thick layers of Bi_{2+x}Te_{3-x} with controlled stoichiometry," *Electrochimica Acta*, vol. 54, no. 2, pp. 755-762, 12/30/ 2008.
- [16] G. J. Snyder, J. R. Lim, C.-K. Huang, and J.-P. Fleurial, "Thermoelectric microdevice fabricated by a MEMS-like electrochemical process," *Nat Mater*, 10.1038/nmat943 vol. 2, no. 8, pp. 528-531, 08//print 2003.
- [17] R. Roth *et al.*, "Design and Characterization of Micro Thermoelectric Cross-Plane Generators With Electroplated Bi₂Te₃ and Sb₂Te₃ and Reflow Soldering," *Journal of Microelectromechanical Systems*, vol. 23, no. 4, pp. 961-971, 2014.
- [18] M.-Y. Kim and T.-S. Oh, "Preparation and Characterization of Bi₂Te₃/Sb₂Te₃ Thermoelectric Thin-Film Devices for Power Generation," *Journal of Electronic Materials*, journal article vol. 43, no. 6, pp. 1933-1939, 2014.

- [19] H. Bottner, J. Nurnus, A. Schubert, and F. Volkert, "New high density micro structured thermogenerators for stand alone sensor systems," in *2007 26th International Conference on Thermoelectrics*, 2007, pp. 306-309.
- [20] S. Lal, D. Gautam, and K. M. Razeeb, "Optimization of annealing conditions to enhance thermoelectric performance of electrodeposited p-type BiSbTe thin films," *APL Materials*, vol. 7, no. 3, p. 031102, 2019/03/01 2019.
- [21] S. Lal, D. Gautam, and K. M. Razeeb, "The Impact of Surfactant Sodium Dodecyl Sulfate on the Microstructure and Thermoelectric Properties of p-type $(\text{Sb}_{1-x}\text{Bi}_x)_2\text{Te}_3$ Electrodeposited Films," *ECS Journal of Solid State Science and Technology*, vol. 6, no. 3, pp. N3017-N3021, January 1, 2017 2017.
- [22] S. Lal, D. Gautam, and K. M. Razeeb, "Synthesis and structural investigation of controlled Cu-doped Te films with high thermoelectric performance," *To be communicated*, 2019.
- [23] W. P. Lin, D. E. Wesolowski, and C. C. Lee, "Barrier/bonding layers on bismuth telluride (Bi_2Te_3) for high temperature thermoelectric modules," *Journal of Materials Science: Materials in Electronics*, vol. 22, no. 9, pp. 1313-1320, 2011// 2011.
- [24] S. Lal, D. Gautam, and K. M. Razeeb, "Fabrication of micro-thermoelectric cooler for the thermal management of photonic devices," in *2018 IEEE 18th International Conference on Nanotechnology (IEEE-NANO)*, 2018, pp. 1-2.
- [25] C.-W. Park and K.-Y. Park, "An effect of dummy cathode on thickness uniformity in electroforming process," *Results in Physics*, vol. 4, pp. 107-112, 2014/01/01/ 2014.
- [26] <http://www.dupont.com/electronic-materials/blogs/tutorials/copper-pillar-electroplating-tutorial.html>.

Chapter 8: Cross plane Micro-Thermoelectric device: Fabrication, Simulation and Evaluation

8.1 Introduction

The recent advancements in microelectronics and MEMS technologies have made the 'Internet of Things' (IoT) an indispensable part of our lives that facilitates tailored fast services to enrich rural and urban lifestyle. This enables ubiquitous sensing through enumerable deployed wireless sensors nodes (WSN) that aims to integrate the physical world with the computer-based systems, bringing ease in communication and computation. These versatile WSNs are widely used in industrial sensing [1], remote healthcare [2], automotive monitoring [3], surveillance [4], etc. and is a potential candidate to find its place in the hitherto unexplored application. However, one of the major impediments in the path of materialising this type of smart connected environment is the perpetual powering of such billions of deployed sensor nodes. Batteries as the only power source not only add unnecessary volume and weight to such a miniaturised system mainly in the case of wearable electronics but also makes it impractical for recharging multiple times once it depletes its energy. Although a lot of strategies have been reported for improving the energy density of supercapacitors and batteries [5-7]. However, these advances, integration of a sustainable and reliable powering source with the wearable electronics is still a great challenge. In this predicament, the most attractive alternative is to scavenge energy from omnipresent ambient energy sources and assisting the energy storage devices for ultimately powering the wearable electronics [8]. Autonomous and real-time powered, reliable and continuous measurements of vital information such as heart rate, electrocardiograph (ECG), respiratory flow, etc. can be facilitated by wearable healthcare devices. They can be used for early-stage disease detection and long-term health monitoring. The recent growth of wearable electronics has captivated interest from both the research and industrial community. Powering such devices with a sole battery which needs multiple charging cycles can be difficult as during the charging the health monitoring can be hindered and cause inconvenience. These devices need to be able to work autonomously with the least human interventions. Scavenging energy from the human body to power such wearable devices and reduce our sole dependence on the batteries is very important for the next generation wearable health monitoring systems. The promising energy source in this context is the thermal energy that a human body generates. There has been a growing trend in the investigation and development of the thermoelectric transducers that generate electricity by exploiting the thermal gradient that

human body heat would offer as compared with the ambient temperature [9-12]. Thermoelectric generators constitute of p-type and n-type semiconductors that are connected electrically in series and thermally in parallel, which enables these materials to generate a sufficiently high number of charge carrier once the opposite junctions are subjected to a substantial temperature gradient.

Thermoelectric generators are solid-state transducers that take thermal energies and converts them to useful electrical form and vice versa. Advantages of using thermoelectric energy harvesters are that they can be used to convert waste heat into useful electrical energy without any moving part, vibration, noise, refuelling. Moreover, have high reliability, low maintenance, and the very long working period over a wide range of temperature [13-15]. The other advantage of the thermoelectric device is for their cooling applications with no moving parts and refrigerant free heat extraction [11].

Body wearable sensors and electronics are getting immense attention with the growth in IoT and TEGs are of interest in the implementation of these self-powered wearable as it utilises the body heat and converts it into usable electrical energy. Studies that have focused on body temperature measurements have revealed that the body parts with highest temperatures are namely the forehead, back of the neck and the chest. All these body parts are capable of creating a temperature gradient of 2-10 K depending upon the ambient temperatures [16, 17].

Scientific reports on the material property enhancement of the next-generation thermoelectric material and optimisation of the fabricated micro-thermoelectric devices (μ TED) have been increasing significantly. In comparison with the conventional microfabrication techniques like epitaxial growth, evaporation or sputtering, the electrochemical deposition of the thermoelectric materials offers various advantages [18-21]. Due to the cost-effectiveness and high scalability, the electrodeposition technique is becoming attractive compared with the other fabrication techniques. The performance of thermoelectric material is evaluated based on the figure of merit, ZT , and is defined by the equation below.

$$ZT = \frac{S^2 \sigma T}{k} \quad 8.1$$

Where S ($V K^{-1}$) is the Seebeck coefficient of the material which is defined as the electric potential developed in response to an applied temperature difference applied across a

material. σ (S m^{-1}) is the electrical conductivity, k ($\text{W m}^{-1} \text{K}^{-1}$) is the thermal conductivity, and T (K) is the absolute temperature.

The maximum value of ZT of the thermoelectric materials has reached a new high over the past two decades for different thermoelectric materials [22]. Bismuth telluride-based materials have been best known for their high thermoelectric performance at near room temperature region and have successfully been used for commercial applications [21, 23-25].

Various methods have been used for the thermoelectric generator fabrication- (a) processes in which all the thermolegs and interconnects are electrodeposited on a single wafer and (b) processes where two separate wafers electroplated n- and p-type thermoelectric material are bonded together by the flip-chip technique [18, 26-31]. The major advantage of the flip-chip bonding approach is its cost-effectiveness due to the reduced lithographic steps involved in the fabrication. However, there are limitations of flip-chip bonding approach due to the increased bonding resistances and bonding difficulties which have been well discussed in our previous work [31]. Single wafer approach constitutes of plating both the p- and n-type materials on a single wafer and direct integration of interconnect materials which in turn minimises the electrical resistance arising from the bonding and interconnects as compared with other approaches. However, the device fabrication becomes complex in this approach with multiple process steps and thermal cycling of the wafer during the processing [32, 33].

In this work, we present the integration of electroplated BiSbTe, Cu doped Te and the Au interconnect materials for the fabrication of cross-plane μ TEDs. Both the thermoelectric materials were deposited on the single wafer alternatively. The bottom and the top interconnect material thickness have been increased by the use of electrodeposition of the Au, which plays a vital role in lowering the overall device resistance. We here present the detailed characterisation of the device both as a micro-cooler and thermoelectric generator.

8.2 Material fabrication

In this work, P-type BiSbTe, n-type CuTe and pure Au materials are chosen for the thermoelectric material, and the interconnect materials respectively and all are electrodeposited using conventional three cell with a CHI660C potentiostat. The effect of the deposition potentials, microstructure, composition and annealing, have been studied extensively on these materials and can be found in our previous works [34, 35].

BiSbTe electrodeposition

For the electrodeposition of the p-type BiSbTe, the electrolyte is prepared with 5 mM Bi(NO₃)₃·5H₂O, 10 mM Sb₂O₃ and 15 mM of Te dissolved in 0.2 M tartaric acid and 1 M HNO₃. Ag/AgCl was used as a reference electrode and platinised Ti mesh as a counter electrode. An optimised pulse deposition was performed using a triple pulse amperometry technique [34].

Cu doped Te electrodeposition

For the electrodeposition of n-type CuTe, the electrolyte was prepared by dissolving 15 mM pure tellurium powder and 2 mM copper (II) sulphate pentahydrate in 1 M nitric acid. Ag/AgCl and the platinised Ti mesh is used as the reference and the counter electrode, respectively. Constant voltage technique is used for the deposition of the thermoelectric pillars [35].

Au electrodeposition

For the Au electrodeposition, standard commercial Au electrolytic bath (Doduco) was used. The Au was electrodeposited using a constant current method at a current density of 0.02 mA/mm², which gave a smoother and better deposition. The Au is electrodeposited as both the bottom and the top interconnect material.

8.3 Device Fabrication

For the fabrication of the micro-thermoelectric device, we have combined photolithographic process with electrochemical deposition (ECD) for material depositions. The fabrication is performed on 500 µm silicon (Si) wafer with 1 µm of thermally grown silicon dioxide (SiO₂) layer. The oxidation layer prevents electrical current leakage from the seed layer to silicon. An electrical seed layer of Ti/Au-20/200 nm is deposited over the SiO₂ using e-beam for the further ECD material depositions. Then the bottom interconnects are patterned using photoresist. The detailed process flow of device fabrication is given in figure 8.1.

Furthermore, Au is electrochemically deposited on the exposed seed to increase the Au bottom interconnect thickness to 3 µm, which decreases the electrical resistance and adds structural stability to the overall structure. This ECD Au bottom interconnects acts as the electrodes for the thermoelectric pillars. For thermoelectric material deposition, the wafer is patterned using photoresist AZ-9260 with the thickness of 20 µm, opening holes for deposition p-type of thermoelectric material. This hole of 50 × 50 µm acts as a mould for

the ECD of thermoelectric material. BiSbTe material is electrodeposited using a triple pulse amperometry technique for 2 hrs, and after completion of the pillar deposition, a thin layer of Au is electrochemically deposited over the deposited pillar. This Au deposition over TE pillar protects TE pillar from degrading the material property over the subsequent environmental changes and also help in bond strengthening of the TE pillar with the top interconnect Au, which will be then deposited in the later stage of device fabrication. The photoresist holding the p-type pillar is dissolved, and a new photoresist is spin-coated to open the hole for the n-type thermoelectric material and covering the p-type thermoelectric pillar for further deposition. Cu doped tellurium is deposited at -50 mV constant potential for 2 hrs, and a protective Au layer is deposited over the TE materials as discussed in the earlier section. Before further processing, the Au seed has to be etched. The Au and Ti layer is wet etched using potassium iodide based etchants and HF based etchants respectively, safeguarding the TE pillars and the bottom interconnects. Maintaining the heights of the p- and n-type thermoelectric materials are complicated, and after the electrodeposition the pillars are no longer smooth. Therefore, a planarization step is necessary for maintaining the parity between heights of all the pillars. The chemical mechanical planarization (CMP) is performed on the wafers, and the SEM image of the polished wafers are shown in figure 8.2. After the planarization of the wafer, Au seed of 200 nm is sputtered, which will act as a seed for the ECD of the top seed layer. A fresh photoresist is spin-coated and patterned to expose the top seed, and then Au is ECD with a thickness of 3 μm . The ECD Au top interconnect is protected with a freshly spin-coated and developed negative-photoresist. Moreover, the Au seed is chemically etched as explained earlier, and the photoresist is stripped away using suitable stripper. The schematic of the final device is shown in figure 8.3.

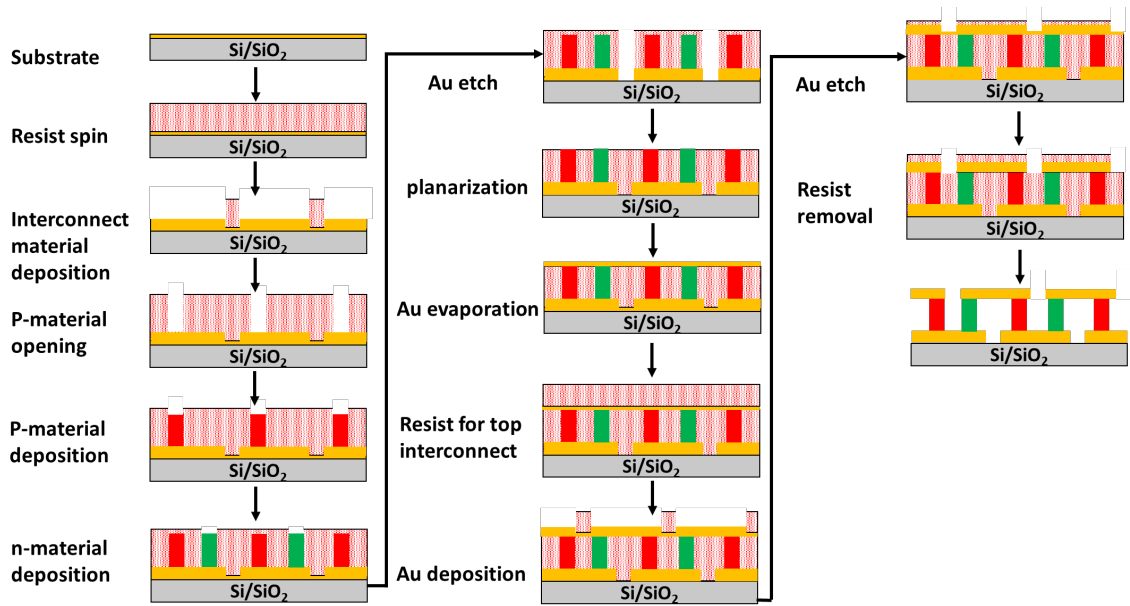


Figure 8.1: Schematic of the fabrication process flow of the micro-thermoelectric device.

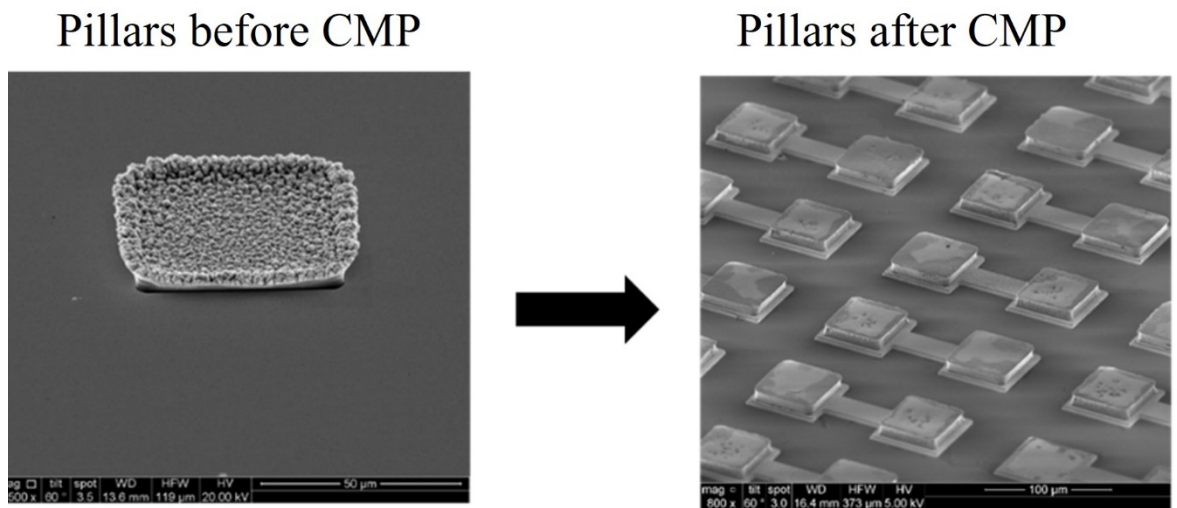


Figure 8.2: SEM images of the electrodeposited thermoelectric pillars before and after CMP.

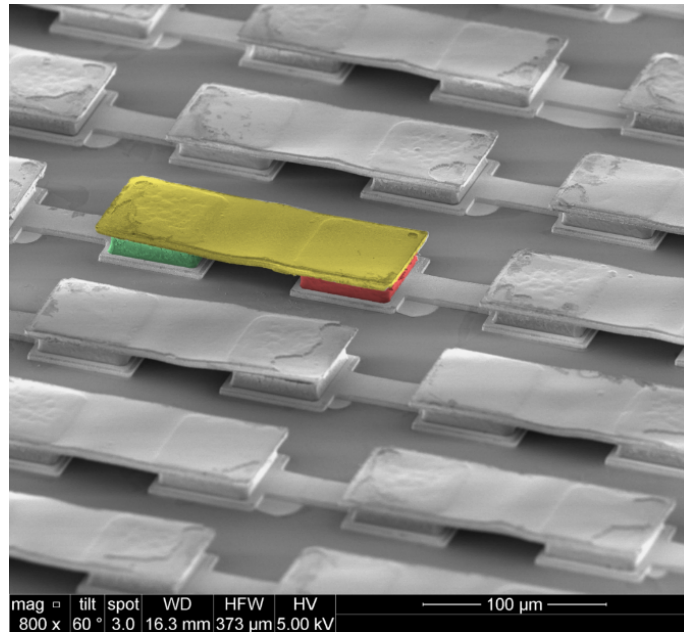


Figure 8.3: SEM image of the fabricated micro-thermoelectric device.

8.4 Simulations

In order to evaluate and optimise the device performance on the basis of geometrical alteration, detailed finite element analysis has been carried out using the material properties which have been calculated/measured before. COMSOL Multiphysics simulation and development software is used to investigate and analyse the performance of the TEG structure using Heat transfer module and AC/DC module in this study. Thermoelectric leg-pair and device are modelled and analysed. The finite element analysis is a powerful tool for solving partial differential equations which characterizes the system as a whole. In general, this method breaks up the structure or domains that are governed by a set of equations into a finite number of elements called a mesh and solves the differential equation with the provided boundary conditions that help to estimate the performance of the fabricated devices. This study also gives us the scope to provide a firm roadmap that would aid in further enhancing and optimising the device output with the alteration of the associated parameters.

Governing equations

The modelling of thermoelectric devices requires leg pair calculation and thermoelectric effects and heat transfer. The governing equations of energy conservations and charge continuity are given by [36]-

$$\nabla(k\nabla T) + \rho j^2 - T \vec{j} \left[\left(\frac{\partial s}{\partial T} \right) \nabla T + (\nabla S)_T \right] = 0 \quad 8.2$$

$$\nabla \cdot \vec{j} = 0 \quad 8.3$$

Where

$$\vec{j} = -\sigma(\nabla E + S\nabla T) \quad 8.4$$

Where k is the thermal conductivity, J is the electric current density, ρ is the electric resistivity, $\sigma = 1/\rho$ is electric conductivity, S is the Seebeck coefficient, E is the electrostatic potential and e is the charge of charged particles.

TEG structure and model

The TEG device is composed of one or more thermoelectric leg pairs. The building block of a TEG device is a pair of P-type and N-type legs that are connected electrically in series and thermally in parallel. The two legs are connected on one side by an electrical conductor forming a junction. A schematic of the TEG single unit is shown in fig. 8.4. The voltage at the terminal connected to the N-type leg on the cold side of TEG is denoted by V_a , while the voltage at the terminal connected to the P-type leg on the cold end of the TEG is denoted by V_b .

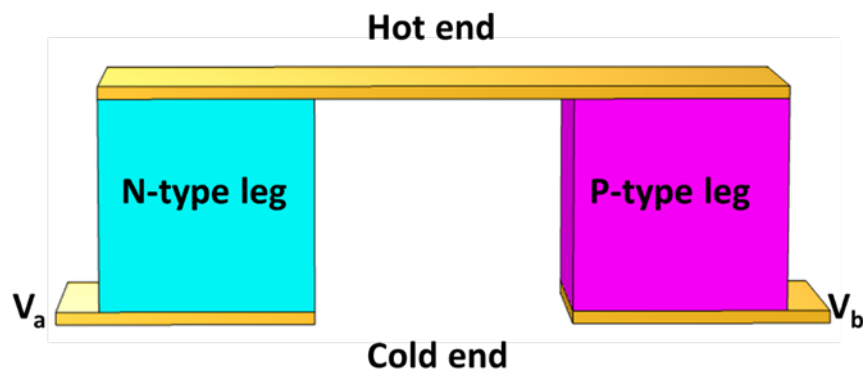


Figure 8.4: Schematic of a thermoelectric leg-pair.

Generally, the performance of the TEG device is evaluated by two parameters. The output power (P) and efficiency (η). When there is a temperature gradient ΔT between the two surfaces of the thermocouple, an output voltage V_0 is given as-

$$V_0 = n \cdot (S) \cdot \Delta T \quad 8.5$$

Where n is the total number of thermocouples, $S = (S_p - S_n)$, S_p and S_n are the Seebeck coefficients for the P-type and N-type materials, respectively. The output power P is

dependent on both the TEG internal electrical resistance R_{in} and the load resistance R_L connected externally which is expressed as [37]-

$$P = I^2 \cdot R_L = \left(\frac{n \cdot S \cdot \Delta T}{n \cdot R + R_L} \right)^2 \cdot R_L \quad 8.6$$

The maximum electrical output power of the TEG is obtained when the load resistance is equal to the internal resistance of the device ($R_L = R_{in}$) and is given as-

$$P_{max.} = n \cdot \frac{(S \cdot \Delta T)^2}{4R} \quad 8.7$$

The conversion efficiency of a TEG is the ratio between the electric output power P delivered to the load and rate of heat Q_h absorbed at the hot end.

$$\eta_{TEG} = \frac{P}{Q_h} \quad 8.8$$

For the ease of analysis, the following assumptions are taken into account-

- a. All the surface except the cold end and hot end are considered to possess heat insulation.
- b. Heat convection and heat radiations on all the surface has been neglected.
- c. All electrical contact resistance and thermal contact resistance have not been considered.
- d. The N-type and the P-type legs have the same cross-sectional area and length.
- e. All temperature differences ΔT , have been defined as the difference between the average temperature of the upper surface of the top contact and the bottom of the substrate, which have been constrained at 300 K.

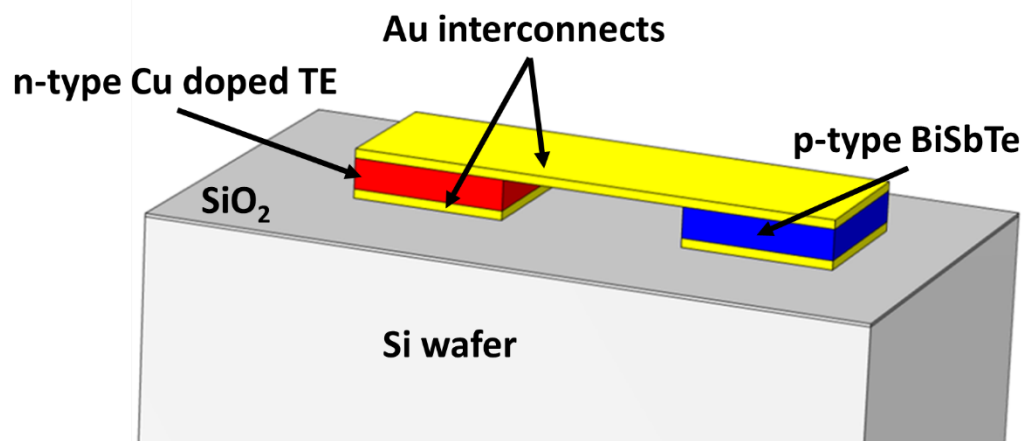
The values used for geometrical dimensions as well as electrical, thermal, and thermoelectric materials properties of all components are found in table 8-1.

Table 8-1: Materials properties along with the geometrical dimensions used for the simulations.

Materials	Dimension (Width)x(length)x(height) (μm)	Electrical conductivity (S m^{-1})	Seebeck coefficient (μVK^{-1})	Thermal conductivity ($\text{Wm}^{-1}\text{K}^{-1}$)
N-type	50×50×10	10.9e4	-227	0.6
P-type	50×50×10	2.6e4	90.5	0.6
Gold	50×50×3 (Bottom) 160×50×3 (Top)	45.6e6	6.5	317
Silicon Dioxide	390×118×1	Electrically isolated	Electrically isolated	1.4
Silicon	390×118×500	Electrically isolated	Electrically isolated	130

For single leg pair

Figure 8.5 shows the reference structure of the unicouple. Si/SiO₂ used as substrate and the thermoelectric materials were defined as electrochemically deposited Cu doped Te (n-type), and BiSbTe (p-type) sandwiched between the gold electrodes. The thickness of the gold electrode is 3 μm . The size of both the n-type legs and p-type legs are 50×50×10 μm .

**Figure 8.5: Schematic of the unicouple along with the respective materials used.**

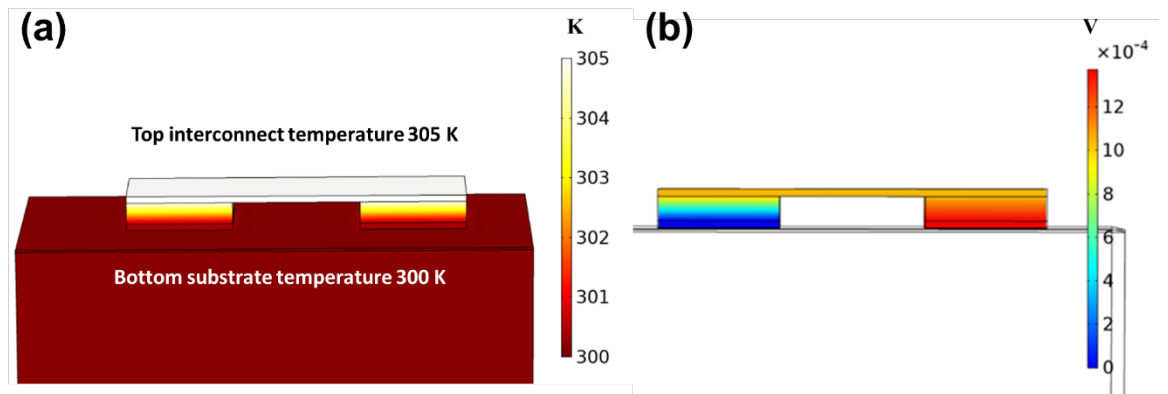


Figure 8.6: Simulation results of unicumple for $\Delta T=5K$ (a) Temperature distribution (b) Output voltage distribution.

Temperature and generated voltage distribution have been investigated and shown in figure 8.6 (a) and (b). Figure 8.6(a) shows the temperature distribution across the top and the bottom interconnect, which have been fixed to 300 K and 305 K, respectively. The temperature distribution across looks identical because of the identical thermal conductivities of the materials being used. Figure 8.6(b) shows the generated potential between the ground contact to the terminal. It can be observed that the potential is developed in the p and n-type thermoelectric materials and Au acts as an electrical interconnect material with negligible potential development.

The thermoelectric generator performance is evaluated on the unicumple subjecting it to different temperature gradient from 1 K to 5 K respectively. The current output of the unicumple subjected to different load resistance has been shown in figure 8.7(a), and the corresponding voltages with respect to the increasing load resistance have been plotted and shown in figure 8.7(b). The calculated power output using the obtained voltage and current values have been plotted and shown in figure 8.7(c). The internal resistance of unicumple affects the current passing through it, which determine the output power. So, it is essential to study the internal resistance characteristics. In figure 8.7(c), a minimal increase in output power appears at the initial development period. With the increase in load resistance, the output power increases first, reaches a maximum point, and then decreases gradually. This maximum output power is obtained when the load resistance equals the internal resistance of the unicumple. It is also noticeable from the graph that with the increment of the temperature difference, the internal resistance of the unicumple also increases due to the characteristics of thermoelectric materials in a specific temperature. Figure 8.7(d) shows the maximum power that could be obtained at a different temperature gradient.

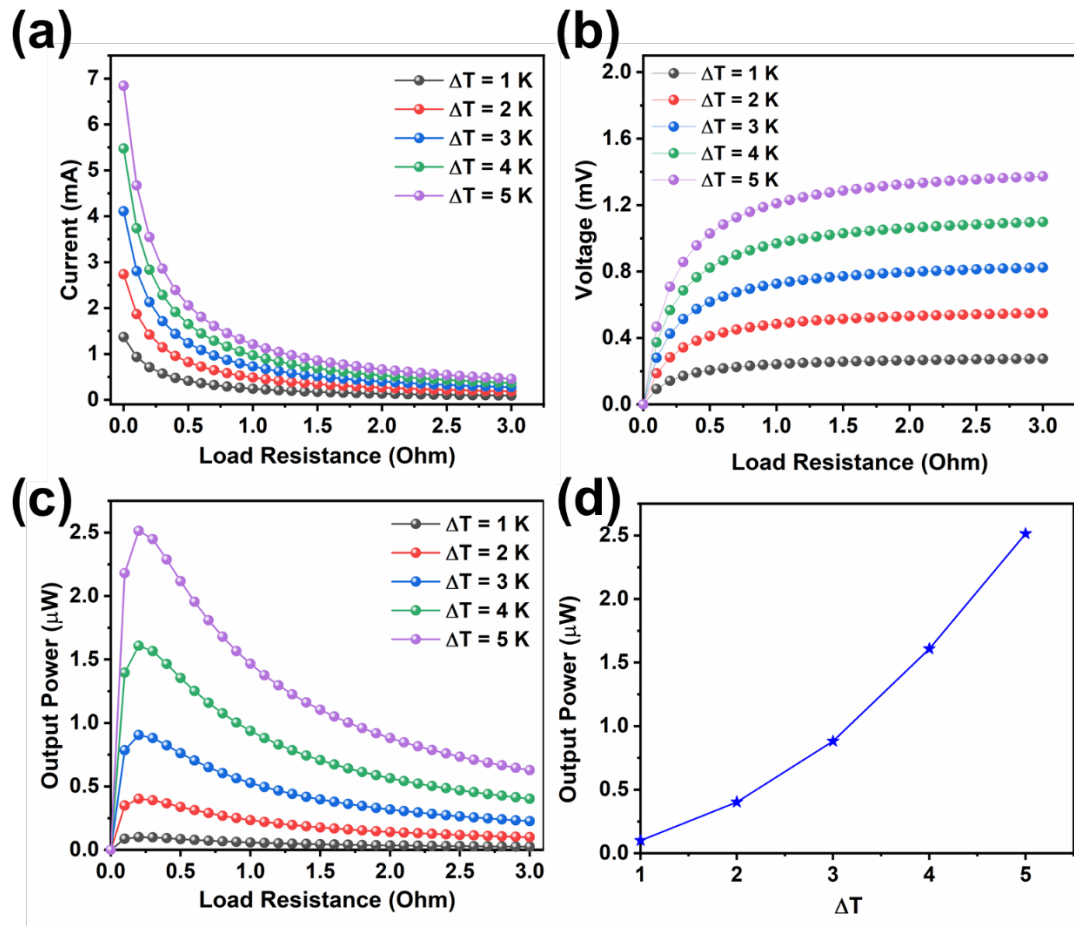


Figure 8.7: Simulation results of uncouple for $\Delta T = 1-5$ K. (a) current vs load resistance, (b) voltage vs load resistance, (c) output power vs load resistance and (d) maximum power vs ΔT .

The extended model under consideration shows thermoelectric device which consists of 210 uni-couple connected electrically in series and thermally in parallel orientation. The active area of the device is $2250 \times 2150 \mu\text{m}$. The schematic of the module is shown in figure 8.8(a). The temperature of the hot end and cold end are set as 305 K and 300 K respectively, as described in the previous section. Figure 8.8(b) depicts the voltage distribution when the device is subjected to a temperature gradient of 5 K. The change in the colour scheme represents the development of potential in the daisy chain of thermoelectric leg pairs and reaches the maximum potential at the ground terminal.

The simulated power outputs of the devices are plotted and shown in figure 8.9(a) as a function of the load resistance applied to the device. The maximum power of $443.94 \mu\text{W}$ is achieved for the device when subjected to a temperature gradient of 5 K and the load resistance of 40Ω . And the figure 8.9(b) depicts the power output and the voltage for the module as a function of electrical current. From this unimodal distribution we can observe that the device when subjected to a temperature gradient of 5 K, the maximum power

output of $443.94 \mu\text{W}$ can be achieved at a load resistance of 40Ω with a corresponding current and voltage of 3.33 mA and 133.26 mV . This performance of the device could potentially fit into the various application, as explained in the introduction section.

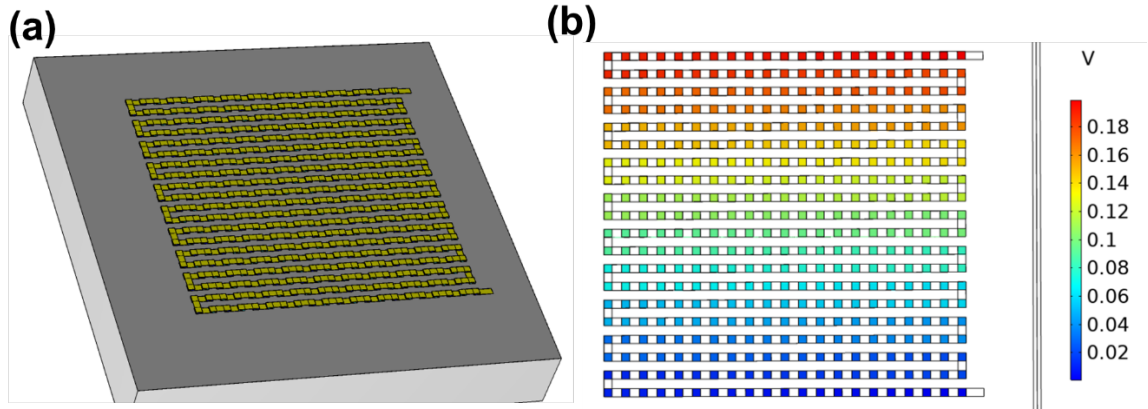


Figure 8.8: (a) Schematic diagram of the TEG module and (b) Voltage distribution of TEG module for $\Delta T=5 \text{ K}$.

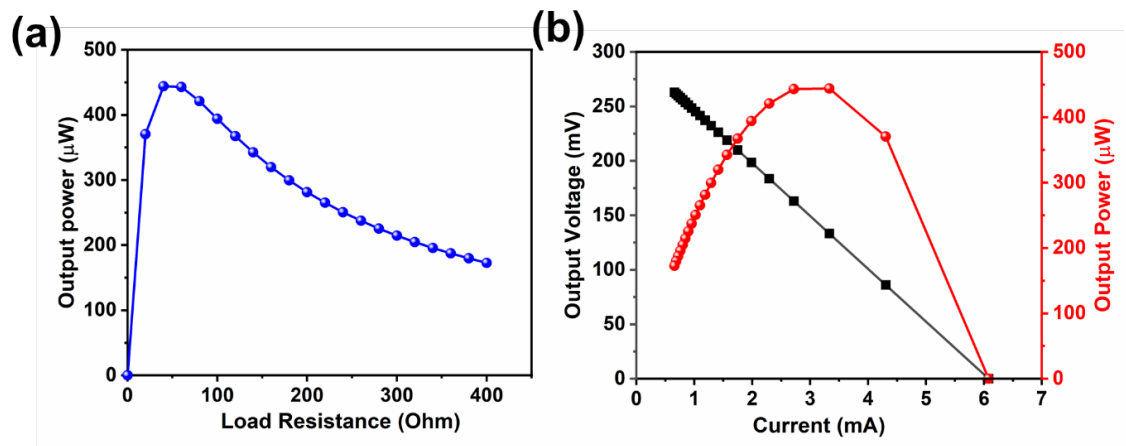


Figure 8.9: Simulation results of TEG module for $\Delta T=5 \text{ K}$, (a) output power vs load resistance (b) Voltage and output power as a function of current.

8.5 Device characterisation

The electrical resistance of the device is evaluated by plotting the electrical resistance of the increasing thermoelectric leg pairs with their corresponding resistance values and show in figure 8.10. The measured resistances are then fit linearly, and the obtained slope of the line corresponds to the average electrical resistance offered by the individual thermoelectric leg pair. The fabricated micro-TEG exhibits a low electrical device resistance of 0.28Ω . The obtained average electrical resistance of the leg pair is very much comparable to the theoretical electric resistance of the leg pair. The obtained electrical resistance is almost half of the electrical resistance of the device fabricated by the flip-chip bonding approach [31]. This ensures that the bonding between the

thermoelectric legs with the top interconnect material is ohmic, and the contact resistance is negligible.

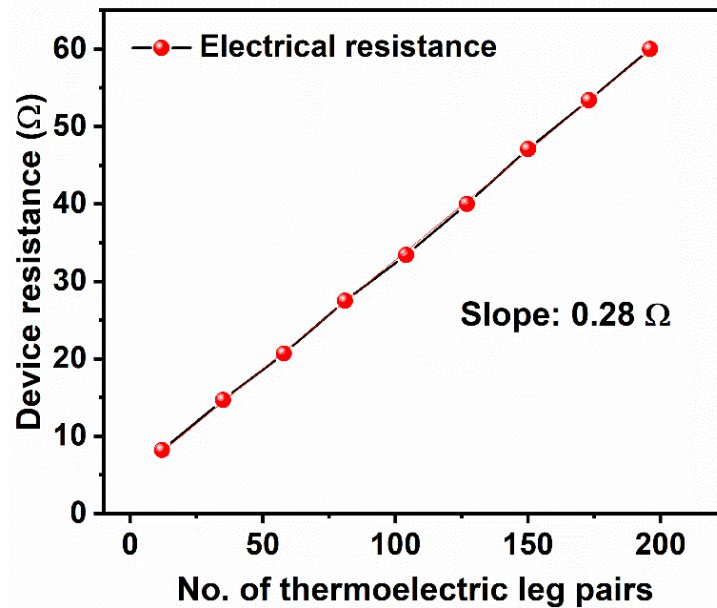


Figure 8.10: Resistance dependence on the number of thermoelectric leg pairs.

8.5.1 Cooling Performance

The thermoelectric device cooling performance evaluation is relatively easy compared to the evaluation of power generation performance due to the use of non-contact optical methods. The fabricated devices were evaluated for their cooling performance using Charge-coupled-device (CCD) based thermo-reflectance microscopy. The change in the surface reflectivity of the material with a change in temperature is quantified using this technique. Once the top surface reflectivity is calibrated, this technique can precisely measure the change in temperature. When a current is applied to the thermoelectric device, the heat is absorbed or rejected at the top and bottom interconnects depending on the current polarity. And this change in the temperature of the top interconnects can be measured using the CCD technique. However, this technique is very sensitive to the roughness of the surface being measured. The top interconnect Au is deposited using electrodeposition and exhibit roughness, unlike deposited by other physical vapour deposition techniques. This causes noise in the measured data. Figure 8.11(a) shows the CCD characterisation set-up used for the measurement of the fabricated device. Micro probes are used to connect the device electrically, and the electric current is applied using a Keithley power source. Figure 8.11(b) shows the temperature change in the top interconnect when an applied current of 200 mA on when single thermoelectric leg pair lines are activated, which consist of 11 thermoelectric leg pairs. And figure 8.11(c) shows

the temperature gradient achieved when two lines of leg pair in the daisy chain are activated. From the temperature scale, it can be seen that the average temperature difference achieved when applied with 200 mA current is ~ 9 -10 K. However, a considerable noise and discrepancy can be observed in these measurements due to the roughness of the electrodeposited gold and reduced reflectivity of the electrodeposited gold due to the rigorous wet chemical processing on the device. Few changes in the temperature measured are much greater at places, and this is due to the change in the height of the Au on the pillar compared to the areas of the connecting joint, this effect might also have come from the increased contact resistance with the pillars due to the bonding issues.

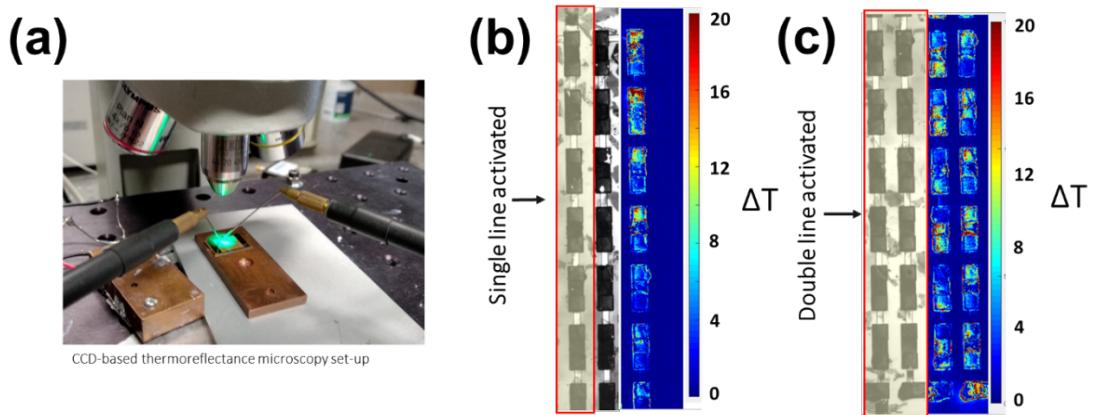


Figure 8.11: (a) CCD based thermoreflectance microscopy set-up, (b) Thermal image of the single daisy chain line activated and (c) Thermal image of the double lines activated with the temperature scale bar.

The cooling performance of the device was also evaluated by using infrared (IR) thermal microscopy. The thermal images of the fabricated device were recorded applying 80 mA of current to the device. Due to the lower emissivity of the Au, the device had to be covered using a non-conductive black adhesive paint to increase the emissivity and decrease the thermal noise. The system is first calibrated to room temperature, and the change in the temperature with time is recorded using the FLIR thermal IR camera. The thermal images of the device with applied current 0 mA and 80 mA are shown in figure 8.12 (a) and (b) respectively. And the plot depicting the temperature gradient when applied with current with respect to the time change is shown in figure 8.12(c). From this figure, we can not only evaluate the temperature gradient achieved for a particular current but also estimate the response time of the device. The device, when applied with 80 mA of current, led to a temperature gradient of 2 K with very fast response time as can be seen in figure 8.12(c). However, it can be seen from the IR image that one pillar depict

higher temperature gradient than the other, and this might be due to the change in the Seebeck properties of the material.

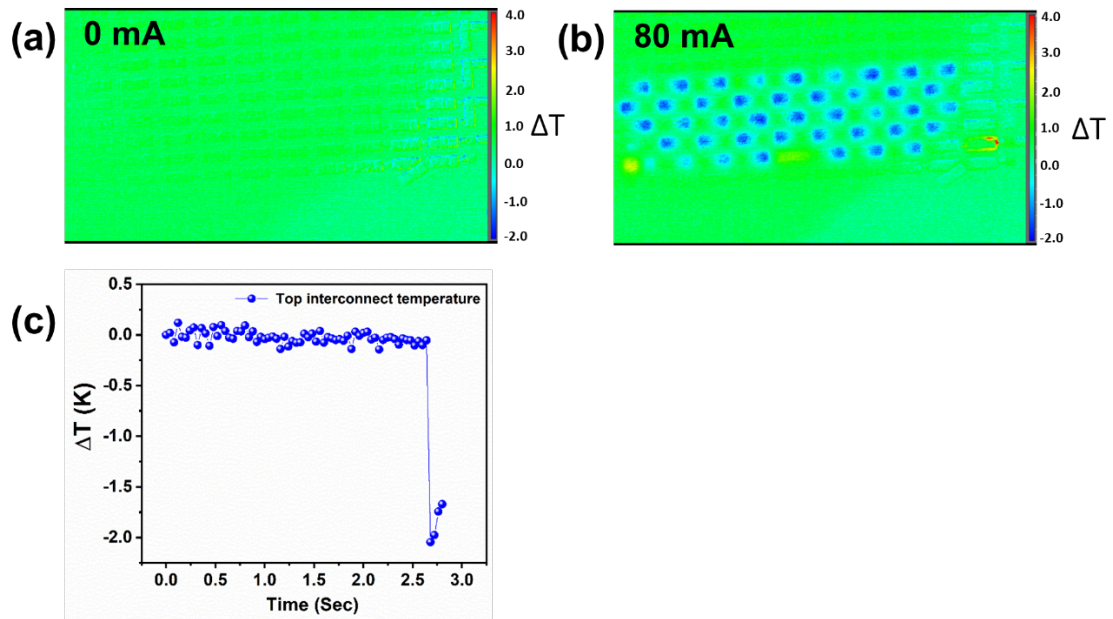


Figure 8.12: (a) IR surface thermal image of the device with no current applied, (b) IR surface thermal image of the device applied with 80 mA current and (c) Temperature differential plot recorded on the top interconnect with the time.

8.5.2 Power Generation performance

The evaluation of μ TEGs is most challenging due to its miniaturised size, multiple parasitic resistances and ability to maintain precise temperature gradient across the generator. The small contact surfaces and impracticality of using a high-conductance permanent bond in the test fixture lead to large thermal contact resistances at the boundaries.

Micro thermoelectric device evaluation set-up is designed to precisely subject the device with a temperature gradient ($\Delta T=1 - 50\text{ }^{\circ}\text{C}$) with a precision of $\pm 0.2\text{ }^{\circ}\text{C}$. The fabricated μ TEGs are mounted on a specially designed test board and will be subjected to different temperature gradients using a resistive heater and a commercially available Peltier cooler, in contact with two copper bars as shown in Figure 8.13. The two copper calorimeter bars will sandwich the TEG. Thereby, the device can be subjected to a wide range of temperature gradients. The measurement system developed will also be capable of measuring the heat flux through the device, and the thermal resistance of the device can be evaluated.

The upper copper bar is screwed into an aluminium heater block in which 250W cartridge heaters are fitted. The bottom copper bar is in direct contact with the Peltier cooler.

Thermistors were fitted into the holes with a small amount of thermal compound (thermal interface material) to improve thermal contact. Strain relief provided to thermistor beads by soldering their leads to an adhesive strip soldering plate which was mounted along the side surfaces of the bars.

Thermistor resistance was measured by using 2 National Instruments TM DAQ-mx USB cards equipped with 4-channels each in 2-wire resistance configuration using a built-in low excitation current to feed the thermistor resistances. Thermistors are temperature probes made from metallic oxides, which exhibit a large change in resistance for a small change in temperature. High nominal resistance values at 25 °C ensure negligible resistance effects in the lead wires whereas these might cause errors in devices such as RTDs whose nominal resistance @ 25 °C is much lower. They are not only cheaper than other resistance-based probes and exhibit high reliability if compared to thermocouples and are quite stable in displaying temperature with usage. Also, good accuracy can be achieved with a proper calibration system because probe accuracy is the factor, which mostly affects the overall measured quantities.

In order to precisely control the load acting on the device, a piezo-resistive load cell is used. As soon as the copper rods get in contact with the device, the linear actuation of the upper copper bars stops ensuring the desired thermal contact between the device and the copper bar. For reducing the interfacial resistance between the device and the copper bars, thermal paste is applied on both the ends of the copper bars.

Once the device is in proper contact with both the copper bars, the thermal gradient can be induced on the device using the resistive heater, and the cooler using the Agilent power source and the gradient can be measured using all the eight thermistors. A LabView program has been designed to completely control the actuation, load, measuring of the temperature gradient applied across the μ TEG and the voltage and current output from the micro-device.

The device is placed in between the copper rods and in proper contact using the boron nitride thermal paste. The device is subjected to a temperature gradient of 5 K slowly using the resistive heater and commercial Peltier module as described earlier. The image of the system, along with the device, is shown in figure 8.13. In this case, 11 thermoelectric leg pairs are subjected to a temperature differential of 5 K, and an output open-circuit voltage of 3.08 mV was measured. The total device constitutes of 210 leg pairs which, when activated, can lead to an open-circuit voltage of 58.8 mV. The obtained

open-circuit voltages at 5 K temperature gradient are less compared to the model evaluation. However, this could be due to the degraded material properties during the device fabrication due to multiple thermal cycling during the lithographic processes as well as the exposure to thermoelectric material with various etchants. Further work needs to be done on the optimisation of the material properties, which could help to achieve the anticipated performance.

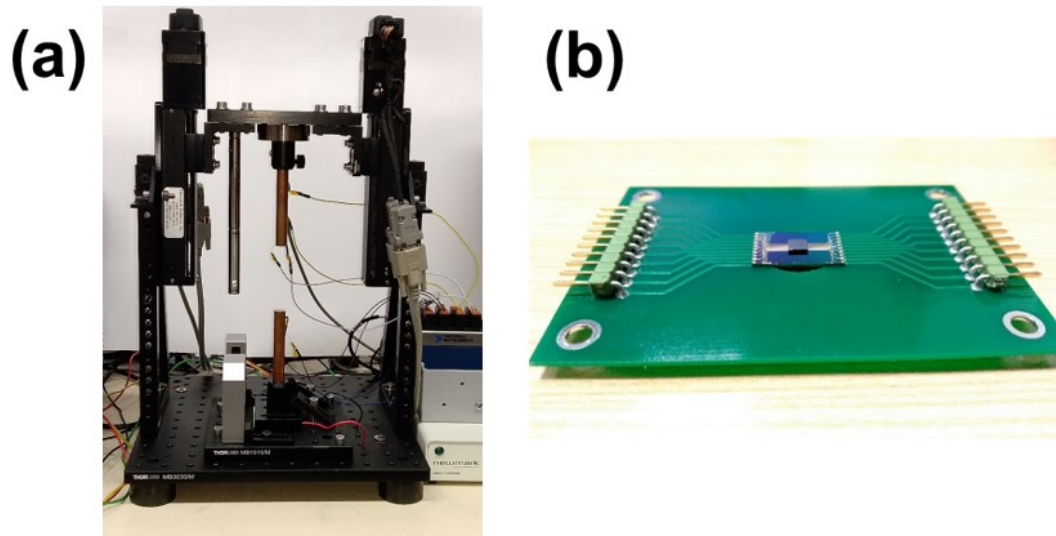


Figure 8.13: (a) Micro thermoelectric device characterisation set-up and (b) Micro device mounted on the test board.

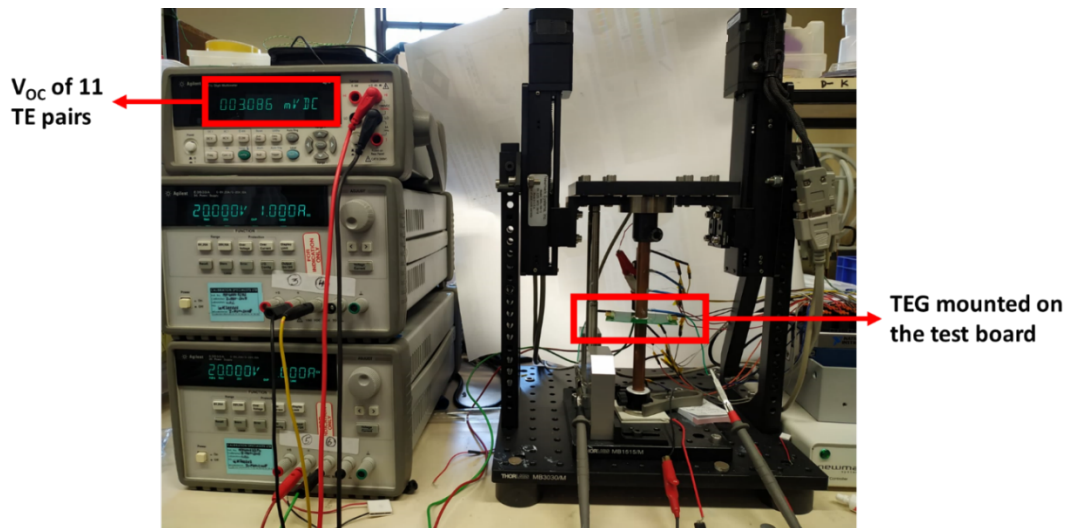


Figure 8.14: Schematic of the measurement set-up for obtaining the open-circuit voltage of the fabricated micro-TEGs at different ΔT .

8.6 Conclusion

In this work, we have successfully fabricated a cross-plane micro thermoelectric device employing electrodeposition technique for the material fabrication for the microdevice. P-type BiSbTe and n-type Cu doped Te materials are used as the thermoelectric materials

and Au is used as the interconnect material. Through a detailed COMSOL simulation the device performance is evaluated, and the expected device performance at different low-temperature gradients are presented. Furthermore, the device was successfully fabricated with a very low electrical device resistance of 58.8 Ω . For this, electrodeposition of the thermoelectric material, as well as the interconnect materials, played a crucial role in decreasing the contact resistance of the device, which is negligibly small. The fabricated device has been tested for cooling performance using the CCD technique and IR thermal imaging. It was observed that the fabricated devices are capable of creating ~ 9 -10 K cooling when applied with 200 mA of current and cooling of 2 K when applied with 80 mA of current. However, the cooling is observed to be non-homogeneous; this is due to the non-homogeneous thermoelectric properties of the material. Further material development work needs to be carried out to match the p-type material property with the n-type to achieve an effective homogenised cooling performance. A new characterisation set-up has been built to evaluate the thermoelectric generation performance of micro-thermoelectric devices. The device has been successfully evaluated for a temperature gradient of 5 K and for 11 active thermoelectric pairs, and an open-circuit voltage of 3.08 mV was developed. To estimate the overall open-circuit voltage that could be developed with all the 210 active thermo-legs would lead to a potential of 58.8 mV. This generated electrical energy could be effectively used for powering wireless sensor nodes especially due to the low-temperature gradient in which the device works, making it a suitable candidate for the wearable applications. These fabricated devices have the potential to generate useful energy by converting body heat into electricity.

8.7 References

- [1] M. Bertocco, G. Gamba, A. Sona, and S. Vitturi, "Experimental Characterization of Wireless Sensor Networks for Industrial Applications," *IEEE Transactions on Instrumentation and Measurement*, vol. 57, no. 8, pp. 1537-1546, 2008.
- [2] H. B. Lim, D. Ma, B. Wang, Z. Kalbarczyk, R. K. Iyer, and K. L. Watkin, "A Soldier Health Monitoring System for Military Applications," in *2010 International Conference on Body Sensor Networks*, 2010, pp. 246-249.
- [3] F. Mieyeville, W. Du, I. Daikh, and D. Navarro, "Wireless Sensor Networks for active control noise reduction in automotive domain," in *2011 The 14th International Symposium on Wireless Personal Multimedia Communications (WPMC)*, 2011, pp. 1-5.

- [4] C. Meesookho, S. Narayanan, and C. S. Raghavendra, "Collaborative classification applications in sensor networks," in *Sensor Array and Multichannel Signal Processing Workshop Proceedings, 2002*, 2002, pp. 370-374.
- [5] P. G. Bruce, S. A. Freunberger, L. J. Hardwick, and J.-M. Tarascon, "Li–O₂ and Li–S batteries with high energy storage," *Nature Materials*, Review Article vol. 11, p. 19, 12/15/online 2011.
- [6] X. Pu, W. Hu, and Z. L. Wang, "Toward Wearable Self-Charging Power Systems: The Integration of Energy-Harvesting and Storage Devices," *Small*, vol. 14, no. 1, p. 1702817, 2018.
- [7] S. Pan, J. Ren, X. Fang, and H. Peng, "Integration: An Effective Strategy to Develop Multifunctional Energy Storage Devices," *Advanced Energy Materials*, vol. 6, no. 4, p. 1501867, 2016/02/01 2016.
- [8] A. S. Weddell, M. Magno, G. V. Merrett, D. Brunelli, B. M. Al-Hashimi, and L. Benini, "A survey of multi-source energy harvesting systems," in *2013 Design, Automation & Test in Europe Conference & Exhibition (DATE)*, 2013, pp. 905-908.
- [9] A. R. M. Siddique, S. Mahmud, and B. V. Heyst, "A review of the state of the science on wearable thermoelectric power generators (TEGs) and their existing challenges," *Renewable and Sustainable Energy Reviews*, vol. 73, pp. 730-744, 6// 2017.
- [10] L. Yang, Z.-G. Chen, M. S. Dargusch, and J. Zou, "High Performance Thermoelectric Materials: Progress and Their Applications," *Advanced Energy Materials*, vol. 8, no. 6, p. 1701797, 2018/02/01 2018.
- [11] L. Bell, "Cooling heating, generating power, and recovering waste heat with thermoelectric systems," *Science*, vol. 321, pp. 1457-1461, // 2008.
- [12] J. Yan, X. Liao, D. Yan, and Y. Chen, "Review of Micro Thermoelectric Generator," *Journal of Microelectromechanical Systems*, vol. 27, no. 1, pp. 1-18, 2018.
- [13] M. Zebarjadi, K. Esfarjani, M. S. Dresselhaus, Z. F. Ren, and G. Chen, "Perspectives on thermoelectrics: from fundamentals to device applications," *Energy & Environmental Science*, 10.1039/C1EE02497C vol. 5, no. 1, pp. 5147-5162, 2012.
- [14] G. J. Snyder and E. S. Toberer, "Complex thermoelectric materials," *Nat Mater*, 10.1038/nmat2090 vol. 7, no. 2, pp. 105-114, 02//print 2008.

- [15] L. E. Bell, "Cooling, Heating, Generating Power, and Recovering Waste Heat with Thermoelectric Systems," *Science*, vol. 321, no. 5895, pp. 1457-1461, 2008-09-12 00:00:00 2008.
- [16] F. Suarez, A. Nozariasbmarz, D. Vashaee, and M. C. Ozturk, "Designing thermoelectric generators for self-powered wearable electronics," *Energy & Environmental Science*, 10.1039/C6EE00456C vol. 9, no. 6, pp. 2099-2113, 2016.
- [17] A. S. Dahiya *et al.*, "Review—Energy Autonomous Wearable Sensors for Smart Healthcare: A Review," *Journal of The Electrochemical Society*, vol. 167, no. 3, p. 037516, 2020/01/02 2020.
- [18] G. J. Snyder, J. R. Lim, C.-K. Huang, and J.-P. Fleurial, "Thermoelectric microdevice fabricated by a MEMS-like electrochemical process," *Nat Mater*, 10.1038/nmat943 vol. 2, no. 8, pp. 528-531, 08//print 2003.
- [19] W. Glatz, E. Schwyter, L. Durrer, and C. Hierold, "Bi₂Te₃-Based Flexible Micro Thermoelectric Generator With Optimized Design," *Journal of Microelectromechanical Systems*, vol. 18, no. 3, pp. 763-772, 2009.
- [20] U. Pelz, J. Jaklin, R. Rostek, F. Thoma, M. Kröner, and P. Woias, "Fabrication Process for Micro Thermoelectric Generators (μ TEGs)," *Journal of Electronic Materials*, vol. 45, no. 3, pp. 1502-1507, 2016/03/01 2016.
- [21] R. Rostek, N. Stein, and C. Boulanger, "A review of electroplating for V–VI thermoelectric films: from synthesis to device integration," *Journal of Materials Research*, vol. 30, no. 17, pp. 2518-2543, 2015.
- [22] Q. H. Zhang, X. Y. Huang, S. Q. Bai, X. Shi, C. Uher, and L. D. Chen, "Thermoelectric Devices for Power Generation: Recent Progress and Future Challenges " *Advanced Engineering Materials*, vol. 18, no. 2, pp. 194-213, 2016.
- [23] H. Bottner, "Thermoelectric micro devices: current state, recent developments and future aspects for technological progress and applications," in *Twenty-First International Conference on Thermoelectrics, 2002. Proceedings ICT '02.*, 2002, pp. 511-518.
- [24] I. Chowdhury *et al.*, "On-chip cooling by superlattice-based thin-film thermoelectrics," (in English), *Nature Nanotechnology*, Article vol. 4, no. 4, pp. 235-238, 2009.
- [25] F. J. DiSalvo, "Thermoelectric Cooling and Power Generation," *Science*, vol. 285, no. 5428, pp. 703-706, 1999.

- [26] H. Bottner, "Micropelt miniaturized thermoelectric devices: small size, high cooling power densities, short response time," in *ICT 2005. 24th International Conference on Thermoelectrics, 2005.*, 2005, pp. 1-8.
- [27] M.-Y. Kim and T.-S. Oh, "Thermoelectric Thin Film Device of Cross-Plane Configuration Processed by Electrodeposition and Flip-Chip Bonding," *MATERIALS TRANSACTIONS*, vol. 53, no. 12, pp. 2160-2165, 2012.
- [28] R. Roth, R. Rostek, G. Lenk, M. Kratschmer, K. Cobry, and P. Woias, "Two-layer process for a micro thermoelectric cross-plane generator with electroplating and reflow soldering," in *2013 Transducers & Eurosensors XXVII: The 17th International Conference on Solid-State Sensors, Actuators and Microsystems (TRANSDUCERS & EUROSENSORS XXVII)*, 2013, pp. 486-489.
- [29] M.-Y. Kim and T.-S. Oh, "Preparation and Characterization of Bi₂Te₃/Sb₂Te₃ Thermoelectric Thin-Film Devices for Power Generation," *Journal of Electronic Materials*, journal article vol. 43, no. 6, pp. 1933-1939, 2014.
- [30] K.-J. Shin and T.-S. Oh, "Micro-Power Generation Characteristics of Thermoelectric Thin Film Devices Processed by Electrodeposition and Flip-Chip Bonding," *Journal of Electronic Materials*, vol. 44, no. 6, pp. 2026-2033, 2015// 2015.
- [31] S. Lal, D. Gautam, and K. M. Razeeb, "Fabrication of micro-thermoelectric devices for power generation and the thermal management of photonic devices," *Journal of Micromechanics and Microengineering*, vol. 29, no. 6, p. 065015, 2019/05/10 2019.
- [32] R. Roth *et al.*, "Design and Characterization of Micro Thermoelectric Cross-Plane Generators With Electroplated Bi₂Te₃, Sb_xTe_y, and Reflow Soldering," *Journal of Microelectromechanical Systems*, vol. 23, no. 4, pp. 961-971, 2014.
- [33] W. Zhang, J. Yang, and D. Xu, "A High Power Density Micro-Thermoelectric Generator Fabricated by an Integrated Bottom-Up Approach," *Journal of Microelectromechanical Systems*, vol. 25, no. 4, pp. 744-749, 2016.
- [34] S. Lal, D. Gautam, and K. M. Razeeb, "Optimization of annealing conditions to enhance thermoelectric performance of electrodeposited p-type BiSbTe thin films," *APL Materials*, vol. 7, no. 3, p. 031102, 2019/03/01 2019.
- [35] S. Lal, K. M. Razeeb, and D. Gautam, "Enhanced thermoelectric properties of electrodeposited Cu-doped Te films," *ACS Applied Energy Materials*, 2020/04/02 2020.

- [36] Y. Wu, T. Ming, X. Li, T. Pan, K. Peng, and X. Luo, "Numerical simulations on the temperature gradient and thermal stress of a thermoelectric power generator," *Energy conversion and management*, vol. 88, pp. 915-927, 2014.
- [37] D. Enescu, "Thermoelectric Energy Harvesting: Basic Principles and Applications," in *Green Energy Advances*: IntechOpen, 2019.

Chapter 9: Conclusions and Future Works

9.1 Thesis summary and main results

The primary aim of this work is the development of high-efficiency thermoelectric materials compatible with the silicon fabrication technology and integrating the developed thermoelectric materials into the micro-thermoelectric devices which aims for the thermal management of photonic devices and as well as power generation from human body heat, suitable for the application of wearable health monitoring system.

Both of these applications (power generation and thermal management) require high-performance thermoelectric materials and novel, cost-effective device fabrication techniques for these micro-devices to be applied in the real-world scenarios. Over the past two decades, the enhancement of thermoelectric material property and optimization of the fabricated μ TED devices have drawn significant research attention. The conventional microfabrication techniques, e.g., electrochemical deposition offers various advantages. Owing to the cost-effectiveness and high scalability, the electrodeposition technique is becoming attractive compared with the other traditional fabrication techniques like epitaxial growth, evaporation or sputtering. Thermoelectric material is evaluated based on its high figure of merit ($ZT=S^2\sigma T/k$), high power factor ($S^2\sigma T$) and low thermal conductivity (k). The maximum value of ZT of the thermoelectric materials has reached new highs over the past two decades for different thermoelectric materials. Bismuth telluride based p- and n-type materials are the most promising materials for devices working at near room temperature regime. Thereby, our primary focus is to develop cost-effective electrodeposited thermoelectric material demonstrating superior thermoelectric properties and integrate them in μ -TED through batch fabrication.

The salient key features of this thesis work are listed below:

The development of high performance thermoelectric thin-films using the cost-effective electrochemical deposition.

Strategies used to further enhance the thermoelectric material properties during and post-material deposition.

Fabrication of low cost, vertical-structure, free-standing micro-thermoelectric devices using only electrodeposition technique for the complete device fabrication.

Two different fabrication strategies performed for the free-standing device fabrication using single photoresist dragging down the cost of overall device fabrication.

The important findings from the studies for each of these areas are described in the following section:

9.2 Material development for high performance thermoelectric thin films

9.2.1 Material property enhancement through additives

Different additives in electrodeposition are used for various purposes. The use of additives like surfactants is capable of altering the microstructure of the material films deposited. Depending on the concentrations of additives into the electrolyte, the presence of the same could significantly affect the property of the deposit. Not only in the microstructural changes but also can change the physical properties of the films such as smoothness, density, the brightness of the electrodeposited films. As they form a part of the electrolyte, surfactants can also participate and have the capability of affecting different deposition parameters and affect the overall material property of the material.

The effect of anionic surfactant Sodium dodecyl sulfate (SDS) was investigated on the p-type $(\text{Sb}_{1-x}\text{Bi}_x)_2\text{Te}_3$ thin films deposited using pulsed electrodeposition. Undoubtedly, homogeneous thin-film thermoelectric materials with the addition of surfactant offer a promising strategy for the fabrication of high-performance thermoelectric devices. The critical finding of this study have been listed below:

- i. Usually, the electrodeposited p-type BiTe based materials are dendritic and rough, and this causes a challenge during the fabrication of the device. With the introduction of surfactant SDS into electrolyte with 0.8 mM concentration results in smooth and dense films of p-type bismuth antimony telluride (Bi-Sb-Te).
- ii. The addition of a surfactant modifies interfacial tension between the solution and the electrode. This enables ease of escape to the gas bubbles from the electrode surface, due to which formation of pinholes and pitting were eliminated.
- iii. The films deposited in the presence of SDS showcased a Seebeck coefficient of $90.50 \mu\text{V/K}$ post-annealing at $350 \text{ }^\circ\text{C}$ in N_2 atmosphere, which is 49% higher compared to films deposited without the SDS. The overall power factor achieved for these films was $263.72 \mu\text{W/mK}^2$ almost twice the value compared to the films without the surfactant.

9.2.2 Material property enhancement through post-deposition annealing

Annealing plays a vital role in enhancing the thermoelectric properties of electrodeposited films. Usually, the electrodeposited thermoelectric materials possess lower mobility

values and crystallinity. Controlled annealing of the deposited materials can increase the crystallinity as well as the mobility of the materials. As a result, the electrical conductivities of the materials can be refined. However, it has a corresponding effect on the charge carrier densities, which are decreased mainly due to a decrease in the density defect. Controlled annealing of the materials can be used to fine-tune the thermoelectric properties of the films by tuning the annealing parameters. This also facilitates to achieve the stoichiometry of the deposited films helping in controlled and reproducible thermoelectric properties of the films.

Therefore, annealing is an important step that can improve the thermoelectric properties of as-deposited thin films. Upon fine-tuning the annealing parameters, the properties of the films can be varied drastically, which has been investigated in detail for p-type BiSbTe thermoelectric materials in this work. This work studied the effect of annealing parameters (time-temperature) on the thermoelectric properties of electrodeposited BiSbTe based ternary alloy system. The thermal treatment of the deposited materials was carried out in rapid thermal annealing (RTA) for a time period of 15 min to 1 h and at different temperatures ranging from 200 °C to 400 °C under controlled heating and cooling rates in the presence of N₂ atmosphere. The salient features of the work have been outlined below:

The effect of annealing parameters on the TE properties of electrodeposited p-type BiSbTe films is studied using various annealing temperatures and times in the nitrogen atmosphere. The impact of annealing temperature-time profile on the microstructure and TE properties were investigated in detail.

Innovative use of Te intermediate layer helping to replenish the depleted Te during annealing. This technique will eliminate the use of Te atmosphere during annealing and excessive annealing time.

Our study demonstrates control over the carrier concentration and mobility by tuning the annealing parameters. The Seebeck coefficient values of the annealed films increase with the annealing temperature, leading to an optimum value of 90.5 $\mu\text{V/K}$ when annealed at 350 °C for 1 h duration in a nitrogen atmosphere under controlled heating and cooling rates. The maximum power factor of 225 $\mu\text{W/mK}^2$ is achieved for the same annealing conditions as above.

9.2.3 Material property enhancement through doping/co-deposition strategy

Doping of different elements is a possible way to enhance the electrical conductivity of thermoelectric materials. Doping also can change the microstructure due to difference of the ionic radius of the dopant material with that of the base material and due to crystal lattice being replaced. It can also be used in altering the electrochemical co-deposition mechanisms. Doping in the material deposited by electrodeposition technique can be performed during the same conventional process with no additional steps required.

9.2.3.1 Doping of Cu in BiTe using electrodeposition

The room-temperature phase transition CuBiTe films with Cu addition by simple electrodeposition technique is developed and evaluated. The experiments are methodically planned and deposited materials with increasing concentration of Cu in the BiTe bath developed in order to analytically comment on the role of Cu doping on BiTe films.

The salient features of the work have been outlined below:

- i. Dopant based phase transition strategy by developing a copper-doped BiTe thin films via electrodeposition has been studied.
- ii. Crystal symmetry breakdown from crystalline to amorphous is evaluated rigorously. It has been observed through the experimental results that just over 13% Cu doping results in crystal symmetry breaking from crystalline to amorphous.
- iii. An Ultra-low thermal conductivity has been achieved for these films ($0.347 \text{ Wm}^{-1}\text{K}^{-1}$).
- iv. Highest Seebeck coefficient of $-275 \mu\text{V/K}$ is achieved for the film with 1 mM Cu concentration in the electrolytic bath.
- v. Extortionate Seebeck coefficient and high electrical conductivity resulted in a high-power factor of 3.02 mW/mK^2 , which is on par with the power factor values reported in the literature.

9.2.3.2 Doping of Cu in Tellurium films using electrodeposition

Cu doped Te films were developed for thermoelectric applications at the room temperature. Films were synthesized using electrodeposition and characterized for structural and TE properties.

The prominent features of the work have been outlined below:

- i. A detailed structural analysis of the electrodeposited Cu-doped Te films has been investigated. An extensive investigation in the collapse of the crystal structure of the electrodeposited films with the effect of the addition of Cu into the Te films using different characterization techniques has been performed.
- ii. This work reports the *n*-type behaviour of these deposited materials with a colossal thermoelectric power factor of 5.6 mW/mK^2 , which is so far the best reported in the literature. This high thermoelectric performance was possible due to a high Seebeck coefficient exhibited by the material ($-227 \text{ } \mu\text{V/K}$) along with relatively high electrical conductivities of these films.
- iii. These excellent TE properties exhibited by Cu-doped Te material can lead to being a potential thermoelectric material for power generation for near room-temperature applications, especially in low-temperature gradient scenarios.

9.3 Micro thermoelectric device (μ -TED) fabrication

9.3.1 Micro-Thermoelectric device fabrication using flip-chip and single wafer approach

The device fabrication is a complex and challenging process, and two different approaches for the fabrication of the μ -TED have been adopted, namely 1) Flip-chip bonded device and 2) Single wafer approach. In the first approach, we successfully demonstrated and explored the fabrication procedure of cross-plane configuration, flip-chip bonded μ -TED. The electrodeposition of gold (Au) and indium (In) were also investigated, which acts as a barrier separation layer for indium diffusion and the bonding material, respectively. The impact of the bonding materials on the internal resistance of the device and the challenges faced during the flip-chip bonding of the device has been thoroughly investigated. The challenges faced during the fabrication of the μ TED and the feasible solutions to overcome the fabrication problems have been methodically presented and finally resulting in the successful implementation of electroplated micro thermoelectric devices. As part of our second approach, we have successfully integrated the developed materials (both p and n-type) in a single wafer. Although, this approach requires complex fabrication process, but leads to better performance of the device. The devices developed by both approaches were highly successful.

The salient features of both the devices fabricated are listed below:

- i) Micro-thermoelectric devices (μ TED) are fabricated using cost-effective electrochemical deposition technique, which offers industrial volume

production of these devices and is compatible with the semiconductor fabrication technology. Flip-chip bonding approach is used to fabricate the devices which cut down the lithographic steps of the device fabrication to half, ultimately making it one of the most inexpensive fabrication approaches for these devices. Inexpensive μ TED is the need of the hour due to the applications in powering up of sensors and/or to cool down the electronic chips for the internet of things (IoT).

- ii) This work discusses in detail the fabrication complexity of the cross-plane configured flip-chip bonded μ TED. The work addresses the challenges faced and the feasible solutions to develop electroplated μ TED successfully. The fabricated μ TED with a device footprint of $3.3 \times 3.3 \text{ mm}^2$ with 210 leg pairs showcased a projected output voltage of 315 mV for a temperature difference of 10 K.
- iii) The incorporation of CuTe based thermoelectric materials with high electrical conductivity led to the low electrical resistance of the individual thermoelectric leg pair of about $0.87 \text{ } \Omega$, with the total device electrical resistance of $182.7 \text{ } \Omega$. which is relatively low compared to the electrodeposited thermoelectric leg-pair literature values.
- iv) Single wafer approach was used to fabricate the devices with p-type BiSbTE and n-type Cu doped Te thermoelectric materials and Au as the interconnect material. The expected device performance is evaluated using COMSOL simulations.
- v) The fabricated device with single wafer approach showcased a low device electrical resistivity of $58.8 \text{ } \Omega$. The device constitutes 210 leg pairs, similar to the device fabricated using flip-chip bonded approach.
- vi) The cooling performance of the fabricated device was evaluated using the CCD technique and IR thermal imaging. A net cooling of $\sim 9\text{-}10 \text{ K}$ is observed when applied a current of 200 mA and a cooling of 2 K when applied with 80 mA of current.
- vii) A characterization setup is built to evaluate the power generation performance of these devices and for an active 11 thermoelectric leg pairs subjected to a temperature gradient of 5 K resulted in an open-circuit voltage

of 3.08 mV. The overall device working could lead to an open-circuit voltage of 58.8 mV for 5 K temperature gradient. Therefore, making these devices highly potential candidate for wearable applications.

9.4 Recommendation for Future Work

9.4.1 Development of materials

In this thesis, significant work has been carried out in enhancing the thermoelectric properties of materials deposited using electrodeposition techniques using various strategies like the use of additives, thermal treatments and doping of the materials. However, it leaves the scope for further developments and more insightful studies for understanding the mechanisms that will optimize the material properties.

Role of different surfactants could be studied, and the role of anionic and cationic surfactants in the electrolyte and the mechanism of altering the electrolytic deposition needs to be further investigated to control the electrodeposition of the materials being deposited. Surfactants like, sodium lignosulfonate, Benzalkonium chloride, Nafion can be used in the development of materials to understand the role of the surfactant in the deposition and in altering the thermoelectric properties of the material.

There is a scope for the development of better p-type material. Although in this thesis, the p-type material properties are enhanced using thermal annealing, there is still a need for better material. For enhancing the performance of the devices, the p-type material should match its performance with its counterpart n-type material. The p-type material properties could be enhanced using different dopant materials like Sn and In. Further studies are required in order to investigate the role of transition metals in enhancing the thermoelectric performance.

Evaluation of thermoelectric material ZT is equally essential, which has been missing in this thesis. The thin films need to be investigated for thermal conductivity in order to calculate the ZT of the material. It would be particularly crucial for our developed n-type CuBiTe and Cu doped Te films as they showcase an amorphous nature and are highly likely to show lower thermal conductivity values, due to which a better ZT material can be obtained. Work on measuring the thermal properties of such thin films on silicon can be carried out using techniques like thermoreflectance method.

Its also equally important to understand the crystal breakdown symmetry of the CuBiTe and Cu doped Te films, which resulted in enhanced thermoelectric properties of the material. This can be investigated by in-situ monitoring of the electrodeposition and in-

situ TEM characterization by varying the energy and understanding the recrystallization of the material. This would be very crucial to understand the material property in much detail. Furthermore, the role of thermal annealing needs to be understood on these deposited materials for their thermal stability.

9.4.2 Development of micro-thermoelectric devices

Lithography constitutes a significant fraction of the overall fabrication cost of the device. Therefore, the number of lithography steps performed for the fabrication needs to be reduced to make the thermoelectric device fabrication cost-effective. Flip-chip bonding approach in this thesis limits the lithography steps. However, it results in increased bonding resistances. Further studies on different bonding materials need to be investigated in order to decrease the contact resistances of the device without affecting the material properties during bonding at elevated temperatures. Also, photoresists play a vital role in the fabrication of the device. Most of the standard photoresist although are stable in acidic medium but are sensitive to the alkaline electrolytes which limit the electrolyte solution which can be used for such kind of material depositions. The search for thicker and high aspect ratio and stable in alkaline electrolytes needs to be taken to ease the use of different alkaline electrolytes as mentioned in the literature and for further densification of the thermoelectric leg pairs for a given footprint of the device.

During device fabrication, due to various baking steps for the photoresists, the thermoelectric materials are also subjected to thermal cycling. This thermal cycling adversely affects the thermoelectric properties of the materials deposited on the device. In order to minimize these effects on the pillars, the wafer level pillar annealing needs to be studied to make the properties of the thermoelectric material stable to these thermal cycling during other processes which the wafer is subjected. The ideal case for the annealing would be the full wafer annealing after the deposition of both the p- and n-type material and before the deposition of the top interconnect material. For long term device working, it's necessary that the interconnect material to be isolated to the thermoelectric material, else the interconnect material can diffuse into the thermoelectric pillars leading to the degradation of the thermoelectric properties. During thermal cycling experience by the device, this effect would be much larger. Therefore, a better barrier material needs to be sandwiched in between the interconnect material and the thermoelectric pillar without increasing the interconnect resistance. Therefore, further work is required in this direction using different material schemes like Ti/Au, W/Au and Sn/Au.